The Pennsylvania State University

The Graduate School

Department of Materials Science and Engineering

OPTIMIZING MEMBRANE ELECTRODE ASSEMBLY

OF DIRECT METHANOL FUEL CELLS FOR

PORTABLE POWER

A Thesis in

Materials Science and Engineering

by

Fuqiang Liu

Submitted in Partial Fulfillment
of the Requirements
for the Degree of

Doctor of Philosophy

Augest 2006

The thesis of Fuqiang Liu was reviewed and approved* by the following:

Chao-Yang Wang
Professor of Materials Science and Mechanical Engineering
Thesis Advisor
Chair of Committee

Stefan T. Thynell
Professor of Mechanical Engineering

Howard W. Pickering
Distinguished Professor of Materials Science and Engineering

Qing Wang
Assistant Professor of Materials Science and Engineering

Gary L. Messing
Distinguished Professor of Materials Science and Engineering
Head of Department of Materials Science and Engineering

*Signatures are on file in the Graduate School.

ABSTRACT

Direct methanol fuel cells (DMFCs) for portable power applications require high power density, high-energy conversion efficiency and compactness. These requirements translate to fundamental properties of high methanol oxidation and oxygen reduction kinetics, as well as low methanol and water crossover. In this thesis a novel membrane electrode assembly (MEA) for direct methanol fuel cells has been developed, aiming to improve these fundamental properties.

Firstly, methanol oxidation kinetics has been enhanced and methanol crossover has been minimized by proper control of ionomer crystallinity and its swelling in the anode catalyst layer through heat-treatment. Heat-treatment has a major impact on anode characteristics. The short-cured anode has low ionomer crystallinity, and thus swells easily when in contact with methanol solution to create a much denser anode structure, giving rise to higher methanol transport resistance than the long-cured anode. Variations in interfacial properties in the anode catalyst layer (CL) during cell conditioning were also characterized, and enhanced kinetics of methanol oxidation and severe limiting current phenomenon were found to be caused by a combination of interfacial property variations and swelling of ionomer over time.

Secondly, much effort has been expended to develop a cathode CL suitable for operation under low air stoichiometry. The effects of fabrication procedure, ionomer content, and porosity distribution on the microstructure and cathode performance under low air stoichiometry are investigated using electrochemical and surface morphology characterizations to reveal the correlation between microstructure and electrochemical

behavior. At the same time, computational fluid dynamics (CFD) models of DMFC cathodes have been developed to theoretically interpret the experimental results, to investigate two-phase transport, and to elucidate mechanism of cathode mixed potential due to methanol crossover.

Thirdly, a MEA with low water crossover has been developed by employing a highly-hydrophobic microporous layer (MPL) to build up hydraulic pressure at the cathode, promoting product water permeation from the cathode to anode to offset water dragged by electro-osmosis. Water crossover through the MEA is further reduced by an anode hydrophobic MPL through facilitating water back diffusion. Under different current densities, the MEA with hydrophobic MPL has consistently low α, several times smaller than those with hydrophilic or without MPL. A simulation study of anode water transport by a two-phase model shows that anode MPL wettability strongly determines liquid saturation in the anode, and thus is identified as playing a crucial role in promoting water back diffusion.

Finally, direct feed of highly-concentrated methanol using the optimized MEA has been successfully demonstrated by a face-feed anode plate, which minimizes methanol crossover by controlling the fuel delivery rate. Using 10 M methanol, a steady-state power density of ~67mW/cm^2 is reached at 60$^\text{o}$C and 175mA/cm^2, which is almost identical to that with 2M methanol.

TABLE OF CONTENTS

LIST OF TABLES

LIST OF FIGURES

NOMENCLATURE

a	Electrochemical area per volume [m^2/m^3]
b	Tafel slope [$mVdec^{-1}$]
$c_{O_2,inlet}$	Oxygen concentration at the inlet in the gas channel [mol/m^3]
$c_{O_2,ref}$	Reference oxygen concentration of cathode kinetics, [mol/m^3]
$D_g^{O_2}$	Oxygen diffusion coefficient, [m^2/s)
E_{rev}	Thermodynamic open circuit potential [V]
E_a^0	Anode standard potential [V]
E_c^0	Cathode standard potential [V]
E_{eq}^0	Overall cell equilibrium standard electromotive force (emf) [V]
E_{Air}^{MeOH}	Cathode performance in DMFC operation [V]
$E_{MeOH/Air}$	Performance in DMFC operation [V]
E_{MeOH/H_2}	Anode over-potential of methanol oxidation [V]
F	Faraday's constant, 96485 [$C\ mol^{-1}$]
$I_{A,lim}$	The anode mass-transport limiting current density [$mAcm^{-2}$]
i_0	Exchange current density [$mAcm_{ECA}^{-2}$]
I_{xover}	The crossover current density [$mAcm^{-2}$]
$I_{xover,oc}$	The crossover current density at open circuit [$mAcm^{-2}$]
$\overrightarrow{j_k}$	Mass flux of phase k [$kg/m^2\ s$]
K	Permeability [m^2]
k_{rk}	Relative permeability of phase k
M^i	Molecular weight of species i [kg/mol]
s	Liquid saturation
L_{Pt}	Pt loading in the CL [$mgPt\ cm^{-2}$]
P	Operating pressure [kPa]
P_{sat}	Saturation pressure of water at cell temperature [kPa]

R	Universal gas constant 8.314 [J mol^{-1} K^{-1}]
$R_{I/C}$	Ionomer to carbon (I/C) ratio
RH	Relative humidity
R_p	Charge-transfer resistance [Ohm cm^2]
R_Ω	Internal ohmic resistance [Ohm cm^2]
S	Stoichiometric parameter
SW	Swelling degree of ionomer upon hydration by weight
t	Time [s]
T	Cell temperature [K]
$\vec{u}$	Velocity [m/s]
V_{oc}	Open circuit potential [V]
X_0	Percolation critical value
$\Delta E_{O_2/air}$	Oxygen gain [V]
ΔG^0	Standard Gibbs free energy of reaction [kJ mol^{-1}]
ΔH^0	Standard Enthalpy of reaction [kJ mol^{-1}]
ΔX_{CL}	Thickness of the catalyst layer [µm]
ΔX_{GDL}	Thickness of the GDL [µm]

Greek symbol

α	Net water transport coefficient
α_c	Transfer coefficient of cathode
$\kappa_{e,0}$	Intrinsic proton conductivity of fully hydrated polymer [S cm^{-1}]
κ_e	Effective ionic conductivity of fully hydrated polymer [S cm^{-1}]
ρ_c	Density of carbon [g cm^{-3}]
ρ_{Nafion}	Density of Nafion [g cm^{-3}]
ρ_{Pt}	Density of Pt [g cm^{-3}]
γ_c	Advection coefficient

λ_k	Relative mobility of phase k
ν	Kinematic viscosity (m^2/s)
θ	Contact angle ($^{\mathrm{o}}$)
σ	Surface tension (N/m)
η	Efficiency or over-potential
η_{fuel}	Fuel efficiency
η_{theo}	Theoretical efficiency
η_{volt}	Voltage efficiency
ϕ_e	Electrolyte potential in the CL [V]
ϕ_s	Electronic potential in the CL [V]
ε_e	Electrolyte volume fraction in the CL
ε_{GDL}	Porosity of the GDL
τ_{GDL}	Tortuosity of the GDL
ξ_a	Anode stoichiometry
ξ_c	Cathode stoichiometry

Acronyms

CCM	Catalyst coated membrane
CDM	Catalyzed Diffusion Media
CL	Catalyst Layer
CO	Carbon Monoxide
CV	Cyclic Voltammetry
DHE	Dynamic Hydrogen Electrode
DMFC	Direct Methanol Fuel Cell
ECA	Electrochemical area
EIS	Electrochemical Impedance Spectroscopy
EOD	Electro-osmotic drag

GDL   Gas Diffusion Layer

I/C ratio   Ionomer to carbon ratio

MEA   Membrane Electrode Assembly

MPL   Micro Porous Layer

OCV   Open-circuit voltage

PEMFC   Proton Exchange Membrane Fuel Cell

RF   Roughness factor

RHE   Reverse Hydrogen Electrode

Subscripts

c Crossover, capillary

CL   Catalyst layer

g Gas

GDL   Gas diffusion layer

l Liquid

MPL   Micro-porous layer

sat Saturation

Superscripts

H_2O Water

MeOH   Methanol

ACKNOWLEDGEMENTS

I extend my sincere gratitude and appreciation to many people who made this Ph.D. thesis possible. I am most grateful and indebted to my thesis advisor, Professor Chao-Yang Wang, for his enthusiastic supervision, assistance, and encouragement during this work. I would like to acknowledge my other committee members, Dr. Howard W. Pickering, Dr. Stefan T. Thynell, and Dr. Qing Wang for being on my committee and their suggestions and insightful comments on my thesis work.

I owe a great deal to my wife, Jie Chen, and my son, Tailai Liu. Their love, encouragement, and understanding have been essential for my success in the Ph.D. program. Sincere thanks also go to my parents for their endless encouragement and support.

Finally, I would also like to thank all others in Electrochemical Engine Center who were not mentioned above and have given me all kinds of help contributing to the success of this work.

Chapter 1 INTRODUCTION

1.1 Background

Fuel cells are electrochemical devices for converting chemical energy stored in fuels (typically hydrogen or alcohols) directly into electrical energy. Fuel cells are usually classified by the type of electrolyte used, and by their operating temperature range. Low-temperature fuel cells include alkaline fuel cells (AFCs), which operate between 100 and 250°C; polymer electrolyte fuel cells (PEFCs); and phosphoric acid fuel cells (PAFCs), operating between 150 and 220°C. High-temperature fuel cells include molten carbonate fuel cells (MCFCs) and solid oxide fuel cells (SOFCs) which operate between approximately 600 to 1000°C.

In the category of PEFCs, there are two kinds of fuel cells: H_2 PEM fuel cells and direct methanol fuel cells (DMFCs), which operate from room temperature to around 100°C. Hydrogen is one of the best reduction agents with very fast reaction kinetics. But as a gaseous fuel, it has low energy density and requires highly pressurized tanks, metal hydride, carbon nanotube or other hydrogen storage materials to achieve higher energy density. Also, hydrogen storage and transportation is not as easy as a liquid fuel. From a practical point of view, methanol is more desirable than hydrogen. The use of liquid methanol as a fuel has the following advantages as compared to hydrogen:

1) Safe handling, easy storage and distribution;

2) Simple operating system without the need for humidification and thermal management;

3) Relatively hydrogen-sense, and high energy density;

4) Inexpensive fuel and compatible with the existing fuel distribution infrastructure;

5) Fast and convenient refueling.

Hence, DMFCs are very attractive power sources for portable applications.

1.1.1 Working principles of direct methanol fuel cells

The working principle and overall reactions of the DMFC is shown in Figure 1.1. The direct electrochemical oxidation of methanol takes place at the anode catalyst layer as follows:

$$CH_3OH + H_2O \rightarrow CO_2 + 6H^+ + 6e^-, \ E_a^0 = 0.016 \ V \qquad [1.1]$$
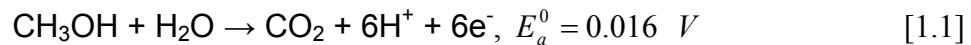
Where methanol reacts with water to produce carbon dioxide, protons and electrons. The protons are transported to the cathode through a proton exchange membrane. The electrons are transported through the external circuit to perform electric work. The electro-reduction of oxygen occurs at the cathode, as described by

$$6H^+ + 6e^- + 3/2O_2 \rightarrow 3H_2O, \ E_c^0 = 1.229 \ V \qquad [1.2]$$
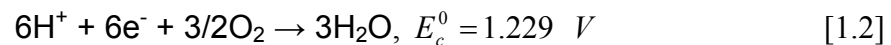
The overall cell reaction is given by

$$CH_3OH + 3/2O_2 \rightarrow CO_2 + 2H_2O, \ E_{eq}^0 = 1.21 \ V \qquad [1.3]$$
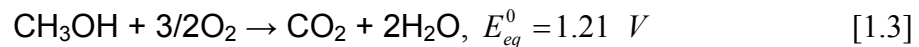
At the same time, as methanol permeates from the anode to cathode through the membrane, it is oxidized at the cathode, leading to a mixed potential, which substantially decreases the cell voltage. This phenomenon is called methanol crossover.

1.1.2 Efficiency of DMFCs

The thermodynamic data of H_2 PEM fuel cells and DMFCs are compared in Table 1.1. The overall DMFC reaction through Eq. 1.3 has thermodynamic data of $\Delta G^0 = -702 kJ/mol$ and $\Delta H^0 = -726 kJ/mol$, which correspond to a theoretical energy density of methanol

$$W = \frac{-\Delta G^0}{3600 \times M} = \frac{702000}{3600 \times 0.032} = 6.09 KWh/kg \qquad [1.4]$$

and to a theoretical energy efficiency under reversible conditions

$$\eta_{theo} = \frac{\Delta G^0}{\Delta H^0} \times 100\% = 96.7\% \qquad [1.5]$$

It can be seen that the theoretical efficiency of a DMFC is almost 100%, much higher than that of a H_2 PEM fuel cell. However, the practical energy efficiency is the product of theoretical energy efficiency, voltage efficiency and fuel efficiency, *i.e.*

$$\eta_{volt} = \frac{V_{cell}}{1.21} \times 100\% \qquad [1.6]$$

$$\eta_{fuel} = \frac{I}{I + I_{xover}} \qquad [1.7]$$

$$\eta = \eta_{theo} \times \eta_{volt} \times \eta_{fuel} = 0.976 \times \frac{V_{cell}}{1.21} \times \frac{I}{I + I_{xover}} \qquad [1.8]$$

where V_{cell}, I and I_{xover} are the cell voltage, operating current density and crossover current density. The practical energy efficiency is relatively low due to high anode and cathode over-potentials and methanol crossover. For example, at cell voltage of 0.4V and fuel efficiency of 80% (*i.e.* 20% methanol crossover), the practical energy efficiency is

only 25.8%. Therefore, fundamental research work is needed to decrease the anode and cathode over-potential as well as to mitigate methanol crossover through the membrane.

1.2   Key Technical Challenges

In spite of all the promising characteristics, several obstacles must be overcome before DMFCs can realize widespread commercial introduction. Key technical challenges associated with DMFCs are:

1) ***Methanol crossover*** reduces the cell performance and energy efficiency (Narayanan et al., 1995; Wang et al., 1996; Heinzel et al., 1999; Ren et al., 2000), primarily because (a) methanol can easily transport through the membrane from the anode to cathode, resulting in a mixed potential at the cathode, and (b) the crossover methanol is wasted without producing electric power. Methanol crossover increases with temperature and concentration of the anode feed. Methanol losses due to crossover can be 40% or higher for some DMFC membranes and design configurations (Johnson, 2004).

2) ***Methanol oxidation and oxygen reduction kinetics*** both limit DMFC performance. The anode kinetics is sluggish, and methanol electro-oxidation cannot occur until the potential is a few hundred milivolts higher than the reverse hydrogen electrode (RHE). It is commonly recognized that intermediates such as carbon monoxide are adsorbed on active catalyst sites, thus blocking further reaction. This means in turn that either power densities are lower, or higher loading of expensive anode catalysts is needed. At the cathode, oxidation of the crossover methanol and oxygen reduction compete for the same catalyst sites, thus deteriorating the cathode performance

(Kauranen, 1996). One important development in future DMFC technology is therefore to identify methanol-tolerant cathode catalysts. In this case, the cathode catalytical activity remains high despite the presence of methanol crossover. Another requirement for the cathode is low air flowrate operation, since water loss from the cell must be controlled and less auxiliary power may be used for portable applications. Under this circumstance, however, removal of product water is inefficient and the cathode catalyst layer must perform well in the presence of slight flooding.

3) *Water management* emerges as a new significant challenge for portable DMFCs. For high energy density, highly concentrated methanol solution or even pure methanol is preferred. However, highly concentrated methanol solution does not contain sufficient water for water crossover from the anode to cathode due to electro-osmotic drag and diffusion. It is thus conventional for DMFCs to use excessively dilute (3-6% by vol.) methanol solution in the anode in order to: (a) limit methanol crossover and hence its detrimental consequences, and (b) supply sufficient water to sustain excessive water crossover to the cathode through the membrane. However, the problem with such a conventional DMFC is that it requires a significant amount of water to be carried in the system, drastically reducing the system energy density.

1.3   Literature survey

To overcome the above-mentioned technical challenges, efforts have been expended to optimize membrane-electrode assemblies (MEAs) and develop new catalyst and membrane materials. The key to resolving the methanol crossover lies in the membrane,

whereas the key to accelerate reaction kinetics lies in the catalyst and MEA, all of which are the subjects of intense research.

1.3.1 MEAs

The performance of a DMFC is strongly affected by electrode/MEA structures as well as their fabrication procedures, making them critical issues in DMFC development. The MEA is the heart of a DMFC, and consists of five layers: two backing layers, two catalyst layers (anode and cathode), and one membrane layer (generally Nafion membrane) serving as the electrolyte. Wet-proofed carbon paper or cloth can be used as the backing. Usually the surface of a backing layer is coated with a thin layer of carbon powder and PTFE mixture, which is called the microporous layer (MPL). The combination of a MPL and a backing layer is called a gas diffusion layer (GDL). The catalyst layer (CL), where the electrochemical reaction takes place, must fulfill three functions: proton conduction, electron conduction and reactant access (Carrette, 2000). The main requirement of a good CL is maximized catalyst/ionomer/reactant interface or triple-phase boundary. Figure 1.2 shows the schematic diagram of a half MEA and the triple-phase boundary. The triple-phase boundary is made by either impregnating the catalyst powder with ionomeric polymer (usually Nafion) before hotpressing onto the membrane, or directly coating the catalyst particles on the surface of membranes (Kocha, 2003).

Accordingly, there are two different MEA configurations: ***catalyzed diffusion media (CDM)*** and ***catalyst-coated membrane (CCM).*** The conventional technology to make CDM, used until a few years ago, consists of ultrasonically mixing catalyst particles and

PTFE emulsion to form a catalyst ink, applying the catalyst ink onto the water-proofed GDL and spraying Nafion solution on the surface, finally followed by a hot-pressing procedure (Aricò, 2001). The function of PTFE in the catalyst layer is to provide a network for gas transport, to remove water generated by fuel cell reaction and to give structure integrity. Later on, this method was modified by directly mixing electro-catalysts with ionomer (Uchida et al., 1995, 1995, 1998; and Shin, 2002) in appropriate solvents (for example, butyl acetate). It is reported that the continuous network of ionomers and mass transport in the catalytst layer increases, which improves the proton conductivity and limiting current density. In CDM, a very large percent of the catalysts are impregnated deeply into the pores of the carbon paper or cloth. Hence, these catalysts are inaccessible for electrochemical reaction and are essentially wasted. Since the binding of the catalyst layer with the membrane is realized by hotpressing, sometimes its internal resistance of the MEA is high.

CCM is prepared by direct application of catalysts onto the membrane (Wilson et al., 1992, 1992, 1995; Ren et al., 1996). In CCM, the catalyst layer is very thin (~ 10 μm) and the thickness of Nafion and electrocatalyst matches with each other. So CCM reduces catalyst waste due to impregnation of the catalyst into the support substrate. This method of directly applying catalyst layers on the membrane offers very high catalyst utilization and improves catalyst/membrane interface. CCM was first used in H_2 PEM fuel cells, since Nafion has sufficient oxygen permeability that a diffusion pathway length of 5-10 μm does not introduce any significant oxygen transport losses through the catalyst layer. In DMFCs, however, sluggish methanol electrochemical oxidation kinetics at the anode require the use of very high catalyst loadings, making the catalyst layer very thick

(>10μm). At the cathode, because there are no special gas channels in the thick catalyst layer, the transport of reactant gas to the reaction sites is retarded at high current densities.

1.3.2   Membranes

Research has focused on three types of polymer electrolyte membranes: perfluorinated (which indludes Nafion), partially fluorinated and non-fluorinated. Nafion, a product of Dupont, is the most commonly used membrane. Nafion has the same backbone as polytetrafluoroethylene (PTFE), with long flexible vinyl ether side chains ending with sulfonic groups (Figure 1.4). The hydrophobic fluorinated backbone of the polymer is believed to promote aggregation of the hydrophilic side chains containing the sulfonic acid groups during processing and/or conversion to acid form (Eisenberg et al., 1990, 1977; Hsu, 1983). Water and methanol molecules can diffuse easily across the membrane through the "ionic clusters", formed by sulfonic groups and water molecules in the membrane. Partially fluorinated membranes, including poly(α, β, β-trifluorostyrene) (Wei et al., 1995; Bassura et al., 2001) and other copolymers, are usually synthesized by grafting fluorinated base polymer films using various techniques. A variety of non-fluorinated ionomer membranes have been proposed as alternative polymer membrane electrolytes such as polyetherketones (Zaidi et al., 2000; Jones et al., 2001), polyethersulfones (Nolte et al. 1993; Wang et al., 2002), polybenzimidazole (PBI) (Wainright et al., 1995; Wang et al., 1996) and polyimides (Gebel et al., 1993) et al. Although they show lower methanol permeability than Nafion, their low proton conductivities and chemical instability limit their applications.

1.3.3   Catalysts

To relieve the CO-poison effect on anode catalyst, Pt must be paired with one or more oxophilic (having a strong affinity for oxygen) metals to form bimetallic or ternary catalyst systems, which are recognized as catalysts that can produce a noticeable enhancement of methanol electro-oxidation at low potentials over pure Pt catalysts. A reaction mechanism based on "bifunctional catalysis" (Watanabe et al., 1975; Gasteiger et al., 1994; and Liu et al., 2004) has been proposed to explain their increased activity. In brief, platinum activates the C-H bond cleavage of methanol adsorbed on the surface. Pt_x-CO species formed in the process (x is supposed to be 3), while strongly held by the Pt surface, can react with oxygen-containing species delivered from the neighboring oxophilic metal sites to form CO_2, thereby releasing the Pt sites for the next round of reaction. The interface between Pt and the oxophilic metal is of utmost importance in the catalysis of methanol electro-oxidation. Although Sn, Ni, Ru, Ge, Os and Mo were suggested (Haner et al., 1991; Markovic et al., 1995, 1996; Chrzanowski et al., 1998, 1998; Iwasita et al., 2000), these O-adsorbing metals may not be stable for long-term applications. At present, Pt-Ru is still considered as the most promising catalyst.

1.4   Motivation and Objectives

Considering the great potential of high-energy power sources and existence of technical barriers, this thesis will focus on optimizing a high-performance DMFC MEA. The first objective is to gain a basic understanding of electrochemical and transport phenomena taking place in DMFCs for portable power. Computational modeling of mass transport and electrochemical kinetics will be used as a guiding tool. The second

objective is to develop and characterize an advanced MEA for portable DMFCs that aims to address the technical challenges described above. Specifically they are: (1) to reduce methanol crossover using an anode barrier; (2) to improve the methanol oxidation kinetics by an optimized anode catalyst layer; (3) to enhance mass transport and eliminate flooding by employing a tailored cathode catalyst layer; and (4) to reduce water crossover from the anode to cathode via highly-hydrophobic micro-porous layers.

Table 1.1 Thermodynamic data of an H_2 PEM fuel cell and a DMFC

Reaction	Temp. (^oC)	ΔH^0 (kJ/mol)	ΔS^0 (J/molK)	ΔG^0 (kJ/mol)	E^0_{eq} (V)	η_{theo}
$H_2 + 1/2\ O_2 \rightarrow H_2O(liq.)$	25	-285.8	-162.4	-237.4	1.23	0.83
$CH_3OH(liq.) + 3/2O_2 \rightarrow CO_2 + 2H_2O(liq.)$	25	-726.3	-80.2	-702.4	1.21	0.97

Anode : $CH_3OH + H_2O \rightarrow CO_2 + 6H^+ + 6e^-$

Cathode : $6H^+ + 6e^- + 3/2O_2 \rightarrow 3H_2O$

Overall reaction : $CH_3OH + 3/2O_2 \rightarrow CO_2 + 2H_2O$
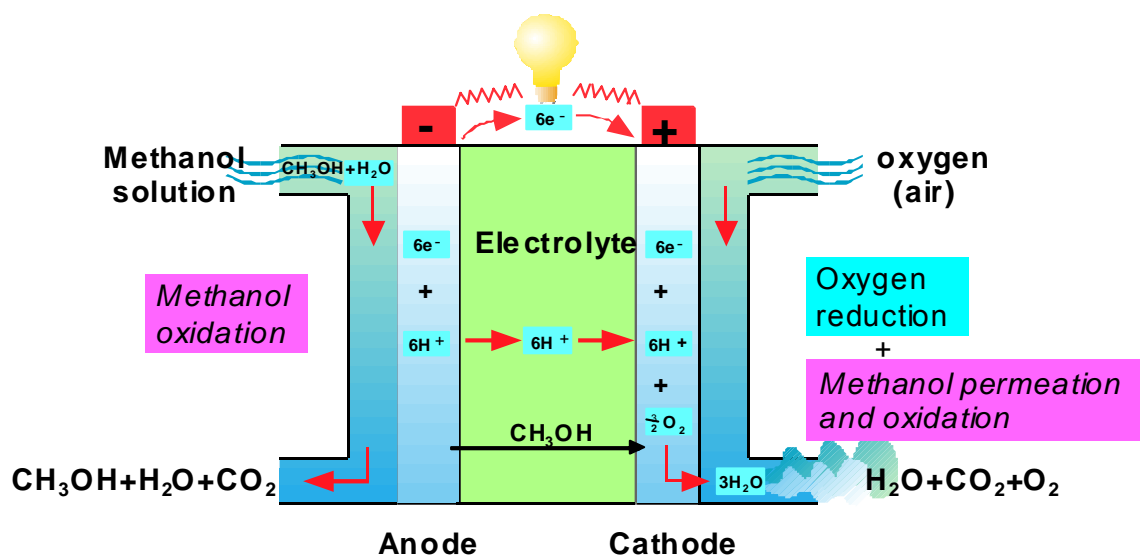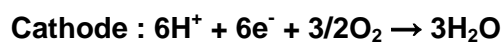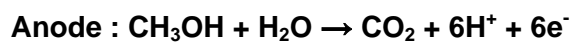
Figure 1.1 Working principle and overall reactions of the DMFC
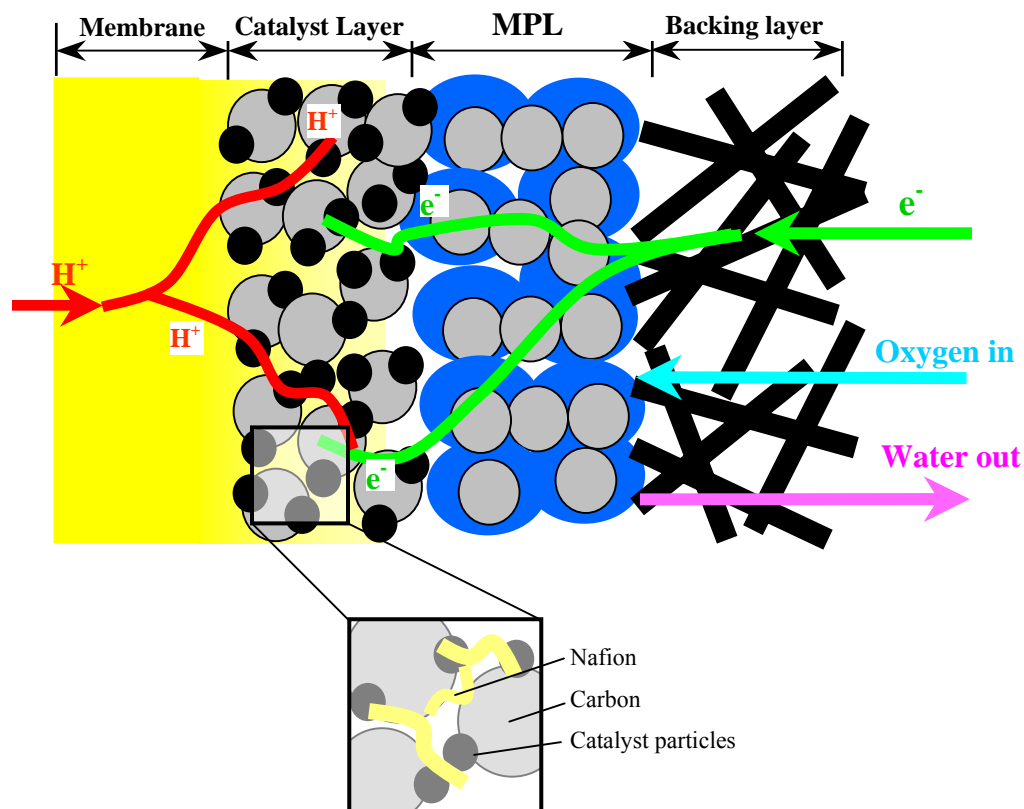
Figure 1.2 Schematic diagram of a half MEA and the microstructure of triple-phase boundary. The half MEA includes a membrane, catalyst layer, MPL, and carbon paper backing layer.
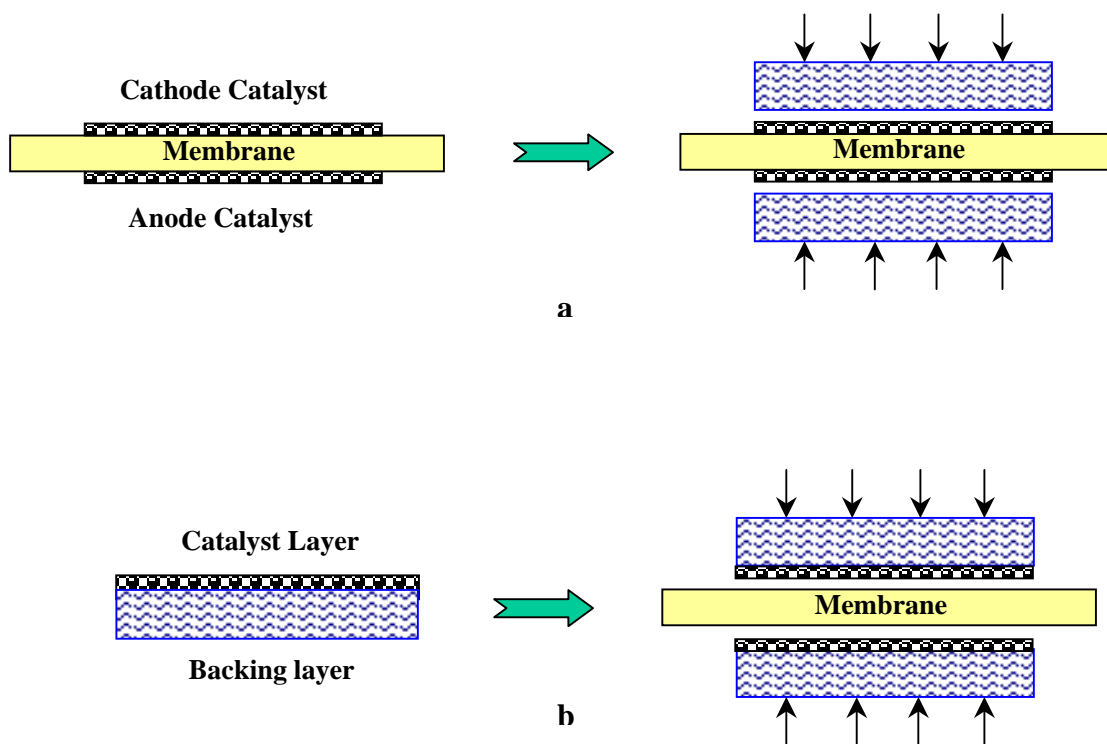
Figure 1.3 Schematic diagram of two different MEA configurations: (a) CCM and (b) CDM.

$$-\{(CF_2\text{-}CF_2)_n(CF_2CF)_m\}-$$

$$\begin{bmatrix} O \\ | \\ CF_2 \\ | \\ CF\text{-}CF_3 \\ | \\ O \\ | \\ CF_2CF_2SO_3^-H^+ \end{bmatrix}_p$$
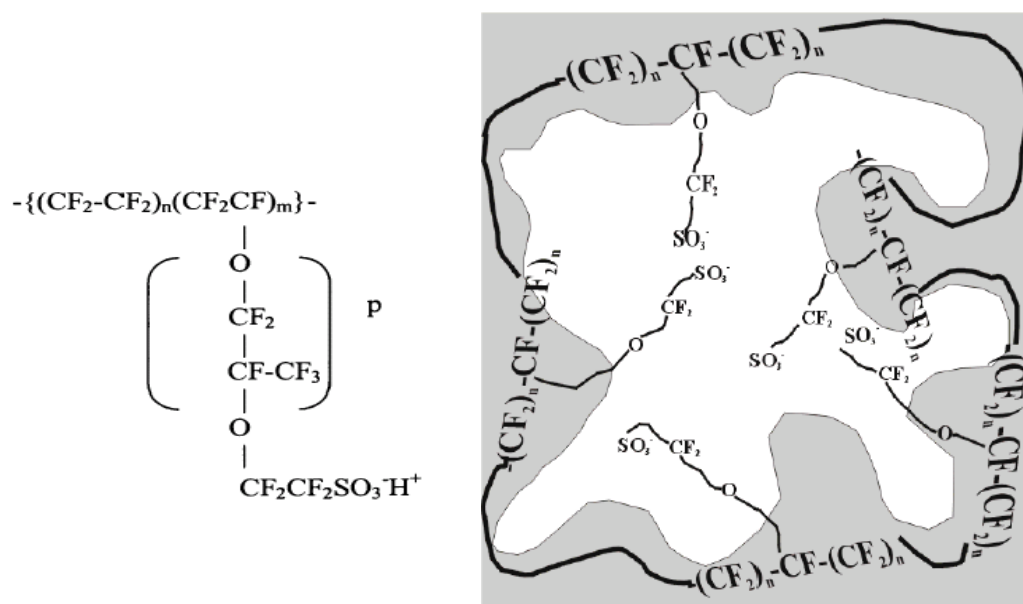
Figure 1.4 Chemical formula and schematic microstructure of Nafion
(Carrette et al, 2001).

Chapter 2 INTERFACIAL PROPERTIES OF ANODE CATALYST LAYER

2.1   Introduction

The presence of ultra-thin ionomer films covering the catalyst particles is important for constructing highly active electrodes. Extended triple-phase boundary or ionomer/catalyst interface is the prerequisite for high cell performance. Wilson and coworker at Los Alamos developed a method in which the catalyst and Nafion were mixed together, and the resultant catalyst ink was applied to a PTFE decal and was subsequently transferred onto a membrane or directly coated on a membrane (Wilson et al., 1992, 1992, 1993, 1993, 1995). It is reported that this method provided better power density and cell internal resistance compared to the conventional method, largely due to an extended catalyst/ionomer interface and hence a dramatic improvement in catalyst utilization. Subsequently, as a preliminary step toward understanding the interaction of the ionomer and catalyst, Uchida et al. (1995, 1995, 1998) reported that good cell performance can be obtained by using solvents with an intermediate dielectric constant of $3 < \varepsilon < 10$ (e.g. butyl acetate), which form a colloid of Nafion. This is due to increased interaction of Nafion and catalyst and extended reaction interface as compared to using high-dielectric-constant solvents such as water or alcohols. Others (Yang et al., 2003, Bender et al., 2003) reported that the electrode prepared using high dielectric-constant solvents could also produce superior performance over those made with lower dielectric constants. Aricó et al. (1998) tried to use XRD, SEM, and TEM to investigate the Nafion/catalyst interface, but no interaction between catalyst and ionomer was detected

and no significant interconnected network of Nafion micelles inside the catalyst layer was observed. To date, a basic understanding of the microstructural interface in electrodes and the influence of solvents is still incomplete.

One of the significant parameters affecting the cell performance is the ionomer-to-carbon (I/C) ratio. The influence of Nafion content on performance of fuel cells has been the subject of much investigation (Lee et al., 1998; Passalacqua et al., 2001). An I/C ratio of 30% is preferred to achieve minimum ionic resistance and maximum contact of ionomer with Pt particles (Kocha, 2003). Even maintaining this I/C ratio, cell performance of MEA fabricated using identical catalyst inks varies significantly for different methods. This may be due to variation in catalyst/ionomer interfaces formed using different fabrication procedures. Thus, in most cases it is difficult to definitively establish the impact of fabrication parameters, such as solvents and Nafion content, upon observed properties such as fuel cell performance and catalyst/ionomer interface.

Although extensive studies have sought to increase the catalyst/ionomer interface and to fabricate high-performance MEAs, due to the complex structure of the catalyst layer and MEA, the precise nature of catalyst/ionomer interface and the method of maximizing it are still unclear. This problem is further complicated by the fact that changes of interfacial properties and interfacial structure of catalyst/Nafion take place during the process of cell conditioning.

In this chapter, variation of interfacial properties during cell conditioning and the influence of heat treatment of ionomer on the anode catalyst layer performance, methanol crossover and catalyst/ionomer interface were investigated. Anode polarization, CO-stripping cyclic voltammetry (CV) and electrochemical impedance spectroscopy (EIS)

measurements were taken to probe the internal structural and interfacial variations during cell conditioning. It is hoped that the results obtained herein will contribute to the understanding of the optimized CL microstructure and in particular, the ionomer/catalyst interface.

2.2 Experimental

2.2.1 MEA fabrication

Pretreatment of the Nafion 112 membrane, preparation of MEAs, and the experimental hardware have been detailed in previous publications (Lim and Wang, 2003; Lu and Wang, 2004). A brief description is given here.

Both anode and cathode backing layers were 20% FEP wet-proofed carbon paper (Toray TGPH-090, E-TEK) of 0.26 mm in thickness. A mixture of Vulcan XC72R carbon black and 40% dry weight TEFLON emulsion (TFE 30, Dupont) was coated on the carbon paper using a gap-adjustable doctor blade to form a MPL. Subsequently, the coated carbon paper was dried in an oven at 100°C for 30 min and then at 360°C for 15 min. Carbon and PTFE loadings of the MPL were controlled at 2mg/cm^2.

A commercial 5 wt.% Nafion solution (EW 1100, Aldrich) was modified by addition of diluted sodium hydroxide solution and a viscous organic solvent to make solvent-substituted Nafion solution. This Nafion solution was mixed with unsupported Pt/Ru black (HiSPEC 6000, Pt:Ru = 1:1 atomic ratio, Alfa Aesar) in a nitrogen-protected environment. The resultant slurry was coated on the MPL using the doctor blade to form the anode catalyst layer. The loadings of Pt/Ru and Nafion in the anode catalyst layer were controled at 5 and 1.2 mg/cm^2, respectively. The cathode was made by the same

method. The 40 wt.% Pt/C (E-TEK) was used and the loadings of Pt and Nafion in the cathode catalyst layer were about 1.3 and 1 mg/cm^2, respectively. After the catalyst slurries were coated onto the MPL, the anode and cathode were cured at 160$^{\text{o}}$C in a nitrogen-filled vacuum oven. By this solution cast and post-heat-treatment process, the ionomer (Nafion) in the catalyst layer forms a durable and insoluble film around the catalyst particles, resulting in a more robust MEA. After being re-protonated to hydrogen form of Nafion by using 0.1 M sulfuric acid solution, the anode and cathode were hotpressed to a pretreated Nafion 112 membrane at 125$^{\text{o}}$C and 100 kgf/cm^2 for 3 min.

2.2.2 Micro-structural analysis

Scanning electron microscopy (SEM, Philips 420 ST)) was used to analyze the thickness and surface of the anode catalyst layer. In order to observe the change in surface morphology before and after wetting the PtRu catalyst layer with methanol solution, a high-resolution 3-CCD video camera (Sony DCR VX2000) was used instead. After the anode catalyst layer was fully hydrated in 2M methanol solution, the surface was analyzed by the high-resolution CCD camera quickly to prevent dehydration of ionomer in the anode catalyst.

2.2.3 Electrochemical studies

The cell consists of anode and cathode graphite plates, which act as current collectors and contain a flow-field in the surface of each plate contacting the MEA to supply the fuel and oxidizer respectively (Figure 2.1). After the MEA was installed in the cell, 2M methanol solution was fed into the anode inlet at flow rate of 3 ml/min by a

peristaltic pump without pre-heating and back pressure, after which the cell temperature was increased. The conditioning time was counted after the desirable cell temperature was reached.

To investigate the interfacial property changes during cell conditioning, electrochemical characterization, including EIS and CO stripping CV, was conducted at room temperature (25°C) using a Solartron 1278 electrochemical interface in conjunction with a Solartron 1260 frequency response analyzer. In EIS experiments, the working electrode was linked to the PtRu anode side, fed with humidified nitrogen, and the reference and counter electrodes were connected to the Pt cathode side, which was fed with humidified hydrogen. The flow rates of H_2 and N_2 were approximately 100 ml/min. EIS spectra were obtained by applying a 10 mV sine wave in the frequency range of 0.1Hz to 10KHz. CO-stripping CVs of the PtRu anode catalysts was carried out at room temperature using a 5-cm^2 graphite cell, with N_2, or CO plus N_2 fed to the anode serving as the working electrode. Humidified H_2 was fed to the Pt cathode at 100ml/min and zero back pressure, which acted as a counter and pseudo-reference electrode (dynamic hydrogen electrode, DHE). Humidification temperatures of the N_2, or CO plus N_2 were $40\,^{o}$C. CO was adsorbed onto the PtRu catalyst surface by feeding 1000ppm CO in N_2 at 500ml/min (zero back pressure) through the anode for 30 min, while holding the PtRu catalyst electrode potential at 0.1 V versus the DHE. The gas was then switched for 10 min to N_2 at the same flow rate, with the potential still held at 0.1 V to remove any CO from the gas phase. Then the potential was scanned from 0.1 V to 0.85 V at 5 mV/s, to record the CO stripping CVs. The anode polarization curves were measured by feeding

room-temperature humidified H_2 to the cathode side as the preudo-reference electrode, with respect to which the voltage was applied.

To investigate the influence of heat-treatment of ionomer in the anode catalyst layer on DMFC performance, non-humidified, 15 psi room-temperature air was fed into a cathode inlet at a flow rate of about 600 ml/min when the cell polarization curves were measured. After each scan, the MEA was soaked with static methanol solution at 80°C without airflow or load to fully hydrate the polymer membrane. Methanol crossover and anode polarization curves were measured by feeding humidified N_2 and H_2 into cathode inlet, respectively. Cell performance, methanol crossover and anode polarization curves were obtained by using an Arbin BT +4 Testing System in a galvanodynamic polarization mode with a scan rate of 3mA/s.

2.3   Results and discussion

2.3.1   Variations in interfacial properties of the anode during cell conditioning

For all results to be presented in this section, the catalyst-coated anode used was cured at 160°C in a nitrogen-filled vacuum oven for 40 min. The cathode remained in the oven overnight.

2.3.1.1   SEM and optical micrograph

Figures 2.2a and 2.2b show SEM micrographs of the cross-section and surface of the anode catalyst layer. Figure 2.2a shows a planar MPL with an average thickness of 30 μm over a carbon paper backing. On top of the MPL, an anode catalyst layer of about 20 μm

in thickness consisting of unsupported PtRu black and Nafion polymer is observed to be more porous than the MPL. Figure 2.2b displays the microstructure of the anode catalyst layer in high magnification. The diameter of the agglomerates formed by PtRu black and Nafion, is found to be from several μm to about 10 μm. Some small pores in the agglomerates can be observed in diameter smaller than 1 μm. Watanabe *et al.* (1985) had characterized the microstructure of a gas-diffusion electrode, reporting that the catalyst layer had two distinctive pore-size distributions with a boundary at ca. 0.1 μm. The small pores (primary pores) were identified within primary particles forming agglomerates, and the larger pores (secondary pores) were between the agglomerates. The results of the present study are consistent with those reported, with the diameter of the secondary pores in the range of about 5 ~ 6 μm.

Figures 2.3a and 2.3b show optical micrographs of the surface of the anode catalyst layer before and after being fully hydrated by 2M methanol solution. In Figure 2.3a, large pores and uniform cracks (mud cracking), introduced into the catalyst layer due to volume shrinkage of the catalyst slurry during annealing, can be observed. In the fully hydrated state, however, as shown in Figure 2.3b, some of these pores and cracks disappear, due to the swelling and expansion of Nafion ionomer after full hydration. In operation of DMFCs, the anode catalyst layer remains in contact with methanol solution, so the Nafion ionomer in the catalyst layer expands and thus the porosity in the catalyst layer is reduced. Its influence on DMFC performance will be discussed in the next subsection.

2.3.1.2   Electrochemical characterization of anode during cell conditioning

Before use in fuel cells, MEAs require a conditioning process to obtain repeatable performance. The conditioning process is accompanied by the time-dependant swelling behavior of ionomer and interfacial property variations in the catalyst layer.

This experiment recorded anode polarization measurements after the exposure to 2M methanol solution at room temperature. CO-stripping CVs and EIS were measured sequentially at various points in time during this conditioning process. The results of EIS, anode polarization curves, and CO-stripping CVs measured over time are shown in Figure 2.4 through 2.6.

Figures 2.4a and 2.4b show the EIS spectra and internal cell resistance variations (intersects of EIS spectra with the real axis) measured over time during cell conditioning, respectively. The internal resistance initially dropped dramatically, from 0.322 $\Omega.cm^2$ at 30 min, to 0.246 $\Omega.cm^2$ at 568 min. Beyond 568 min the curve begins to level off, indicating a negligibly small variation with time or attainment of steady state.

It is indicated by Boyer $et\ al$. (1998) that the specific proton conductivity of a catalyst layer prepared with recast Nafion is proportional to the volume fraction of Nafion in the catalyst layer. Saab $et\ al.$ (2002) reported that when swelled by water vapor, the ionic resistance in the catalyst layer decreased, while the electronic resistance increased. In the process of conditioning, the Nafion ionomer in the catalyst layer continues swelling with time until steady state is reached, therefore the effective ionic and electronic conductivities in the catalyst layer vary: the ionic resistance decreases, while the electronic resistance increases with time. In the present experiment, the diameter of the high-frequency semi circles expanded with time, a trend unlike that

reported in the literature where at high frequencies, a Warburg-like region (45° slope) corresponding to ion migration through the catalyst layer became smaller as the ionic resistance decreased (Lefebvre et al., 1999; Murth, 2002; and Kocha, 2003). These contrasting results may be attributed to some unexpected interfacial property changes occurring during methanol conditioning or different electrode structures employed.

Figure 2.5 shows anode IR-corrected polarization curves as a function of conditioning time after correcting the cell ohmic drop. The anode potentials shift significantly to lower values over time; however at 2119 and 3516 min, the anode voltages continue shifting to lower values at low current density region (< 60 mA/cm^2). Beyond 60 mA/cm^2, however, the voltages curve upward very steeply, exceeding previous values. The curves beyond 3516 min remains largely unchanged with time, and is not plotted here.

Figure 2.6 shows the CO stripping CV curves measured over time during cell conditioning with methanol, indicating a trend of significant broadening and negative shifting to lower cell voltage. For example, the peak potential shifts to 0.4355 V versus DHE after about 3516 min compared to 0.4706 V initially. Interestingly, the integrated areas under the peak do not change with conditioning time within the experimental error. Ha *et al*. (2002) observed similar phenomenon when using H$_2$ and methanol to condition formic acid fuel cells: the methanol-conditioned anode showed a CO-stripping peak broadening and negative shifting compared with the H$_2$-conditioned anode.

CO-stripping peak potential can be correlated to Ru surface content, and can be used as an in-situ tool to probe the PtRu anode surface composition (Dinh et al., 2000). According to the calibration curve (Dinh et al., 2000) at the same temperature (25$^{\mathrm{o}}$C) and

scan rate (5mV/s), the potential of 0.4706 V and 0.4355 V (Figure 2.6) observed at 30 min and 3516 min correspond to PtRu metal alloy with Ru surface content of ~15% and 45%, respectively. Note here that the average bulk composition of the as-received catalyst is Ru:Pt= 50:50. It is thus shown that Ru oxides at the catalyst surface can be reduced continuously during cell conditioning. The near constant integrated areas under the CO-stripping peaks and broadened peak shapes indicate a stable number of PtRu bimetallic alloy surface sites, yet the surface composition distribution is broadened. It appears that reduction of Ru oxides and possible subsequent PtRu alloying occur in the DMFC anode during cell conditioning.

Combining the data shown in Figure 2.5 and Figure 2.6, the variation in anode polarization curves during cell conditioning can be explained by the surface composition change of the PtRu catalyst. Surface Ru enrichment can enhance the kinetics of methanol oxidation, as indicated by the negative shift of the peak potential and onset potential of CO-stripping CVs. When the potential scans beyond the peak potential, however, metal oxides (Li et al., 2002) or weakly absorbed intermediates (Gojković, 2003) form on the PtRu surface to prevent further reaction of methanol, causing the abrupt increase of anode potential at higher current density region or what is known as the limiting current. The porosity loss in the anode catalyst layer caused by Nafion swelling can also cause the mass transport limiting current, as will be elaborated in the next section.

2.3.2 Influence of heat-treatment of ionomer on the anode

To investigate the influence of heat-treatment of ionomer in the anode catalyst layer on the cell characteristics, two different MEAs, MEA-1 and MEA-2, were prepared.

Anodes of MEA-1 and MEA-2 were cured in vacuum for 40 and 60 min, respectively. The cathodes of the two MEAs were identical and were treated in the oven overnight.

2.3.2.1   Performance variation in two different MEAs during conditioning

Variations of performance over time for the two MEAs are plotted in Figure 2.7. The first scans of the two MEAs (at 3rd min for MEA-1, 4th min for MEA-2) are almost identical. With time, however, the performance of MEA-1 improved and finally developed a very apparent limiting current phenomenon. For MEA-2, the changes are not so apparent, with no identifiable limiting current phenomenon. Beyond 1386 and 1225 min for MEA-1 and MEA-2, respectively, the performance of the two MEAs remained unchanged with time and can maintain stable performance for days. Performance beyond these time limits can be considered as stable and therefore no polarization curves are plotted here.

Figure 2.8 shows the plot of current densities over time at the cell voltages of 0.45V, 0.4V, 0.3V, 0.25V and 0.2V. In the first 100 minutes, the current densities increase dramatically over time, with MEA-1 changing faster. Beyond 500 minutes, the current densities for MEA-2 at higher cell voltages remain unchanged with time, and the current densities at lower cell voltages increased somewhat. On the contrary, for MEA-1, the current density at 0.3V cell voltage remains almost unchanged with time beyond 100 minutes during conditioning. What is most interesting is that the current density variations with time at higher cell voltages of 0.4V and 0.45V show different trends than those at lower cell voltages of 0.2V and 0.25V. At lower cell voltages, the current densities continue to increase throughout conditioning, while at higher cell voltages, the

current densities first increased very quickly followed by a plateau, and then decreased. For example, the current density at 0.2V cell voltage increased from 470 mA/cm^2 at 3 min to 700 mA/cm^2 at 636 min and then dropped down to less than 600 mA/cm^2 at 1375 min. The limiting current density of MEA-1 after conditioning is only slightly above 600mA/cm^2.

Besides the surface properties of catalysts, limiting current phenomenon can be caused by mass transport limitation of reactant or proton migration through the ionomer of the electrode. Proton migration cannot provide a reasonable explanation for the limiting current phenomenon observed in this experiment. The anode backing and MPL can serve as a methanol barrier (Ren et al, 2000; Lim and Wang, 2003; Lu and Wang, 2004), but in this case, they cannot explain the increasingly severe limiting current phenomenon over time using the same anode backing and MPL. As discussed above, the limiting current may be caused by a combination of surface Ru enrichment and decrease of porosity in the catalyst layer. The influence of surface Ru oxide reduction on anode polarization has been discussed previously, thus only the influence of the hydration of ionomer is considered here.

Dry Nafion membranes are composed of ionic clusters dispersed in a perfluorinated matrix which are fused together in the catalyst layer fabrication. The swelling behavior of these polymers is very sensitive to external conditions, such as temperature, relative humidity, equilibrating solution, and heat treatment history (Rollet, 2001). In these membranes, phase separation between the hydrophobic fluorocarbon backbone and the hydrophilic sulfonic acid groups occurs. Nafion recast at low temperature has very low crystallinity, resulting in high solubility and inferior mechanical properties (Yeo, 1986;

Gebel et al., 1987, 1993; Moore et al, 1998), but with annealing of the solution-recast films at high temperature, the fluorocarbon chains in the polymer film can again fuse together to form a durable and insoluble layer (Gebel et al., 1987; Moore et al, 1998; Liu et al., 2003). The size of the clusters formed by ions and water molecules in the anode catalyst layer tends to increase when contacting methanol solution, but the extent of growth is limited by the covalent bonds between these clusters and crystalline fluorocarbons. Extended or high-temperature heat treatment can increase the crystallinity of fluorocarbon, reducing the swelling of ionic clusters of ionomer in catalyst layers. In this work, the ionomers in the anode catalyst layer were cured for a selected time of 40 min and 60 min for MEA-1 and MEA-2, respectively. So the crystalline contents of the ionomers in the anode catalyst layers of the two MEAs are different: the 60-min-treatment anode had higher crystallinity than that with the 40-min-treatment. Thus, for MEA-2 the ionomer in the anode catalyst layer could not swell appreciably, while for MEA-1, a larger degree of swelling due to low crystallinity was evident.

When contacting methanol solution, the anode catalyst layer would swell with time, but as the volume increases of the catalyst layer are limited by the anode backing, GDL and polymer electrolyte membrane on both sides, it tends to compress itself and possibly reduce the pore size and porosity. The anode catalyst layer of MEA-1 is much denser than that of MEA-2. Limiting current phenomenon of MEA-1 is attributed to a very dense anode structure. These experimental results indicate that in addition to anode backing and MPL, the anode catalyst layer can also act as a methanol barrier.

2.3.2.2   Anode polarization and methanol crossover measurements

Figure 2.9 presents the anode polarization curves of the two MEAs after conditioning. The anode of MEA-1 performs better than that of MEA-2 at current density below ca. 550 mA/cm^2, but at higher current density, the potential versus DHE increases dramatically. Beyond current density of 550 mA/cm^2, the anode of MEA-1 showed considerably more severe limiting current phenomena. Uchida *et al.* (1998) found that increasing the amount of Nafion increases the catalyst coverage, fills the pores and decreases the pore volume, since the polymer penetrates only into the secondary pores between the agglomerates of catalyst particles. As discussed earlier, the ionomer in MEA-1 swelled more than MEA-2, causing the secondary pores to be reduced and hence, a lower mass-transport limiting current.

Figure 2.10 displays the methanol crossover measurements of the two MEAs after conditioning. The oxidation current increases with the potential applied at the cathode side fed with room-temperature humidified N_2, until a limiting current occurs. The limiting current corresponds to the oxidation current of the entire cross-over methanol from the anode to cathode. The methanol crossover current densities of MEA-1 and MEA-2 are 395 and 455mA/cm^2, respectively. MEA-1 shows a smaller methanol crossover current than MEA-2, which can be explained by the much denser anode structure of MEA-1.

The polarization curves and power densities of the two MEAs after conditioning are compared in Figure 2.11. At 0.4V, MEA-1 reaches a current density of 350 mA/cm^2, corresponding to 140 mW/cm^2; while MEA-2 produces only 225 mA/cm^2 and power density of 90 mW/cm^2 at the same cell voltage. By comparing Figure 2.9 and Figure

2.11, it is unlikely that the slight superior anode polarization behavior of MEA-1 over MEA-2 can explain the large performance difference between the two MEAs, assuming that the cathodes of the two MEAs behave identically. Instead, this can be explained by the larger methanol crossover of MEA-2, since at lower current densities (higher cell voltage), there is a large amount of methanol crossover from the anode to cathode.

The methanol crossover current density can be mathematically formulated by a simple relation between the crossover current, I_{xover}, and the anode mass-transport limiting current density, $I_{A,\lim}$ (Lu and Wang, 2005). That is:

$$I_{xover} = I_{xover,oc}(1 - \frac{I}{I_{A,\lim}}) \qquad [2.1]$$

where $I_{xover,oc}$ is the crossover current density at open circuit, and I the operating current density. The anode limiting current density of MEA-1 is about 610 mA/cm^2, while that of MEA-2 is not so well defined, having an approximate value of 750 mA/cm^2. According to Eq. 2.1 and using the methanol crossover rate at open circuit in Figure 2.10, the crossover current densities at 0.4 V for the two MEAs are 168 and 319 mA/cm^2, respectively. The methanol crossover current of MEA-2 nearly doubles that of MEA-1. In DMFCs, the fuel efficiency due to methanol crossover is defined in Eq. 1.8 and it follows that the fuel efficiency for MEA-1 reaches 68% compared with only 41% for MEA-2.

In this work, a thin Nafion membrane (Nafion 112, 50 μm) was used. A thin membrane reduces the cell internal resistance, but increases methanol crossover as well. The crossover methanol from the anode to cathode not only reduces fuel efficiency, but also deteriorates cathode performance. The larger methanol crossover is the major reason that causes the inferior performance of MEA-2 compared to MEA-1 at higher cell

voltages. The performance of a DMFC is controlled by the anode polarization, cathode polarization and methanol crossover through the polymer electrolyte membrane. Thus, controlling the heat-treatment of ionomer in the anode catalyst layer provides a useful tool to optimize these factors in order to attain high DMFC performance, high fuel efficiency and thus high energy efficiency.

2.4   Summary

During cell conditioning, the Nafion ionomer in the catalyst layer expands and hence the pores in the catalyst layer shrink, leading to lower anode potential in the low current density region and development of severe limiting current. The internal resistance initially drops dramatically but eventually levels off, indicating that a steady state of ionomer swelling in the catalyst layer has been reached.

It appears that Ru oxides at the catalyst surface can be reduced continuously during cell conditioning. The near constant integrated areas under the CO-stripping peaks and broadened CO-stripping shapes indicate that the number of PtRu bimetallic alloy surface sites does not vary, but the surface composition distribution broadens.

Heat-treatment can have a major impact on the characteristics of anodes in DMFCs, since heat-treatment influences the ionomer crystallinity and hence affects its swelling behavior. The 40-min-cured anode with low ionomer crystallinity swells more during cell conditiong and creates a much denser anode structure, thus giving rise to higher methanol crossover resistance and different anode polarization characteristics when compared with the 60-min-cured anode. Various characterization data and our analysis suggest that heat treatment influences primarily the transport properties of the anode, while the interfacial

properties between the catalyst and ionomer, i.e. on the triple-phase boundary, remain unaltered. Future work is needed to further assess the implication of heat treatment on the anode long-term performance as the present results are concerned with beginning-of-the-life behaviors only.

During cell conditioning, the enhanced kinetics of methanol electrochemical oxidation and severe limiting current phenomena are due to the combination of variation in time-dependent interfacial properties and swelling behavior of ionomer in the anode catalyst layer.
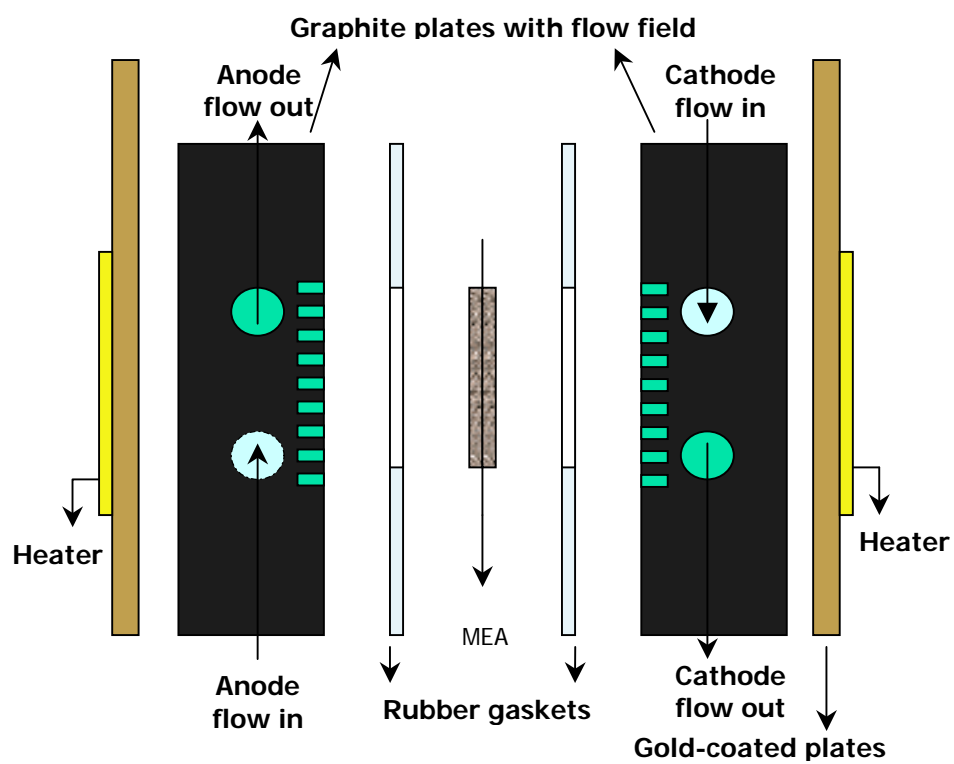
Figure 2.1 Single cell hardware setup.
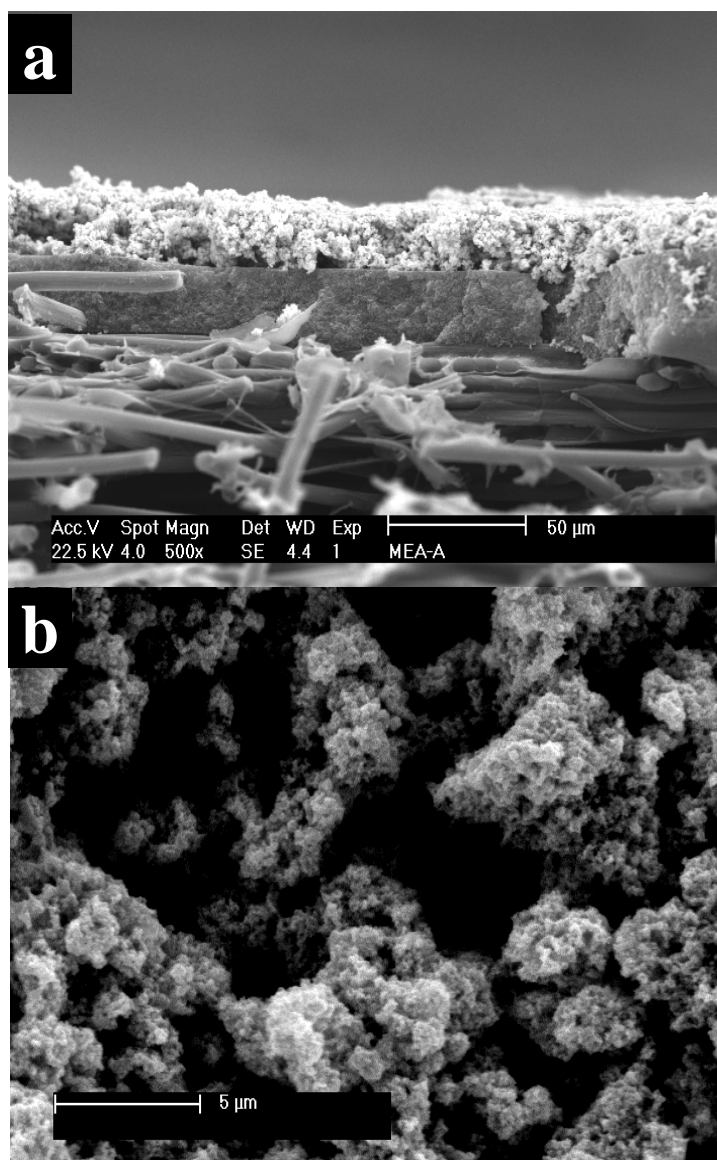
Figure 2.2 SEM micrographs of: (a) cross-section and (b) surface of anode catalyst layer. The anode electrode was cured at 160°C in a nitrogen-filled vacuum oven for 40 min. Unsupported PtRu was used as the anode catalyst.
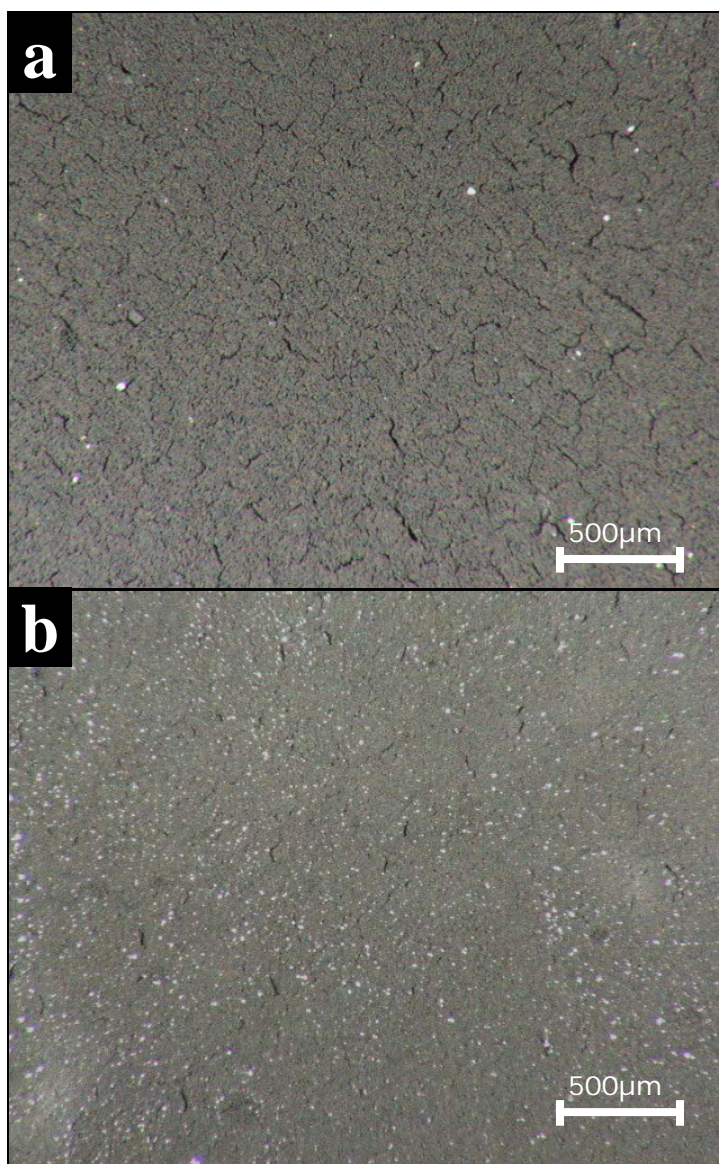
Figure 2.3 Optical micrographs of anode catalyst surface: (a) dry state and (b) fully-hydrated state by 2M methanol solution at room temperature.
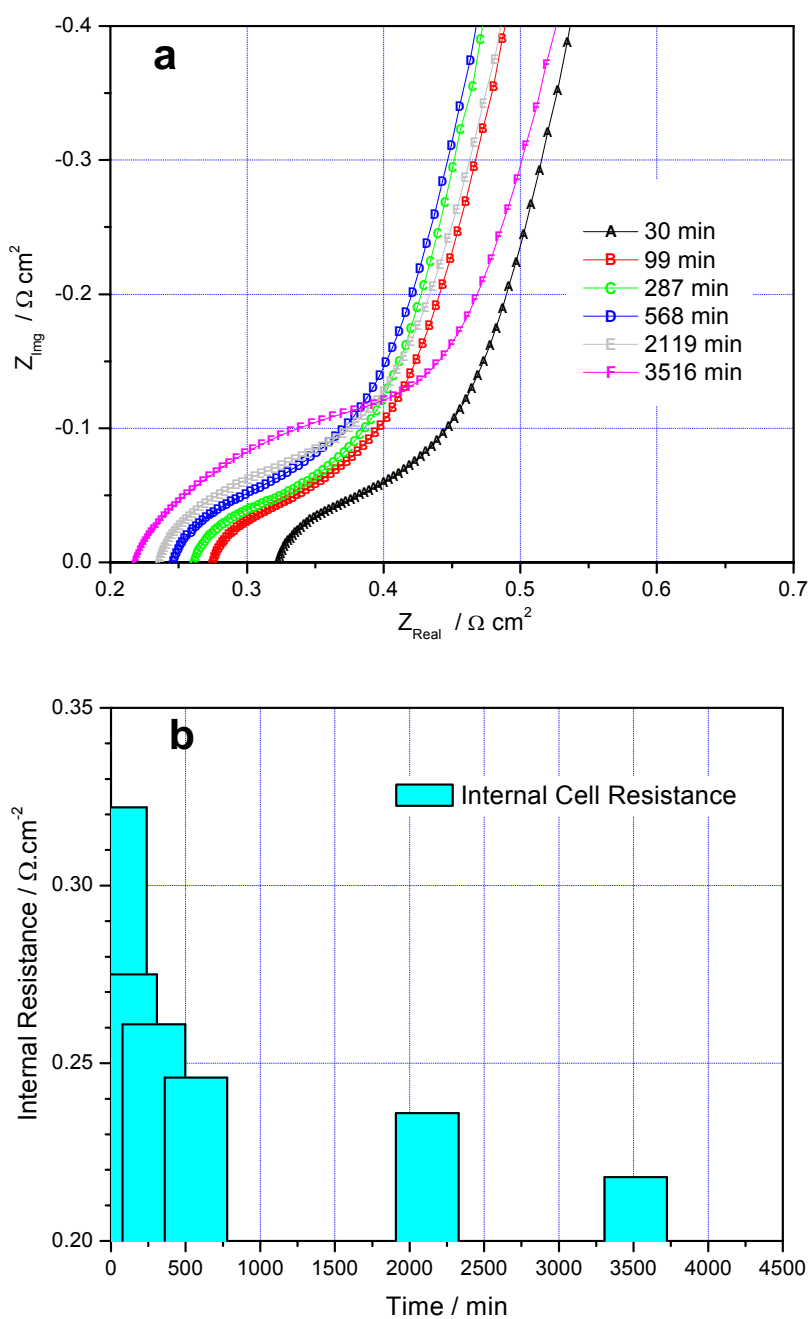
Figure 2.4 (a) Nyquist plots as a function of conditioning time and (b) internal cell resistance versus conditioning time. The cell was operated under 25°C, using humidified H_2/N_2 at cathode and anode, respectively. The frequency range was from 100KHz to 0.1 Hz.
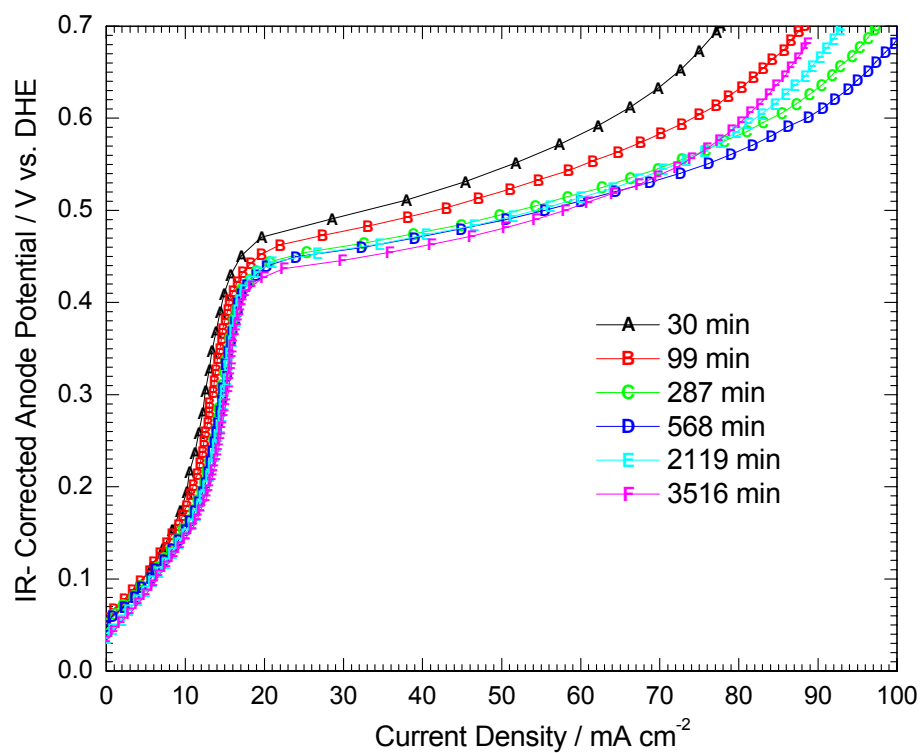
Figure 2.5 IR-corrected anode polarization curves recorded over time during cell conditioning. The experiment was operated at 25°C, using 2M methanol and 3mA/s scanning rate.
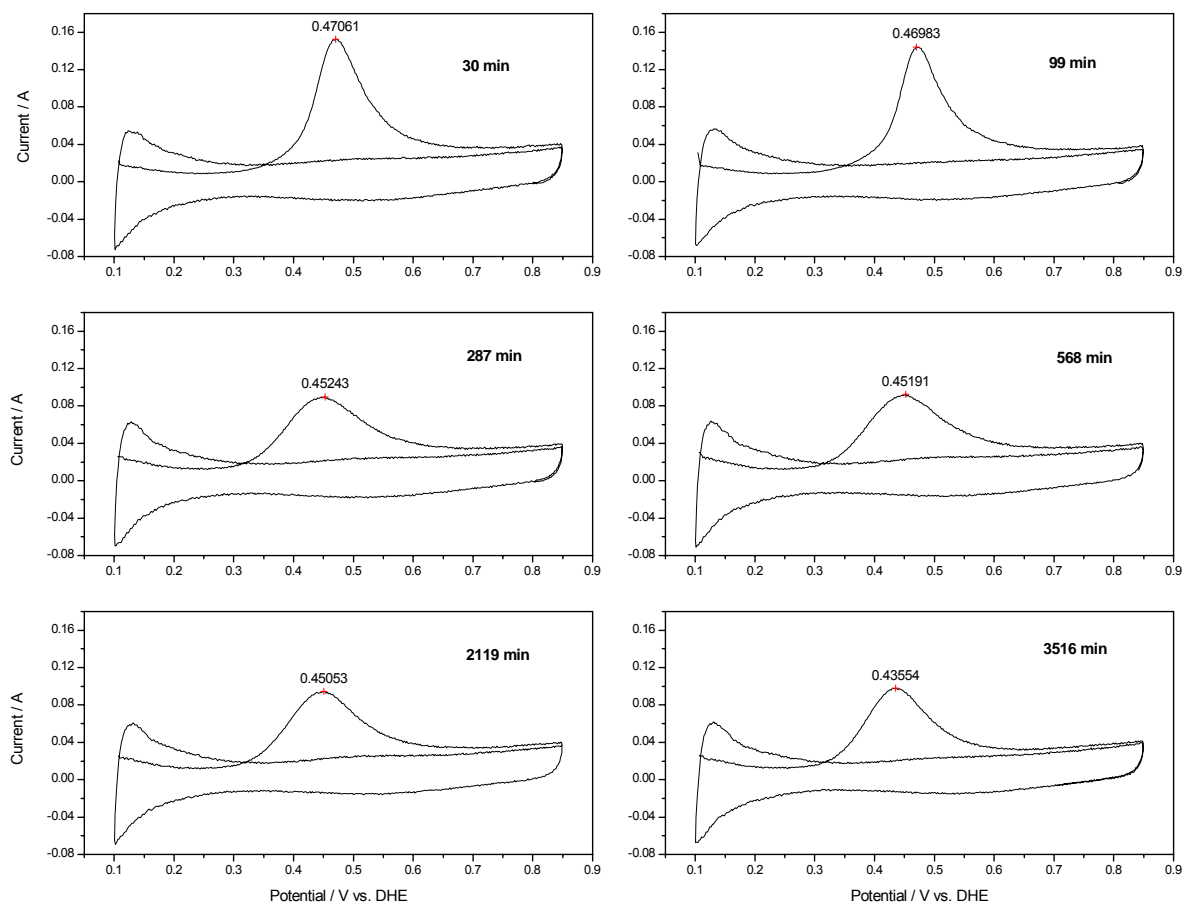
Figure 2.6 CO stripping CVs curves measured over time during cell conditioning using methanol at scan of 5 mV/s, in N_2 environment.
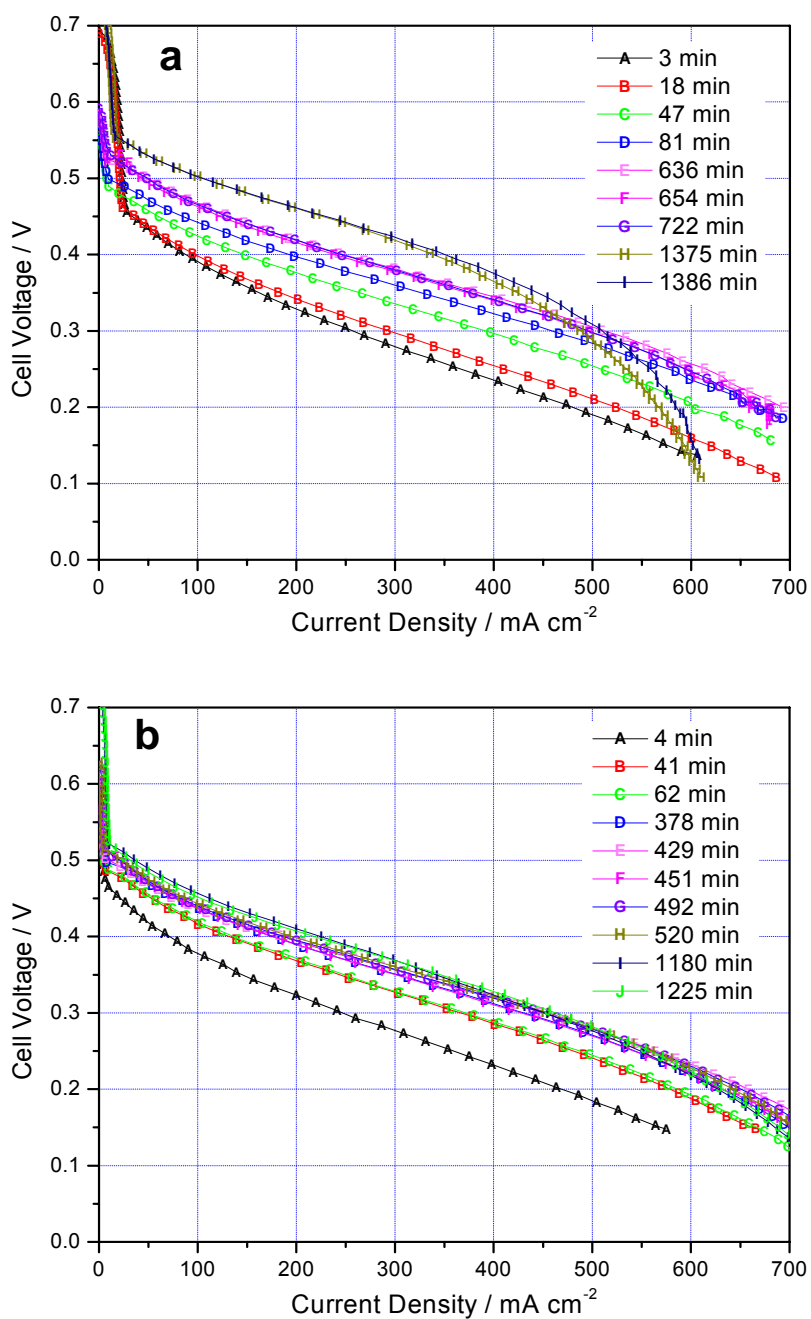
Figure 2.7 Performance variation over time for two MEAs: (a) MEA-1 and (b) MEA-2.The cells were operated at 80°C, using 3 ml/min of 2M methanol solution and 15 psi, 600 ml/min dry air.
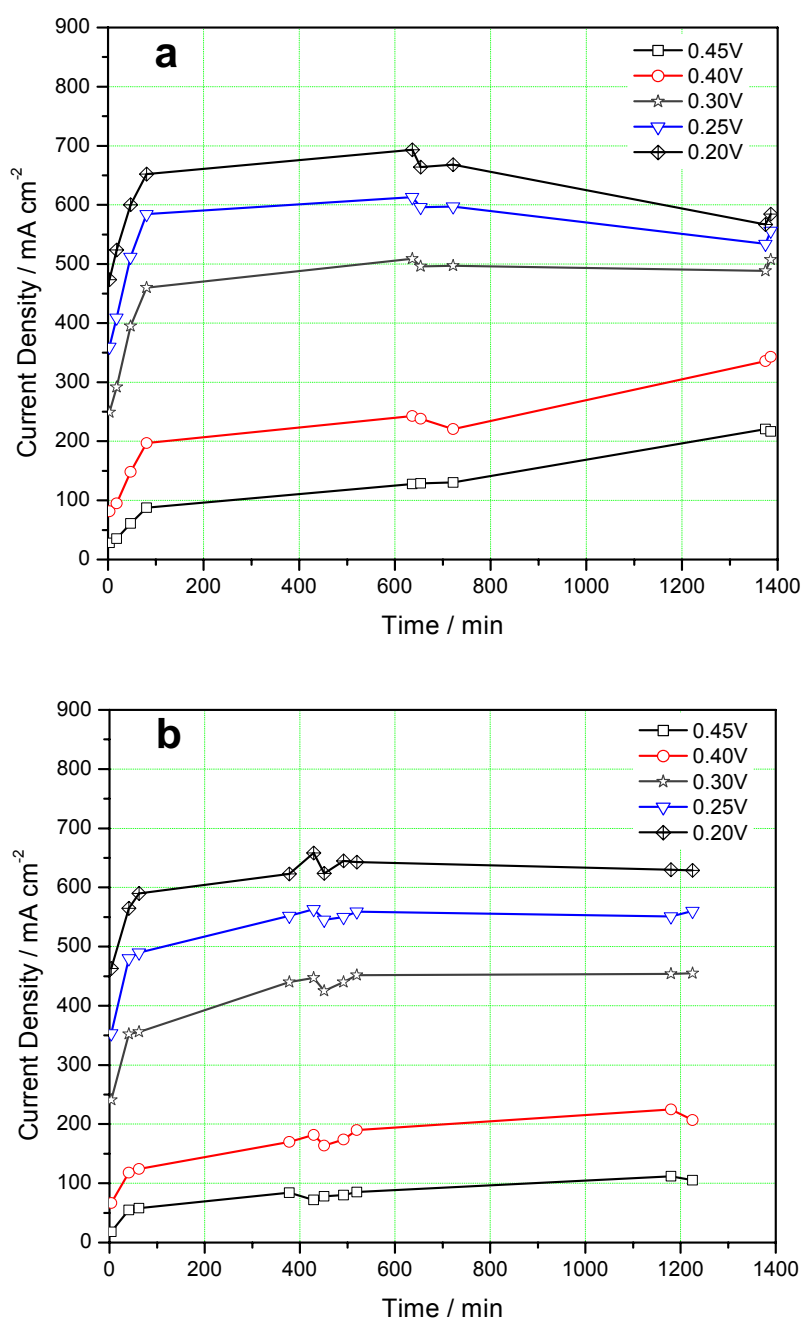
Figure 2.8 Current densities at 0.45V, 0.4V, 0.3V, 0.25V and 0.2V cell voltages over time for two MEAs: (a) MEA-1 and (b) MEA-2. The cells were operated at 80°C, using 3 ml/min of 2M methanol solution and 15 psi, 600 ml/min dry air.
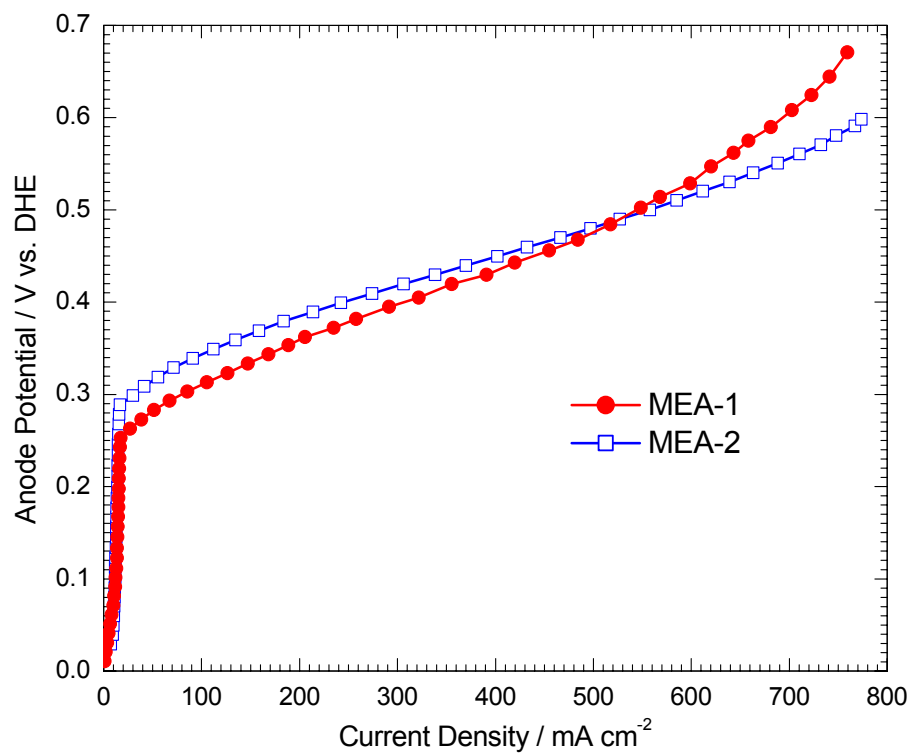
Figure 2.9 Anode polarization curves of two MEAs after conditioning. The cells were operated at 80°C, using 3 ml/min of 2M methanol solution and 15 psi, 100 ml/min humidified H_2.
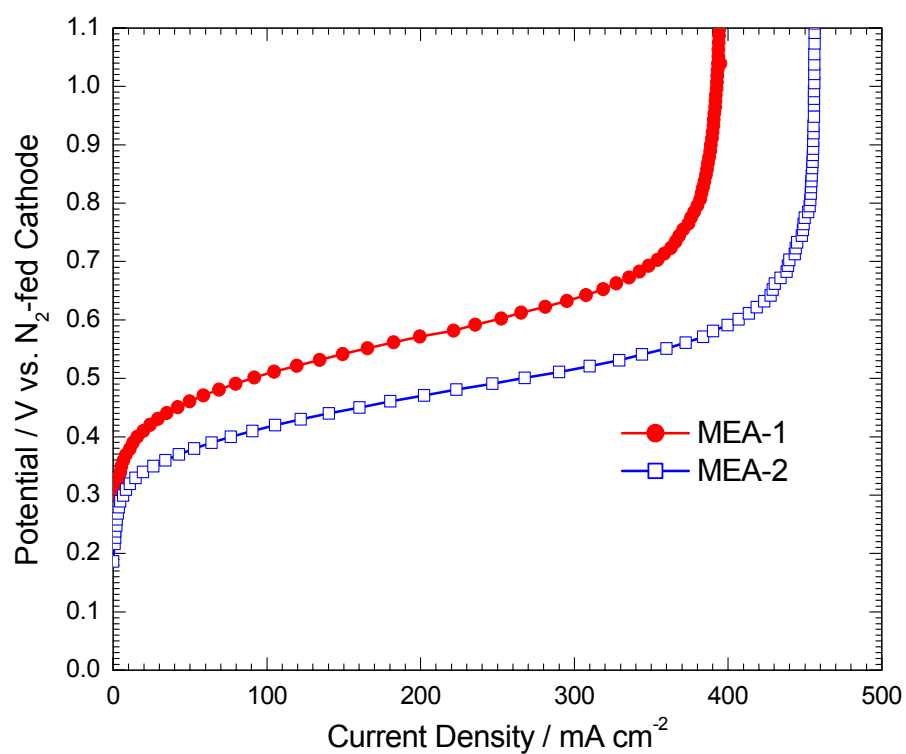
Figure 2.10 Methanol crossover results of two MEAs after conditioning. The cells were operated at 80°C, using 3 ml/min of 2M methanol solution at anode side and 15 psi, 100 ml/min room-temperature humidified N_2 at cathode side.
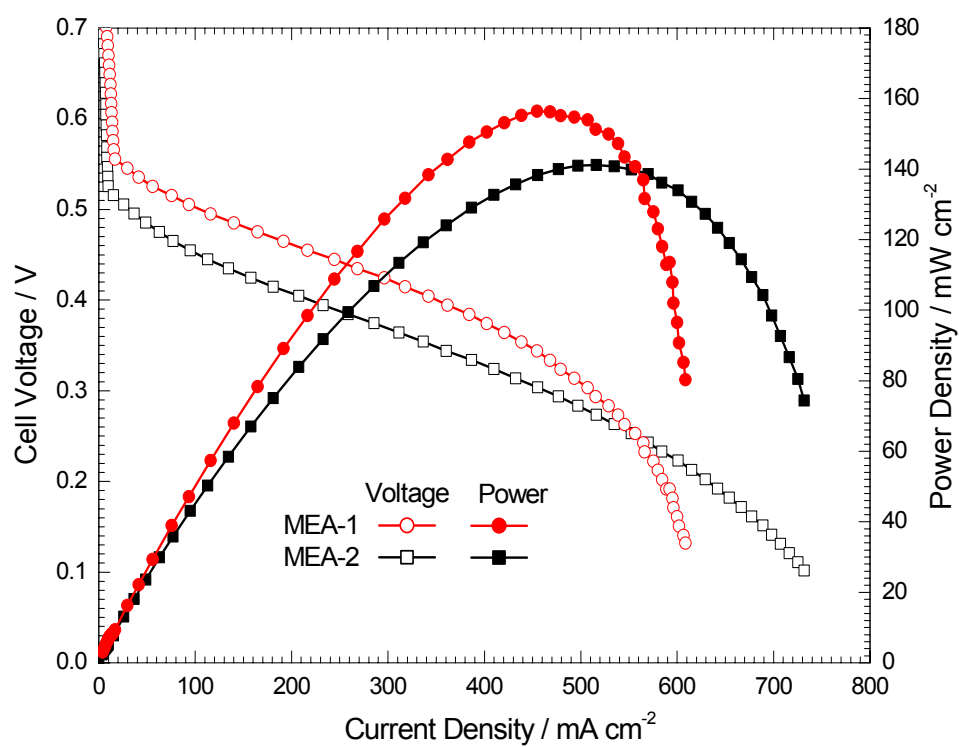
Figure 2.11 Polarization and power density curves for two MEAs after conditioning. The cells were operated at 80°C, using 3 ml/min of 2M methanol solution at anode and 15 psi dry air at cathode.

Chapter 3 OPTIMIZATION OF CATHODE CATALYST LAYER FOR DIRECT METHANOL FUEL CELLS: EXPERIMENTAL STUDY

3.1   Introduction

An effective cathode catalyst layer (CL) must serve multiple functions simultaneously (as shown in Figure 1.2): electron and proton conduction, oxygen supply and product water removal. Nafion ionomer in the CL provides protonic conduction, and helps to maintain structural integrity and robustness. An optimized cathode CL structure has a good balance between electrochemical activity and oxygen transport capability with effective water removal. There are many experimental studies on the optimization of CL compositions in H_2/air fuel cells. Most of these efforts were focused on optimization of cell performance as a function of Nafion content. Lee et al. (1998) evaluated the effect of Nafion loading on charge-transfer resistance and mass transport. Uchida et al. (1995, 1998) investigated the gas-supplying network formed by Nafion colloids. The optimum Nafion weight fraction was reported to be in the range of 30–40% (Antolini et al., 1999; Passalacqua et al., 2001; Song et al., 2001; Qi and Kaufman, 2003; and Sasikumar et al., 2004).

The same half-cell reaction and characteristics of cathodes in H_2/air fuel cells are also important for an effective DMFC cathode, but with a few differences. There is significantly more water at the DMFC cathode due to water crossover from the liquid-fed anode (Lu et al., 2005), in addition to ORR-produced water. The other key difference

relates to methanol crossover. Although the crossover methanol is almost completely oxidized at the DMFC cathode (Ren and Gottesfeld, 2001), the oxidation reaction not only produces a mixed potential, but also consumes oxygen. Both result in additional oxygen transport limitation through a thick DMFC cathode CL that features much higher loading of catalyst in order to mitigate the mixed potential effect. DMFC cathode CLs must be carefully considered in order to optimize the performance.

So far, little attention has been paid to DMFC cathode CL structure optimization for portable application. For high-loading cathodes operated at low air stoichiometry, the existing optimum structure in hydrogen PEM fuel cells must be modified. In this chapter, influences of fabrication techniques and ionomer distributions in DMFC cathode CLs are investigated. Various electrochemical methods are combined with surface morphology characterization to closely examine CL structures.

3.2 Experimental

3.2.1 Preparation of membrane electrode assembly

Carbon cloth was used as the cathode GDL and carbon-supported Pt catalyst (40% Pt/Vulcan XC72; E-TEK) was used as catalysts. CLs were made in two configurations: CCM and CDM; while anodes were made in CCM configuration only. The CDM cathodes were prepared by spraying catalyst inks onto the surface of a carbon cloth GDL, and CCM was prepared by the decal method (Lu et al., 2005). MEA was obtained by hot-pressing two catalyst-coated PTFE decals (in some cases CDM cathode was used) onto a piece of pretreated Nafion 112 membrane at 125°C and 100 atm for 3 min.

3.2.2   TEM micrographs

Cross-sectional TEM specimens of CCM MEAs were prepared by ultramicrotomy. MEAs were first embedded into a suitable resin for 24 hours at 60°C. Low embedding temperatures prevent catalyst grain growth and impose less impact on the microstructure of the catalyst layer. Ultra-thin sections were cut with glass knives in floating water and then transferred to specimen support grids. In this work, TEM observation of cross-sectional specimens was done on a JEOL 2010 operated at 200 kV (LaB_6).

3.2.3   Electrochemical characterization

A fuel cell fixture with active area of 12 cm^2 was used. The flowfield, consisting of machined two-pass serpentine grooves on graphite blocks, was identical for both anode and cathode. CV measurement was conducted at room temperature with a scan rate of 5mV/s from 0 to 1.2 V versus DHE, by feeding humidified N_2 and H_2 to the cathode and anode, respectively. The surface roughness of the electrode was evaluated by the amount of charge required to oxidize atomic hydrogen absorbed on Pt electrocatalysts, after correcting the double layer charge (at 0.4V vs. DHE). Assuming a value of $210\mu C.cm^{-2}$ for the oxidation of atomic hydrogen on a smooth Pt surface, surface roughness factor (RF) is obtained by

$$RF = \frac{S}{v \times 210\mu C.cm^{-2} \times A}10^9 \qquad [3.1]$$

where v is the voltage scan rate (5mV s^{-1}), S is the integration area of the hydrogen desorption peak, and A is the electrode geometric area.

3.3   Results and discussion

3.3.1   Electronic micrographs of cathode catalyst layers

The surface morphologies of a carbon cloth GDL with a pre-coated MPL, a low-loading CDM (0.6 mg Pt cm^{-2}) and a high-loading CDM (1.2 mg Pt cm^{-2}) are shown in Figures 3.1a, b and c, respectively. The cracks on the surface of the MPL provide a path for gas transport to the CL. In Figure 3.1b, there are some small cracks and voids scattered on the surface of the catalyst layer. The area between these cracks and voids forms a non-defective layer. Higher catalyst loading and thicker CL would induce higher surface tension, thus causing more severe surface roughness and cracks, commonly referred to as mud cracking, as shown in Figure 3.1c.

Figures 3.2a and b show the surface morphologies of a low-loading (0.6 mg Pt cm^{-2}) and a high-loading (1.2 mg Pt cm^{-2}) catalyst-coated decal prepared by tape casting, before they are hotpressed onto Nafion membranes. The catalyst and ionomer composite layers form cake-like structures on a Teflon decal. Some uniform and small cracks can be easily identified on the surface of the low-loading decal, while for the high-loading one, although their number declines, the cracks widen and deepen, and the Teflon decal is visible at the bottom of the cracks.

Figures 3.3a and b display the TEM images of the CL/membrane interface and bulk of cathode CL in a used CCM MEA, respectively. Recast Nafion in the catalyst layer integrates perfectly with the membrane, and there is intimate binding between the CL and membrane. The catalyst particles and ionomer are well mixed and uniformly distributed at the micro-scale. However at the large scale, catalyst particle agglomeration and macro-pores (with diameter about 100 nm) are visible in the bulk of the CL. The agglomeration

and macro-pores are defects, which are introduced into the CL during MEA fabrication due to insufficient mixing. The influence of macro-pores on oxygen concentration distribution and cell performance will be analyzed in Chapter 4.

3.3.2   Evaluation of different MEAs

In this portion of the work, different MEAs were fabricated with varying catalyst loading, I/C (ionomer to carbon) ratio and ionomer distribution in cathode catalyst layers, as summarized in Table 3.1. The cathode performance was evaluated in an H_2/air fuel cell instead of a DMFC, since it is difficult to single out the cathode over-potential from a DMFC polarization curve.

3.3.2.1   Influence of fabrication techniques

The iR-corrected cell polarization curves for different MEAs are plotted in Figure 3.4. The hydrogen flow rate is 100 ml min^{-1}, corresponding to a stoichiometry of *ca.* 7.3@150 mA cm^{-2}, so the cell performance is only limited by the cathode. Comparing the cell performance of different MEAs at the same Pt loading, *i.e.*, comparing MEA-B and MEA-D, or MEA-A and MEA-C, it is interesting to note that CCM MEAs show better performance than CDM MEAs at low current density regime (40~70 mA cm^{-2}), while the situation is reversed at high current density regime (100~400 mA cm^{-2}). MEA-C has a lower limiting current density, indicating poorer mass transport in the CL. MEA-E, with a composite structure, shows better characteristics than MEA-C and MEA-A at low and high current density regimes, respectively. CDM cathodes have lower open circuit voltage (OCV), only 0.91 and 0.89V for MEA-C and MEA-D, respectively. This is probably because CDM MEAs do not have intimate CL/membrane interface as CCM

MEAs do, since it is difficult for the solid polymer membrane to penetrate into the cracks on the CL surface (Figure 3.1). The corresponding Tafel slopes of different MEAs, also indicated in the figure, are obtained by fitting the data points under the current density of 100 mA cm^{-2}. The CDM MEAs (MEA-C and MEA-D) have smaller Tafel slopes than the CCM MEAs (MEA-A and MEA-B), with MEA-E between them.

As a diagnostic tool, the performance of H_2/O_2 cells was also measured. The difference in cell voltage between a pair of H_2/air and H_2/O_2 performance curves is often termed as the oxygen gain (Kocha, 2003) and can be expressed as

$$\Delta E_{O_2/air} = E_{O_2} - E_{air} \qquad [3.2]$$

Figure 3.5 displays the oxygen gains of different MEAs at 60°C and cathode stoichiometry ξ_c=3@150 mA cm^{-2}. Higher oxygen gain is a qualitative indication of mass-transport loss in a CL structure that, for instance, floods easily. Between 50~250 mA cm^{-2}, CDM cathodes show higher oxygen gain, and thus more severe mass-transport resistance than CCM cathodes. The high-loading CCM MEA (MEA-A) also shows high mass-transport resistance at higher current densities.

The different behaviors of CCM and CDM MEAs are probably caused by their different Pt distributions in the CLs. After the catalyst-coated decals (Figure 3.2) are hotpressed to the membranes to form CCMs, catalysts are distributed uniformly between the membrane and GDL. In CDM, part of the catalysts sprayed on the GDL surface may settle internally, thus the catalysts are located preferentially near the GDL. When a current is applied, especially at low air stoichiometry, the oxygen concentration profile in the CL may not be uniform, starting to decline from the catalyst layer/GDL interface and reaching the lowest value toward the CL/membrane interface. In the presence of an

oxygen concentration gradient, all the catalytical sites are not equally accessed by the oxygen; that is, the catalysts near the membrane contribute less to the overall electrochemical reaction than those near the GDL. Thus CDM MEAs, with more catalyst near the GDL/CL interface, probably have higher catalyst utilization and higher performance at moderate current density.

Figure 3.6 displays the EIS results of different MEAs at 0.8V cell voltage for H_2/air fuel cells. The high-frequency portion is shown in the inset. As expected, semi-circular loops that correspond to ORR are observed. Higher Pt loading reduces the ORR resistance, as indicated by smaller semi-circles. At high frequencies, a Warburg-like response (45° slope) is observed, especially for high-loading CCM (MEA-A), which corresponds to the ion migration and capacitance between agglomerates within the catalyst layer. The intercept of EIS spectra with the real axis at high frequency corresponds to the internal ohmic resistance of the cell, R_Ω, which represents the sum of uncompensated resistance in the CL, membrane, backings, graphite end plates and the contact resistance between them. Another important parameter that can be derived from the EIS results is R_p, which corresponds to the charge-transfer resistance of ORR (Hsu and Wan, 2003). The values of R_Ω and R_p of different MEAs are listed in Table 3.2. Low-loading MEAs have a thinner catalyst layer, and thus low R_Ω. However, their R_p values are higher than high-loading MEAs. At the same catalyst loading, CCM has slightly larger R_Ω than that of CDM. High-loading CDM (MEA-C) shows the smallest R_p value, 0.524 and 0.578$\Omega.cm^2$ under oxygen and air, respectively; while low-loading CCM (MEA-B) has the largest R_p values. The ratios of R_p values between oxygen and air operation are also listed in Table 3.2. For the same MEA under air and oxygen operation,

the only differences are oxygen concentration and diffusion. Therefore, the ratio has the same characteristics as the oxygen gain. A larger ratio (approaching unity) represents more favorable oxygen transport through the CL. MEA-B (low-loading CCM) has the biggest R_p ratio, and MEA-C (high-loading CDM) has the smallest R_p ratio. It seems that CCM is a good choice for low-Pt-loading MEA, but high-loading CCM may result in large cell internal resistance and mass transport limitation.

3.3.2.2   Influence of ionomer content and distribution in the cathode CL

Figure 3.7 compares the iR-corrected polarization curves of H_2 PEM fuel cells of MEA-A, MEA-F and MEA-G at 60°C using different oxidants. I/C ratios of these MEAs are 1:2.4, 1:2.1 and 1:1.8, respectively; that is, MEA-G has the largest ionomer content, while MEA-A has the smallest. MEA-F and MEA-G have higher OCV than MEA-A in both air and oxygen. The three MEAs produce almost identical performance in oxygen. When air was used as the oxidant, different MEAs have almost identical performance at lower current density region (< 100 mA/cm^2), with MEA-F and MEA-G showing slightly higher cell voltages. At higher current densities, their behaviors differ markedly. The cell voltage of MEA-G bends downwards dramatically with current density and the limiting current density is smaller than 400 mA/cm^2. MEA-A, which has the smallest Nafion content, can extend current density to higher values, *ca.* 500 mA/cm^2, while the limiting current density of MEA-F is slightly lower, although it shows the best performance in the moderate current density. Porosity in the CL is inversely proportional to its ionomer content. MEA-G has the smallest porosity, thus the worst mass transport. MEA-A has the largest porosity; however, at the same time, the effective proton conductivity of the CL is

sacrificed. MEA-F seems to have the best compromise between the oxygen mass transport and proton conduction. Nafion weight fraction is only 22% in the cathode CL of MEA-F, much smaller than that in H_2/air cells.

In the CV results shown in Figure 3.8, the charge required for hydrogen desorption (below 0.4V) is used to evaluate the roughness factor of the electrodes, namely 290, 381, and 349cm^2.cm^{-2} for MEA-A, MEA-F and MEA-G, respectively. When increasing the ionomer content in the catalyst layer, the roughness factor or electrochemically active area (ECA) seems to increase at first, but it then starts to decrease when the ionomer content is beyond a certain point. When fabricating CL by mixing the catalyst with ionomer solution, some Pt active area is not available for the electrochemical reaction due to either insufficient contact with the electrolyte, or electrical isolation of catalyst particles from each other by the non-conducting Nafion film. MEA-F seems to possess a good balance.

From the EIS results (not shown here), MEA-G has the smallest R_Ω, and MEA-A has the largest R_Ω and R_p. MEA-F has the smallest R_p, which is consistent with its superior performance. Figure 3.9 shows the iR-corrected H_2/O_2 cell performance curves with the current density normalized to the surface roughness. The thermodynamic open circuit potential (E_{rev}) at 60°C and ambient pressure is estimated to be ~ 1.19 V using the following equation (Bernardi and Verbrugge, 1992):

$$E_{rev} = 1.23 - 0.9 \times 10^{-3}(T - 298) + \frac{RT}{4F}\ln(p_{H_2}{}^2 \, p_{O_2}) \qquad [3.3]$$

The exchange current densities, obtained by extending the fitted Tafel slopes to 1.19V, are 5.29×10^{-10}, 6.85×10^{-10} and $3.84 \times 10^{-9} A \, cm_{ECA}{}^{-2}$ for MEA-A, MEA-F and MEA-G, respectively. It seems that higher Nafion loading in the CL increases the exchange

current density, probably due to the increased oxygen solubility and hence higher concentration at the ionomer/catalyst interface (Gottesfeld and Zawodzinski, 1998; Xie et al, 2004).

The effect of ionomer distribution in the CL on cell performance is demonstrated in Figure 3.10. Both MEAs have composite cathode structures but different ionomer distributions: MEA-E has identical I/C ratio throughout its catalyst layer; while MEA-I has non-uniform ionomer distribution, with higher I/C ratio near the membrane and lower I/C ratio near the GDL. The two MEAs have almost identical performance using oxygen. However, MEA-I shows better features using air, *i.e.,* higher OCV and higher cell voltage in moderate current density regime, although its limiting current density is slightly lower than that of MEA-E.

Appropriate pore size and distribution in the CL are very important to reduce the mass transport resistance and realize uniformly high catalyst utilization. Large porosity facing the GDL in the CL facilitates gas access to the catalytic sites, increasing the limiting current density; small porosity (or higher density of Nafion and Pt composite) near the membrane/CL interface increases the oxygen solubility and hence the ORR kinetics. MEA-E and MEA-I show better characteristics than MEA-A and MEA-C because they have better pore distribution in the cathode CLs, so that the porosity variation across the CL favors both oxygen solubility and oxygen transport, resulting in better ORR kinetics and higher limiting current density.

3.3.3 Cathode performance evaluation in DMFCs

As discussed earlier, the polarization curves of the MEA with composite CL structures show better features in both kinetic and mass-transport regimes than those with pure CDM and CCM structures. Therefore, the subsequent research work was to evaluate its performance in DMFCs.

One MEA using the same cathode as MEA-E was fabricated. The anode is in the configuration of CCM with a PtRu loading of about 4.5mg/cm^2. Figure 3.11 shows the quick-scan performance of a DMFC and an H$_2$/air cell. All the polarization curves clearly show the kinetic, ohmic and mass-transport regimes. The DMFC performance shows much smaller limiting current densities than the H$_2$/air cell, due to additional mass-transport limitation at the anode. The H$_2$/air cell yields voltages of 0.797 and 0.786V at air stoichiometries of 4 and 2@150 mA/cm^2, respectively, while the DMFC produces much lower cell voltages of only 0.406 and 0.362 V at the same air stoichiometries, which correspond to power densities of 60.1 and 54.3mW/cm^2, respectively. It seems that DMFC performance is more sensitive to air stoichiometry, and there is a minimum air flowrate required to sustain efficient and stable operation. It is believed that the crossover methanol from the anode is almost completely converted to carbon dioxide and water in the presence of the cathode catalyst; however, this reaction consumes oxygen from the air supplied to the cathode that would otherwise be required for the oxygen reduction reaction (Colbow et al., 1996; Müller et al., 2003). It is estimated that at a methanol crossover current of 100mA/cm^2, the air needed for methanol oxidation is roughly 20 SCCM, which is almost 1/3 of the air flowrate at stoichiometry of 2@150mA/cm^2.

To evaluate the cathode performance in a DMFC, if the over-potentials of hydrogen-evolving and hydrogen-oxidizing electrodes are negligibly small, the following equation can be used (Thomas et al, 2002):

$$E_{Air}^{MeOH}(I) = E_{MeOH/Air}^{*}(I) + E_{MeOH/H_2}^{*}(I) \qquad [3.4]$$

where the asterisk designates 'iR-free', $E_{Air}^{MeOH}(I)$ is the air cathode potential at relevant DMFC conditions that contains the effects of methanol crossover and mixed over-potential, and where $E_{MeOH/Air}^{*}(I)$ and $E_{MeOH/H_2}^{*}(I)$ are the iR-free voltages under DMFC and anode polarization modes. From the EIS results (not shown here), the cell ohmic resistances are nearly identical under the DMFC and anode polarization modes, *ca.* 0.181 $\Omega.cm^2$, so Eq. 2.4 can be simplified as

$$E_{Air}^{MeOH}(I) = E_{MeOH/Air}(I) + E_{MeOH/H_2}(I) \qquad [3.5]$$

Figure 3.12a and b show the quick-scan and constant-current cell voltages under different operating modes, including DMFC, anode polarization, H_2/air cell and the evaluated cathode performance using Eq. 3.5. The DMFC and anode polarization curves have almost identical limiting current densities, indicating that the maximum DMFC current is limited by the anode. The evaluated cathode performance approaches that of the H_2/air cell at high current densities, where methanol crossover and hence its detrimental effects become trivial. At 150mA/cm^2 a potential reduction of ~ 37 mV due to methanol crossover is observed, which is larger than the value (20 mV for NF117) reported by Thomas et al. (2002) at the same operating temperature. Since they used only 0.5M methanol solution and a much thicker membrane (NF117), it is reasonable to expect a smaller methanol crossover.

In Figure 3.12 b the voltages in all the curves are relatively stable over 2500 seconds. Several sudden voltage drops in H_2/air operation are supposed to be related to periodic (> 10 min) water droplet growth and removal in the GDL and gas channels (Yang et al, 2004). There is no noticeable voltage decay on a longer time scale for H_2/air operation; however, both the anode over-potential and DMFC cell display evident decay, which are enlarged in the inset. The DMFC and methanol oxidation exhibit periodic voltage fluctuations on a time scale of *ca.* 2 min, which is probably caused by the intervallic CO_2 bubble removal at the anode GDL/CL interface, induced by the peristaltic pumping of methanol solution. The DMFC cell voltage decay is dramatic in the first 500s and then gradually slows down. The initial (0 ~ 500s) DMFC cell voltage drop amounts to about 37 mV. The anode contribution is only 14 mV, as indicated in the figure, leaving about 23 mV contribution from the cathode, which is mainly due to cathode flooding. Linear fitting of the experimental data after 500s shows that the slope of the DMFC cell voltage decay is about 2 times larger than that of the anode over-potential, indicating that both the anode and cathode contribute equally to the cell voltage decay. The cell voltage decay can be recovered by current interruption or air flow fluctuations, which may either blow off liquid water accumulated in the cathode channel or refresh the active surface of the anode or cathode catalysts under reagent starvation.

Long-term cell performance loss may be caused by several factors: intermediate species adsorption on the surface of anode PtRu catalysts, cathode flooding, cathode surface oxidation, and Ru crossover. Long-term operation can cause 35-40% loss of the active surface area of the anode (Zelenay, 2003); however, such loss appears to have relatively limited impact on the anode performance in methanol oxidation if high

loadings of PtRu are used (~ 5 mg/cm^2). On the other hand, cathode flooding at small air stoichiometry is obvious, ultimately leading to severe water management problems and cell voltage loss. Furthermore, an increased concentration of water may facilitate water oxidation and surface oxide formation on Pt surface at high voltage (Paik et al., 2004). Surface oxidation of the Pt cathode causes a loss of ECA up to $\sim 40\%$ (Zelenay, 2004), and a significant amount of the surface oxide (hydroxide) occurs in the initial stage of fuel cell operation. Ru crossover from the anode to cathode is another possible source of DMFC performance loss (Zelenay, 2003; Piela et al., 2004), which is non-recoverable. Nevertheless, the accumulation of Ru at the cathode interface would require operating a test cell for hundreds of hours (Piela et al., 2004), so it cannot account for the cell voltage decay within one or two hours seen in this study.

3.4   Summary

Fabrication techniques have a large influence on the performance of cathode CLs of DMFCs. CCM and CDM MEAs have different Pt catalyst distributions in their CLs, and CCM MEAs have higher cell OCVs and produce higher cell voltages at lower current densities (< 50 mA.cm^{-2}). However, at higher current densities, their performance is inferior to that of CDM MEAs. More catalysts are supposed to locate near the GDL in the CL, resulting higher Pt utilization at higher current density. Composite structures, consisting of both CCM and CDM, have better porosity distribution, thus better polarization characteristics. In the CLs with appropriate ionomer distributions, the porosity variation across the catalyst layers favor both oxygen solubility, oxygen

transport and proton conduction, resulting in better ORR kinetics and higher limiting current density.

DMFC performance is more sensitive to the air stoichiometry, and there is a minimum air flowrate required to sustain efficient and stable operation of the cathode. The evaluated cathode performance in the DMFC approaches that of the H_2/air cell at high current densities, where methanol crossover and hence its detrimental effects become trivial. At 150mA/cm^2 a potential reduction of $\sim$ 37 mV due to methanol crossover is observed. Intermediate species adsorption on the surface of anode PtRu catalysts, cathode flooding, and cathode surface oxidation are the possible reasons that cause cell voltage decay over time at constant-current operation.

Table 3.1 Summary of different MEA specifications

MEA	Anode		Membrane	Cathode	
	Catalyst layer configuration and loadings	I/C ratio		Catalyst layer configuration and loadings	I/C ratio
MEA-A	CCM, 0.6 mg Pt cm^{-2}	1 : 2.4	NF 112	CCM, 1.2 mg Pt cm^{-2}	1 : 2.4
MEA-B	CCM, 0.6 mg Pt cm^{-2}	1 : 2.4	NF 112	CCM, 0.6 mg Pt cm^{-2}	1 : 2.4
MEA-C	CCM, 0.6 mg Pt cm^{-2}	1 : 2.4	NF 112	CDM, 1.2 mg Pt cm^{-2}	1 : 2.4
MEA-D	CCM, 0.6 mg Pt cm^{-2}	1 : 2.4	NF 112	CDM, 0.6 mg Pt cm^{-2}	1 : 2.4
MEA-E	CCM, 0.6 mg Pt cm^{-2}	1 : 2.4	NF 112	Composite structure, MEA-B +MEA-D, 1.2 mg Pt cm^{-2}	1 : 2.4
MEA-F	CCM, 0.6 mg Pt cm^{-2}	1 : 2.4	NF 112	CCM, 1.2 mg Pt cm^{-2}	1 : 2.1
MEA-G	CCM, 0.6 mg Pt cm^{-2}	1 : 2.4	NF 112	CCM, 1.2 mg Pt cm^{-2}	1 : 1.8
MEA-H	CCM, 0.6 mg Pt cm^{-2}	1 : 2.4	NF 112	CCM, 0.6 mg Pt cm^{-2}	1 : 1.8
MEA-I	CCM, 0.6 mg Pt cm^{-2}	1 : 2.4	NF 112	Composite structure, MEA-H +MEA-D, 1.2 mg Pt cm^{-2}	—

Table 3.2 Data obtained from EIS results

MEA	Oxygen operation		Air operation		Ratio of R_p under oxygen and air
	R_Ω ($\Omega.cm^2$)	R_p ($\Omega.cm^2$)	R_Ω ($\Omega.cm^2$)	R_p ($\Omega.cm^2$)	
MEA-A	0.280	0.867	0.248	0.955	0.830
MEA-B	0.196	1.025	0.198	1.033	0.993
MEA-C	0.183	0.524	0.178	0.578	0.853
MEA-D	0.167	0.639	0.162	0.703	0.873
MEA-E	0.207	0.715	0.195	0.755	0.906
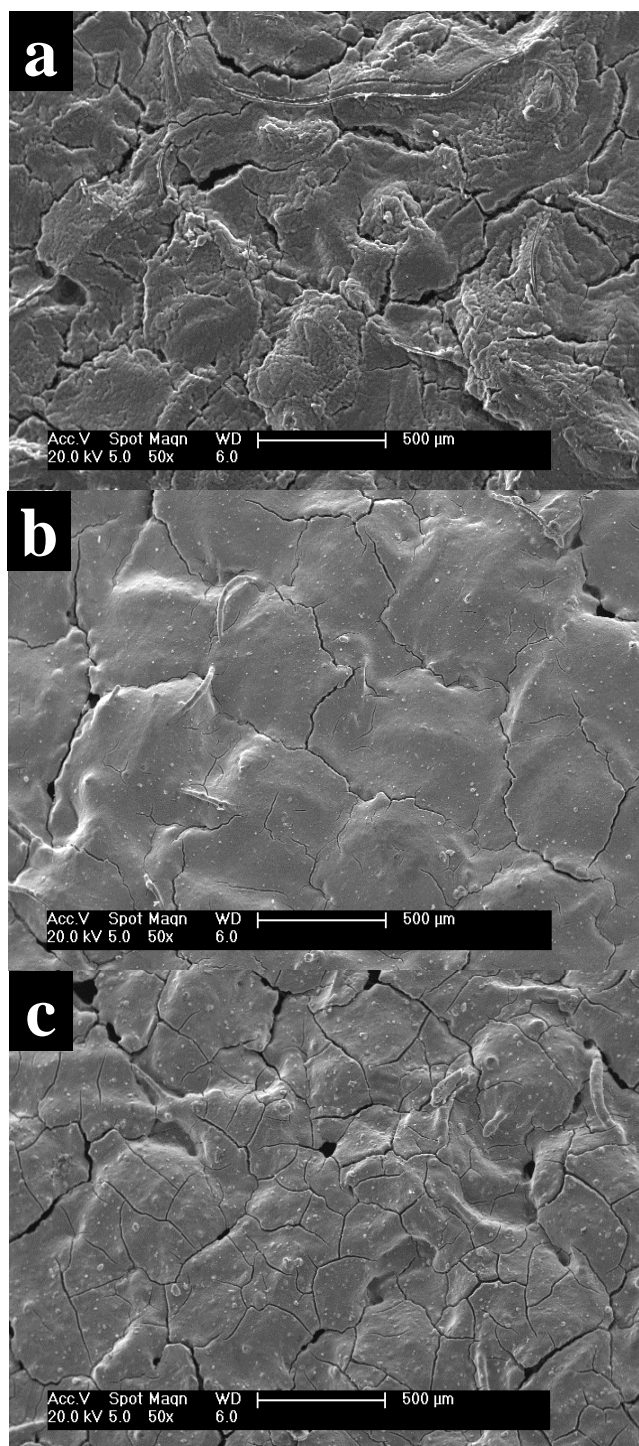
Figure 3.1 Surface morphologies of (a) a carbon cloth GDL, (b) a low-loading CDM (0.6 mg.cm^{-2}) and (c) a high-loading CDM (1.2 mg.cm^{-2}).
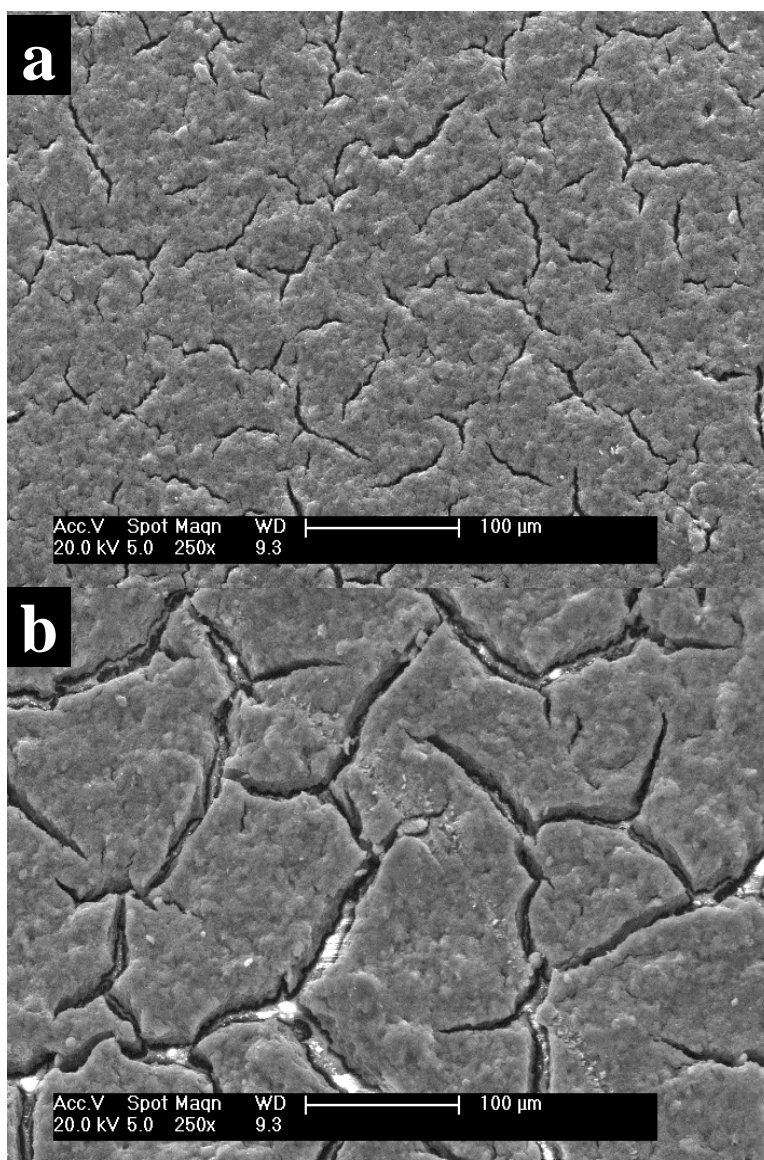
Figure 3.2 Surface morphologies of (a) the low loading (0.6 mg.cm^{-2}) and (b) high loading (1.2 mg.cm^{-2}) catalyst-coated decals
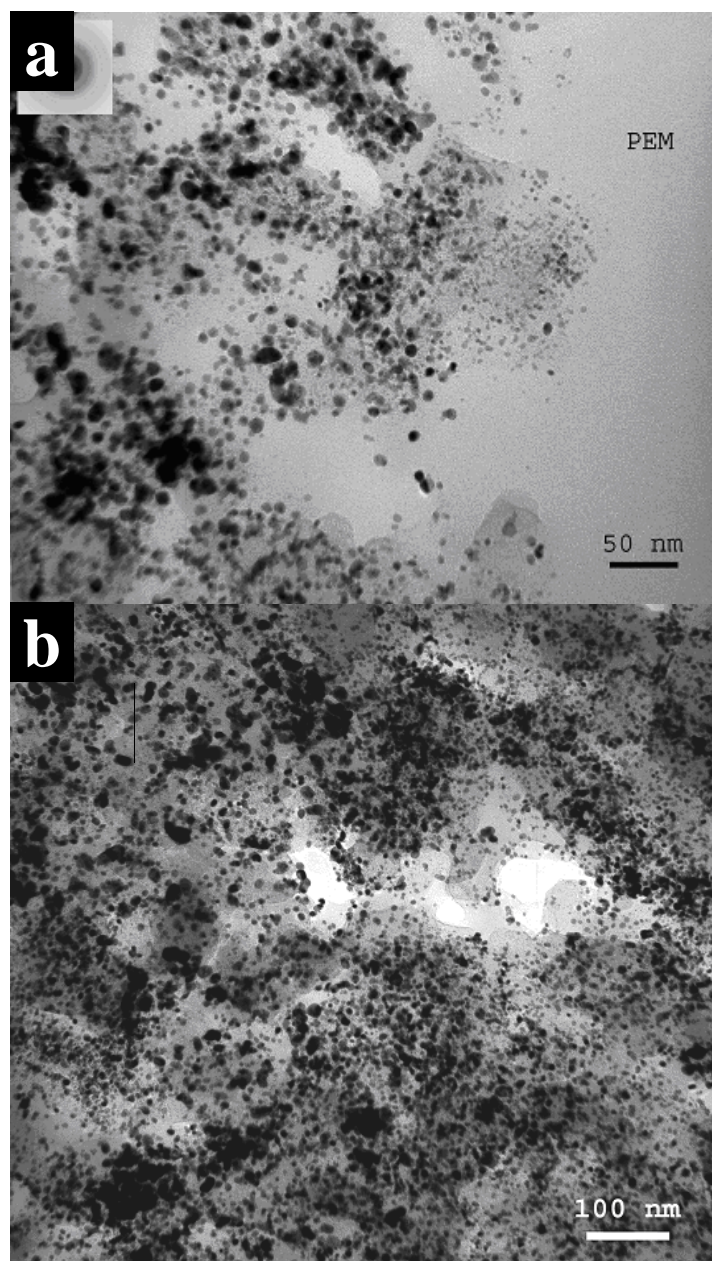
Figure 3.3 TEM image of the cathode CL in a used CCM MEA: (a) the interface between the catalyst layer and the polymer membrane, (b) the bulk of the catalyst layer.
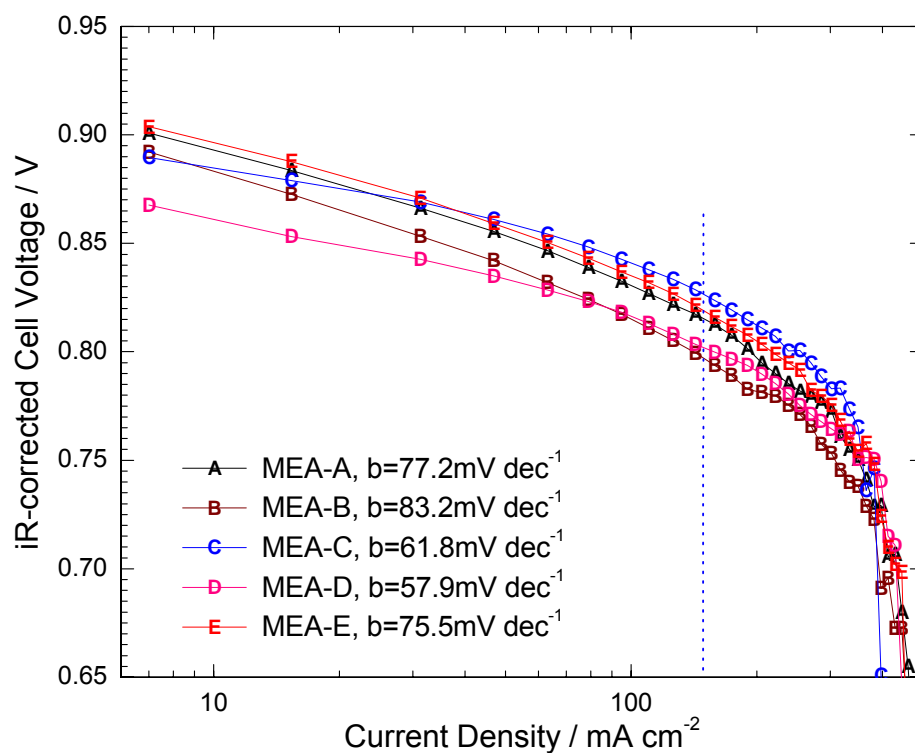
Figure 3.4 iR-corrected polarization curves of different MEAs. The flowrate of fully-humidified H_2 and air was 100 and 97 ml min^{-1} at the anode and cathode, respectively. The air flowrate corresponds to a stoichiometry of 3@150mA.cm^{-2}. The cell was operated at 60°C and ambient pressure at both anode and cathode.
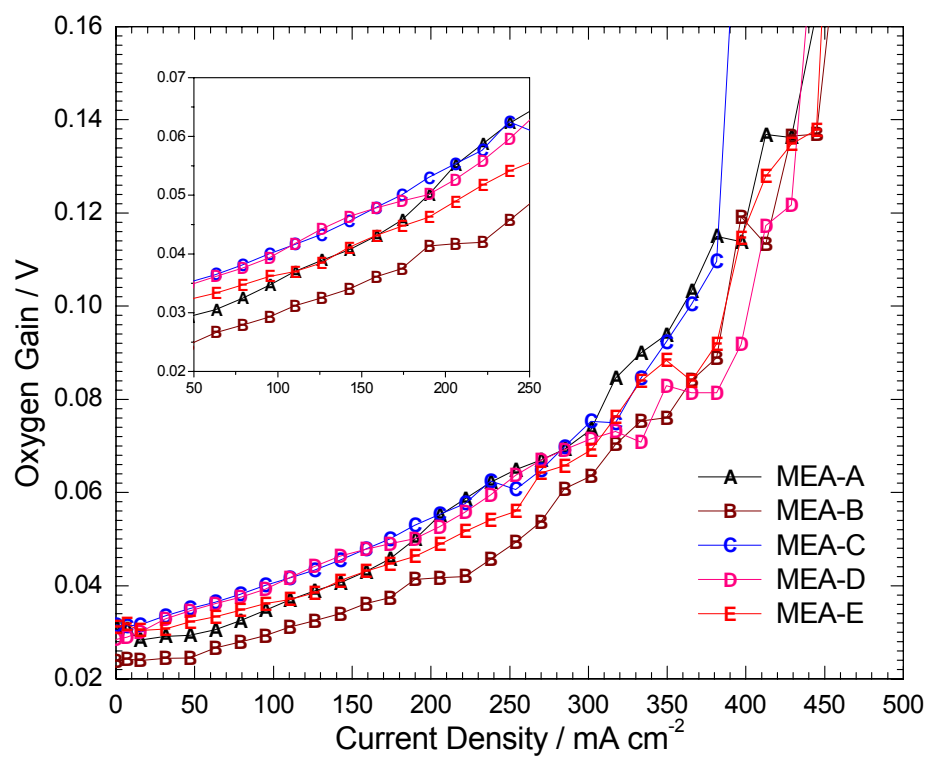
Figure 3.5 Oxygen gains of different MEAs at 60°C.
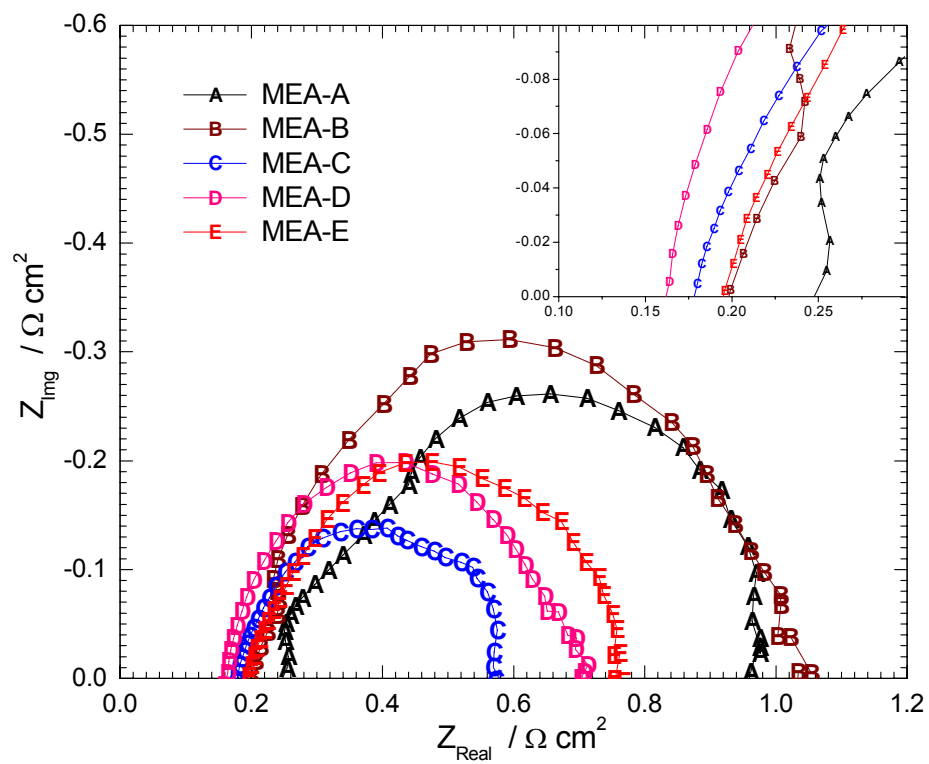
Figure 3.6 EIS results of different MEAs using air (at 0.8V). The operating conditions were the same as in Figure 3.4.
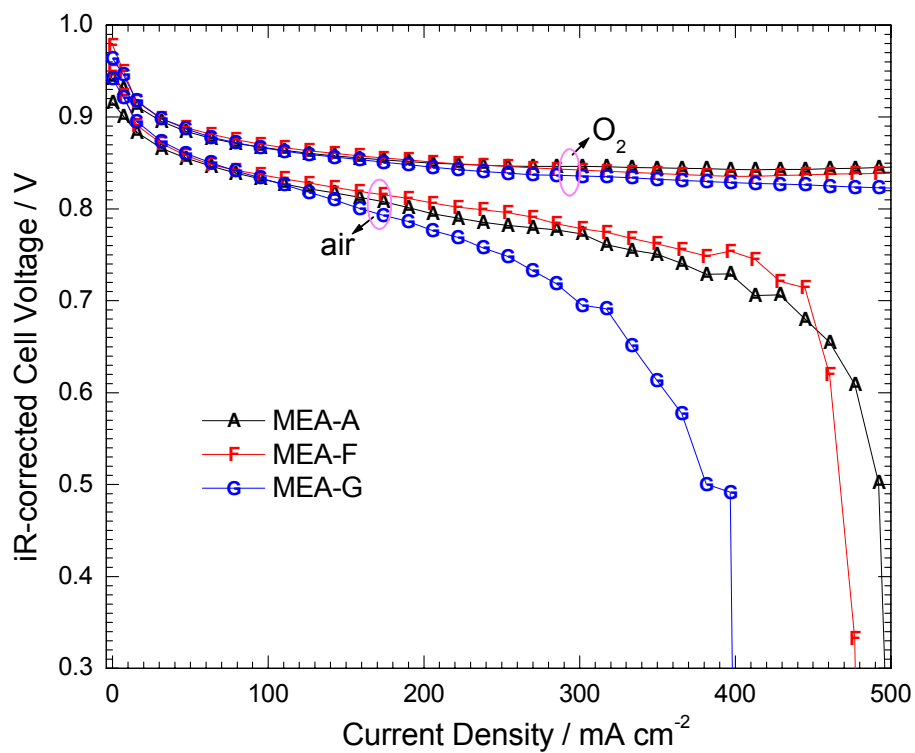
Figure 3.7 iR-corrected polarization curves of different MEAs using air and oxygen. The flowrate of fully-humidified H_2 and oxygen was 100 and 97 ml min^{-1} at the anode and cathode, respectively. The air flowrate is 97 ml min^{-1}. The cell was operated at 60°C and ambient pressure at both anode and cathode.
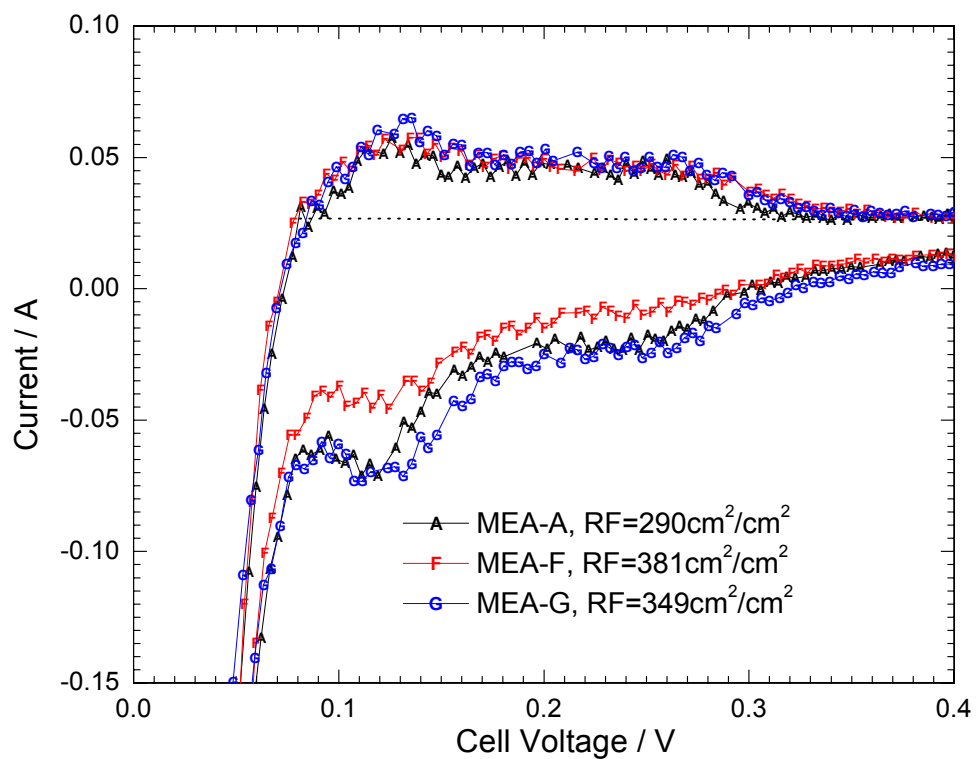
Figure 3.8 Cyclic voltammetry (CV) curves of different MEAs. The results were obtained at room temperature and fully humidified H_2 and N_2 were fed into the anode and cathode, respectively. The surface roughness factors are shown in the figure.
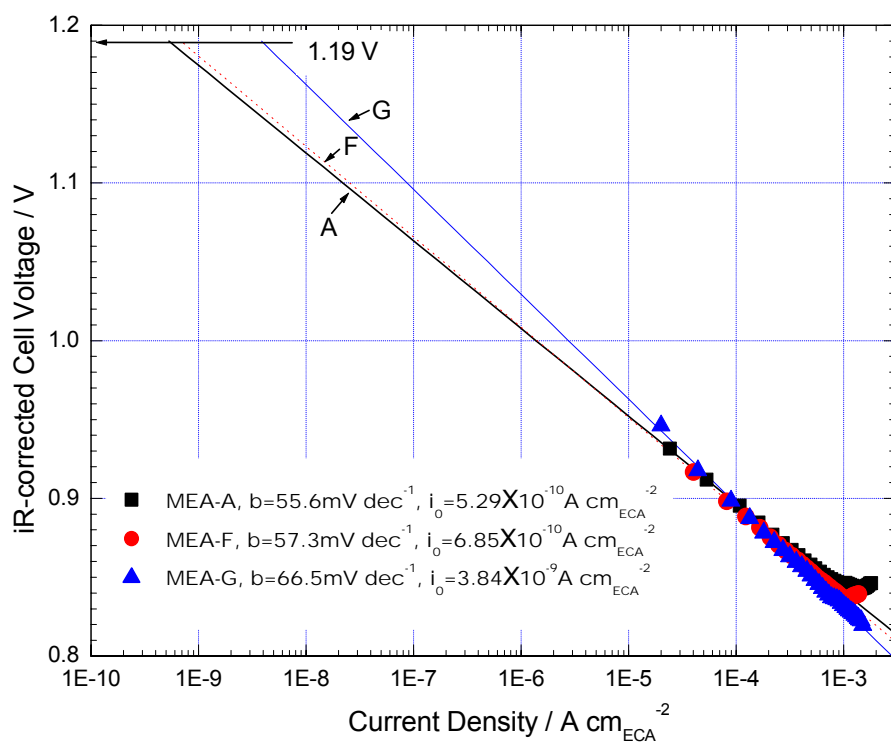
Figure 3.9 Hydrogen/oxygen performance curves corrected for ohmic losses at 60°C. The current densities are normalized to the surface roughness of different MEAs.
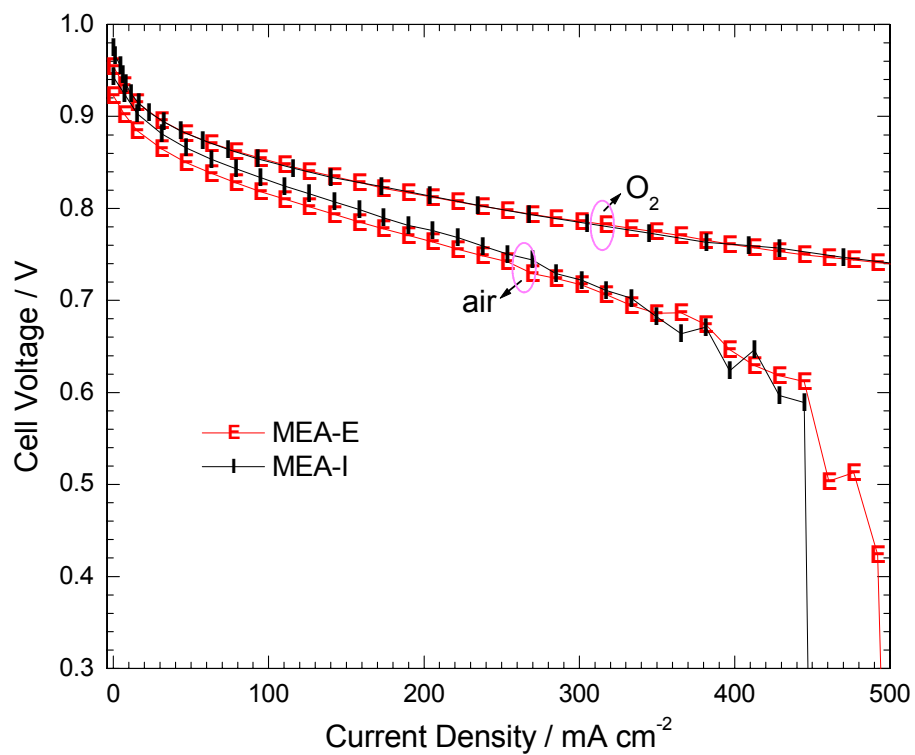
Figure 3.10 Polarization curves of different MEAs using air and oxygen. The operating conditions were the same as in Figure 3.8.
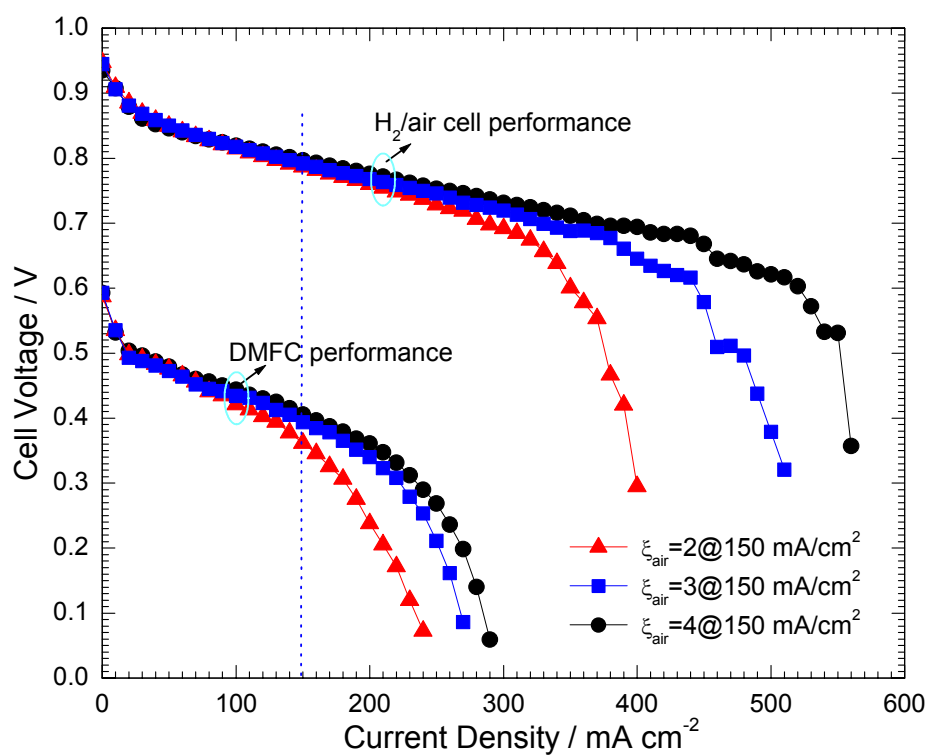
Figure 3.11 Polarization curves of an H_2/air fuel cell and DMFC at different air stoichiometries. 2M methanol solution was used in DMFC operation and its flow rate corresponds to a stoichiometry of 2@150mA/cm^2. Other operating conditions were the same as in Figure 3.7.
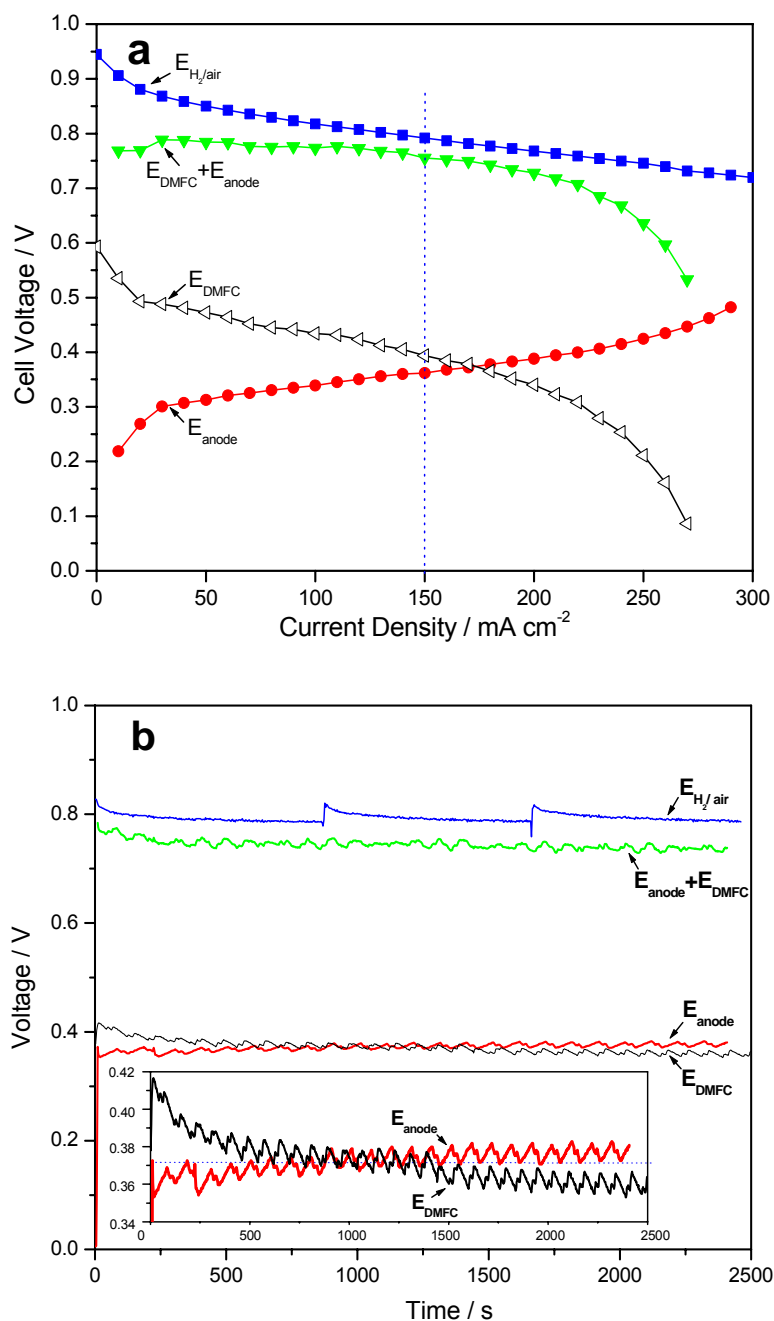
Figure 3.12 (a) Quick-scan polarization curves and (b) constant-current cell voltage variations under different operating modes, including DMFC, anode polarization, H_2/air cell and the evaluated cathode performance. Refer to Figure 3.11 for operating details.

Chapter 4 OPTIMIZATION OF CATHODE CATALYST LAYER FOR DIRECT METHANOL FUEL CELLS: COMPUTATIONAL MODELING AND DESIGN

4.1   Introduction

Both oxygen diffusion and proton conduction in the thicker cathode CLs are more critical issues in DMFCs than in H_2 PEFCs. As shown in Chapter 3, electrode structure, ionomer and Pt distributions in a DMFC cathode CL have remarkable influence on its kinetic, ohmic and mass-transport characteristics. The aim of this chapter is to theoretically examine the influence of ionomer, porosity, pores and their distributions on DMFC cathode performance, thus providing guidance for MEA and CL design.

Computational modeling is widely used for basic understanding of transport and electrochemical phenomena in fuel cells, as well as for structure optimization. Notable work includes that of Springer et al. (1991), and Bernardi and Verbrugge (1992), whose models are used to predict water transport through the membrane. Fuller and Newman (1993), Nguyen and White (1993), Um and Wang (2000), and Gurau et al. (1998) developed multidimensional models to address heat and water management in H_2 PEFCs. In these models, the active CL is not the main point of interest, but rather simplified as an infinitely thin film interface. There are only few detailed models specifically developed for PEFC CLs (Eikerling and Kornyshev, 1998, 1999; Marr and Li, 1999; and Song et al., 2004). In these models, optimization of the cathode CLs in H_2 PEFCs was conducted to

determine the optimal Nafion content, Pt loading and CL thickness, by assuming that the Nafion content and Pt loading were uniformly distributed in the CLs. Recently, improvement in PEFC cathode CL performance was realized by introducing concepts involving functionally graded Pt loadings or Nafion contents (Wang et al., 2004; Antoine et al., 2000; and Song et al., 2004). However, only 1-D models were developed in their work and the porosity distribution in the CLs has not been studied. To date, DMFC cathode CL optimization and modeling under portable operating conditions have not been attempted.

In this chapter, a macro-homogeneous model is developed, where the properties and variables of each phase are averaged over a representative elementary volume. Further, a 2-D model for oxygen and proton transport in the CL has been developed, where the CL is described using porosity, interfacial area per unit volume, effective conductivity and diffusivity through a porous medium. The effective conductivity and diffusivity are corrected as functions of ionomer fraction and porosity in the CL. This model enables direct analysis of not only the influence of ionomer and porosity distribution but also the effect of the location of macro-pore in the CL on the electrochemical characteristics. The present study is only concerned with the CL on the cathode side, with methanol crossover effect on DMFC cathode performance to be explored theoretically in Chapter 5.

4.2   Numerical model

The cathode CL consists of a matrix of carbon and Pt catalyst, with ionomer and pores distributed within. In the cathode half-reaction, oxygen is reduced to produce water at the triple-phase boundary. Assumptions made in this study are: (1) the system is

assumed to be isothermal and at steady state, (2) at the reaction interface, O_2 diffusion resistance through the ionomer film is ignored due to its small thickness (i.e. ~ 5 nm), (3) product water is assumed to be removed efficiently, thus does not affect the diffusion of O_2, and (4) the intrinsic proton conductivity is taken as a constant due to sufficient hydration in a DMFC environment.

4.2.1 Governing equations

Similarly to Chapter 3, H_2 PEFCs are used to evaluate the cathode performance and methanol crossover or the anode overpotential is not considered here. An optimized cathode CL structure in DMFCs should have a good balance between proton conduction and oxygen mass transport through its thickness. The governing equations can be written as:

$$\nabla \cdot (\kappa_e \nabla \phi_e) + aj = 0 \qquad [4.1]$$

and
$$\nabla \cdot (D_{CL}^{O_2, eff} \nabla c_{O_2}) + \frac{aj}{4F} = 0 \qquad [4.2]$$

where j, κ_e, ϕ_e, a, $D_{CL}^{O_2, eff}$, c_{O_2} and F are the transfer current, effective ionic conductivity, electrolyte potential, electrochemical area (ECA) per unit of electrode volume, effective oxygen diffusivity, oxygen concentration and Faraday constant, respectively. Eq. 4.1 describes proton conservation through the electrolyte phase, and Eq. 4.2 governs oxygen diffusion through the CL. The second term in both equations represents a source/sink term, accounting for the electrochemical reaction in the cathode CL.

The transfer current j, or the rate of ORR is governed by the Tafel kinetics as follows

$$j = -i_0 \frac{c_{O_2}}{c_{O_2,ref}} \exp(-\frac{\alpha_c F}{RT} \eta) \qquad [4.3]$$

where i_0, $c_{O_2,ref}$, α_c and η are the exchange current density, reference oxygen concentration, cathode transfer coefficient and overpotential. The overpotential, η, is defined as

$$\eta = \phi_s - \phi_e - V_{oc} \qquad [4.4]$$

where ϕ_s and ϕ_e stand for potentials of electronic phase and electrolyte at the reaction site, respectively. V_{oc} is the thermodynamic open circuit potential of cathode at the operation temperature. If we assume that the Pt/C phase provides an infinitively large electronic conductivity, which is reasonable in practice; thus, the entire CL has a uniform electronic phase potential. Letting $\eta = -\phi$, we have the following relation

$$\frac{\partial \phi_e}{\partial x} = \frac{\partial(\phi_s - V_{oc} - \eta)}{\partial x} = \frac{\partial(-\eta)}{\partial x} = \frac{\partial \phi}{\partial x} \qquad [4.5]$$

Substituting Eq. 4.5 and Eq. 4.3 into Eq. 4.1 and Eq. 4.2, respectively, the governing equations can be rewritten as

$$\nabla \cdot (\kappa_e \nabla \phi) - ai_0 \frac{c_{O_2}}{c_{O_2,ref}} \exp(\frac{\alpha_c F}{RT} \phi) = 0 \qquad [4.6]$$

and $\qquad \nabla \cdot (D_{CL}^{O_2,eff} \nabla c_{O_2}) - \frac{ai_0}{4F} \cdot \frac{c_{O_2}}{c_{O_2,ref}} \exp(\frac{\alpha_c F}{RT} \phi) = 0 \qquad [4.7]$

Based on the reference that the membrane phase potential is zero at the membrane/cathode interface, the cathode potential is then obtained by

$$V_{cath} = V_{oc} + \eta = V_{oc} - \phi \qquad [4.8]$$

According to the percolation theory (Eikerling and Kornyshev, 1998, 1999; Wang et al., 2004), the effective proton conductivity and oxygen diffusivity in the CL can be obtained through the following equation

$$\kappa_e = \kappa_{e,0} \cdot (\frac{\varepsilon_e - X_0}{1 - X_0})^2 \qquad [4.9]$$

$$D_{CL}^{O_2,eff} = D_g^{O_2} \cdot (\frac{\varepsilon_{CL} - X_0}{1 - X_0})^2 \qquad [4.10]$$

where $\kappa_{e,0}$, ε_{CL}, ε_e, X_0, and $D_g^{O_2}$ are the intrinsic proton conductivity of fully hydrated polymer, porosity, electrolyte volume fraction in the CL, percolation critical value, and bulk oxygen diffusivity, respectively.

According to Chapter 3, DMFC cathode Pt loading is about 1.2~1.5 mg.cm^{-2}, coresponding to a CL thickness about 25~30μm (from the SEM picture of a MEA cross section). The porosity can thus be estimated by

$$\varepsilon_{CL} = 1 - [\frac{1}{\rho_{Pt}} + \frac{1.5}{\rho_c} + \frac{1.5 \times SW \times R_{I/C}}{\rho_{Nafion}}] \frac{L_{Pt}}{\Delta X_{CL}} \qquad [4.11]$$

where $R_{I/C}$ is the I/C ratio, SW is the swelling degree of dry ionomer upon hydration by weight, and L_{Pt} is the Pt loading. In the above equation, 1.5 corresponds to the weight ratio of carbon to Pt in 40% Pt/C catalyst, which was used to fabricate CLs for DMFCs in Chapter 3. Similarly, the ionomer volume fraction in the CL is calculated by the following equation, assuming that Pt/C catalyst and ionomer are well mixed

$$\varepsilon_e = (1 - \varepsilon_{CL}) \frac{\dfrac{1.5 \times SW \times R_{I/C}}{\rho_{Nafion}}}{\dfrac{1}{\rho_{Pt}} + \dfrac{1.5}{\rho_c} + \dfrac{1.5 \times SW \times R_{I/C}}{\rho_{Nafion}}} \qquad [4.12]$$

where ρ_{Nafion}, ρ_{Pt}, and ρ_c are the density of hydrated Nafion, Pt and carbon, respectively. From the above equations, it can be seen that increasing ionomer content leads to reduction of porosity and effective oxygen diffusivity in the CL, but to an increase of the effective proton conductivity. In the case of non-uniform porosity distribution in the CL, the effective proton conductivity and oxygen diffusivity at different locations along the CL can at be calculated using Eq. 4.9 and 4.10.

It is assumed that ECA is independent on Nafion loading. At constant Nafion content, ECA is linearly proportional to the local volume fraction of Pt/Nafion composite in the catalyst layer, expressed as

$$a = a_0 \frac{1 - \varepsilon_{CL}}{1 - \varepsilon_0} \qquad [4.13]$$

where a_0 is the reference ECA value at porosity ε_0 in the catalyst layer. All the parameters used are listed in Table 4.1 and the governing equations in a multi-dimensional situation are solved by the finite volume method (Patankar, 1980).

4.2.2 Boundary conditions

A 2-D computational domain, as shown Figure 4.1, is symmetric in y direction. The boundary conditions in y directions are

$$y = 0 , \; y = y_L , \; \frac{\partial c_{O_2}}{\partial y} = 0 , \; \frac{\partial \phi}{\partial y} = 0 \qquad [4.14]$$

At the left boundary (bonded with the membrane), it can be written as

$$x = 0 , \; \frac{\partial c_{O_2}}{\partial x} = 0 , \; -\kappa_e \frac{\partial \phi}{\partial x} = I \qquad [4.15]$$

while at the right boundary (connected with GDL), oxygen concentration is assumed to be constant, which is dependent on operating current density

$$x = x_L, \ c_{O_2} = c_{O_2,0}, \ \frac{\partial \phi}{\partial x} = 0 \qquad [4.16]$$

Oxygen concentration drop across GDL is included in the oxygen concentration boundary condition, $c_{O_2,0}$, given by (Wang, 2003)

$$c_{O_2,0} = S \cdot c_{O_2,inlet} - \frac{I \cdot \Delta X_{GDL}}{4F \cdot D_{g,GDL}^{O_2,eff}} \qquad [4.17]$$

where ΔX_{GDL} represents the thickness of GDL, $D_{g,GDL}^{O_2,eff}$ is effective diffusion coefficient in GDL, $c_{O_2,inlet}$ is the inlet oxygen concentration in the gas channel, and S the stoichiometric parameter, which is the ratio of oxygen concentration at the interface of GDL/gas channel to that at the inlet. $S=1$ corresponds to large air stoichiometry, where the concentration gradient in the gas channel is eliminated; when the stoichiometry is small, S is less than 1. The porosity ε and tortuosity τ are employed to obtain the effective diffusivities in porous media (Wang, 2003)

$$D_{g,GDL}^{O_2,eff} = D_g^{O_2} \cdot \frac{\varepsilon_{GDL}}{\tau_{GDL}} \qquad [4.18]$$

Two scenarios are simulated: one in the absence of macro pores (thus reduced to a 1D problem) and the other in the presence of pores.

4.3   Results and Discussion

4.3.1   Effect of Nafion content on performance

Figure 4.2 shows the effect of Nafion loading on the cathode performance at 60°C under fully humidified air at ambient pressure. A stoichiometic factor S=0.65 is used, corresponding to a low air stoichiometry. At I/C ratios of 1:1.8, 1:2.1 and 1:2.4, porosities of the CL are estimated to be about 0.18, 0.25, and 0.33, and the electrolyte volume fractions are estimated to be about 0.31, 0.27, and 0.24 according to Eqs. 4.11 and 4.12, respectively. The effect of Nafion loading on the cathode performance is consistent with the experimental results in Chapter 3. Cathode 3 with I/C ratio of 1:2.4 shows the highest limiting current density around 500 mA.cm^{-2}, while those of the other two are much smaller, around 450 and 480 mA.cm^{-2} for cathode 1 and 2, respectively. The difference between the three cathodes is diminishing with decreasing current density. According to Uchida et al. (1995), the volume of secondary pores in the CL, formed between agglomerates, increases linearly with the decrease of Nafion loading. This indicates that lower Nafion fraction (cathode 3) leads to larger pore volume, thus better mass transport in CL. Cathode 2 performs better than the other two in the moderate current region, i.e., between 150 and 400 mA.cm^{-2}. Further increase of Nafion loading only slightly improves the performance only at low current densities, since higher Nafion fraction leads to a reduction of ohimc losses. However, when current density increases (> 200 mA.cm^{-2}), the O$_2$ transport limitation becomes more severe, reducing the performance. I/C ratios of 1:1.8, 1:2.1, and 1:2.4 correspond to Nafion weight fractions of 25%, 22%, and 20%, respectively, which are much smaller than those in H$_2$ PEFCs, where the peak performance is usually achieved at much higher Nafion weight fraction between 30% and

40% (Antolini et al., 1999; Passalacqua et al., 2001; Song et al., 2001; Qi & Kaufman, 2003; and Sasikumar et al., 2004). This is because that the optimum Nafion loading depends on Pt loading. Higher Pt loading in the CLs of DMFCs requires smaller optimum Nafion loading, since a larger porosity is needed for oxygen supply and water removal through a thicker CL.

Simulation results of oxygen concentration profile and overpotential distribution in the three CLs are shown in Figure 4.3a and b at 150 mA.cm^{-2} and 400 mA.cm^{-2}, respectively. Clearly, the consequence of increasing Nafion loading is two-fold: oxygen transport becomes worse and simultaneously ohmic resistance decreases significantly. The cathode performance is determined by two competing factors, i.e., oxygen transport and ionic resistance in the CL. Therefore an optimized performance is achieved through a good balance of the two at certain Nafion weight fraction. Reducing Nafion content always makes mass transport easier, as demonstrated in the figures that lower Nafion fraction reduces concentration drop through the CL, pushing the reaction zone towards the membrane. However, lower Nafion content increases the potential drop across the CL at lower current density as shown for CL 3 in Figure 4.3a. In this case the rate of oxygen diffusion is relatively large compared to the electrochemical reaction rate. At higher current density, a large amount of oxygen is consumed, thus making mass transport the limiting step. Inspection of the oxygen concentration profile in Figure 3b reveals that up to 60~70% of the catalytic sites in the CL experiences zero oxygen concentration and could not contribute to the ORR. The overpotential at the front interface, η_0, which is the indicator of the total voltage loss, is about 100mV larger at I/C ratio of 1:1.8 than the

other two cases, indicating that oxygen transport dominates over the ionic resistance in determining the cathode performance in this case.

4.3.2 Effect of porosity distribution on cathode performance

In order to study the porosity distribution effect solely, other parameters, including the I/C ratio, thickness and ECA are set constant. Six cathode CLs with different porosity distributions are investigated in this study. In Figure 4.4, (A) has a uniform porosity distribution; the porosity distributions in the CLs of (B), (C) and (F) are stepwise; and (D) and (E) are linear. All porosity distributions have the identical average porosity of 25%. Although the local ECA per unit volume depends on the local porosity, ε_{CL}, according to Eq. 4.13, the overall ECA obtained by integrating Eq. 4.13 through the whole CL is constant.

Figure 4.5 compares the performance of the six cathode CLs (I/C ratio=1:2.1) with different porosity distributions. Cathode (A) is the baseline, which has a uniform porosity distribution of 25% along the thickness. First, by comparing the performance of the baseline with cathodes (B), (C), (D) and (E), which have either 20% or 30% porosity at the membrane/CL or GDL/CL interfaces, it is clear that higher porosity near the interface of CL/GDL is helpful for O_2 transport and water removal. All these CLs perform almost identically when the current density is smaller than 50 mA.cm^{-2}, but the difference becomes larger with increasing current density. At 400 mA.cm^{-2} the cathode potential of (B) is 60mV and 260mV larger than (A) and (C), respectively. The reason is evident from Figure 4.6a, b and c, which show the O_2 concentration profiles through the catalyst layer. At small current density (50 mA.cm^{-2}), O_2 concentration distributions of all the CLs are

more homogeneous, with small variations along the thickness. However, at high current density (400 mA.cm^{-2}), there are significant O_2 concentration drops in these CLs: (B) exhibits a more even distribution than (D) and (A); (C), a reverse configuration to (B), has the lowest O_2 concentration throughout the whole CL, and there are significant fractions (up 50%) of the CLs of (C) and (E) operated under O_2 depletion. For the same porosities at the membrane/CL and GDL/CL interfaces, stepwise porosity distribution (B) has better performance and oxygen distribution than the linear distribution (D).

Second, to further explore the effect of stepwise distribution, (B) and (F) are compared, both of which have the stepwise distribution and identical average porosity. In the half sublayer near the GDL, because of larger porosity (35%), (F) has higher O_2 concentration than (B) as shown in Figure 4.6; however, it has larger ohmic drop due to smaller ionomer fraction to conduct protons. In the half sublayer near the membrane, O_2 concentration in (F) decreases dramatically far below that of (B) and it cannot be compensated by its smaller ionic resistance. So the net result is that (B) has better performance than (F) at almost all the current densities, except that the current density is very high (larger than 450 mA.cm^{-2} in Figure 4.5), where oxygen transport dominates over ohmic loss.

4.3.3   Influence of macro-pores

During CL fabrication process, some macro-pores can be formed due to insufficient mixing, as shown in the TEM image in Figure 3.3. These can be as large as several μm in diameter. Supposing that there is a 10-μm-diameter pore in a cathode CL of 30-μm thick and 30-μm wide, the influence of its position on cathode performance, proton conduction

and O_2 concentration distribution are investigated here in three cases: 1, 2 and 3, corresponding to its location near the GDL, in the middle of the CL, and near the membrane, respectively. The computational domain and locations of the pores in the three cases are shown in Figures 4.9, 4.10, and 4.11, respectively. Mathematical description of a macro-pore in the CL includes: no electrochemical reaction; effective oxygen diffusivity equal to the bulk value; and effective proton conductivity of zero. Obviously the macro-pore cannot contribute to electrochemical reaction, but it will influence proton conduction and O_2 distribution profile in the CL.

The location of pores plays an important role in affecting the performance, as shown in Figure 4.7. Case 1 and case 2 have almost identical cathode performance up to ~350 mA.cm^{-2}, beyond which case 1 shows better performance and larger limiting current density. For case 3 with the macro-pore near the membrane side, the cathode potential reduces from 15 mV to 55 mV comparing to case 1 between 100 and 400 mA.cm^{-2}.

The performance gain of case 1 over the other two cases can be explained in term of both proton conduction and oxygen transport. Figure 4.8 shows the total voltage loss (overpotential) along the CL/PEM interface for three different cases at 100 mA.cm^{-2}, where cathode performance is dominated by proton transport. The overpotential distributions of case 1 and case 2 along the interface are relative uniform; however, the overpotential bulges up in the middle for case 3, much higher than the other two cases. This is because protons transport over the macro-pore through the CL with more difficulty for case 3 with a macro-pore near the membrane, as proton conduction in the pores is impossible. Since a uniform current density at the CL/PEM interface is assumed

in Eq. 4.15, the overpotential, therefore, has to increase to sustain the desired current, especially in the middle area facing the pore.

Oxygen concentration contours of the three cases at 400 mA.cm^{-2} are shown in Figures 4.9, 4.10, and 4.11, respectively. Inside the macro-pore gases diffuse much faster than in the surrounding area, so the oxygen concentration is relatively constant there and higher than in the area around the pore. Therefore, macro-pores in a CL play a dual role. First, in the space between the front surface of the pore and the GDL, oxygen concentration profile lags compared to the surrounding area, since there is no oxygen consumed within the pore and the diffusion lacks driving force. Second, in the space between the back surface and the membrane, the oxygen concentration profile is pushed forward toward the membrane because of the higher O_2 diffusivity in the pore. To provide more active Pt sites in the CL for operation at higher O_2 concentration, the space between the front surface and GDL must be shrunk or the space between the back surface and the membrane must be expanded. For this reason, case 1 shows better performance than those of case 2 and 3. In Figure 4.9 where the pore is near the GDL side, it is clear that the O_2-depletion area shrinks and the reaction zone is extended toward the inside facing the membrane.

4.4   Summary

DMFC cathode CL features a large thickness and mass transport loss and must be carefully considered in order to optimize its performance. At low air stoichiometry, ambient pressure and low temperature, both diffusion of O_2 and conduction of proton in the thick DMFC cathode CL layer are more critical. Optimized performance is achieved

through a good balance of the two factors at medium Nafion weight fraction (22 wt%) in CL. The smaller optimum Nafion fraction in this study than reported values (around 35 wt%) in H_2 PEFCs is intended to provide more pore volume in the CL, thus improving the O_2 diffusion. CL structure with higher porosity near the GDL is helpful for O_2 transport and byproduct removal. The CL with stepwise porosity distribution, with higher porosity near the GDL and lower one near the membrane, performs better than that with linear distribution, especially at high current density. This is because it exhibits a healthier O_2 distribution in the CL, thus extending the reaction zone forward toward the membrane side. The position of macro-pores plays an important role in affecting proton conduction and oxygen transport in the CL, hence the performance. A cathode CL has superior performance and favorable oxygen concentration profile when the pore is near the GDL.

Table 4.1 Parameters used in the simulation of the cathode catalyst layer

Parameters	Value
Intrinsic proton conductivity of fully hydrated polymer, $\kappa_{e,0}$ (S/cm)	0.1
Reactive area per volume, a (m^2/m^3)	400
Oxygen diffusion coefficient, $D_g^{O_2}$ (m^2/s)	1×10^{-5}
Transfer coefficient of cathode, α_c	1.0
Reference exchange current density, i_0 (A/m^2)	5×10^{-5}
Reference oxygen concentration of cathode kinetics, $c_{O_2,ref}$ (mol/m^3)	8.825
Air pressure in gas channel inlet, p (kPa)	100
Operating temperature, T (^{o}C)	60
Thickness of the GDL, ΔX_{GDL} (μm)	300
Tortuosity of the GDL, τ_{GDL}	4
Porosity of the GDL, ε_{GDL}	0.4
Swelling degree of ionomer upon hydration by weight, SW	1.2
Percolation critical value, X_0	0.13
Stoichiometric parameter, S	0.65
Thermodynamic open circuit potential at 60°C and ambient pressure, E_{oc}(V)	1.19
Density of Nafion, ρ_{Nafion} (g/cm^3)	1.9
Density of Pt, ρ_{Pt} (g/cm^3)	21.5
Density of carbon, ρ_c (g/cm^3)	2.0
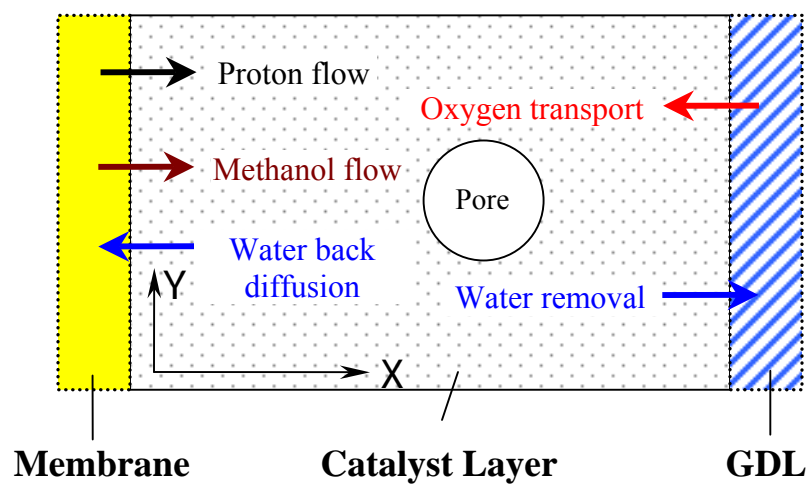
Figure 4.1 Schematic diagram of transport process in cathode CL of a DMFC
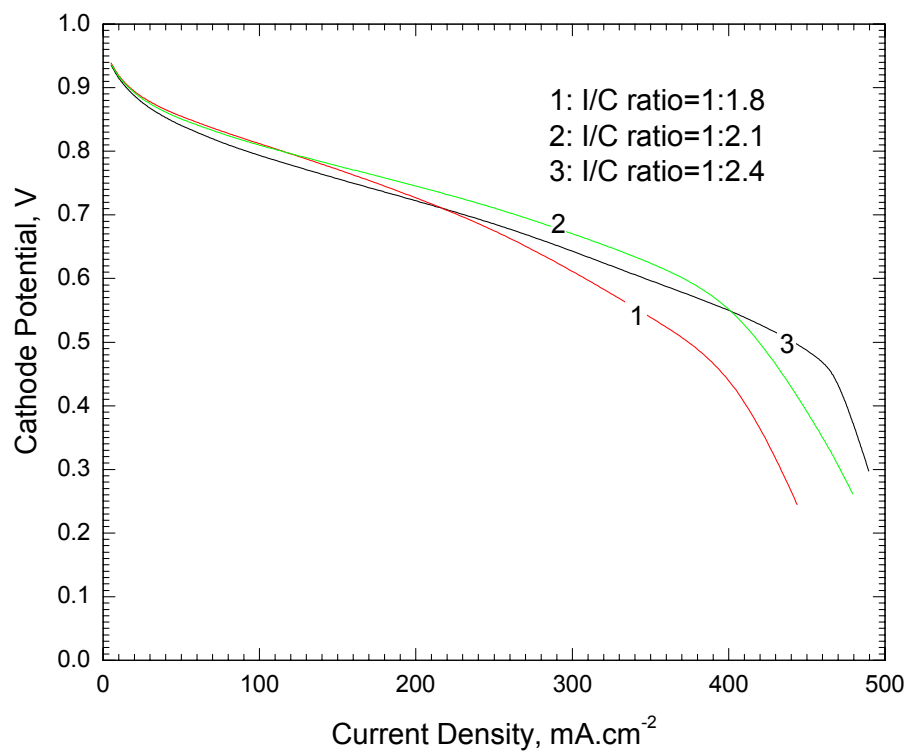
Figure 4.2 Effect of Nafion content in the cathode CL on the polarization behavior of MEAs at 60°C using fully humidified air at ambient pressure.
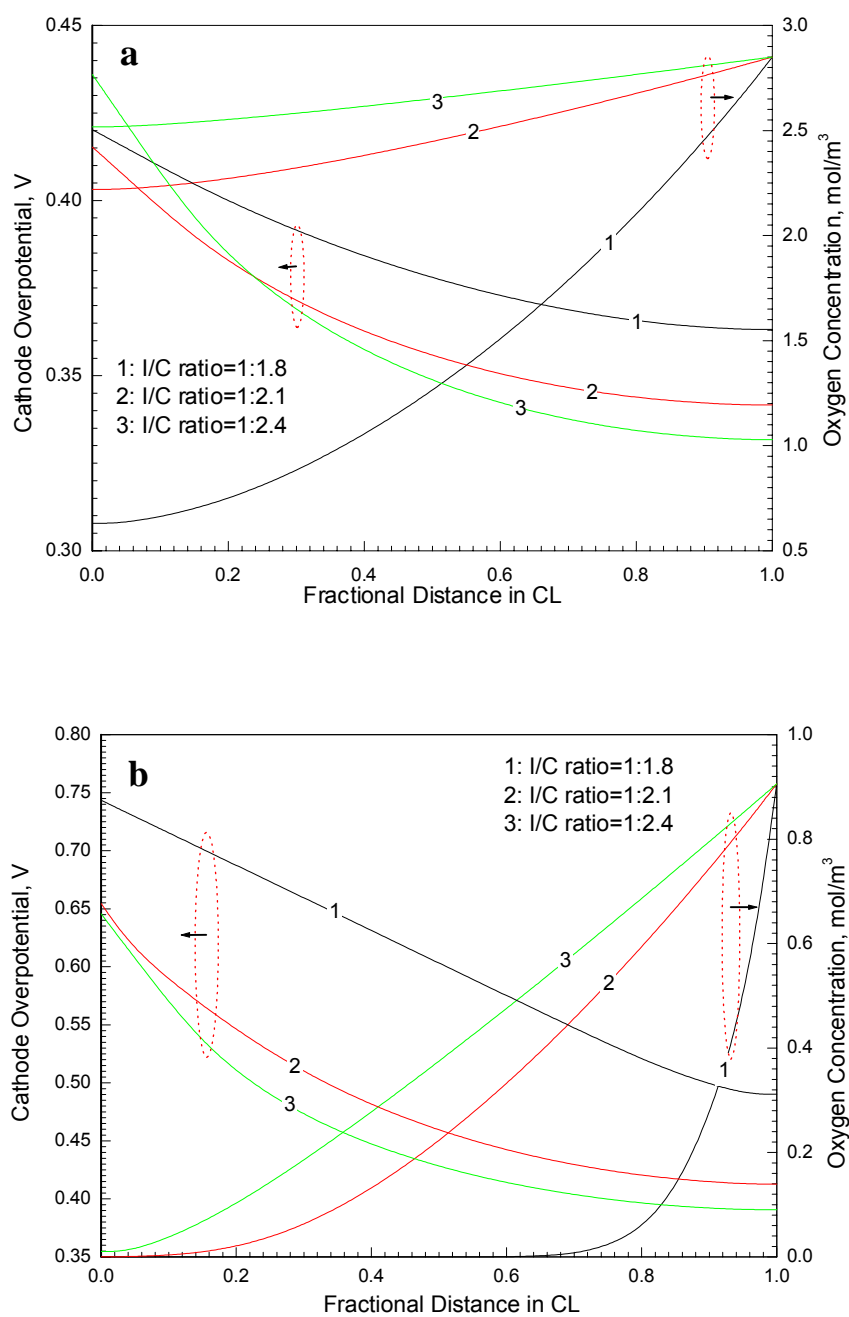
Figure 4.3 Distribution of oxygen concentration and cathode overpotential at (a) 150 mA.cm^{-2} and (b) 400 mA.cm^{-2} in the cathode CLs. The operating condition is 60°C, using fully humidified air and ambient pressure.
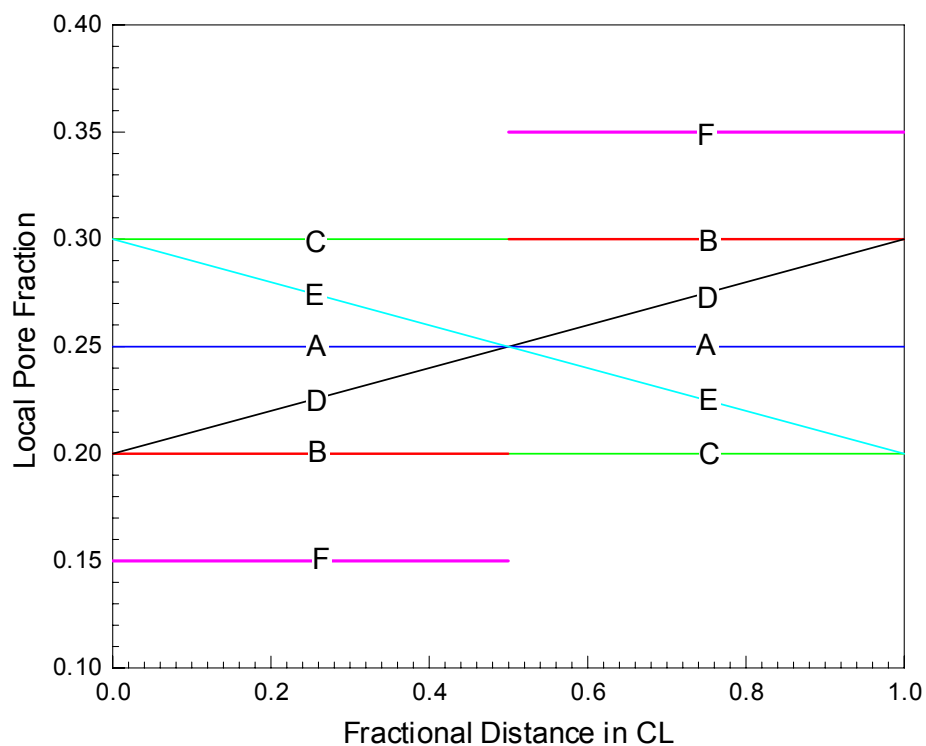
Figure 4.4 Porosity distribution of the six different cathode CL structures: (A) uniform; (B), (C) and (F) are step-wise; and (D) and (E) are linear distribution.
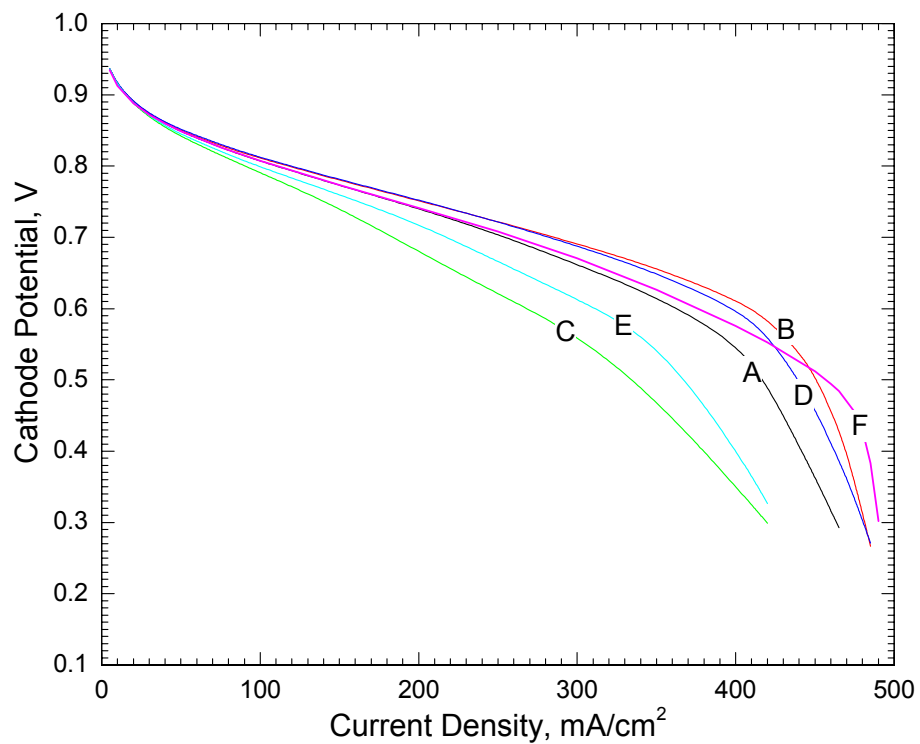
Figure 4.5 Performance for different cathode CLs (I/C ratio=1:2.1) at 60°C. The porosity distributions of these cathode CLs are depicted in Figure 4.4.
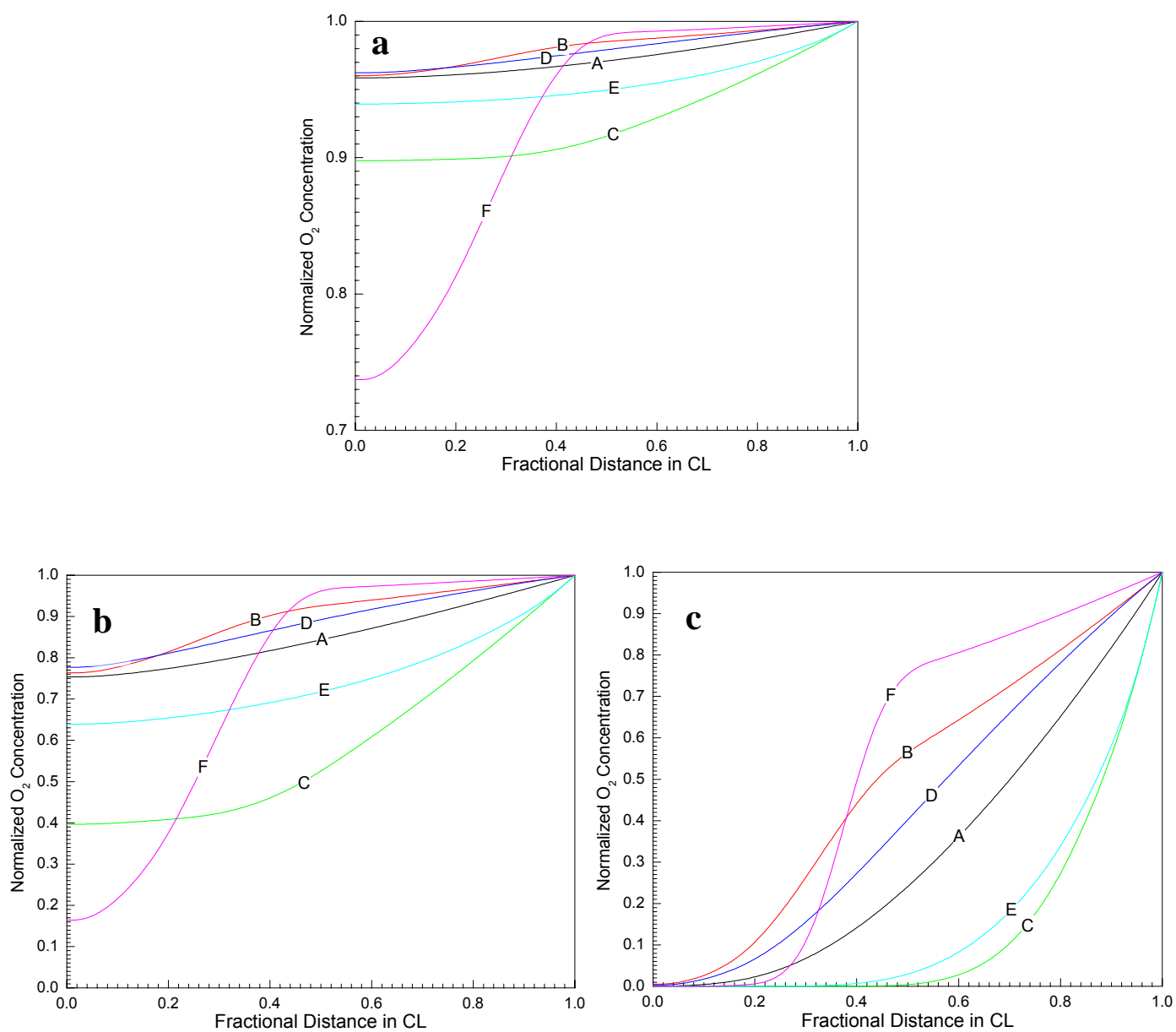
Figure 4.6 Oxygen concentration distributions in the CLs A~E (I/C ratio=1:2.1) at current densities of (a) 50 mA.cm^{-2}, (b) 150 mA.cm^{-2}, and (c) 400 mA.cm^{-2}.
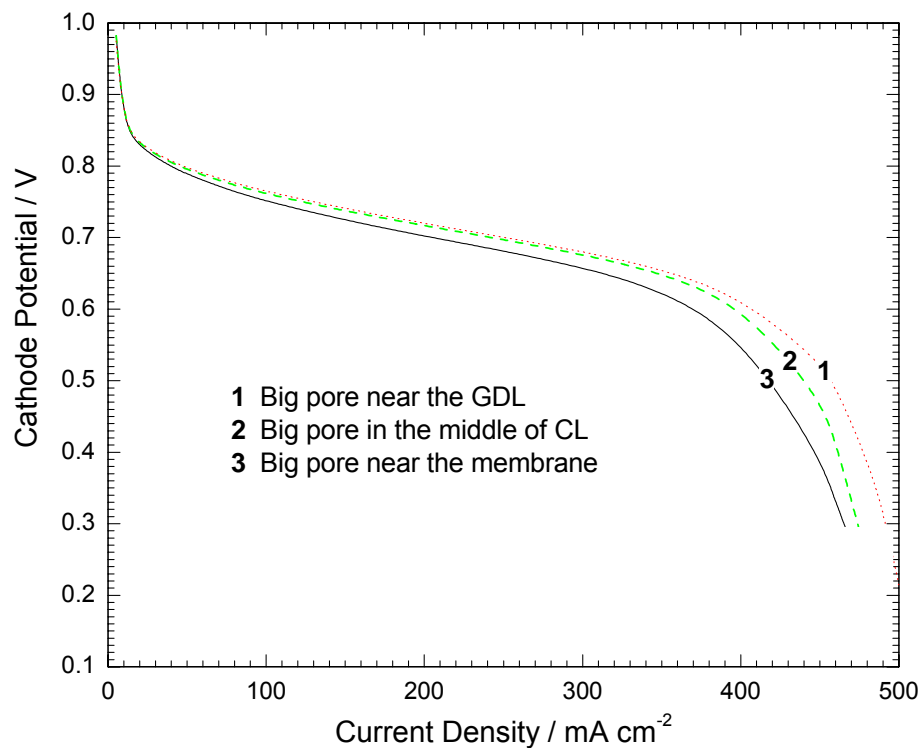
Figure 4.7 Cathode performance for three cases (I/C ratio=1:2.1): (1) the pore near the GDL, (2) in the middle of CL, and (3) near the membrane. The diameter of the pore is 10 μm and the thickness of cathode CL is 30 μm.
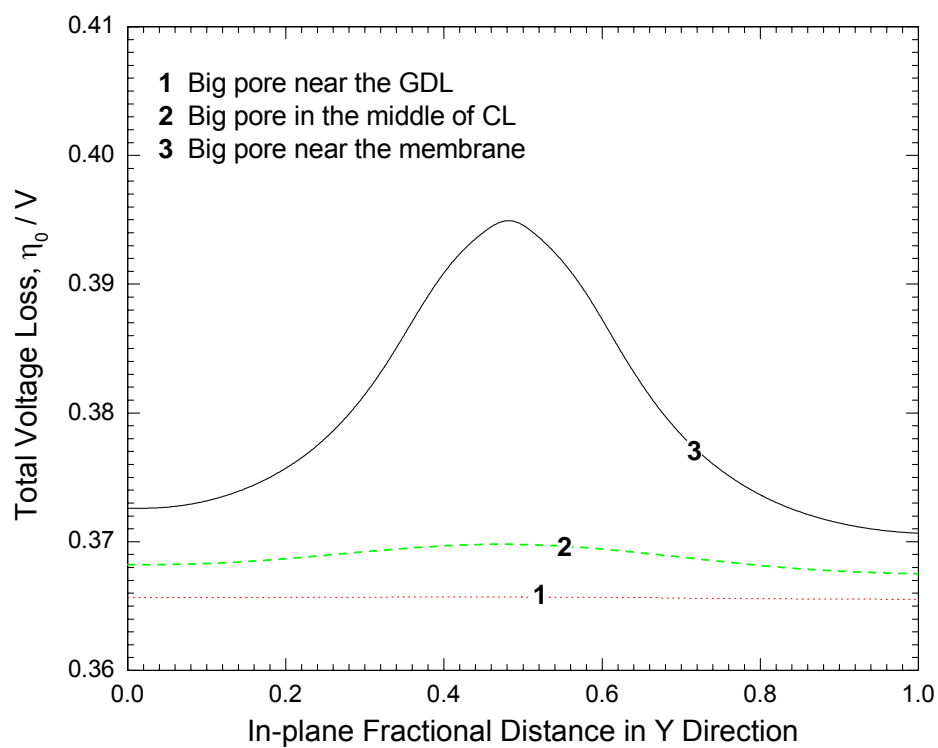
Figure 4.8 Total voltage loss distribution along the CL/PEM interface at 100 mA.cm^{-2} for three different cases.
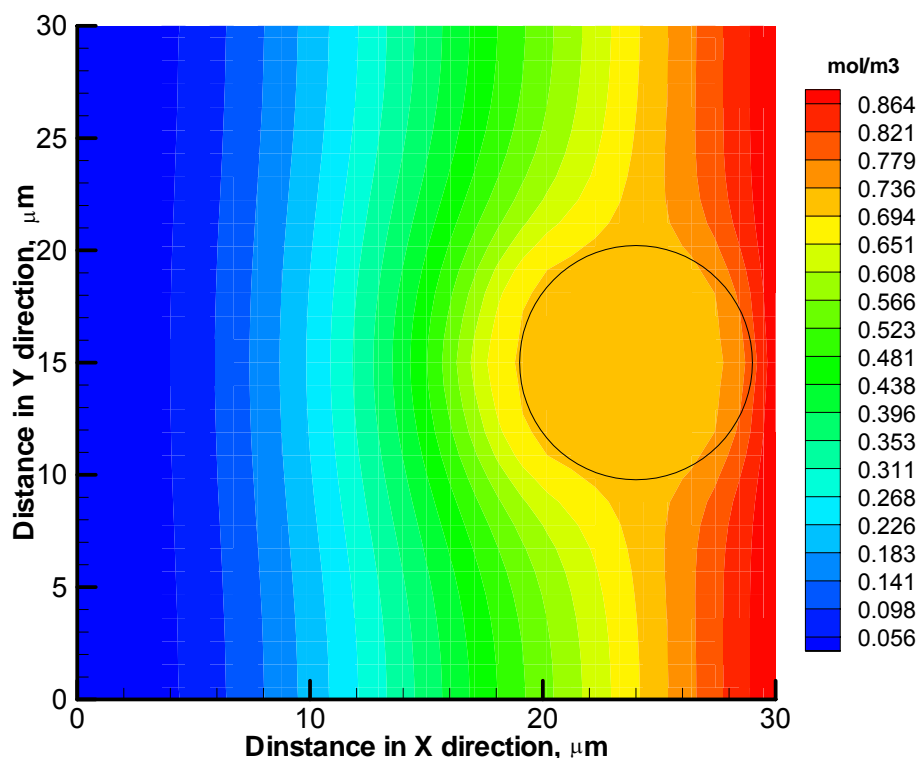
Figure 4.9 Oxygen concentration contour in the cathode CL at 400 mA.cm^{-2} when a macro pore (indicated by the circle) is near the GDL side (case 1).
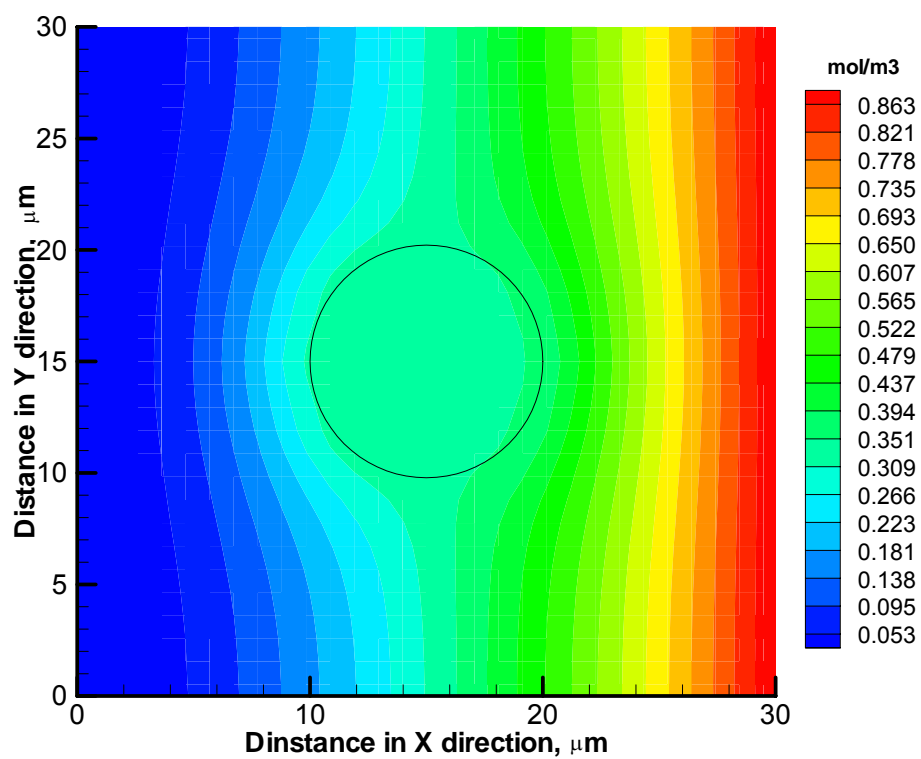
Figure 4.10 Oxygen concentration contour in the cathode CL at 400 mA.cm^{-2} when a macro pore (indicated by the circle) is in the middle of the CL (case 2).
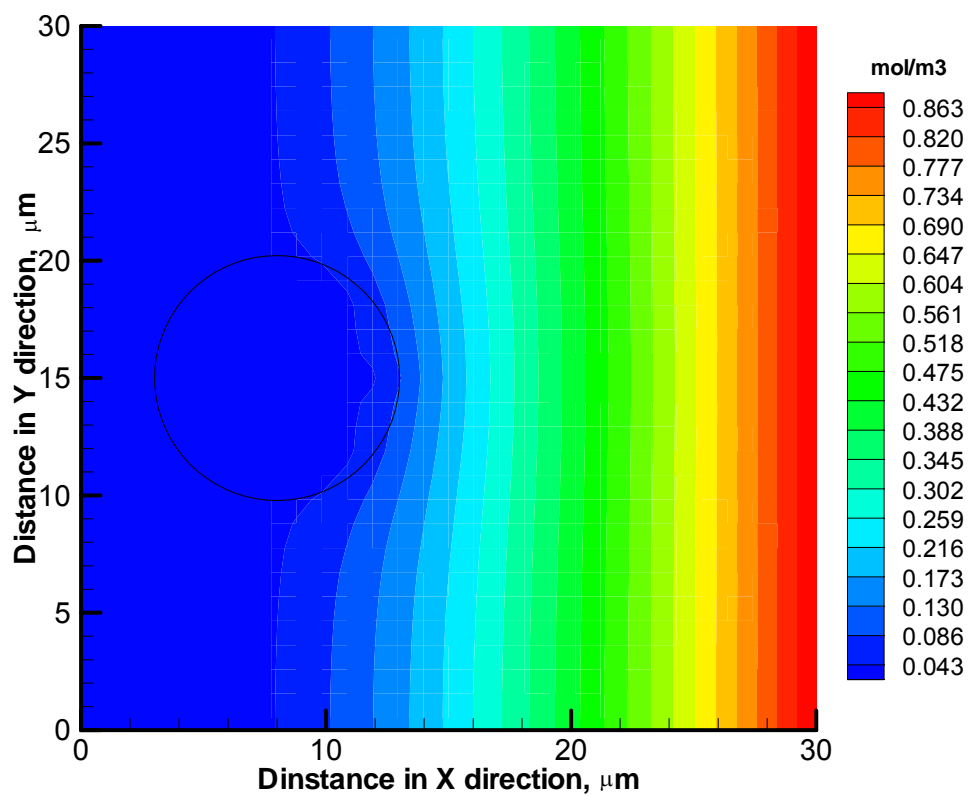
Figure 4.11 Oxygen concentration contour in the cathode CL at 400 mA.cm^{-2} when a macro pore (indicated by the circle) is near the membrane side (case 3).

Chapter 5 TWO-PHASE MODELING OF THE CATHODE CATALYST LAYER IN A DIRECT METHANOL FUEL CELL

5.1 Introduction

A primary factor limiting DMFC cathode performance is methanol crossover through the electrolyte membrane. This includes loss of methanol fuel from the anode and performance loss at the cathode, where simultaneous reduction of O_2 (oxygen reduction reaction, ORR) and oxidation of methanol (methanol oxidation reaction, MOR) lead to lower cathode potential and hence decreased cell voltage.

The mixed-potential phenomenon has been the subject of numerous experimental studies. Bittin-Cataneo et al. (1993) investigated the interaction of methanol and oxygen at a PTFE-bonded gas diffusion electrode and found that MOR partial current was enhanced and the onset of MOR occurred 100mV more cathodic in the presence of oxygen. Chu and Gilman (1994) claimed, however, that the ORR rate is reduced by surface poisoning of methanol oxidation fragments or organic impurities in the methanol. Similar results were reported by Paulus et al. (2003) but in contrast, the ORR was proven to be unaffected by the presence of methanol. Vielstich et al. (2001) proposed a purely chemical reaction between oxygen and methanol at the platinum interface in a gas diffusion electrode. It was found that this chemical pathway, accompanied by a strong increase in the fuel consumption rate, considerably decreases ORR. Recently, Jusys et al.

(2004) determined separately the rates of the simultaneous MOR and ORR on a Pt/C in O_2-saturated methanol solution. Their results showed a slight deviation from a simple additive superposition of ORR and MOR currents, by an increased formation of partly oxidized by-products. The conclusions from different groups are contradictory; therefore, in spite of extensive studies, the origin of the methanol crossover effect is still not fully understood.

Numerical models are also used to describe the phenomenon and to attempt to understand the mechanism. Wang and Wang (2003) presented a multi-component model for a liquid-feed DMFC. The two-phase transport in the porous media is elaboratively treated in the model and the catalyst layer was considered as an infinitesimally thin layer. Murgia et al. (2003) proposed a one-dimensional, multi-component model, in which the effective cathodic current density is treated as a summation of the load current and methanol crossover current to account for the crossover effect on the cathode polarization. Most recently, Kulikovsky (2004, 2005) has developed a 1D + 1D model of a DMFC based on semi-empirical equations. Considering the rather complex nature of the MOR and ORR, semi-empirical solutions seem inappropriate and lack physical meanings. The above-mentioned studies introduced some fundamental knowledge on species transport and electrochemical reaction; however, the most important ORR and MOR kinetics and their mutual interactions have been ignored. To our best knowledge, there is no reliable model to estimate the crossover effect on cathode performance in a DMFC to date.

The objective of the present study is two-fold to address these unresolved issues. The first goal is to introduce a 1-D model of the DMFC cathode CL, which incorporates

recent experimental findings on electrochemical kinetics as well as the well-established multi-phase mixture (M^2) approach to two-phase transport developed by Wang et al. (Wang and Cheng, 1996, 1997; Wang, 2004; Pasaogullari and Wang, 2004, 2005). Considering the highly flooded nature of the cathode CL in DMFCs, two-phase transport models are essential. The combination of the two aspects, therefore, permits a more accurate modeling of liquid-water transport, species diffusion across the CL, and the mixed potential due to methanol crossover. The second objective is to optimize CL thickness. Model predictions of cathode CL performance at various thicknesses are given, and the effects of two-phase transport and electrochemical kinetics are discussed.

5.2   Mathematical Model

A M^2 model for two-phase transport is combined with a multi-step electrochemical kinetics model in this work. The same assumptions mentioned in Chapter 4 are made here.

5.2.1   Two-phase transport model

The M^2 formulation is used to simulate two-phase species transport in the DMFC cathode CL. Readers are referred to references (Wang and Cheng, 1996, 1997; Wang, 2004; Pasaogullari and Wang, 2004, 2005) for details of this model. Here only a brief description is given. Figure 5.1 shows the schematic one-dimensional computational region and related transport processes. The governing equations of species and charge conservation with sink/source terms are summarized in Table 5.1. Some of them are taken from Pasaogullari and Wang (2004) and modified for use in this work.

The governing equation for water transport in the GDL is modified to describe water transport in the CL

$$\frac{d}{dx}(\gamma_c u C^{H_2O}) + \frac{d}{dx}\left[\left(\frac{1 - C_l^{MeOH} M^{MeOH}/\rho}{M^{H_2O}} - \frac{C_{sat}^{H_2O}}{\rho_g}\right)j_l\right] + \frac{d}{dx}\left(\frac{n_d}{F}I_e\right) = S^{H_2O} \qquad [5.1]$$

The three terms at the left-hand side describe water transport by convection, capillary transport, electro-osmotic drag and the right-hand side term is the source term due to reaction. Here, I_e is the current density conducted through the electrolyte in the CL, $C_l^{MeOH} M^{MeOH}/\rho$ is the mass fraction of methanol in the liquid, u is the superficial two-phase mixture velocity, and γ_c is the advection factor. The advection factor is expressed as

$$\gamma_c = \begin{cases} \dfrac{\rho}{C^{H_2O}}\left(\dfrac{\lambda_l}{M^{H_2O}} + \lambda_g \dfrac{C_{sat}^{H_2O}}{\rho_g}\right) & \text{for water} \\[2em] \dfrac{\rho\lambda_g}{\rho_g(1-s)} & \text{for other species} \end{cases} \qquad [5.2]$$

where ρ, λ_l and λ_g are the two-phase mixture density, relative mobility of liquid and gas phases, respectively

$$\rho = \rho_l s + \rho_g(1-s) \qquad [5.3]$$

$$\lambda_l = \frac{k_{rl}/v_l}{k_{rl}/v_l + k_{rg}/v_g} \qquad \lambda_g = 1 - \lambda_l \qquad [5.4]$$

where k_{rg} and k_{rl} are the relative permeabilities of individual phases, which equal to the cube of phase saturations.

In Eq. 5.1, j_l is the liquid flux driven by capillary pressure gradient

$$j_l = \frac{\lambda_l \lambda_g \rho K}{\mu} \frac{d}{dx}\left(\sigma \cos(\theta_C)(\frac{\varepsilon}{K})^{1/2} J(s)\right)$$ [5.5]

where $J(s)$ is the Leverett function and is given for both hydrophilic and hydrophobic

media as

$$J(s) = \begin{cases} 1.417(1-s) - 2.120(1-s)^2 + 1.263(1-s)^3, & \text{if } \theta_c < 90^o \\ 1.417s - 2.120s^2 + 1.263s^3, & \text{if } \theta_c > 90^o \end{cases}$$ [5.6]

where θ_c is the contact angle.

The total water concentration (mol/m^3) in the two-phase mixture is described by

$$C^{H_2O} = \frac{\rho_l s}{M^{H_2O}} + (1-s)C_{sat}^{H_2O}$$ [5.7]

Thus $\qquad \dfrac{dC^{H_2O}}{dx} = (\dfrac{\rho_l}{M^{H_2O}} - C_{sat}^{H_2O})\dfrac{ds}{dx}$ [5.8]

Substituting Eqs. 5.2, 5.5 and 5.8 into Eq. 5.1 yields the governing equation for water

transport as shown in Table 5.1, where $D_{CL}^{H_2O}$ is expressed as

$$D_{CL}^{H_2O} = -\frac{\dfrac{1 - C_l^{MeOH} M^{MeOH}/\rho}{M^{H_2O}} - \dfrac{C_{sat}^{H_2O}}{\rho_g}}{\dfrac{\rho_l}{M^{H_2O}} - C_{sat}^{H_2O}} \frac{\lambda_l \lambda_g \rho}{\mu} \sigma \cos(\theta_C)(\varepsilon K)^{1/2} \frac{dJ(s)}{ds}$$ [5.9]

In the governing equations for both oxygen and methanol, diffusion in liquid is

ignored due to low O$_2$ solubility and low liquid methanol diffusivity. The effective

diffusivities of oxygen and methanol in vapor phase are described by the percolation

theory as

$$D_{CL}^{i,eff} = D_g^i \cdot \left(\frac{\varepsilon_{CL}(1-s) - X_0}{1 - X_0}\right)^2$$ [5.10]

where D_g^i, ε_{CL}, and X_0 are the bulk species diffusivity, porosity of the CL, and percolation critical value, respectively. Other parameters can be found in Table 5.2.

For the vapor and liquid phase equilibrium, Henry's law is simply employed to calculate the methanol vapor pressure (Wang and Wang, 2003)

$$p_g^{MeOH} = k_H x_l^{MeOH} \qquad [5.11]$$

where k_H and x_l^{MeOH} are the Henry constant and methanol molar fraction in liquid, respectively. In dilute solution the molar concentration of methanol in vapor can thus be simply determined by

$$C_g^{MeOH} = \frac{p_g^{MeOH}}{RT} = \frac{k_H}{RT} \frac{M^{H_2O}}{\rho_l^{H_2O}} C_l^{MeOH} \qquad [5.12]$$

5.2.2 Electrochemical kinetics

In a DMFC cathode CL, oxygen is reduced and the crossover methanol is oxidized via Eqs. 1.2 and 1.1, respectively. Similarly to Eq. 4.3, the rate of ORR is governed by the Tafel kinetics as follows

$$j_{rxn}^{O_2} = -i_0^{O_2} a \frac{(1-s)C^{O_2}}{C_{0,ref}^{O_2}} \exp(-\frac{\alpha_c F}{RT} \eta) \qquad [5.13]$$

where a is the local active reaction area, which equals to the total ECA divided by the CL thickness, (1-s) accounts for the fraction of ECA that is available for ORR, and other symbols have their usual meanings as in Chapter 4. The DMFC cathode potential is obtained by

$$V_{cath} = V_{rev} + \eta \qquad [5.14]$$

The MOR is a multi-step reaction and its kinetics is based on the following reaction mechanism (Kauranen and Skou, 1996; Nordlund and Lindbergh, 2002)

$$CH_3OH \underset{k_1'}{\overset{k_1}{\longleftrightarrow}} CH_3OH_{ads} \qquad [5.15]$$

$$CH_3OH_{ads} \overset{k_2}{\longrightarrow} CO_{ads} + 4H_{ads} \qquad [5.16]$$

$$H_2O \underset{k_3'}{\overset{k_3}{\longleftrightarrow}} OH_{ads} + H_{ads} \qquad [5.17]$$

$$CO_{ads} + 2OH_{ads} \overset{k_4}{\longrightarrow} CO_2 + H_2O \qquad [5.18]$$

$$H_{ads} \overset{k_5}{\longrightarrow} H^+ + e^- \qquad [5.19]$$
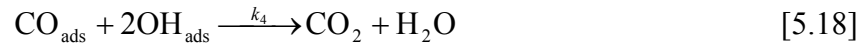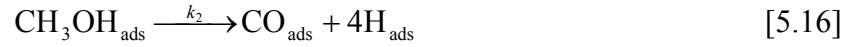
The H_{ads} produced in Eqs. 5.16 and 5.17 is immediately oxidized via Eq. 5.19 when the voltage is above 0.3V (Kauranen and Skou, 1996), so the surface coverage of H_{ads} is assumed to be zero at the cathode CL. At steady state, the surface coverage of different species is constant with time. Following the same procedure described by Nordlund and Lindbergh (2002), the obtained species surface coverages are

$$\theta_{CO} = b \frac{k_2 \exp(\dfrac{\alpha_2 FV_{cath}}{RT})}{k_4 \exp(\dfrac{(1-\beta_4)FV_{cath}}{RT})} \qquad [5.20]$$

$$\theta_{OH} = \frac{k_1 C^{MeOH}(1-\theta_{CO})}{b\left[k_1' + k_2 \exp(\dfrac{\alpha_2 FV_{cath}}{RT}) + k_1 C^{MeOH}\right] + k_1 C^{MeOH}} \qquad [5.21]$$

where k_i, α_i and β_i are rate constants, transfer coefficients and symmetry factors of different reactions, respectively, which are listed in Table 5.3. In the above two equations, b is expressed as

$$b = \frac{k_3' \exp(-\frac{\beta_3 FV_{cath}}{RT})}{\left(k_1' + k_2 \exp(\frac{\alpha_2 FV_{cath}}{RT})\right) k_3 \exp(\frac{(1-\beta_3)FV_{cath}}{RT})/(k_1 C^{MeOH}) + k_2 \exp(\frac{\alpha_2 FV_{cath}}{RT})} \qquad [5.22]$$

where C^{MeOH} is the molar concentration of methanol in the two-phase mixture, *i.e.*

$$C^{MeOH} = sC_l^{MeOH} + (1-s)C_g^{MeOH} \qquad [5.23]$$

Thus, the MOR current is proportional to any of the reactions 5.15-5.19, for example

$$j_{oxi}^{MeOH} = 6aFKk_4 \exp(\frac{(1-\beta_4)FV_{cath}}{RT})\theta_{CO}\theta_{OH} \qquad [5.24]$$

which is based on Eq. 5.18. In the above equation K is a proportionality constant. The concentration dependence of the anode polarization curves is shown in Figure 5.2, where the pure kinetics is plotted, omitting all the mass transfer limitations. There is no MOR current density until the cathode voltage is beyond 0.4V; however, when the potential is beyond the peak, the current density decreases due to surface oxide formation, blocking further reaction (Li et al., 2002).

In addition, a purely chemical gas phase reaction between methanol vapor and oxygen at the Pt interface (Vielstich et al., 2001) in the cathode CL is considered

$$CH_3OH + 1.5O_2 \longrightarrow 2H_2O + CO_2 \qquad [5.25]$$

The chemical reaction rate is described as

$$r = aK_r \left(C_g^{MeOH}\right)^{\beta} \left(C^{O_2}\right)^{\gamma} \qquad [5.26]$$

where K_r is a rate constant, and β and γ are concentration exponents. This chemical reaction consumes additional oxygen and yields severe concentration gradient across the cathode CL.

5.2.3   Source terms

In a DMFC cathode CL, the ORR and MOR take place simultaneously. The mutual interaction between the ORR and MOR is symbolized in the source term of the governing equation for the proton transport. As discussed in the introduction, there are two contradicting opinions in the literature: (i) the ORR activity decreases while MOR rate remains constant or; (ii) the MOR rate decreases while ORR remains unaltered. For simplicity, a simple additive superposition of the two partial processes is adopted in this work, since one of the two partial reactions is only slightly affected by the other (Jusys and Behm, 2003; Kauranen and Skou, 1996). Therefore, the source term in proton transport is a summation of the MOR and ORR currents. The cathode potential, where the MOR and ORR produce zero net current, is referred to as the mixed potential. For other species, such as water, oxygen and methanol, both electrochemical and chemical reactions contribute to the source terms, as shown in Table 5.1.

5.2.4   Boundary conditions

The boundary conditions are listed in Figure 5.1. The total water concentration at the GDL/CL interface is calculated as

$$C_{GDL/CL}^{H_2O} = \frac{\rho_l s_{GDL/CL}}{M^{H_2O}} + (1 - s_{GDL/CL})C_{sat}^{H_2O} \qquad [5.27]$$

where the liquid saturation at GDL/CL interface is obtained according to Pasaogullari and Wang (2004).

Oxygen concentration at the GDL/channel interface is obtained from the convective mass transport analysis and expressed as

$$h_m(C^{O_2}_{GDL/chann} - C^{O_2}_{chann}) = -\frac{I}{4F} \qquad [5.28]$$

where h_m and $C^{O_2}_{chann}$ are the convective mass transfer coefficient and oxygen concentration in the channel. $C^{O_2}_{chann}$ is obtained by averaging the inlet and outlet oxygen molar fraction, *i.e.*

$$C^{H_2O}_{chann} = \left(\frac{x^{chann}_O + 0.21}{2}\right)\frac{P}{RT} \qquad [5.29]$$

where, the oxygen molar fraction at the outlet is

$$x^{chann}_O = \frac{0.15S_R - I - I_{xover}}{0.15S_R - I - I_{xover}/3 + 0.15S_R \times \dfrac{0.79}{0.21}} \frac{P - P^{H_2O}_{sat}}{P} \qquad [5.30]$$

in which I_{xover} and S_R are the methanol crossover current density and air stoichiometry ratio at 0.15A/cm^2, a reference operating current density in this study. In the above equation, $I_{xover}/3$ accounts for the carbon dioxide produced by methanol oxidation. The methanol crossover current can be mathematically formulated by a simple relation existing between the crossover current, I_{xover}, and anode mass transport limiting current, $I_{A,lim}$, as shown in Eq. 2.1. The methanol crossover current density at open circuit is assumed to be 240 mA/cm^2.

Superficial velocities at the two interfaces are calculated according to

$$\rho u = j_m \qquad [5.31]$$

where j_m is the total mass flux through the interface in both phases.

5.3   Results and Discussion

5.3.1   Model validation

In the present model validation, a 12-cm^2 MEA in CCM configuration was utilized. The catalyst loadings are 4.5 mgPtRu/cm^2 and 1.2 mgPt/cm^2 at the anode and cathode, respectively. A Nafion 112 membrane was employed and the cell was operated at 60°C. More details of the MEA fabrication, cell fixture, and operating conditions will be described in Chapter 6. In the DMFC operation, the anode and cathode stoichiometries of 2.0 and 3.0 at 150mA/cm^2 are utilized, representing a practically reasonable stoichiometry for portable power. For comparison, an H$_2$/air cell performance was also recorded at the same cathode stoichiometry, but the anode stoichiometry was controlled at 8.3 at 150 mA/cm^2, ensuring that only the mass transport limitation at the cathode contributes to the cell overpotential. Each voltage data point is obtained by averaging the values recorded for 3~5min at a certain current density. High-frequency resistance (HFR) of the cell at each current density was measured using an Agilent 4338B Milliohmmeter at 1kHz.

DMFC cathode potentials are evaluated according to the same procedure described in section 3.3.3. Figure 5.3 compares the simulated and measured cathode performance in a DMFC and H$_2$/air cell at 60°C with a cathode stoichiometry of 3 at 150 mA/cm^2. The steady-state DMFC and anode polarization data are also displayed in the figure for comparison. Cathode data points in DMFC with current density larger than 250 mA/cm^2 could not be obtained because of the limited methanol supply at the anode. It is seen that the model has excellent agreement with experimental data. Methanol crossover and its detrimental effect diminish with the current density, and vanish when the current density

is higher than the anode limiting current density (i.e. 290 mA/cm^2), where the cathode potential in a DMFC consequently approaches that in an H$_2$/air cell. This observation is slightly different from the data reported in the literature, where the DMFC cathodes are still suffered from the mixed potential at very high current densities, or even through the entire polarization curves. This is because that very high methanol flowrate (real stoichiometry > 10) is commonly employed; therefore it is not surprising to expect a large methanol crossover and its detrimental effect at high current densities.

5.3.2   Mixed potential

To study the mixed potential of an air cathode in the presence of methanol crossover, polarization curves under different cathode environments are compared, including: (1) air with methanol crossover, (2) air with methanol crossover and infinite oxygen diffusivity, (3) air without methanol crossover, (4) oxygen with methanol crossover, and (5) oxygen without methanol crossover. The results are summarized in Figure 5.4. Curves (3) and (5) show the cathode performance using air and oxygen without methanol crossover, respectively. When oxygen is used, the cathode performance improves by ~ 80mV in both kinetic and ohmic regimes, and there is no severe mass transport limitation in curve (5). In the presence of methanol crossover at the cathode, the performance using air and oxygen is displayed by curves (1) and (4), respectively. The open circuit voltage loss due to methanol crossover is almost 100 mV using air, compared to only 20 mV with oxygen; and at 50 mA/cm^2, the cathode voltage drops due to methanol crossover are about 66 and 21 mV for air and oxygen, respectively. Therefore, the detrimental effect of methanol crossover is more pronounced when air is used at the cathode. These simulated results are

consistent with experimental results (not shown), where the methanol crossover effect is minimized by oxygen and the DMFC performance improves $\sim$ 91mV at 150mA/cm^2 compared with air. The cause can be explained by analyzing Eq. 5.13, in which the ORR current is expressed as an exponential function of overpotential. At the DMFC cathode catalyst surface, both ORR and MOR proceed simultaneously, thus the cathodic and anodic currents cancel each other, leading to a dramatic decrease in the net current. The only way to maintain the prescribed load current is to increase the overpotential or reduce the cathode voltage. However, the oxygen concentration is much smaller in air than in pure oxygen, and further reduced by the chemical pathway and electrochemical reduction. Therefore, the cathode overpotential has to increase to a greater extent to offset the small oxygen concentration in air. The present explanation can further be verified by curve 2 in Figure 5.4, in which oxygen diffusivity in air was set to be infinity. The DMFC cathode performance improves dramatically at high current densities, but only slightly at small current densities. This indicates that at small load the improved oxygen diffusion in curve 2 does not contribute as much as the oxygen enrichment in air, thus leading to the same mixed potential as in curve 1.

5.3.3 Methanol crossover effects

Driven by diffusion and electro-osmotic drag (Ren et al., 2000), methanol permeates through the polymer membrane and eventually reacts electrochemically or chemically with oxygen at the cathode platinum surface, resulting in a mixed potential. Figures 5.5, 5.6, and 5.7 compare oxygen concentration, overpotential, and water saturation profiles in a DMFC cathode, respectively, with a H$_2$ PEFC cathode. From Figure 5.5a, it is clear that

the oxygen concentration decreases dramatically starting at the GDL/CL interface down inside the DMFC cathode CL. For the CL without methanol crossover, however, there is negligible oxygen concentration gradient within the cathode CL. At high current densities, oxygen concentration profiles in the CL with and without methanol crossover approach each other when methanol crossover becomes trivial. Water saturation and overpotential profiles in the CLs have the similar trend, as shown in Figure 5.6 and 5.7. Water saturation and overpotential are much higher in the CL with methanol crossover than that without crossover, especially at low current densities. At high current densities (>200 mA/cm^2), their profiles in the two cases overlap.

The crossover methanol from the anode is almost completely converted to carbon dioxide and water (Wang et al., 1996) in the presence of cathode catalysts; however, this reaction consumes oxygen from the air supplied to the cathode that would otherwise be required for the ORR (Müller et al., 2003). Therefore, oxygen is relatively deficient in the CL when methanol crossover is high. At the same time, the water produced from MOR results in an additional mass transport resistance. These results clearly show that DMFC cathodes are easily flooded with considerable mass transfer resistance; therefore, they are operated under more critical conditions than H$_2$ PEM cell cathodes.

The influence of MOR parameters, such as methanol crossover current density and kinetic rate constant K (in Eq. 5.24), is investigated in Figures 5.8 and 5.9. Variation in the methanol crossover current density at open circuit only influences the OCV and DMFC cathode performance at small current densities. A larger methanol crossover corresponds to a lower voltage as well as a low OCV. At high operating current densities where methanol crossover decreases, the effect of methanol crossover diminishes and all

the curves overlap each other. The MOR kinetic rate constant K is a parameter to quantify methanol-tolerance of cathode catalysts. In this model, ORR kinetics is assumed not affected by the presence of methanol; therefore small K means that the CL is relatively inert to MOR and highly selective toward ORR. In Figure 5.9, smaller K results in higher methanol concentration profile through the cathode CL, yielding smaller overpotential thus better performance. Note that the methanol crossover current densities are identical in all cases, thus it is clear that crossover methanol is detrimental to cathode performance only if oxidized electrochemically. For higher K, for example, $K=1.0\times10^7$, methanol concentration drops dramatically from about 1.5 mol/m^3 at the PEM/CL interface down to 0 near the CL/GDL interface. At the same time, the overpotential has to increase to offset the mixed potential and oxygen deficiency in the cathode CL. These results have a direct implication on the design of DMFC cathode catalysts. There are essentially two approaches to reduce the detrimental effect of methanol crossover. One is to block methanol crossover rate using new polymer materials or MEA designs; the other is to develop and employ new methanol-tolerant cathode catalysts, which are required to have high reactivity toward the ORR against the MOR.

5.3.4   Effect of cathode CL thickness

In a DMFC, high cathode Pt loading is commonly employed to mitigate the methanol crossover effect and enhance the ORR kinetics. However, a higher Pt loading corresponds to a thicker CL, dramatically increasing the resistances to oxygen diffusion and proton conduction. Reducing CL thickness may be an effective way to improve species transport, thus the cathode performance. Nevertheless, a thinner CL possesses

less reaction sites for current transfer, which would increase the kinetics loss. Therefore, the thickness of the CL needs to be optimized to balance the effects of the number of reaction sites, ohmic loss, oxygen diffusion, and water removal under the target operation conditions.

Performance of DMFC cathode CLs with various thicknesses is compared in Figure 5.10. Thinner CLs show better performance in the mass transport limitation regime; however, the electrochemical kinetics is suffered by their limited number of reaction sites (or limited ECA). Thicker CLs show better ORR kinetics with the sacrifice of cathode performance at high current densities. Therefore, the optimized thickness depends on the operating current. From the inset of Figure 5.10, the 20-μm-thick CL displays the highest voltage at 150 mA/cm^2, a practical design point for portable applications. Optimized performance is achieved by two competing factors, *i.e.*, oxygen transport and protonic resistance in the CL, which can be best explained by water saturation and overpotential profiles displayed in Figures 5.11 and 5.12, respectively. Water saturation in the thicker cathode CLs is higher since water removal is more difficult; thus a significant fraction of the catalytically active area is covered by liquid water and cannot contribute to electrochemical reaction. On the contrary, oxygen transport is more favorable in thinner CLs, leading to higher and more uniform oxygen concentration profiles along the thickness at different current densities (results not shown). In Figure 5.12, although potential drop across the 10-μm CL at 150mA/cm^2 is smaller, its overpotential is relatively larger than those of thicker CLs. The 20-μm CL has the smallest overpotential at the PEM/CL interface, which is the total voltage loss, indicating an optimized combination of mass transport and ionic resistance. To summarize, an ideal CL has a

maximum active area and a thin layer, where both ORR kinetics and species transport are facilitated.

5.4   Summary

A mathematical model has been developed for the DMFC cathode and is validated against experimental data with excellent agreement. The model incorporates the two-phase, multi-component species transport dynamics, multi-step electrochemical kinetics, and a chemical pathway between methanol and oxygen vapor, which are essential for accurate prediction of species distribution, polarization curve and the mixed potential due to methanol crossover.

The detrimental effect of methanol crossover is found to be more pronounced when air is used at the cathode than pure oxygen. The origin of the mixed potential is attributed to the deficient oxygen and parasitic MOR current at the DMFC cathode, caused by the chemical and electrochemical oxidation of the crossover methanol. The cathode overpotential, therefore, has to increase to maintain the prescribed load current. Methanol crossover was studied and reducing methanol crossover rate and utilization of methanol-tolerant cathode catalysts are identified as two effective approaches to control the methanol crossover effects. Small methanol crossover corresponds to high OCV as well as high cathode voltage in the kinetics region. High reaction selectivity toward ORR against MOR implies high methanol tolerance ability of the cathode catalysts, and hence small cathode voltage loss. Cathode CL thickness effect is also studied by this model and the optimized thickness is found to depend on the operating current density. Oxygen concentration drop across thinner CLs is smaller than that of thicker CLs; however, its

overpotential is relatively larger, as a result of less catalytic sites. The highest voltage at 150 mA/cm^2 is achieved by a 20-μm CL, representing a trade-off between oxygen transport and protonic resistance in the CL.

Table 5.1 Governing equations with source/sink terms in the cathode catalyst layer of a DMFC.

	Conservations	Source terms
Proton	$$\frac{d}{dx}(\kappa_e \frac{d\phi_e}{dx}) + S^{\Phi} = 0$$	$$S^{\Phi} = -j_{rxn}^{O_2} + j_{oxi}^{MeOH}$$
Water	$$\frac{d}{dx}(\gamma_c u C^{H_2O}) = \frac{d}{dx}\left(D_{CL}^{H_2O}\frac{dC^{H_2O}}{dx}\right) - \frac{d}{dx}\left(\frac{n_d}{F}I_e\right) + S^{H_2O}$$	$$S^{H_2O} = \frac{j_{rxn}^{O_2}}{2F} - \frac{j_{oxi}^{MeOH}}{6F} + 2r\ *$$
Oxygen	$$\frac{d}{dx}(\gamma_c u C^{O_2}) = \frac{d}{dx}\left(D_{g,CL}^{O_2,eff}\frac{dC^{O_2}}{dx}\right) + \frac{d}{dx}\left(\frac{C^{O_2}}{\rho_g}j_l\right) + S^{O_2}$$	$$S^{O_2} = -\frac{j_{rxn}^{O_2}}{4F} - 1.5r\ *$$
Methanol	$$\frac{d}{dx}(\gamma_c u C^{MeOH}) = \frac{d}{dx}\left(D_g^{MeOH,eff}\frac{dC_g^{MeOH}}{dx}\right) -$$ $$\frac{d}{dx}\left[\left(\frac{C_l^{MeOH}}{\rho_l} - \frac{C_g^{MeOH}}{\rho_g}\right)j_l\right] + S^{MeOH}$$	$$S^{MeOH} = -\frac{j_{oxi}^{MeOH}}{6F} - r\ *$$

*r is the gas-phase chemical reaction rate between methanol vapor and oxygen.

Table 5.2 Parameters used in the simulation of the cathode catalyst layer.

Parameters	Value
Anode limiting current density, $I_{A,\lim}$ (mA/cm²)	290
Air pressure in gas channel inlet, p (kPa)	100
Cathode gas viscosity, ν_g (m²/s)	2.06×10^{-5}
CL permeability at reference porosity (0.25), K_{CL}^0 (m²)	2.0×10^{-15}
Concentration exponent of methanol, β	1.9
Concentration exponent of oxygen, γ	0.01
Contact angle of CL, θ_{CL} (º)	10
Contact angle of GDL, θ_{GDL} (º)	120
GDL permeability, K_{GDL} (m²)	5.0×10^{-13}
Henry's law constant, k_H (Pa)	145696
Intrinsic proton conductivity of fully hydrated polymer, $\kappa_{e,0}$ (S/cm)	0.1
Liquid-water viscosity, ν_l (m²/s)	3.49×10^{-7}
Methanol vapor diffusion coefficient, D_g^{MeOH} (m²/s)	1.89×10^{-5}
Net water transport coefficient, α	0.8
Operating temperature, T (ºC)	60
Oxygen diffusion coefficient, $D_g^{O_2}$ (m²/s)	1.29×10^{-5}
Percolation critical value, X_0	0.085
Porosity of the GDL, ε_{GDL}	0.4
Proportionality constant of MOR, K	1.0×10^7
Reactive area per volume, a (m²/m³)	400
Reference exchange current density of ORR, i_0 (A/m²)	1.5×10^{-5}
Reference oxygen concentration, $c_{O_2,ref}$ (mol/m³)	4.12
Reference porosity of CL, ε_{CL}^0	0.25
Saturated water vapor molar concentration, $C_{sat}^{H_2O}$ (mol/m³)	7.20
Surface tension, σ (N/m)	0.0625
Thickness of the GDL, ΔX_{GDL} (µm)	300
Transfer coefficient of cathode, α_c	1.0

Table 5.3 MOR kinetics parameters.

Parameters	Value
Gas-phase chemical reaction constant, K_r	4.5×10^{-3}
k_1 (m/s)	4.0×10^{-12}
k_1' mol/(m^2 s)	1.54×10^{-10}
k_2 mol/(m^2 s)	3.6×10^{-16}
k_3 mol/(m^2 s)	1.2×10^{-13}
k_3' mol/(m^2 s)	1.3
k_4 mol/(m^2 s)	2.0×10^{-2}
α_2	0.80
β_3	0.5
β_4	0.5

Oxygen: $\left.\dfrac{dC^{O_2}}{dx}\right|_{x=0} = 0$ $\left.C^{O_2}\right|_{x=X_{CL}} = C^{O_2}_{GDL/CL}$

Proton: $\left.-\kappa_e \dfrac{d\phi_e}{dx}\right|_{x=0} = I$ $\left.\dfrac{d\phi_e}{dx}\right|_{x=X_{CL}} = 0$

Water: $\left.-D^{H_2O}_{CL}\dfrac{dC^{H_2O}}{dx}\right|_{x=0} = \dfrac{(\alpha - n_d)I}{F}$ $\left.C^{H_2O}\right|_{x=X_{CL}} = C^{H_2O}_{GDL/CL}$

Methanol: $\left.D^{MeOH,eff}_g\dfrac{dC^{MeOH}}{dx}\right|_{x=0} = -\dfrac{I_{xover}}{6F}$ $\left.\dfrac{dC^{MeOH}}{dx}\right|_{x=X_{CL}} = 0$

Velocity: $\left.u\right|_{x=0} = \dfrac{\alpha I M^{H_2O}}{F\rho} + \dfrac{I_{xover} M^{MeOH}}{6F\rho}$ $\left.u\right|_{x=X_{CL}} = \dfrac{(0.5+\alpha)I M^{H_2O}}{F\rho} + \dfrac{I_{xover} M^{CO_2}}{6F\rho} - \dfrac{I M^{MeOH}}{4F\rho}$
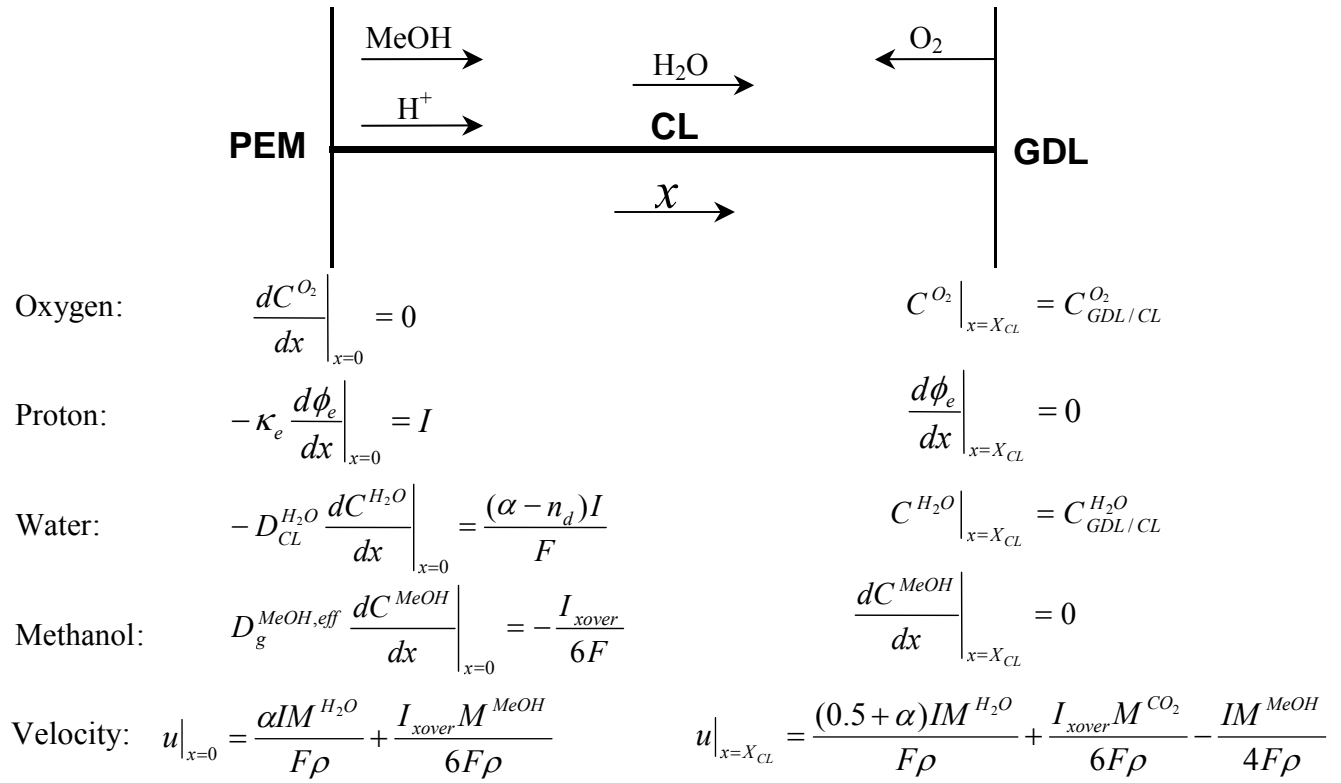
Figure 5.1 Schematic representation of one-dimensional computational region and related transport processes. Boundary conditions at two interfaces are also given.
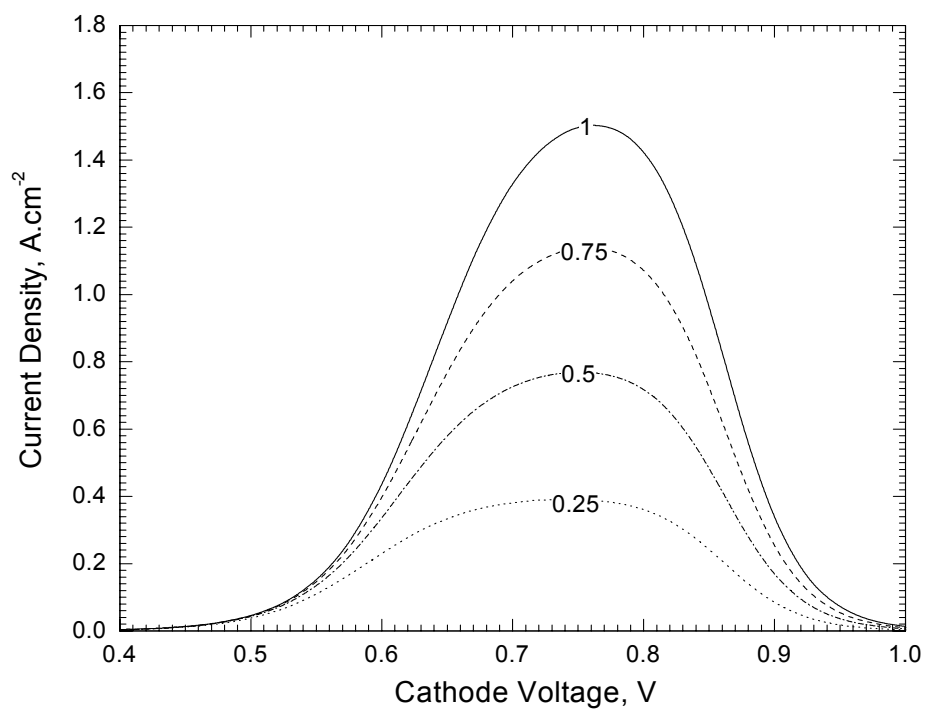
Figure 5.2 Methanol oxidation current density in the cathode as predicted by the model. The temperature is 60°C and concentrations of methanol are 0.25, 0.5, 0.75, and 1.0 M.
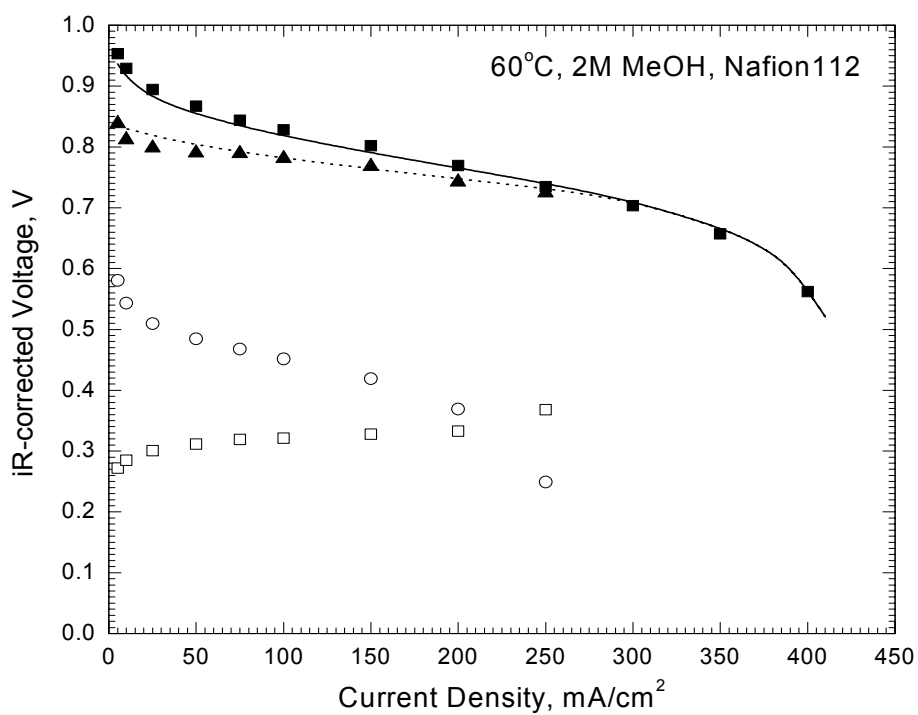
Figure 5.3 Comparison of experimental data with model predictions: (■) iR-corrected
H$_2$/air cell; (▲) iR-corrected DMFC cathode performance; (□) iR-corrected DMFC
anode polarization; and (○) iR-corrected DMFC cell performance. The solid and dotted
lines are simulated results for the cathode with and without methanol crossover,
respectively.
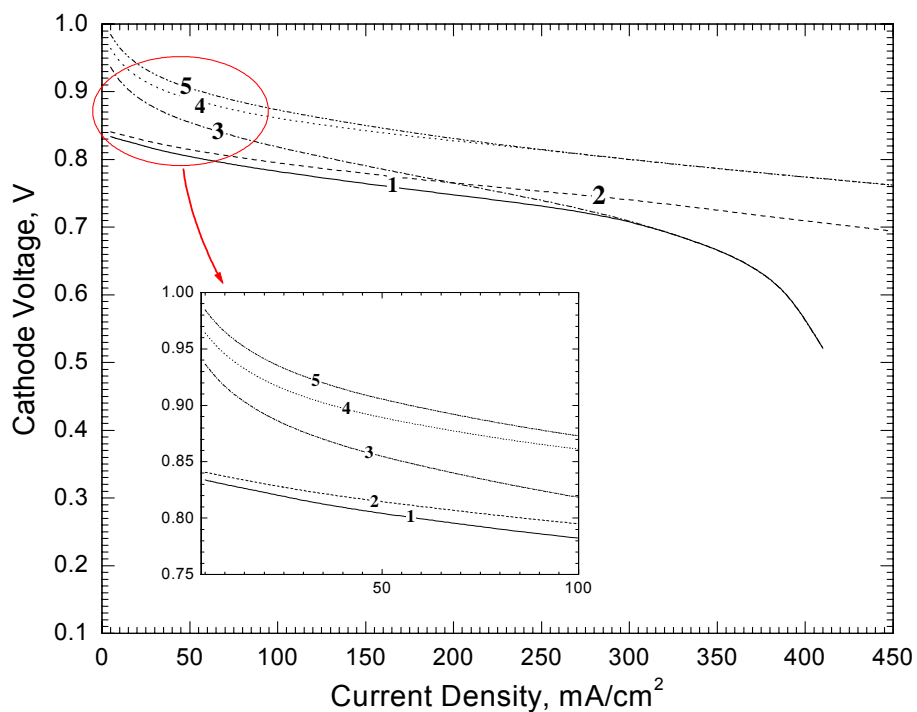
Figure 5.4 Cathode polarization curves under: (1) air with MeOH crossover, (2) air with MeOH crossover and infinite oxygen diffusivity, (3) air without MeOH crossover, (4) oxygen with MeOH crossover, and (5) oxygen without MeOH crossover.
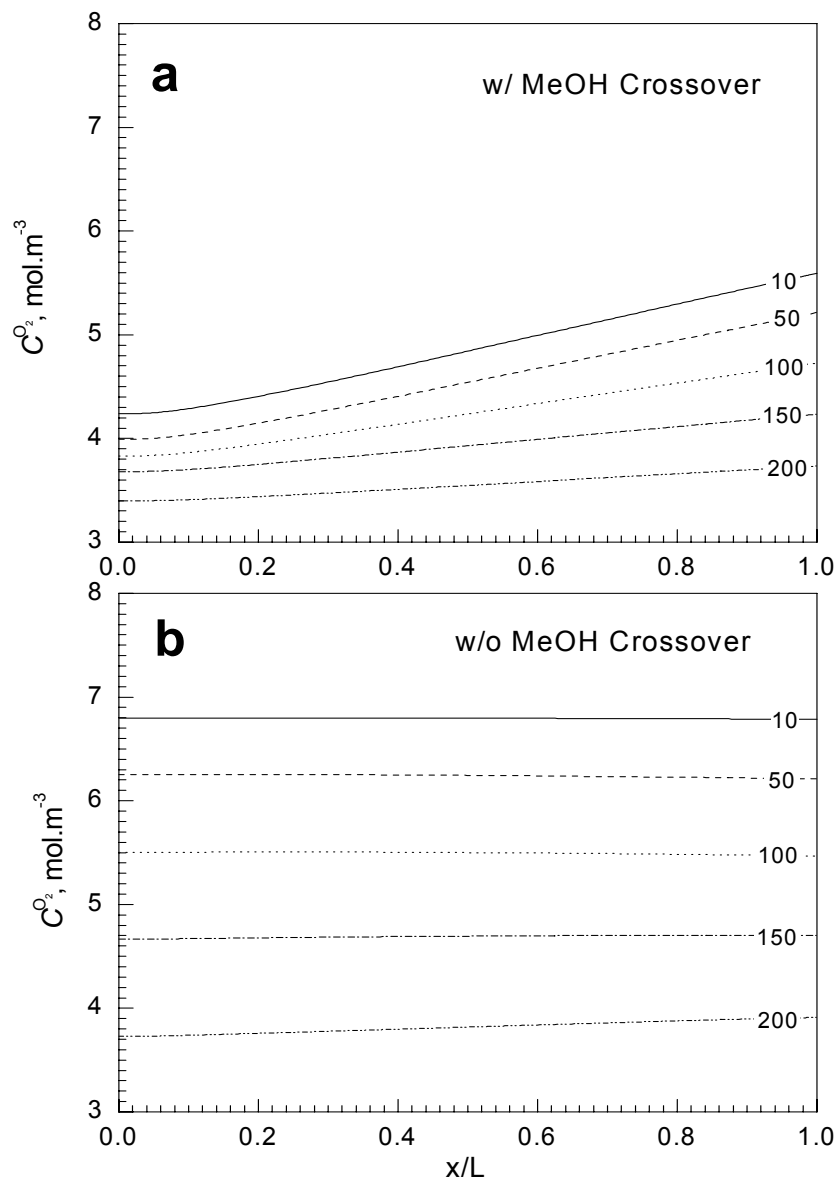
Figure 5.5 Oxygen concentration profiles along the thickness of cathode CLs: (a) with MeOH crossover and (b) without MeOH crossover. Different current densities (in mA/cm^2) are indicated in the figures.
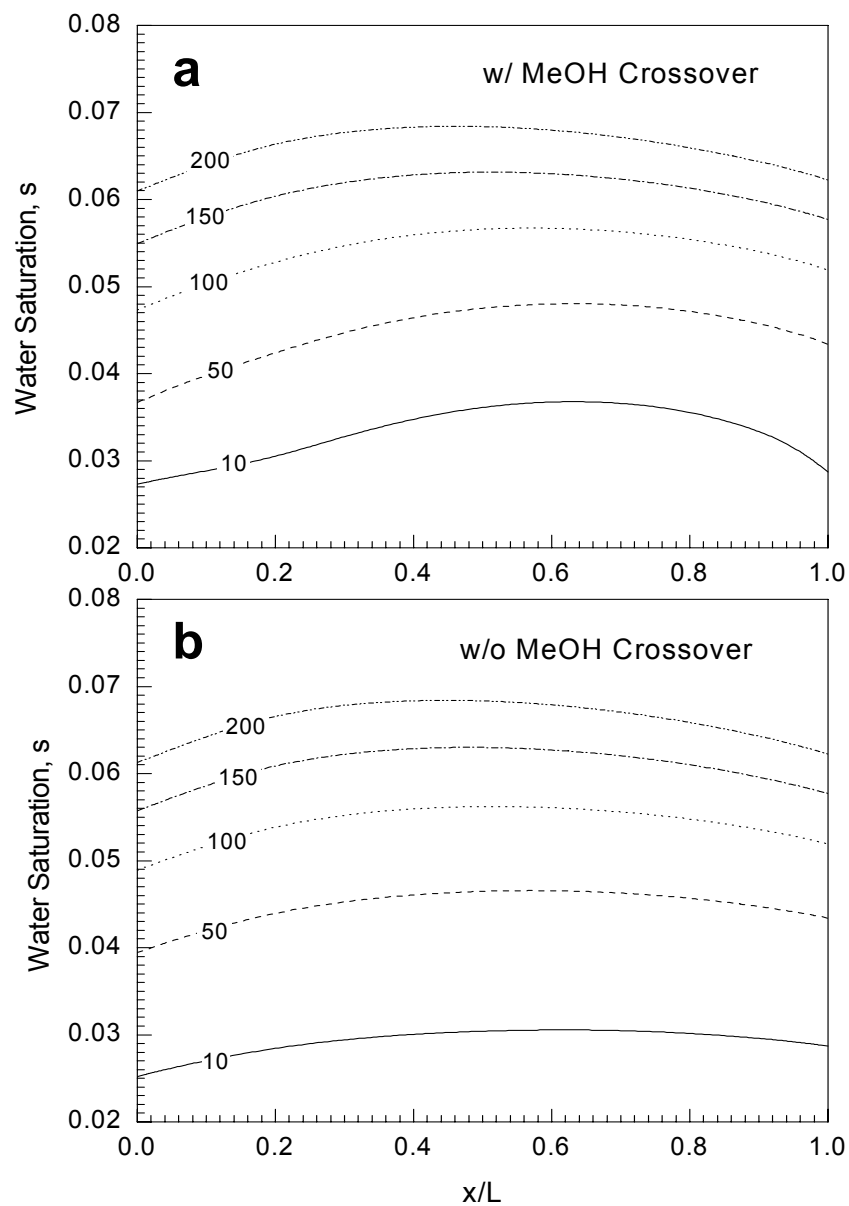
Figure 5.6 Water saturation profiles along the thickness of cathode CLs: (a) with MeOH crossover and (b) without MeOH crossover. Different current densities (in mA/cm^2) are indicated in the figures.
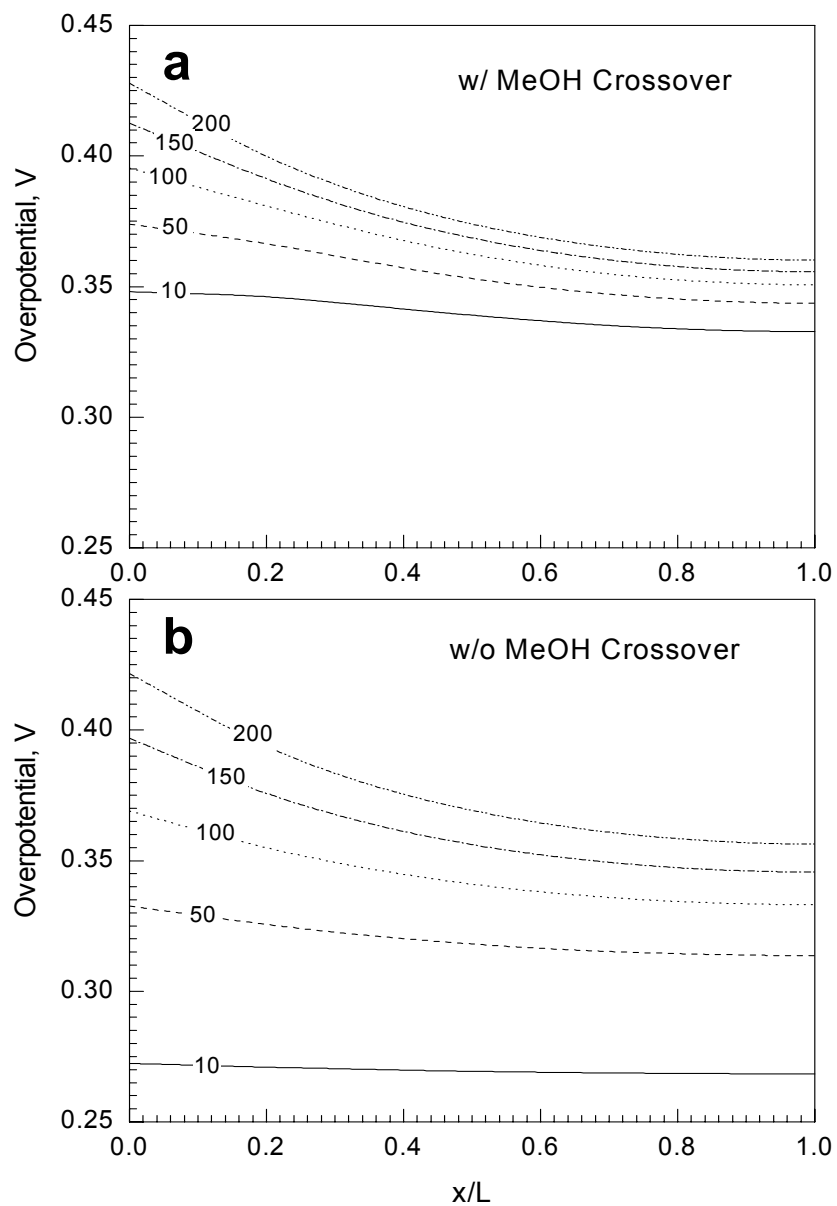
Figure 5.7 Ionic phase overpotential profiles along the thickness of cathode CLs: (a) with MeOH crossover and (b) without MeOH crossover. Different current densities (in mA/cm^2) are indicated in the figures.
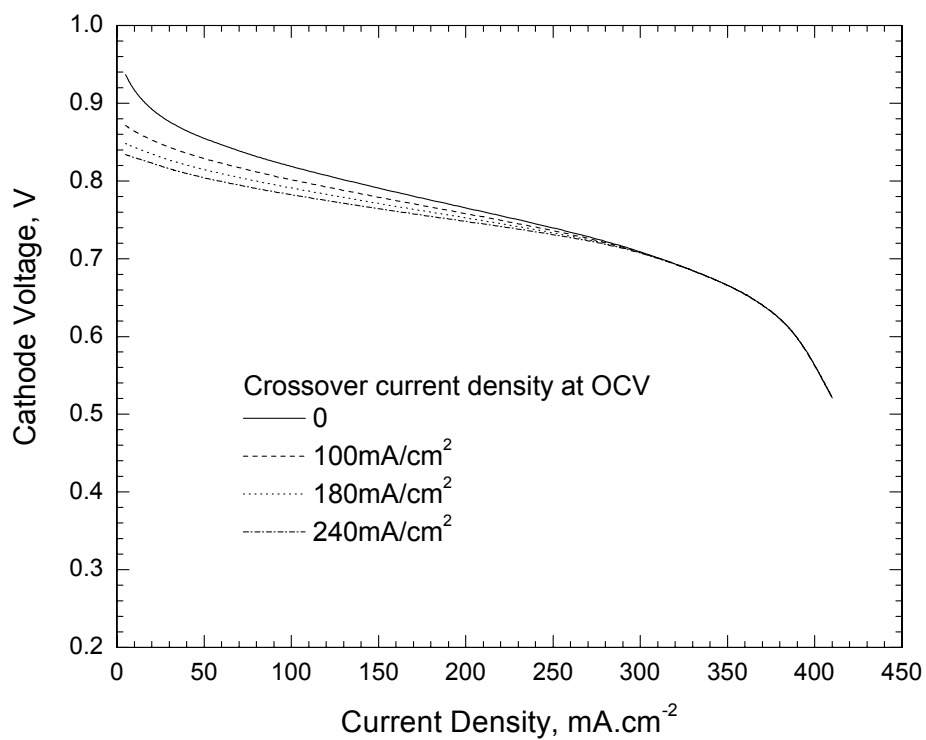
Figure 5.8 Effect of methanol crossover current density at open circuit on DMFC cathode performance.
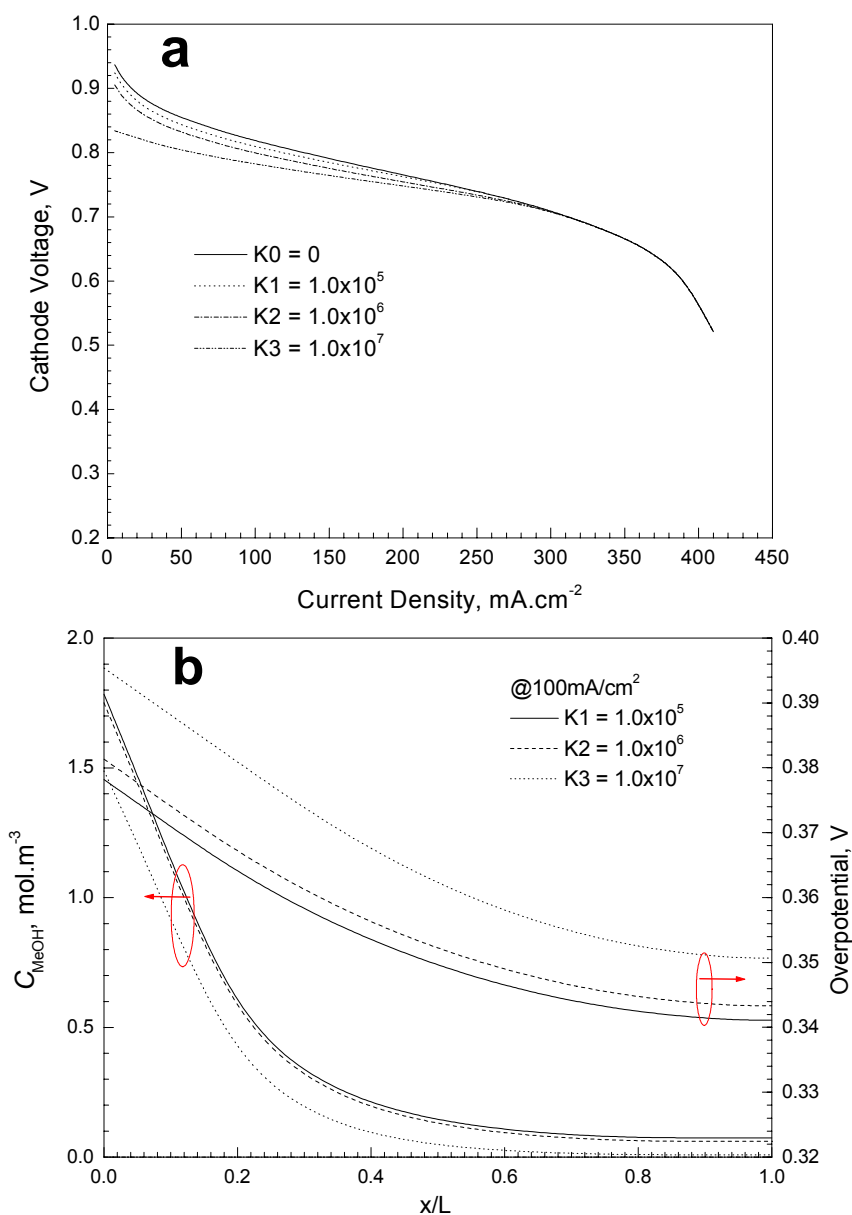
Figure 5.9 Effect of methanol tolerance of cathode catalyst: (a) on DMFC cathode performance, and (b) methanol concentrations and overpotentials along the thickness of cathode CL.
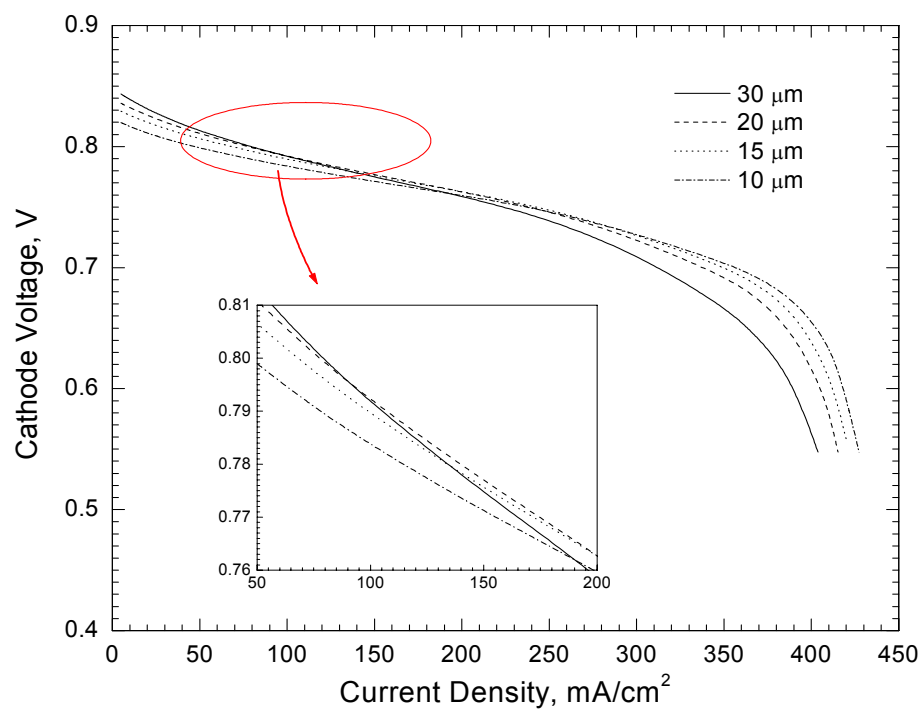
Figure 5.10 DMFC cathode performance with different thickness of CLs. The active surface area (for both ORR and MOR) in each CL are proportional to its thickness.
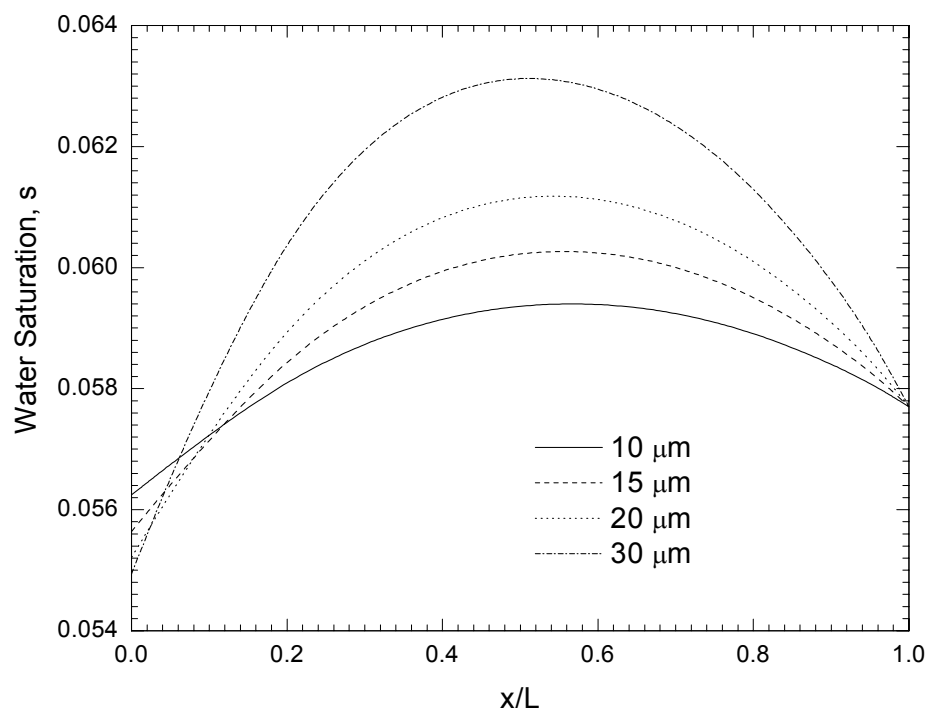
Figure 5.11 Methanol concentration profiles along the thickness of cathode CL at 150mA/cm^2 for different DMFC cathode CLs with various thickness.
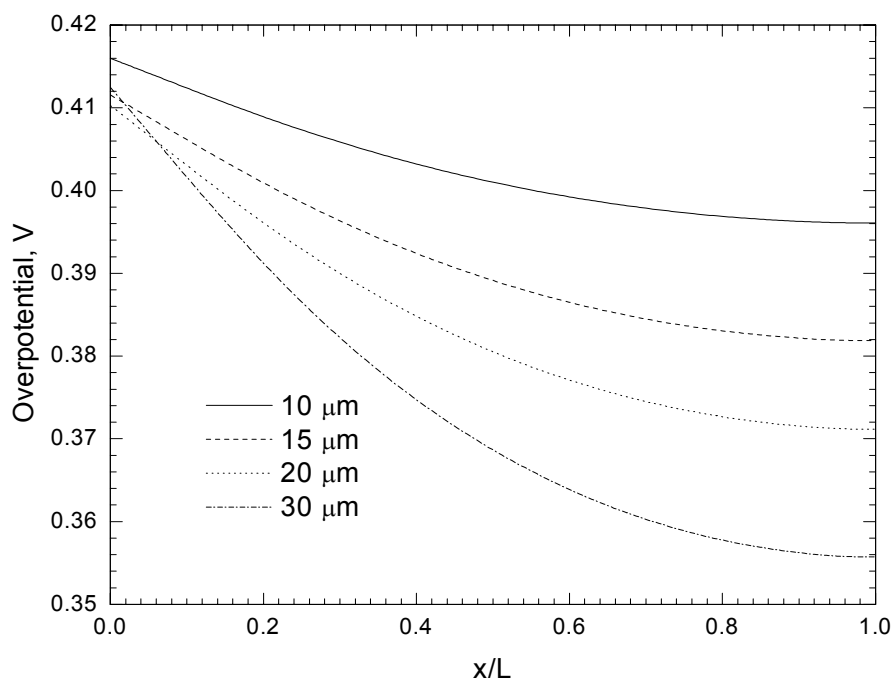
Figure 5.12 Overpotential profiles along the thickness of cathode CL at 150mA/cm^2 for different DMFC cathode CLs with various thicknesses.

Chapter 6 WATER TRANSPORT IN DMFCS

6.1   Introduction

Highly concentrated methanol solution, including pure methanol, is preferred for portable power applications. Unfortunately, the ability to use highly concentrated methanol solution in the anode is hampered by excessive methanol crossover that causes a mixed potential on the cathode and waste of fuel. While the majority of the DMFC literature attributes methanol crossover to the PFSA membrane exhibiting a large methanol permeability, we shall demonstrate in this chapter that it is also related to excessive water crossover through the same membrane. Water crossover from the anode to cathode occurs under the influence of electro-osmotic drag (EOD) and molecular diffusion through the membrane. The anode reaction of a DMFC requires an equivalent number of water and methanol molecules, but roughly 2.5×6 water molecules must be dragged through a thick membrane such as Nafion 117 towards the cathode, assuming that one methanol molecule is completely oxidized to produce six protons and the EOD coefficient of water is 2.5 per proton transported through the membrane (Ren and Gottesfeld, 2001). This then causes 16 water molecules lost from the anode for every methanol molecule consumed, which translates to a methanol concentration of only 10% by weight or about 3M methanol solution. This calculation clearly indicates that water crossover through a thick membrane already limits the maximum methanol concentration to approximately 3M, let alone any consideration of methanol crossover.

On the other hand, there exists a large amount of water inside the cathode. For example, for the consumption of each methanol molecule at the anode, there are 15 water molecules transported from the anode plus 3 water molecules produced by oxygen reduction reaction. Cathode flooding is thus difficult to avoid at low cell temperatures and/or low air stoichiometry required in portable DMFCs.

Minimizing water crossover through a DMFC membrane is therefore an equally important requirement for portable DMFCs besides methanol crossover mitigation. Let's define the net water transport coefficient, α, as the net water flux through the membrane from the anode to cathode normalized by the protonic flux. To illustrate why low-α is key to the deployment of concentrated fuel, consider an ideal membrane that features zero methanol crossover but water crossover characterized by α. Then, the highest concentration of methanol solution in the anode must require that the H_2O to CH_3OH molecular ratio be greater than $(1+6\alpha)$. Table 6.1 gives the corresponding MeOH molarity for various α-values. It is clear that for $\alpha \approx 3$ as in typical DMFCs based on Nafion 117, the maximum operational MeOH concentration is about 3M, as explained earlier. Likewise, in order to enable direct use of 10M methanol fuel, α must be reduced to below ~0.4. Further, when $\alpha = -1/6$, there is no need to add water in the anode feed or pure methanol operation becomes theoretically possible, in which situation the water molecule needed to oxidize one methanol molecule will come from the product water of oxygen reduction reaction on the cathode.

Peled *et al.* (2003) demonstrated low α values by using a PVDF-based nanoporous proton-conducting membrane, a liquid water barrier layer (LWBL), and pure oxygen at three bars on the cathode. The LWBL is a hydrophobic layer free of holes larger than 0.5

μm. Based on the theory of liquid water transport in polymer electrolyte fuel cells (Pasaogullari and Wang, 2004), we have designed a unique MEA structure which utilizes the microporous layer to build up the hydraulic pressure on the cathode side and then uses a thin membrane (i.e. Nafion 112) to promote the water back flow under this hydraulic pressure difference. Such MEAs, first published by Lim and Wang (2003) and modified by Wang *et al.* (2005), exhibit extraordinarily low α and hence are generally termed low-α MEA technology.

In this chapter, a novel MEA to meet simultaneous requirements of low-α, low methanol crossover and high power density, by applying a cathode MPL, is described. Using methanol solution (up to 4 M), we have obtained α values smaller than 0.8 and 0.4 at 60°C and 50°C, respectively. Different anode catalyst structures, cathode GDLs, membranes, and operating conditions were explored. At 60°C, a power density of 58.1 mW/cm^{2} was achieved at low stoichiometry using ambient air and 3M methanol solution.

6.2   Hydraulic Water Back-transport

Parameters governing liquid water formation and distribution in the cathode include the air stoichiometry, current density, cell temperature, and membrane water transport properties such as the diffusion coefficient and EOD coefficient. The water flux (in mol/s) to the cathode by diffusion, electro-osmosis, and hydraulic permeation can be expressed as (Lu et al., 2005):

$$N_{transH_2O} = -DA\frac{\Delta c_{c-a}}{\delta_m} + n_d\frac{IA}{F} - \frac{K}{\mu_l}A\Delta p_{c-a}\frac{\rho}{M_{H2O}}$$ [6.1]

where I is the current density, ρ the molar water density, δ_m the membrane thickness, F Faraday constant, K the hydraulic permeability, n_d the EOD coefficient of water, μ_l the liquid water viscosity, D the diffusion coefficient, M_{H2O} the molecular weight of water, Δc_{c-a} and Δp_{c-a} the water concentration difference and the hydraulic pressure difference across the membrane, respectively. Clearly, the three terms on the right hand side in Eq. 6.1 represent three modes of water transport through the membrane. The molecular diffusion is driven by the concentration gradient. The electro-osmotic drag is proportional to the current density, and the permeation flux is driven by the hydraulic pressure difference.

The net water flux through the membrane can be conveniently quantified by a net water transport coefficient, α, defined as:

$$N_{transH_2O} = \alpha \frac{IA}{F} \qquad [6.2]$$

This parameter dictates water management strategies in DMFC systems. It is a combined result of electro-osmotic drag, diffusion, and hydraulic permeation through the membrane. For thick membranes like Nafion 117, α approaches the pure EOD coefficient as the other two modes of water transport are weakened with increasing membrane thickness. From the viewpoint of water management in DMFCs, it is an ultimate goal to achieve α values as low as possible or even negative. This requires using thin membranes like Nafion 112 and enhancing hydraulic permeation fluxes though the membrane.

The hydraulic pressure in the cathode can be increased by using a highly hydrophobic GDL, as suggested by Peled et al. (2003) and Pasaogullari and Wang

(2004). The capillary pressure of the hydrophobic GDL in the cathode can be expressed as:

$$p_c = p_g - p_l = 2\sigma \frac{\cos \theta_c}{r_c}$$ [6.3]

where θ_c is the contact angle ($>90°$ for hydrophobic GDL) and r_c the pore radius. Thus, the hydraulic pressure difference across the membrane for the liquid-feed DMFC is given by:

$$\Delta p_{c-a} = p_l - p_a = (p_g - p_a) - 2\sigma \frac{\cos \theta_c}{r_c}$$ [6.4]

where p_a is the pressure in the anode. For a DMFC operating at the same pressure in both anode and cathode, $p_g - p_a = 0$. This makes the hydraulic pressure differential depend on the contact angle and pore radius of the cathode GDL, which can be enabled by a highly hydrophobic MPL.

Eq. 6.4 indicates that increasing the cathode GDL hydrophobicity will result in a larger hydraulic pressure gradient, thus leading to a lower α value. However, excessive Teflon content in the MPL may reduce the electronic conductivity and subsequently lower the cell performance. It is expected that there is an optimum hydrophobicity in the MPL for proper water management and improved performance. Eq. 6.4 also indicates that a smaller pore radius gives rise to a larger hydraulic pressure difference, while a substantially reduced pore radius results in a mass-transport limitation in the cathode. These trade-offs will be pursued by the careful MPL design.

6.3   Experimental

6.3.1   MEA development

Two different electrode configurations, CDM and CCM, were employed as the anode catalyst layer, while CCM was used as the cathode catalyst layer. By combining different anode and cathode structures, two types of MEAs were obtained and studied in this work. MEA-A is composed of a CCM anode and a CCM cathode, while MEA-B is made of a CDM anode and a CCM cathode. A wet-proofed carbon paper (Toray TGPH-090, E-TEK) of 0.26 mm thickness was used as a backing layer on the anode side. While different materials, including carbon paper and carbon cloth, were employed as the cathode backing. MPL was fabricated by coating a mixture of PTFE and carbon on the surface of a wet-proofed backing layer. Carbon cloth with MPL was employed as the cathode GDL for most of the cases in this work, while other cathode diffusion media were used as indicated. Unsupported Pt/Ru black (HiSPEC 6000, Pt:Ru = 1:1 atomic ratio, Alfa Aesar) and Pt/C catalyst (40% Pt/Vulcan XC72; E-TEK) were used as catalysts for anode and cathode, respectively. The loadings of the catalyst layer in this paper were 4.8 mg PtRu/cm^2 and 1 mg Pt/cm^2 for anode and cathode, respectively. The ratio of catalyst to ionomer was maintained to be 4:1 (dry weight) for both anode and cathode.

6.3.2   Single cell testing

Electrochemical performance evaluation was conducted in a 12-cm^2 graphite cell fixture. The flow fields, consisting of machined two-pass serpentine grooves on graphite blocks, were identical for both anode and cathode. A digital pump (Series I digital pump, Laballiance) with flow rate ranging from 0.01 to 10 mL/min was used to deliver

methanol solution and control its flow rate. The flow rate of non-preheated and non-pressured dry air was controlled by a flow rate controller and the cell temperature was controlled by a digital temperature controller. A water trap containing anhydrous calcium sulfate (W.A. Hammond Drierite Co. LTD) was connected to the exit of the cathode to collect the water contained in the cathode exhaust. A constant current was maintained for *ca.* 2 hours and the water collected from the cathode was used to calculate the net water transport coefficient, α.

6.3.3 Water balance measurement

α is a combined result of EOD, diffusion and hydraulic permeation through the membrane. For thick membranes such as Nafion 117, α approaches the EOD coefficient as the other two modes of water transport become negligible. Positive α corresponds to a net water flow from the anode to cathode, while negative α indicates a reserve in the water transport direction.

In the operation of a DMFC, dry air is fed to the cathode, where oxygen is reduced electrochemically via Eq. 1.2. The water produced from power generation can thus be described as

$$N_{powerH_2O} = 0.5\frac{IA}{F} \qquad [6.5]$$

Assuming all crossover methanol is oxidized by the positive potential at the cathode, the water produced by methanol oxidation can be calculated from

$$N_{oxiH_2O} = \frac{1}{3}\frac{I_cA}{F} = \frac{1}{3}\frac{1-\eta_{fuel}}{\eta_{fuel}}\frac{IA}{F} \qquad [6.6]$$

where I_c is the methanol crossover current density, and η_{fuel} the fuel efficiency defined in Eq. 1.7. Combining Eqs. 6.2, 6.5 and 6.6 yields the total water flow rate at the cathode exhaust

$$N_{H_2O} = 0.5\frac{IA}{F} + \alpha\frac{IA}{F} + \frac{1}{3}\frac{1-\eta_{fuel}}{\eta_{fuel}}\frac{IA}{F} \qquad [6.7]$$

Note that the above equation is valid with dry air inlet only. The net water transport coefficient can thus be measured according to

$$\alpha = N_{H_2O}\cdot\frac{F}{IA} - 0.5 - \frac{1}{3}\frac{1-\eta_{fuel}}{\eta_{fuel}} \qquad [6.8]$$

The last term in Eq. 6.8 can be estimated from the fuel efficiency, e.g. it is equal to 0.083 at 80% fuel efficiency. For convenience, we will report α by its apparent value that includes water produced from the oxidation of crossover methanol, i.e. $(N_{H_2O}F/IA - 0.5)$. The difference between the actual α and its apparent value is equal to $(1-\eta_{fuel})/(3\eta_{fuel})$. It should thus be noted that α-values reported in this paper are higher than the actual net water transport coefficient through the membrane by ~0.1.

6.4   Results and Discussion

6.4.1   Scanning electron micrographs (SEM)

Cross-section and surface morphologies of CCM and CDM catalyst layers are shown in Figures 6.1 and 6.2. The surface of the CCM cathode catalyst layer is very flat with small cracks scattering on it. Its thickness is only *ca.* 25 μm as shown in Figure 6.1a. High loading (1mg Pt/cm^2) and very thin cathode catalyst layer ensure good activity and

low mass transport resistance. The CDM anode is more porous than the CCM anode and its catalyst layer forms a bimodal pore distribution with small primary pores in the agglomerates formed by PtRu black and Nafion, and large secondary pores with diameter of *ca.* 5~10 μm between agglomerates. The catalyst and ionomer are considered to be more closely packed in the CCM anode and the diameter of secondary pores in the catalyst layer is much smaller, as shown in the SEM picture of Figure 6.1b. The thickness of the CCM anode catalyst layer is about 20~30 μm, much thinner than that of CDM, about 50 μm in thickness (Figure 6.2a). Since the same PtRu black and Nafion loading were used for the two anode catalyst layers, the thick CDM anode is expected to exhibit higher methanol transport resistance than the CCM anode; hence it has a lower methanol crossover current density, as will be shown below.

6.4.2 Influence of anode catalyst layer

As shown in the SEM pictures, CDM and CCM anode catalyst layers feature different micro-structures; therefore they may have different methanol and water transport properties. The methanol crossover and anode polarization of the two anode catalyst layers are characterized in Figure 6.3a and 6.3b. In Figure 6.3a, the cell with the CDM anode has a lower methanol crossover current density than the CCM anode, owing to the thicker CDM anode. For example, at 3M methanol solution, the crossover current density at open circuit in the cell with the CDM anode is 206 mA/cm^2, compared with 227 mA/cm^2 of the cell with the CCM anode. At 2M methanol solution, the crossover current density in the CDM anode cell declines further to 169 mA/cm^2. Also, different internal structure, the interaction between PtRu catalyst and ionomer, and the catalyst

layer thickness of the two anode catalyst layers result in different anode polarization behaviors. With 2M methanol feed, the CDM anode has a smaller limiting current density, *ca.* 210 mA/cm^2, compared with 247 mA/cm^2 of the CCM anode, but it outperforms the CCM anode cell at current density below *ca.* 130 mA/cm^2, indicating that methanol crossover is smaller and there is a more extensive catalyst/ionomer interface forming in the CDM anode catalyst layer. At current densities higher than 130 mA/cm^2, the potential versus DHE in the CDM anode increases dramatically and shows severe mass transport limiting current.

Water transport and cell performance of MEA-A and MEA-B are analyzed under various operating conditions in Figures 6.4 and 6.5, respectively. Note that the only difference of the two MEAs is the anode: MEA-A has a CCM anode while MEA-B has a CDM anode. The anode catalyst layers have no effect on the water crossover coefficient; the net water transport coefficient α is about 0.4 at 50°C and 0.8 at 60°C for the 2M methanol solution, regardless which anode configuration is used.

Nonetheless, performance of the cells with two MEAs differs owing to different anodes. As expected, the limiting current densities in quick-scan polarization curves for the CCM anode cell are always larger than that of the CDM anode cell, and the difference between them is approximately 50 mA/cm^2. For example, at 60°C and anode/cathode stoichiometries of 2/3 at 150 mA/cm^2, the limiting current densities of the CCM anode and CDM anode cells are 264 mA/cm^2 and 221 mA/cm^2, respectively. The difference between these two MEAs is more significant under steady-state constant current discharge. In Figure 6.4a, the cell voltages at 150 mA/cm^2 are almost independent of the anode stoichiometry in the CCM anode cell at 60°C. Even at 50°C the difference between

average cell voltages for anode stoichiometries of 1.75 and 2.5 is only 15 mV. While the anode stoichiometry has a much larger effect on the CDM anode cell, especially at low cell temperatures. It is seen from Figure 6.5a that the average cell voltage at 150 mA/cm^2 in the CDM anode cell is 0.246, 0.290 and 0.309 V for anode stoichiometries of 1.75, 2 and 2.5, respectively. At 50°C the difference between average cell voltages for various anode stoichiometries becomes much larger: 180 mV between stoichiometries of 1.75 and 2.5 at 150 mA/cm^2. In fact, the CDM anode cell cannot operate stably at 50°C and low anode stoichiometry. However, it is interesting to note that the quick-scan polarizations display little dependence on anode stoichiometries. In the Figure 6.5b inset, cell voltages are almost identical up to *ca.* 150 mA/cm^2, and the difference between limiting current densities at different anode stoichiometries is within *ca.* 10 mA/cm^2.

Anode sthoichiometry is a more critical parameter of performance stability at constant current discharge than in quick-scan polarization, especially for the CDM anode at 50°C. Constant current discharge over an extended period of time requires steady-state or quasi steady-state operation; that is, the rate of fuel delivery from the anode channels through the backing into the catalyst layer should balance with the rate of fuel consumption in the catalyst layer. Otherwise, cell discharge performance would not be stable. Figure 6.6 displays performance of a CDM anode cell based on Nafion 1135 membrane discharged with 3M methanol solution. It is seen that the cell voltages are very stable and show small variation and decay with time for all anode stoichiometries. The difference between the average voltages at different anode stoichiometries is very small, indicating that diffusion of methanol to the anode catalyst layer is sufficient even at low stoichiometry, which is favored by higher methanol concentration gradient across the

anode catalyst layer. A steady-state power density of 58.1 mW/cm^2, obtained by averaging the power densities over the discharge time, was reached with anode/cathode stoichiometry of 2.5/3 at 150 mA/cm^2 using ambient air and 3M methanol solution. In quick-scan polarization curves (see the inset of Figure 6.6), the limiting current density can reach 300 mA/cm^2 for anode stoichiometry of 2.5 at 150 mA/cm^2.

The thicker CDM anode catalyst layer creates a higher resistance to methanol transport, thereby controlling the rate of methanol reaching the polymer membrane and reducing the crossover current density. Liu *et al.* (1998) pointed out that PtRu black catalysts showed a lower mass transport resistance than carbon supported PtRu catalysts in the anode catalyst layer for DMFCs. Our results further indicate that the anode catalyst layer properties are highly sensitive to the fabrication procedures; with the same PtRu and Nafion loadings, the CDM anode is more methanol-resistant than the CCM anode.

Both the methanol-resistant anode and low-α MEA are useful to achieve the ultimate goal of feeding highly concentrated or pure methanol to DMFCs. A methanol-resistant anode can regulate methanol crossover through the Nafion membrane even in the presence of highly concentrated methanol solution on the anode side, and low α ensures the water loss from the anode will always be less than the small amount of water supply available from a high concentration methanol solution. Tailoring the anode catalyst layer is thus an important means to realize both goals simultaneously. A thicker and denser anode catalyst layer can substantially mitigate methanol crossover through the membrane, while affecting water crossover through the membrane only insignificantly. More work is underway to optimize the anode catalyst layer for further simultaneous reduction in both methanol and water crossover.

6.4.3   Membrane thickness effect

Methanol and water transport through the cell can be enhanced or retarded by membrane thickness. Figure 6.7 summarizes methanol crossover current densities of Nafion 112 and 1135 membranes at 60°C using different methanol concentrations. It is seen that the crossover current density is approximately linearly proportional to the methanol concentration, with Nafion 112 membrane featuring higher crossover rate, as expected. The difference in crossover current density between the two membranes diminishes with methanol concentration; for example, the difference decreases from 32 mA/cm^2 at 2M to 11 mA/cm^2 at 4 M.

The cell resistance, net water transport coefficient and power density for Nafion membranes of differing thickness are given in Table 6.2 for 60°C and 3M methanol solution. Thicker membranes have higher cell internal resistance, but lower methanol crossover. Therefore, the cell using Nafion 1135 has the best electrochemical performance, where the power density increases slightly with anode stoichiometry. Further, it is seen from Table 6.2 that the net water transport coefficient, α, is nearly independent of the anode stoichiometry. It is interesting to note that the thinner membranes appear to have only slightly smaller α value than the thicker one, although the resistance of water back flow from the cathode to anode via hydraulic permeation is much reduced in thinner membranes. The net water transport coefficients are 0.70, 0.87 and 1.10 for Nafion 111, 112 and 1135 membranes, respectively, at the stoichiometry (A/C) of 2.5/3. The effect of membrane thickness on water crossover may have been under-estimated here because our reported α-value includes water produced from

oxidation of methanol crossover. Under common conditions, this is a reasonable assumption because the correction in α would be only about ~0.1, as discussed earlier. However, thinner membranes may have resulted in large methanol crossover current density, I_c and hence much lower fuel efficiency than 80% used in the estimate of correction. Therefore, the actual water crossover rate through thinner membranes should be smaller than the α-values reported in Table 6.2.

6.4.4   Methanol concentration and anode/cathode stoichiometry effects

As indicated earlier, methanol diffusion to the anode catalyst layer could be hindered at a low methanol concentration; therefore part of the catalytic sites cannot be accessed by reactants. On the other hand, a high concentration causes large methanol crossover. Figure 6.8 shows the steady-state power density and net water transport coefficient at 60^oC for various methanol concentrations and anode stoichiometries. The highest steady-state power density is achieved with 3M methanol solution, as a compromise. For example, at anode/cathode stoichiometries of 1.75/3, the power density in 150 mA/cm^2 discharge increases dramatically from 45.7 mW/cm^2 at 2M to 56.4 mW/cm^2 at 3M. However, when the concentration is further increased to 4M, the power density drops to 55.2 mW/cm^2. The steady-state power density increases more noticeably with anode stoichiometry for 2M methanol solution than 3M and 4M. For 2M methanol solution, when anode stoichiometry varies from 1.75 to 2, the power density increases markedly from 45.7 to 52.2 mW/cm^2; and the power density slowly reaches 55.5 mW/cm^2 when the anode stoichiometry further increases to 2.5. For 3M and 4M methanol solutions, only slight increase in power density is observed with an increase in the anode stoichiometry.

Although anode stoichiometry and methanol concentration have a large impact on cell performance, they have different influences on water transport. α value is almost independent of anode stoichiometry, as shown in Figure 6.8. On the contrary, methanol concentration seems to have a large impact on α value, *i.e.*, highly concentrated methanol solution results in high α. This trend could be misleading, again, due to the fact that our reported α-value includes water produced from oxidation of crossover methanol. With high methanol solutions, the error of neglecting the methanol crossover effect in estimating α could be gross. For instance, when fuel efficiency decreases to 50% and 40%, respectively, the error becomes 0.333 and 0.5, or greater than 30-50%.

The cathode stoichiometry effect on the net water transport coefficient and cell performance is also studied in Figure 6.9. As can be seen, the air flow rate has small influence on steady-state and quick-scan performance, indicating that either cathode flooding is not severe or the cathode can still perform reasonably even under partial flooding. However, the net water transport coefficient α has a strong dependence on cathode stoichiometry, increasing from 0.74 to 0.99 when the air stoichiometry varies from 3 to 4. This can be simply explained by the enhanced water evaporation under higher cathode stoichiometry.

6.4.5   Current density and temperature effects

Water transport through the membrane can be influenced by the operating current density and cell temperature. Combing Eq. 6.1 and 6.2, α can be described as

$$\alpha = -\frac{FD}{I}\frac{\Delta c_{c-a}}{\delta_m} + n_d - \frac{F}{I}\frac{K}{\mu_l}\Delta p_{c-a}\frac{\rho}{M_{H2O}}$$ [6.9]

According to Eq. 6.9, one would expect an increase of α value with current density if both Δc_{c-a} and Δp_{c-a} are constants. However, the experimental results indicate an opposite trend as shown in Table 6.3. Even after correcting the water produced from oxidation of crossover methanol, the net water transport coefficient through the membrane declines from 1.09 at 100 mA/cm^2 to 0.71 and 0.47 at 150 and 200 mA/cm^2, respectively. This clearly indicates that both Δc_{c-a} and Δp_{c-a} are current-dependant variables, and indeed they increase dramatically with the current as the cathode accumulate more water and the anode becomes more gaseous. Both consequences provide a driving force to promote water back-transport from the cathode to anode.

To investigate the effect of temperature on cell performance and water transport, a series of quick-scan polarization curves and net water transport coefficient were measured at different temperatures, and the results are shown in Figure 6.10a and 6.10b, respectively. The well-defined limiting current densities shown in Figure 6.10a are believed to be caused by starvation of methanol at the anode side. Low methanol flow rate not only reduces the pumping power in a portable application but also lowers methanol crossover through the membrane. In Figure 6.10b, the average power density from constant current discharge increases with temperature, as expected. It increases rapidly from 34.6 mW/cm^2 at 40°C to 49.0 mW/cm^2 at 50°C, and levels off when temperature is further increased to 60°C and finally reaches 56.1 mW/cm^2 at 70°C. The net water transport coefficient also increases with temperature, but the trend is contrary to the power density, increasing slowly initially but markedly when the temperature is raised from 60°C to 70°C. At 70°C, α becomes 1.61, almost doubling that at 60°C.

It can thus be concluded that 50-60°C is the optimal temperature range. Operating temperature above 70°C is undesirable due to excessive water loss from the cathode exhaust, and temperature below 50°C does not yield high power density.

6.4.6   Influence of cathode gas diffusion media

Figures 6.11a, b and c display SEM images of the surfaces of MPL, carbon-paper and carbon-cloth backings. Carbon paper is a microscopically complex fibrous structure with pore size distribution ranging from a few microns to tens of microns and with a large fraction of blocked passages. Carbon cloth is a woven structure and is generally coarser than carbon paper. Differences in porosity, permeability, pore size distribution, surface wettability and liquid retention of the two diffusion media result in different two-phase flow and transport characteristics. The MPL is a highly hydrophobic porous structure with pore size much smaller than the backing layers. The combination of high hydrophobicity and small pore size of a MPL creates a substantial liquid pressure on the cathode, which drives liquid water back to the anode side thus leading to a low net water flux through the membrane. This subsection will explore the roles of various diffusion media and MPL on the cathode side in affecting the power density and water crossover coefficient. Four diffusion media samples were tested: carbon paper with and without MPL, and carbon cloth with and without MPL.

Figures 6.12a and 6.12b show the quick-scan polarization curves and constant current discharge curves of the cells with different cathode gas diffusion media. Carbon cloth with MPL shows the best performance, and carbon paper without MPL the worst. The variation in performance with different diffusion media results primarily from the

cell internal resistance as well as the ability of a GDL to facilitate oxygen transport. The cell internal resistance was taken from EIS spectra intercept with real axis as shown in Figure 6.13. The internal resistances of carbon cloth with MPL, carbon paper with MPL, carbon cloth without MPL and carbon paper without MPL are 0.181, 0.209, 0.205 and 0.261Ω.cm2, respectively. It is clear that the presence of MPL improves the electric contact between the catalyst layer and backing layer, thereby resulting in smaller internal resistance, but the difference in internal resistance is responsible for only 12 mV voltage gain at 150 mA/cm2, much smaller than the 40 mV seen in the quick-scan polarization curves in Figure 6.12a or nearly 100 mV exhibited in the constant current discharge. These results show that the dominant effect of carbon cloth backings and MPL is clearly their ability to remove liquid water and thus avoid severe flooding in the cathode catalyst layer. In contrast, carbon paper GDLs are more susceptible to cathode flooding.

Surprisingly, we note from Figure 6.12b that carbon paper GDLs have smaller α values than carbon cloth GDLs, and α does not change much with the addition of a MPL. The latter observation can be explained by the capillary flow theory of Pasaogullari and Wang. Under steady-state operation, the liquid pressure in a hydrophobic medium is given by capillary pressure expressed as (Pasaogullari and Wang, 2004; Wang, 2003)

$$p_l = \sigma \cos\theta_c \left(\frac{\varepsilon}{K}\right)^{1/2} J(s) \qquad\qquad [6.10]$$

where ε is the porosity, θ_c contact angle, σ surface tension, and $J(s)$ is the Leverett function of liquid saturation, *i.e.*, the volume fraction of liquid within open pores. The term $(K/\varepsilon)^{1/2}$ is characteristic of the pore size. Because the MPL pore size is an order-of-magnitude smaller than that of carbon paper backing layer and the contact angle in MPL

is higher, the liquid pressure can be greatly increased by the presence of a MPL under the same liquid saturation, as shown in Figure 6.14. On the other hand, if GDLs with MPL and without MPL achieve a similar α due to a similar hydraulic pressure differential across the membrane, the liquid saturation level in the backing layer without MPL must be much higher than that of GDL with MPL, as can be seen from Figure 6.14. Therefore, the performance of the backing layer without MPL will suffer greatly from cathode flooding. This is consistent with the observation shown in Figure 6.12 during constant current discharge. The present explanation can be further verified by the experiments shown in Figure 6.15a, in which the air stoichiometry was increased in the cell using carbon paper backing layer without MPL. As expected, the degree of cathode flooding is reduced to a level similar to that with MPL, thus producing a comparable or slightly better performance than that with MPL. However, the decreasing liquid saturation in the backings without MPL under large air stoichiometry also reduces the liquid pressure on the cathode, thus leading to higher water crossover from the anode to cathode (shown in Figure 6.15b), an undesirable effect from the viewpoint of water management.

6.5   Summary

Low water crossover, low methanol crossover and high power density are essential requirements of a direct methanol fuel cell for portable application. In this paper we have described a new MEA design intended to achieve all the three goals simultaneously. Specifically, we use a thick and dense CDM anode as a methanol diffusion barrier to mitigate methanol crossover. This approach of limiting methanol crossover through the anode differs from use of thick membranes or development of new membrane materials.

Secondly, a MPL is coated on the cathode backing layer to build up the hydraulic pressure, enabling water back flow from the cathode to anode. This, in conjunction with a thin polymer membrane, results in 3-4 times lower water crossover coefficient between the anode and cathode. The resulting low-α MEA provides a basic element for future DMFC systems using high concentration or pure methanol. In addition to achieving low crossover of methanol and water, we have demonstrated steady-state power density of ~60 mW/cm^2 at 60$^{\text{o}}$C and ~0.4 V at constant current discharge over several hours.

Extensive parametric studies have been performed to elucidate the effects of materials properties, MEA fabrication processes, and operating conditions. Important materials properties are the membrane thickness, cathode gas diffusion media, and the microporous layer. It is also found that a CDM anode is more methanol-resistant than a CCM anode. Finally, the key parameters of operating conditions include the anode stoichiometry (primarily affecting the methanol crossover), cathode stoichiometry (significantly affecting the water crossover), cell temperature and current density (both influencing water crossover and power density). A suitable operating range in DMFCs for portable application is found to be between 50 and 60$^{\text{o}}$C, in which high power density (~60 mW/cm^2) is attainable while crossover of water and methanol can be controlled within an acceptable level.

Table 6.1 Dependence of maximum allowable anode
methanol molarity on α

Molarity (M)	H_2O/MeOH molar ratio	α
1	53.31	8.72
2	25.53	4.09
4	11.64	1.77
6	7.01	1.00
8	4.70	0.62
10	3.31	0.39
17	1.02	0.00
25	0.0	-0.17

Table 6.2 Net water transport coefficient, average steady-state power density and cell internal resistance of various membranes*.

Membranes		Net water transport coefficient / Steady-state power density (mW/cm^2)		
		Nafion 111	Nafion 112	Nafion 1135
Stoichiometries @ 150mA/cm^2 (ξ_a/ξ_c)	1.75/3.0	0.65 / 19.5	0.64 / 44.6	1.09 / 56.4
	2.0 /3.0	0.61 / 25.2	0.83 / 47.1	1.05 / 57.3
	2.5 /3.0	0.70 / 32.5	0.87 / 48.6	1.10 / 58.1
Internal resistance (mΩcm^2)		135	208	220

* MEA-B was used at 3M methanol solution and 60°C, where both anode and cathode catalyst layers are CDM type, with carbon paper and wet-proofed carbon cloth with pre-coated MPL as anode and cathode backing layers, respectively.

Table 6.3 Effects of operating current density on water crossover coefficient and steady-state power density at 60°C*.

Current Density (mA/cm^2)	Net water transport coefficient, α	Average steady-state power density (mW/cm^2)
100	1.40	40.8
150	0.85	54.6
200	0.53	61.4

*MEA-A, carbon cloth w/ MPL as cathode diffusion media, Nafion 112 membrane, 97 ml/min dry air and 0.19 ml/min 2M MeOH solution.
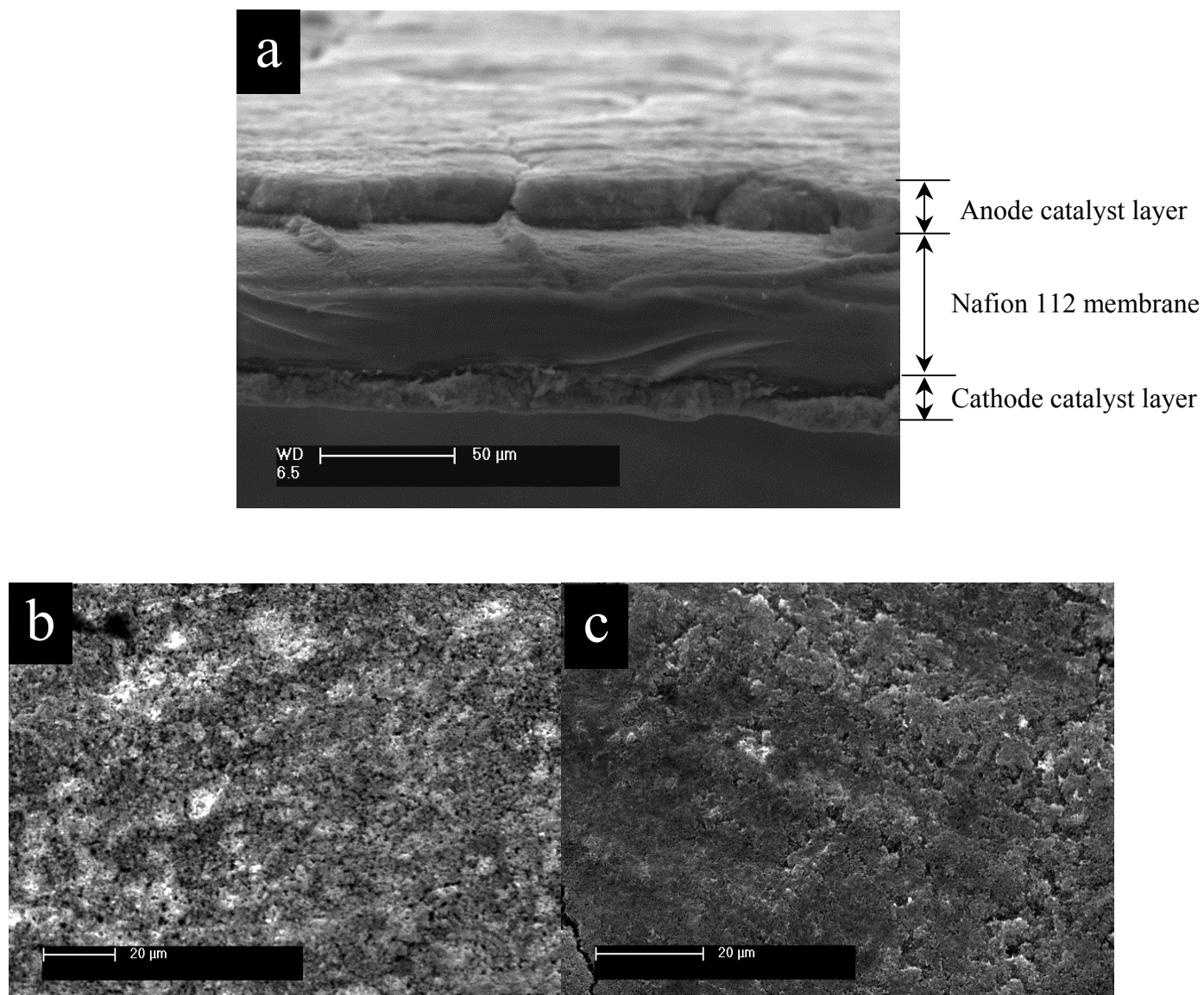
Figure 6.1 SEM micrographs of MEA-A: (a) cross section, (b) surface of CCM anode catalyst layer, and (c) surface of CCM cathode catalyst layer.
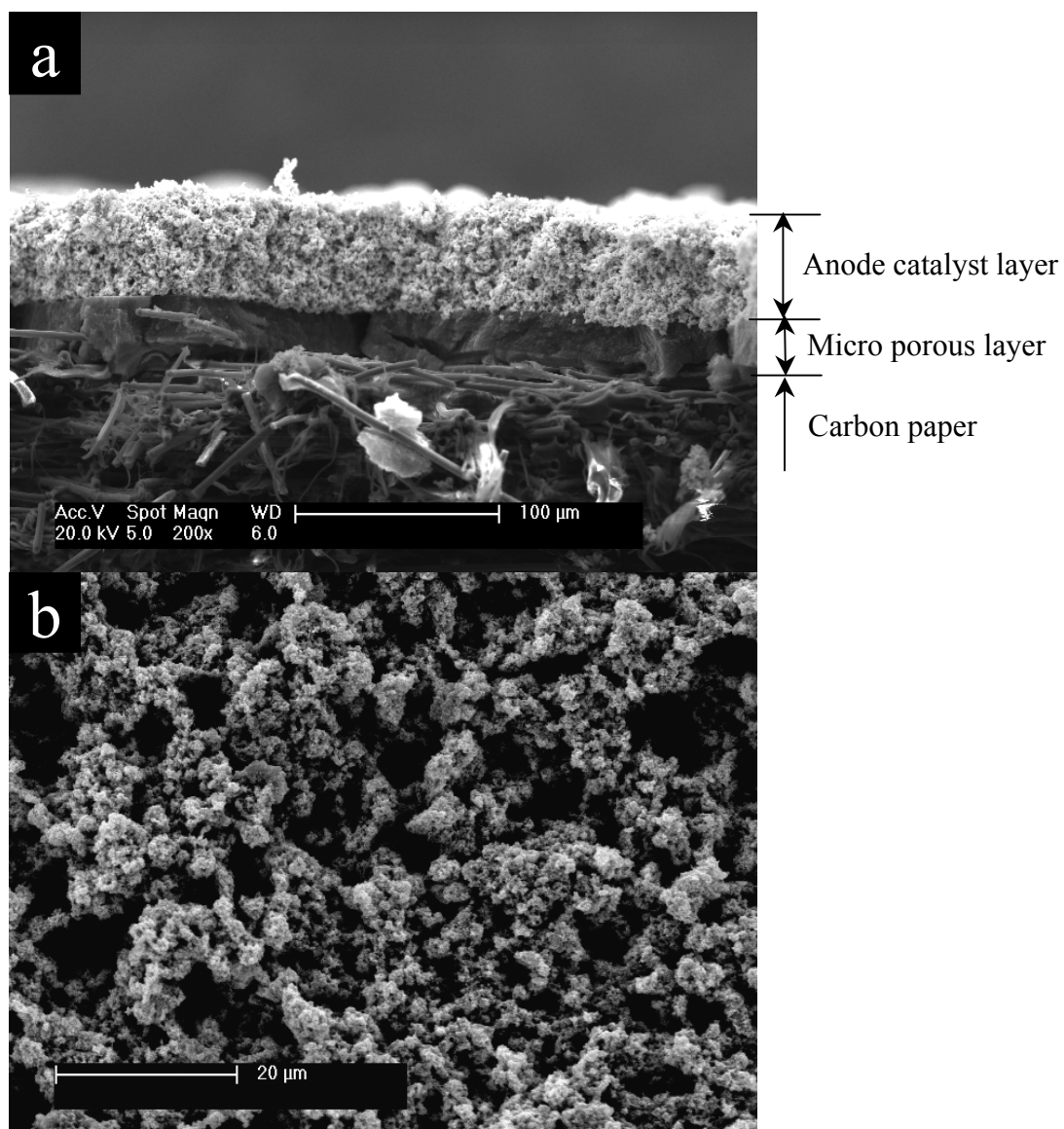
Figure 6.2 SEM micrographs of MEA-B: (a) cross section, and (b) surface of CDM anode.
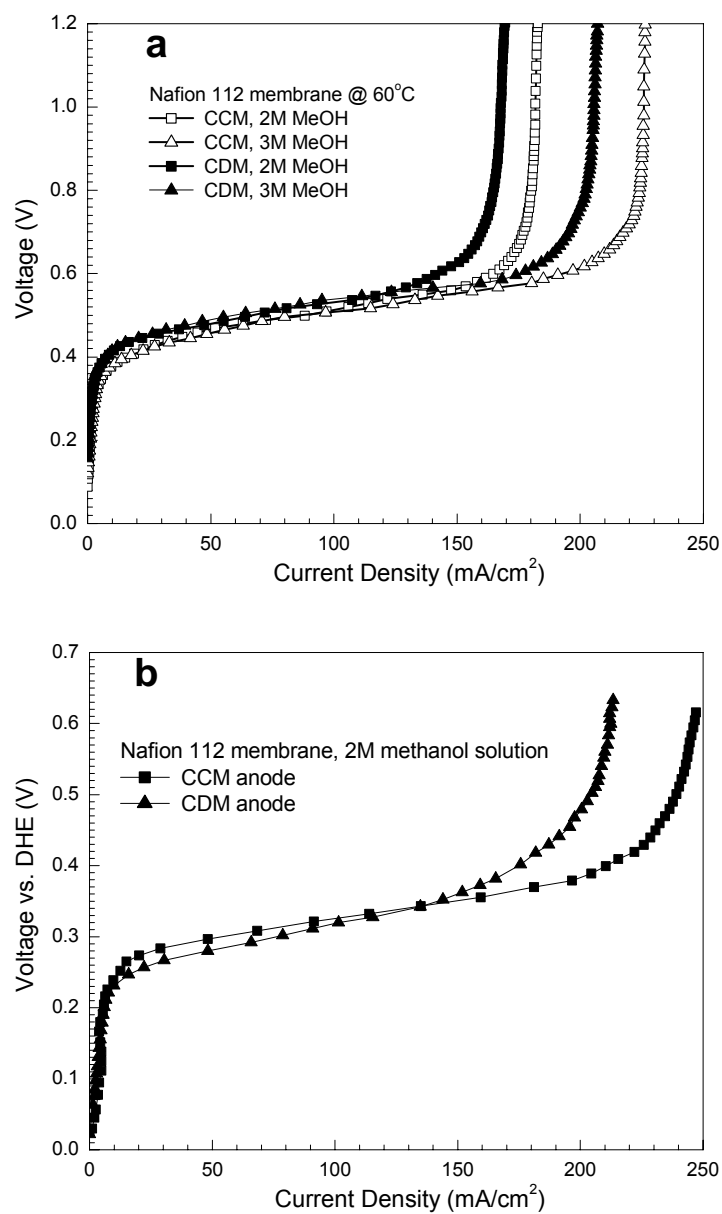
Figure 6.3 Comparison of CCM and CDM anode catalyst layers: (a) methanol crossover, and (b) anode polarization. Carbon paper and carbon cloth both with MPL were employed as diffusion media in the anode and cathode, respectively. The cell temperature is 60°C. The flow rate of methanol solution corresponds to 1.75 at 150 mA/cm².
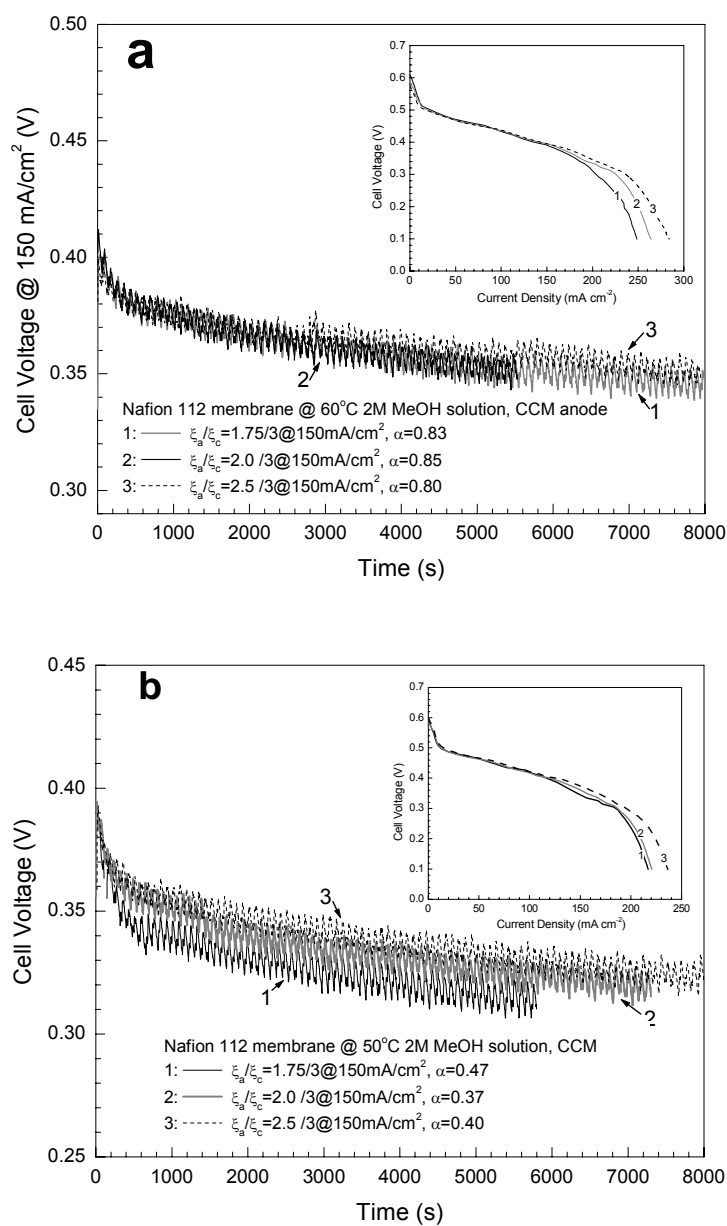
Figure 6.4 Influence of anode stoichoimetry on constant current discharge in the CCM anode cell using 2M methanol solution at: (a) 60°C, and (b) 50°C. The insets show quick-scan polarization curves at different anode stoichiometries.
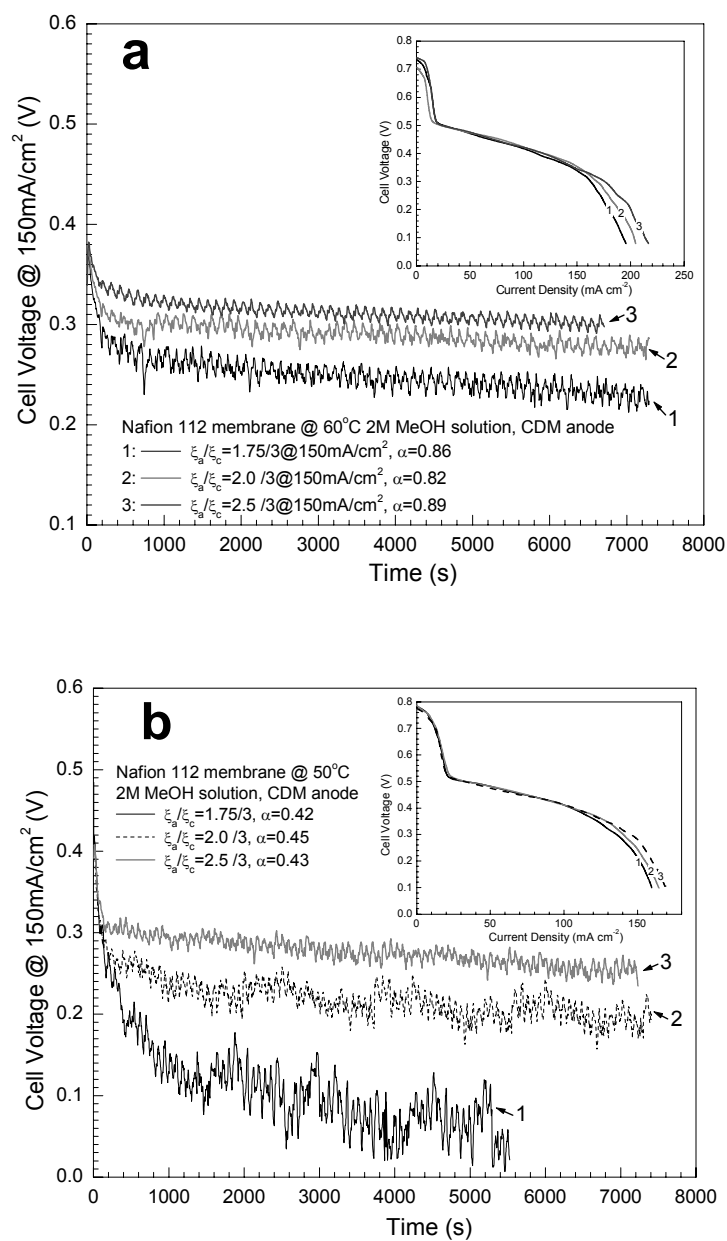
Figure 6.5 Influence of anode stoichoimetry on constant current discharge in the CDM anode cell using 2M methanol solution at: (a) 60°C, and (b) 50°C. The insets show quick-scan polarization curves at different anode stoichiometries.
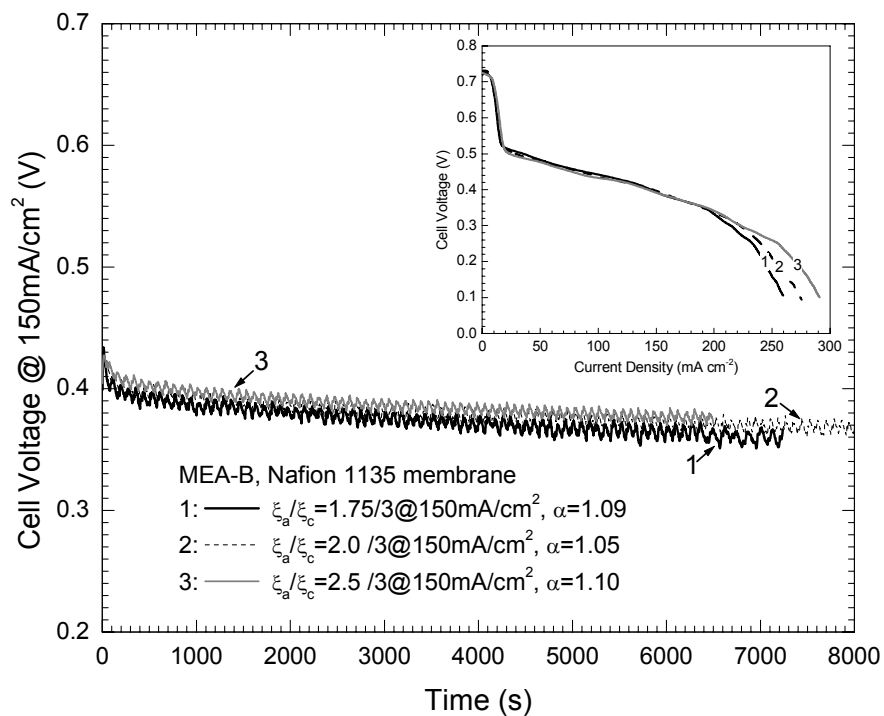
Figure 6.6 Constant current discharge performance of the CDM anode cell with Nafion 1135 membrane under various anode stoichiometric flow ratios (3M, 60°C).
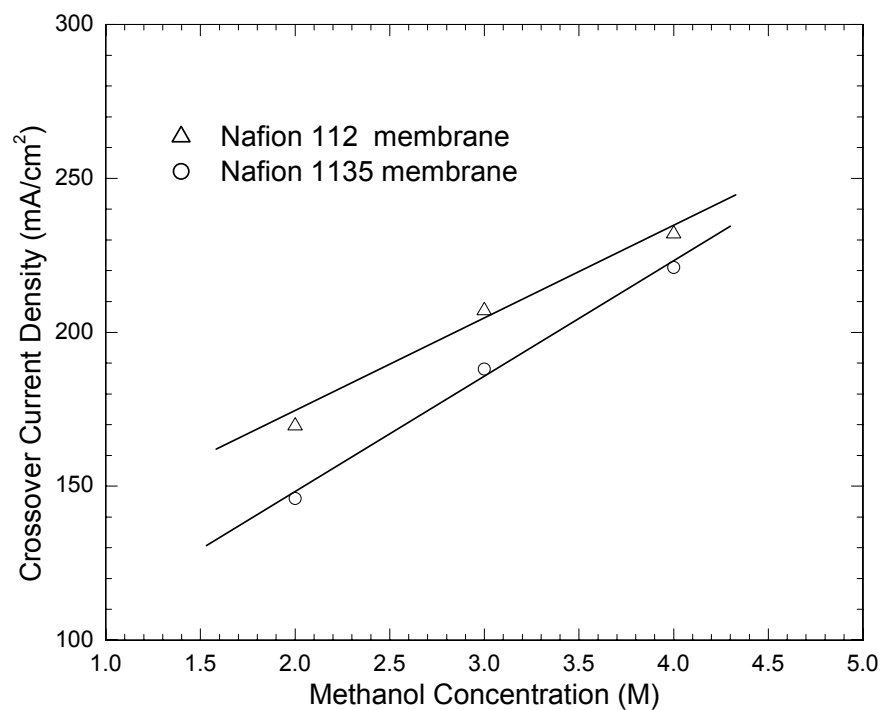
Figure 6.7 Comparison of methanol crossover current density of Nafion 112 and 1135 membranes at 60°C and different methanol concentrations. MEA-B was used with carbon paper and carbon cloth, both with MPL, as diffusion media in the anode and cathode, respectively.
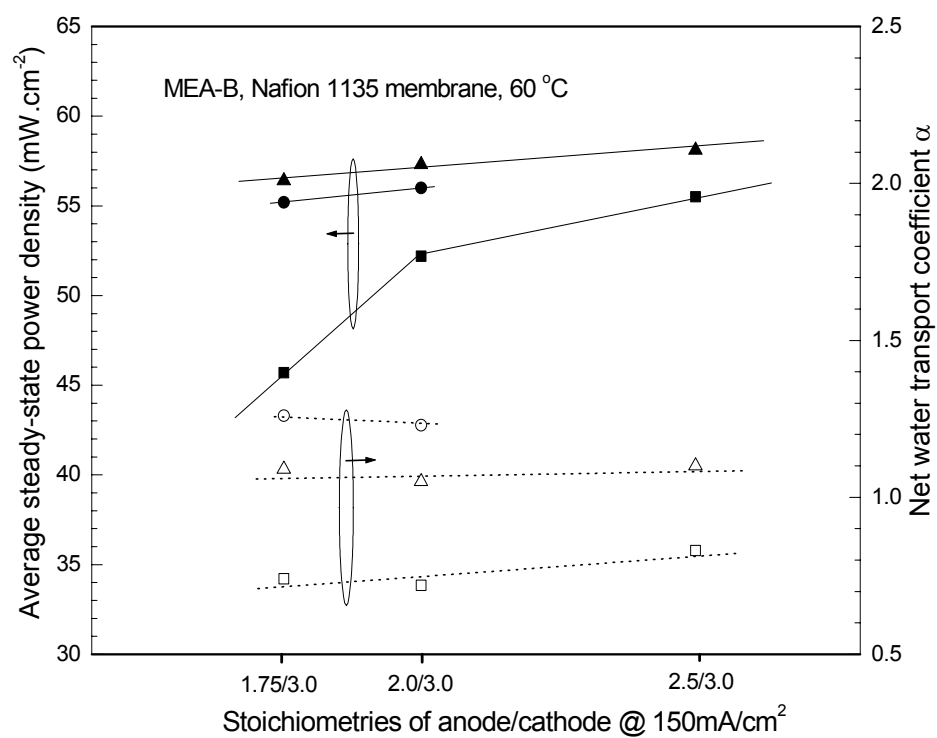
Figure 6.8 Influence of anode stoichiometry and methanol concentration on average steady-state power density and net water transport coefficient, α. Squares, 2M methanol solution; triangles, 3M methanol solution; circles, 4M methanol solution.
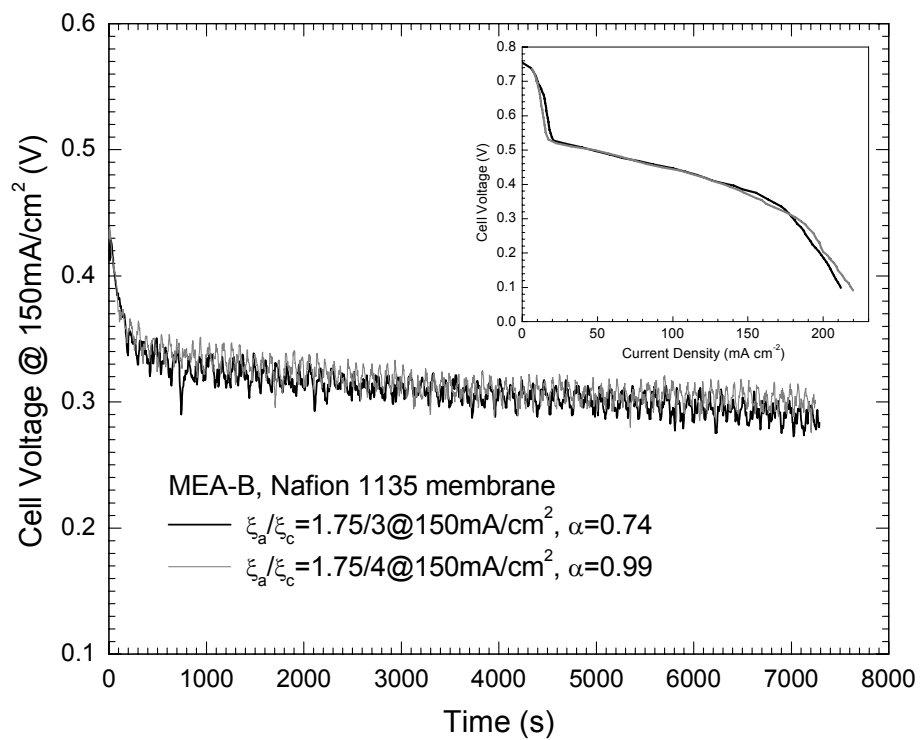
Figure 6.9 Cathode stoichiometry effect in the CDM anode cell on constant current discharge, net water transport coefficient and quick-scan performance at 60°C and 2M.
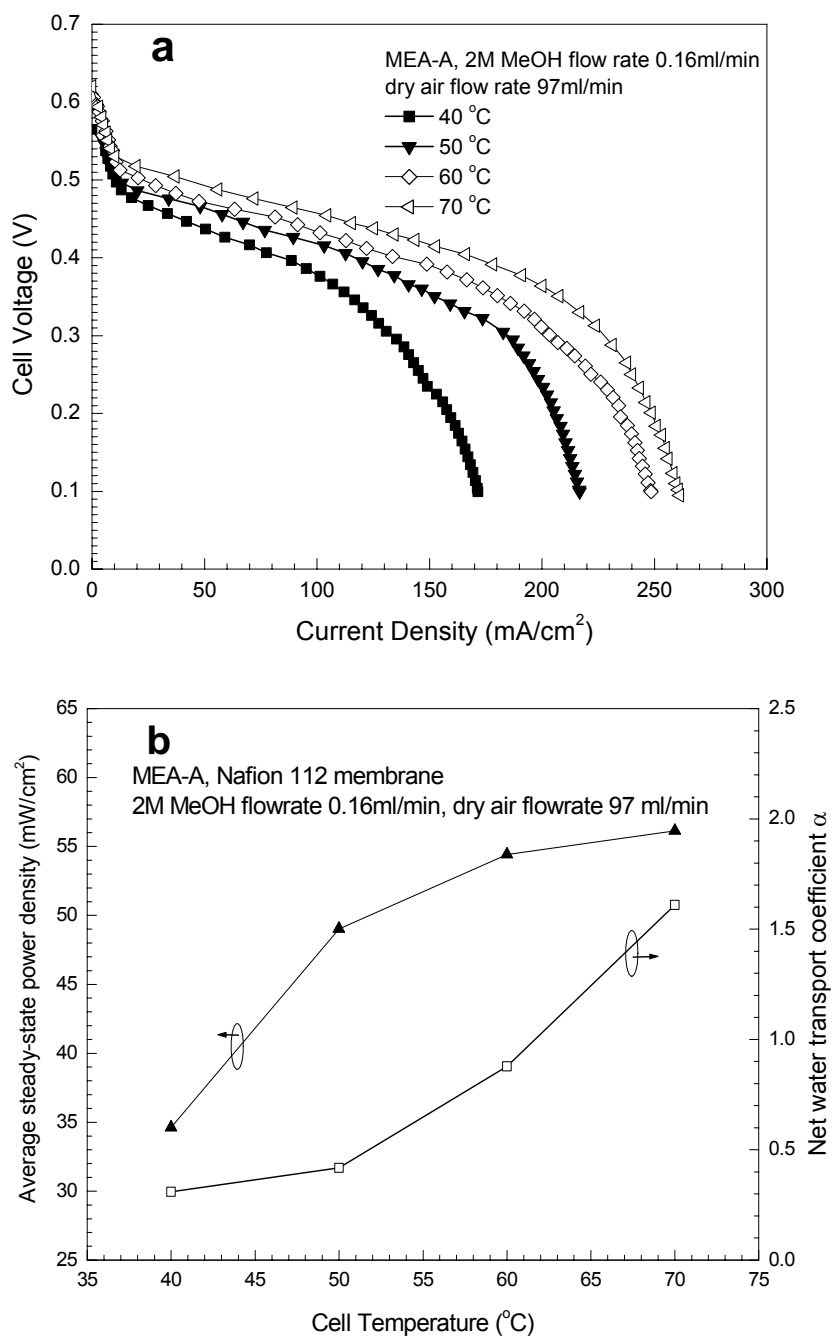
Figure 6.10 Temperature effects on: (a) quick-scan polarization, and (b) average steady-state power density and net water transport coefficient in constant current discharge. In figure 10b, the operation current density at 40°C is 100 mA/cm^2, while it is 150 mA/cm^2 at 50, 60, and 70°C.
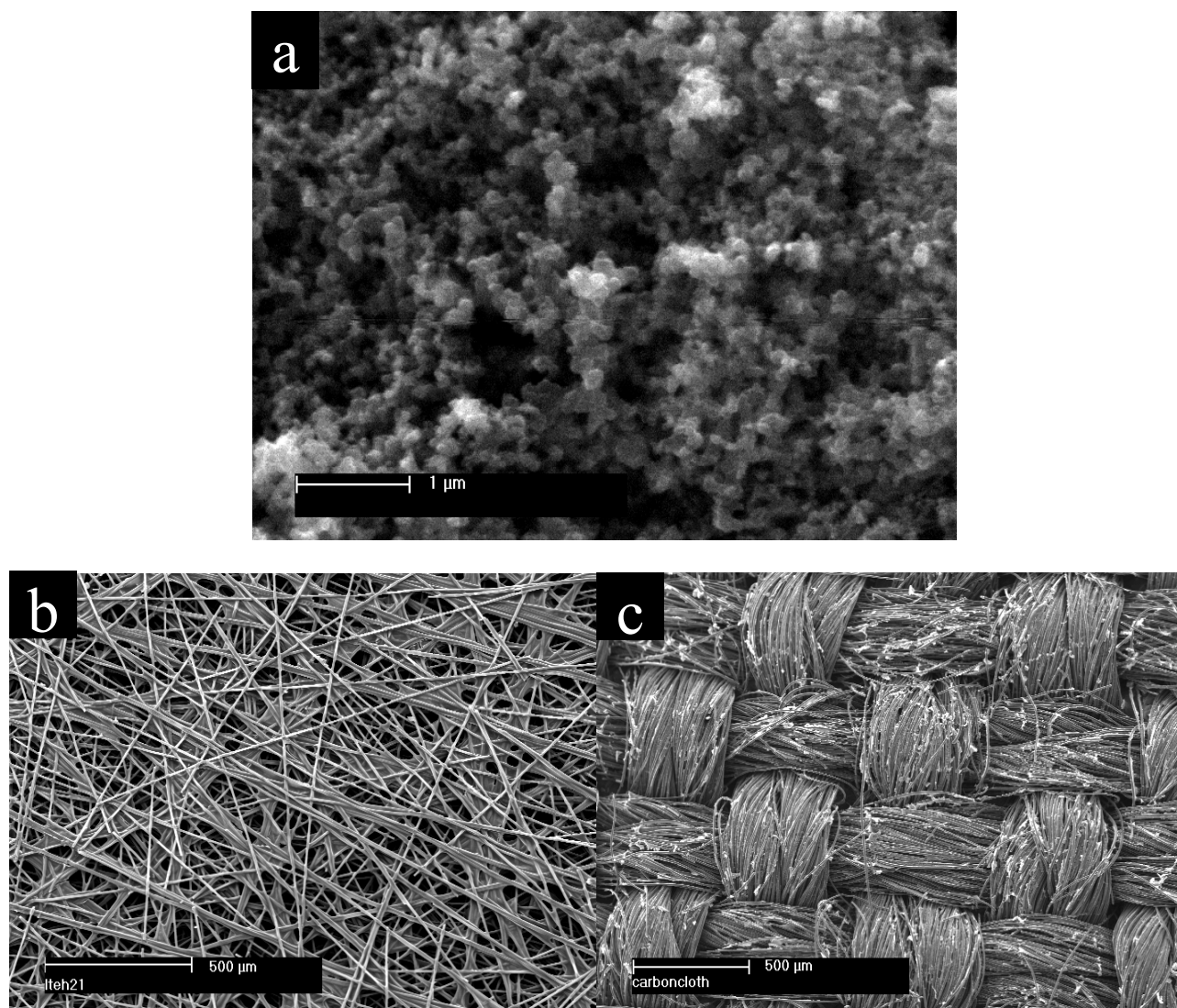
Figure 6.11 SEM graphs of gas diffusion media: (a) surface of micro porous layer (MPL), (b) wet-proofed carbon paper and (c) wet-proofed carbon cloth.
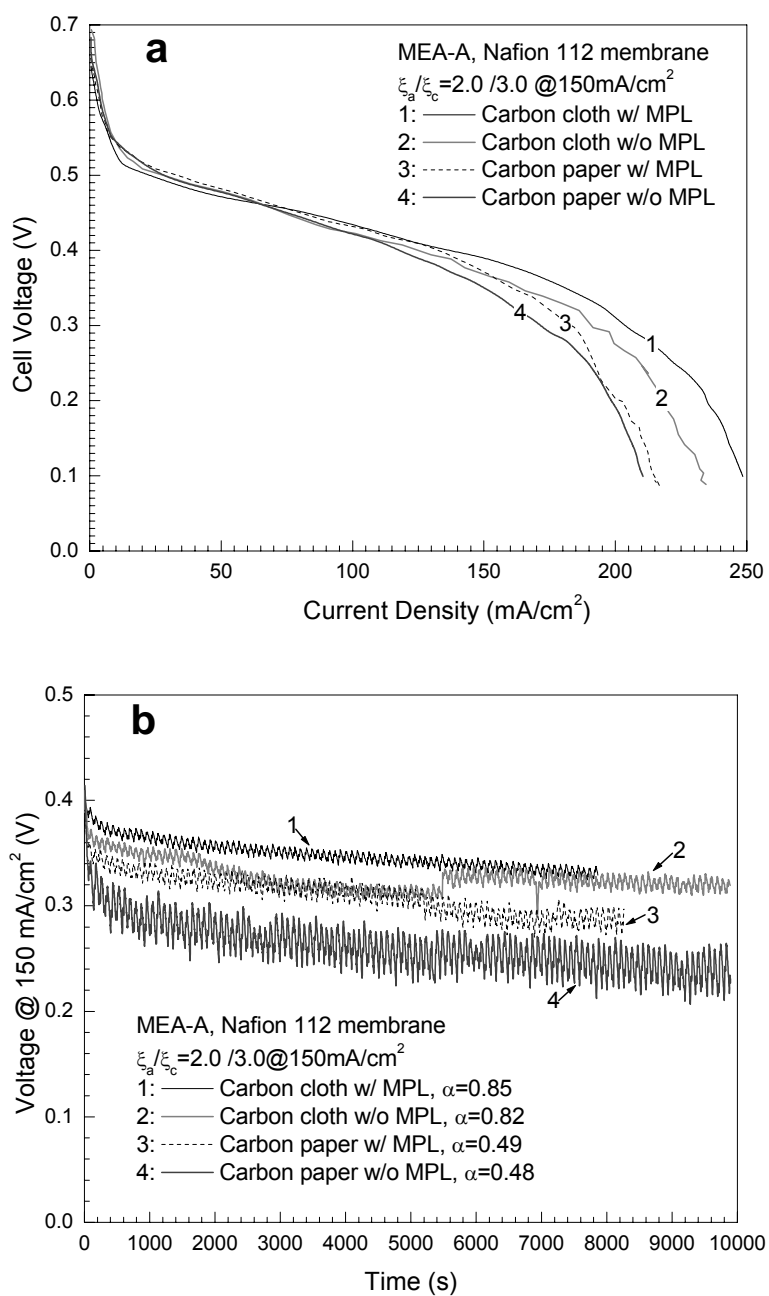
Figure 6.12 Influence of cathode gas diffusion media on cell performance and net water transport coefficient for MEA-A using 2M methanol solution at 60°C: (a) quick-scan polarization, and (b) constant current discharge at 150 mA/cm².
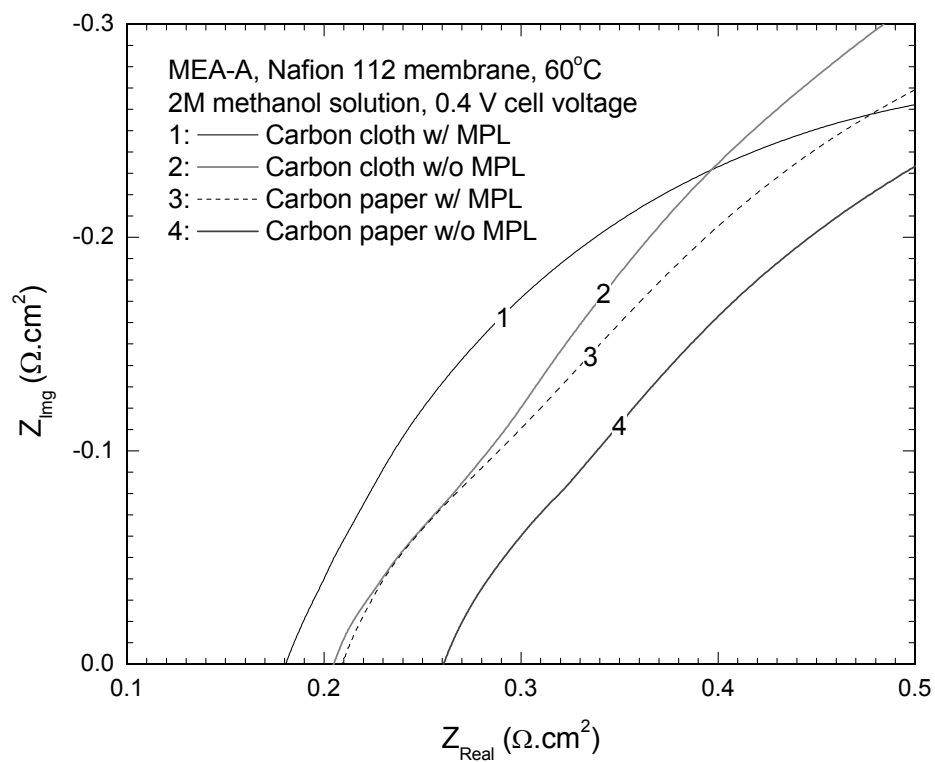
Figure 6.13 High-frequency portion of EIS spectra of DMFCs using different cathode diffusion media. Anode and cathode stiochiometries are 2 and 3 at 150mA/cm^2.
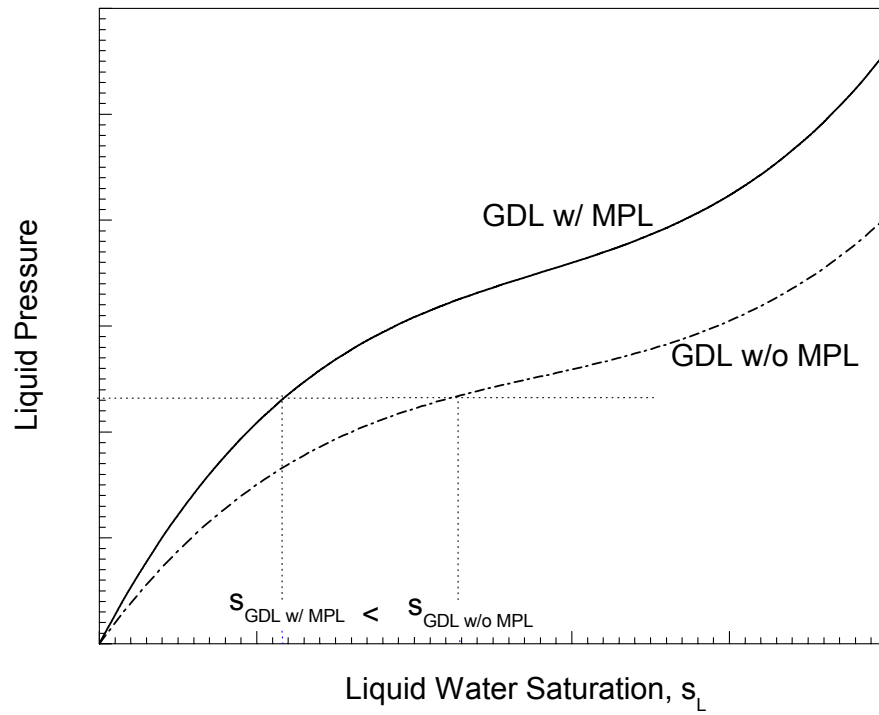
Figure 6.14 Schematic illustration of liquid pressure as a function of liquid water saturation for GDLs with and without MPL.
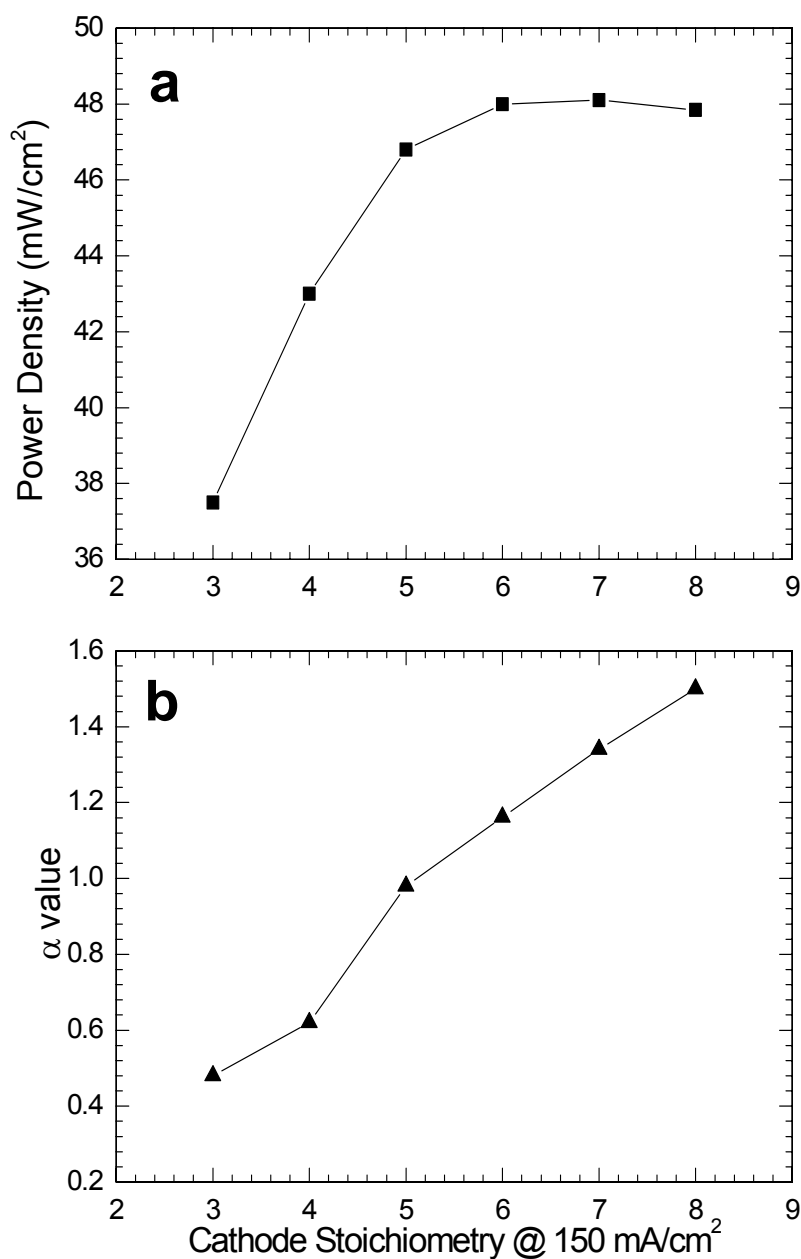
Figure 6.15 Influence of cathode stoichoimetry on: (a) average power density, and (b) net water transport coefficient in constant current discharge of MEA-A with carbon paper without MPL on the cathode. Anode stoichiometry is 2 at 150 mA/cm^2, and 2M methanol solution is used at 60°C.

Chapter 7 MINIMIZING WATER CROSSOVER IN DMFCS BY TAILORING ANODE DIFFUSION MEDIA

7.1   Introduction

In Chapter 6, very low α is achieved by applying a highly hydrophobic MPL between the cathode GDL and CL. Based on this design principle, various operating parameters and components have been optimized to obtain low α and reasonable cell performance. Notable measures are reducing the operating temperature and cathode air stoichiometry to minimize water evaporation from the cathode exhaust, and employing thinner membranes (NF111) to promote water back transport. However, these measures also lead to either low cell performance or increased methanol crossover.

New methods that can achieve low α as well as high cell performance are highly desirable. Note that the net water transport coefficient α is a combined result of electro-osmotic drag and back transport through the membrane. The electro-osmotic water flux and the formation of liquid water at the cathode result in either a cathode hydraulic pressure buildup (assisted by a hydrophobic cathode MPL) or a gradient in the water content (or liquid water saturation), leading to water permeation from the cathode to the anode, as shown in Figure 7.1. The two modes of water transport originate from different driving forces. The water content gradient causes a gradient in osmotic pressure (Meier and Eigenberger, 2004) – or more general in the chemical potential of water – between the cathode side and anode side of the membrane. In addition to increasing the cathode

hydraulic pressure, enhancing water content or water saturation gradient across the membrane is therefore another possible approach to reduce α. This approach requires modification of the MEA structure while maintaining higher cell power.

The effect of MEA and electrode structures on water transport has been investigated mostly in H_2 PEFCs. Staiti et al. (1992) studied water transport in MEAs containing Toray paper electrodes with varying loading of a hydrophobic agent, fluoroethylenepropylene (FEP). There was a clear decrease of the net drag with increasing FEP loading. Janssen and Overvelde (2001) found that an additional layer of hydrophobic MPL was beneficial for water back transport. However, its influence on net water transport is very small in H_2 PEFCs. To date, little attention has been paid to the influence of the MEA structure on water transport in DMFCs.

In this chapter, the effect of anode diffusion media on DMFC water transport is investigated. It is shown theoretically that diffusion media properties have a dramatic effect on anode water saturation. An additional layer of hydrophobic anode MPL between CL and backing layer in the anode is found to be essential to achieve low α. After correcting the water produced from oxidation of the crossover methanol, α is only ~0.3 at 150 mA/cm^2 for the MEA with a hydrophobic anode MPL. This is due to its lower water saturation in the anode CL, as explained by a two-phase transport model, than those of MEAs with and without a hydrophilic MPL. The findings point to a future direction that could further lower α by improving MPL surface hydrophobicity.

7.2   Experimental

Both MEA fabrication and experimental hardware have been detailed in previous chapters and thus are not repeated here. The cathode GDL is carbon cloth with a pre-coated hydrophobic MPL containing carbon black and PTFE. Carbon papers with 10% wet-proofing (Toray TGPH 090) were used as the anode backings. A mixture of Vulcan XC72R carbon black and 40 wt% PTFE (TFE 30, Dupont) or Nafion was coated on the carbon paper using a gap-adjustable blade to fabricate either a hydrophobic or a hydrophilic MPL with the same loading of 2mg/cm^2 (carbon and binder). CCM MEAs of 12 cm^2 were prepared by the decal method. The catalyst loadings in the anode and cathode CL were 5.3 mgPtRu/cm^2 and 1.2 mgPt/cm^2, respectively.

To investigate the surface morphologies of different diffusion media, scanning electron microscopy (SEM, Philips XL20) was used. Fresh samples of different anode diffusion media without Ad plating were examined at relatively small magnification to reveal porosity and surface structure.

The MEAs were mounted between two identical graphite flow plates with two-pass serpentine channels. The cell was operated at 60$^\mathrm{o}$C and ambient pressure on both sides. 2M methanol solution (0.19 mL/min) and dry air (97.3 mL/min) were fed to the anode and cathode, corresponding to stoichiometries of 2 and 3 at 150 mA/cm^2, respectively. The total water collected from the cathode exit at constant-current discharge, N_{H_2O} (mol/s), after correcting the water produced from oxidation of the crossover methanol, was used to calculate the net water transport coefficient, α, via Eq. 6.8. Methanol crossover current at certain current density, I_{xover}, is calculated according to Eq. 2.1.

7.3   Liquid water transport at the DMFC anode

The multiphase mixture (M2) formulation is used to simulate two-phase water transport in the anode. Governing equation of water transport in both carbon paper and MPL is described as (Pasaogullari and Wang, 2004)

$$\nabla(\gamma_c \vec{u} C^{H_2O}) + \nabla\left[\left(\frac{1 - C_l^{MeOH} M^{MeOH}/\rho}{M^{H_2O}} - \frac{C_{sat}^{H_2O}}{\rho_g}\right)\frac{\rho}{\rho}j_l\right] = 0 \qquad [7.1]$$

The two terms at the left-hand side describe water transport by convection and capillary transport. Here, $C_l^{MeOH} M^{MeOH}/\rho$ is the mass fraction of methanol in the liquid, assuming a uniform methanol concentration everywhere in the diffusion media.

Integration of Eq. 7.1 over the GDL thickness yields

$$\gamma_c u C^{H_2O} + \left(\frac{1 - C_l^{MeOH} M^{MeOH}/\rho}{M^{H_2O}} - \frac{C_{sat}^{H_2O}}{\rho_g}\right)j_l = \frac{I}{6F}(1 + 6\alpha) \qquad [7.2]$$

Superficial velocities in the above equation at the two interfaces are calculated as

$$u = j_m/\rho = \frac{1}{\rho}\left[\frac{I}{6F}(1 + 6\alpha)M^{H_2O} + \frac{I}{6F}M^{MeOH} - \frac{I}{6F}M^{CO_2}\right] \qquad [7.3]$$

where j_m is the total mass flux through the interface in both phases. The total water concentration is expressed in terms of liquid saturation, s, as

$$C^{H_2O} = sC_l^{H_2O} + (1 - s)C_{sat}^{H_2O} \qquad [7.4]$$

Expression of other parameters can be found in Chapter 5. Inserting the mixture velocity from Eq. 7.3, mixture density from Eq. 5.3, advection correction factor from Eq. 5.2 and liquid flux from Eq. 5.5 into Eq. 7.2, a governing equation can be rewritten using s as the primary variable. The liquid saturation profiles in the anode GDL and MPL can be obtained using 4-order Runge-Kutta method.

At small anode stoichiometry, water saturation at the anode GDL/channel interface is less than 100%, since CO_2 bubbles cannot be removed efficiently from the surface of the backing layer and remain, covering the backing surface. Saturation at the anode GDL/channel interface is arbitrarily assumed to be 65%. Liquid saturation at the GDL/MPL interface in the MPL can be calculated by assuming a continuous gas and liquid pressures across the GDL/MPL interface, *i.e.,*

$$p_c^{GDL}\Big|_{GDL-MPL\ int} = p_c^{MPL}\Big|_{GDL-MPL\ int} \qquad [7.5]$$

The different properties of two layers cause a discontinuity in saturation across the interface.

7.4   Results and discussion

We are interested primarily in how the structure and wettability of anode diffusion media yields low α. Our first attempt is to investigate the effect of anode MPL. Three anode diffusion media are investigated in this study, with details listed in Table 7.1. Carbon paper, carbon paper with a hydrophilic MPL and with a hydrophobic MPL are employed in MEA-1, MEA-2, and MEA-3, respectively. SEM images of their surfaces are shown in Figure 7.2. Carbon paper is a microscopically complex fibrous structure with pore size distribution ranging from a few microns to tens of microns. MPLs have much smaller pore sizes (~ 1μm), with uniform cracks (mud cracking), induced by volume shrinkage of carbon/PTFE (or carbon/Nafion) slurry during annealing. Although it is difficult to find any noticeable structural difference of the two MPLs from the SEM images, it is assumed that pore size and porosity in the hydrophilic MPL would decrease due to swelling and expansion of ionomer upon full hydration; while those of

hydrophobic MPL remain the same. Differences in porosity, permeability, pore size distribution, surface wettability, and liquid retention of the three diffusion media would result in different two-phase flow and water transport characteristics (Wang, 2003).

The quick-scan DMFC polarization curves of the three MEAs are shown in Figure 7.3. The limiting current densities of MEA-1 and MEA-3 are almost identical, approximately 50 mA/cm^2 larger than that of MEA-2. At 150 mA/cm^2, the two MEAs have cell voltages about 25 mV higher than that of MEA-2. The performance curves of the three MEAs are consistent with their anode polarizations as shown in Figure 7.4. MEA-2 has the smallest anode limiting current density, around 300 mA/cm^2, which is roughly 50 mA/cm^2 smaller than those of MEA-1 and MEA-3. This indicates that methanol transport in the anode is barely influenced by a hydrophobic MPL, but is inhibited by a hydrophilic MPL, due to reduced porosity by ionomer hydration and expansion. This is probably the reason why MEA-1 and MEA-3 show smaller methanol oxidation overpotential than that of MEA-2 when the current density is beyond ~100mA/cm^2.

The HFR and methanol crossover at open circuit of the three MEAs are also shown in Table 7.1. HFR is taken as the value where AC impedance spectra intercept with the real axis. The hydrophilic MPL has the smallest HFR and methanol crossover, which are 0.183 Ω.cm^2 and 223 mA/cm^2, respectively. This probably originates from good contact between carbon paper backing and anode catalyst layer via a compact hydrophilic MPL using Nafion ionomer as the binder. It also gives the lowest methanol crossover rate, consistent with its smallest anode limiting current density. MEA-3 with a hydrophobic

MPL has slightly higher HFR and methanol crossover, and MEA-1 without anode MPL has the largest methanol crossover.

Constant-current discharge of these MEAs at various current densities was performed at 60°C and ambient pressure on both sides. DMFC voltage variations over discharge time at 150 mA/cm^2 are recorded in Figure 7.5. The average cell voltage during constant-current discharge is 0.398V for MEA-3, much higher than 0.328V of MEA-2 and 0.379V of MEA-1. It is interesting to note from Figure 7.5 that MEA-1 and MEA-3 operate more stably than MEA-2, which shows large voltage fluctuations during constant-current discharge. These fluctuations are believed to be caused by liquid water accumulation and subsequent removal in the cathode GDL and channels (Yang et al., 2004), corresponding to slow voltage decay and sudden recovery, as confirmed by experiments with increased cathode stoichiometry (results not shown here). During constant-current discharge at 150 mA/cm^2, the water collected from cathode outlet stream was used to calculate α values, which are listed in Table 7.1. MPL wettability has a dramatic effect on water transport in DMFCs. The α values of the MEAs with hydrophobic and hydrophilic MPLs are 0.335 and 1.743, respectively; MEA-1 without anode MPL has α value right between the above two cases. Recall the definition of α, higher value means larger amount of water transported from the anode through the membrane to the cathode; thus, the transported water plus the generated water would easily flood the cathode. This is the reason why MEA-2 displays so large cell voltage fluctuation during constant-current discharge.

To investigate more clearly the effect of anode diffusion media properties on water transport in DMFCs, α values are measured at a series of current densities and plotted in

Figure 7.6. For all MEAs, α values initially decrease dramatically with current densities and then diminish gradually when current densities are beyond 100 mA/cm^2. This clearly indicates that the driving force for water back flow is current-dependant and increases dramatically with the current as the cathode accumulate more water and the anode becomes more gaseous. Another significant feature is that the hydrophobic MPL has consistently lower α than the hydrophilic one over the whole spectra of current density. For example, at 150 mA/cm^2, α value for the hydrophobic MPL is 1/5 less than that of the hydrophilic one! This surprising result offers a new way to reduce α using a hydrophobic MPL.

The hydrophobic and hydrophilic MPLs studied in this chapter provide dramatically different ways of liquid water transport and thus water saturation in the porous anode. The liquid-phase transport in porous media is governed by a gradient in capillary pressure (wicking action), which is defined as the difference between gas-phase and liquid-phase pressures. In hydrophobic diffusion media, the capillary pressure is negative, hence the liquid pressure is larger than the gas-phase pressure, whereas in hydrophilic media, the gas-phase pressure is higher than that of the liquid phase (Wang, 2004). When two diffusion media with different wettability contact, liquid pressure difference between the hydrophobic and hydrophilic media always pushes liquid water from the former into the latter, rendering the latter fully saturated and the former only partially saturated, as schematically shown in Figure 7.7. For all diffusion media, the capillary pressure increases with the liquid saturation. At the MPL/GDL interface, if a continuous liquid pressure is assumed (shown as a dotted line in the figure), the capillary pressure would push liquid water into the hydrophilic MPL. Eventually, no more gas phase will be

displaced by the liquid phase, even with further increases in capillary pressure (as indicated by an arrow in the figure); therefore, a residual or irreducible gas saturation (Wang and Cheng, 1997), s_{ir}^g (= 0.1), is assumed. The three points I, II, and III in Figure 7.7 indicate the liquid saturations in carbon paper, hydrophobic MPL, and hydrophilic MPL, respectively, under that continuous pressure. Clearly, the hydrophobic MPL exhibits much lower anode water saturation than the hydrophilic MPL and carbon paper.

Figure 7.8 shows the calculated water saturation profiles in the three anode diffusion media. The thickness of carbon paper is 260 μm, and both hydrophilic and hydrophobic MPLs have the same thickness of 30 μm. There are three important interfaces in the DMFC anode: (1) GDL/channel interface, where the liquid saturation is assumed to be 0.65, which is a reasonable assumption because of gaseous nature of DMFC anode due to CO_2 evolution; (2) GDL/MPL interface, where a saturation jump is expected due to a continuous liquid pressure; and (3) MPL/anode CL interface, where the water saturation determines the water back-transport driving force and thus α value. In Figure 7.8, A, B, and C correspond to liquid saturations at the anode CL surface for the three anode diffusion media: hydrophilic MPL, carbon paper, and hydrophobic MPL, respectively. In the carbon paper GDL, saturation decreases almost linearly, from 0.65 at the GDL/channel interface to 0.58 at GDL/MPL interface (point A). At this point, it rises to (1- s_{ir}^g) (i.e. the maximum liquid saturation possible) in the hydrophilic MPL and it reduces to around 0.13 in the hydrophobic MPL. Water saturation decreases in both MPLs, and eventually reaches 0.76 (point B) and 0.1 (point C) at the anode CL surface for the hydrophilic and hydrophobic MPLs, respectively.

The reason the MEA-3 with hydrophobic MPL shows the lowest α is related to its ability to depress anode liquid water saturation and enhance water content gradient across the membrane. The water back-permeation under this gradient can be interpreted by the osmosis theory (Meier and Eigenberger, 2004). Figure 7.1b shows the schematic diagram of water back-permeation driven by a gradient in the osmotic pressure across the membrane (in MEA-3). A low water content or low liquid saturation at the anode side leads to small hydrophilic clusters, in which exists a high concentration of ionic groups. The force caused by the water cluster, and acting on both the water in the cluster and the hydrophobic polymer backbone surrounding the cluster, is relatively small. In contrast, at the cathode side of the membrane, the higher water saturation results in a higher swelling of the hydrophilic domains. The corresponding concentration of ionic groups is low and the contractile force acting on the water clusters is high. The so-formed elastic force gradient of the polymer backbone, identified as the negative of the gradient in the osmotic pressure in the water cluster, dominates the back transport (Meier and Eigenberger, 2004). Water permeation from the cathode to the anode, driven by this osmotic pressure gradient, yields the very low α of MEA-3. On the contrary, the MEAs with hydrophilic or without MPL have relatively smaller osmotic pressure gradient across the membrane, thus higher α.

The hydrophobicity (contact angle) and thickness of the hydrophobic MPL are explored to further depress the water crossover in DMFCs. Variations of liquid water saturation at the hydrophobic MPL/anode CL interface with MPL contact angle and thickness are shown in Figure 7.9. MPL thickness has a marginal effect on liquid saturation at the anode CL surface. Water saturation is almost independent of the

thickness until 35μm, beyond which saturation slowly decreases with the thickness. Contact angle of anode MPL, however, seems to have a dramatic effect on liquid saturation, which decreases steeply from ~ 0.6 at 93° to ~0.1 at 100°.

Increasing the MPL contact angle or making the MPL more hydrophobic seems more effective to reduce α than using a thicker MPL. To evaluate the calculated results, two additional MEAs, MEA-4 with double-layer MPL and MEA-5 with higher PTFE fraction (60 wt%) in the MPL, were fabricated and tested. The purpose of using higher PTFE fraction is to increase the MPL contact angle. From Table 7.1, the two MEAs seem to have no significant influence on cell resistance and methanol crossover, which are all comparable to that of MEA-3 with a single-layer MPL. However, the limiting current densities of the two MEAs are 20~30 mA/cm^2 smaller than that of MEA-3, as indicated in the anode polarizations in Figure 7.4. This can be easily explained by increased methanol transport resistance due to either additional diffusion length of thicker MPL or reduced porosity by higher PTFE fraction in the MPL. This also explains why these two MEAs show slightly lower DMFC performance than MEA-3 in both quick-scan polarization and steady-current discharge as shown in Figures 7.3 and 7.5, respectively. There is an average 10~20mV voltage drop at 150 mA/cm^2 when MPL thickness doubles or PTFE loading increases, as shown in Table 7.1.

α values of the two MEAs were measured at different current densities and displayed in Figure 7.6. For MEAs with single MPL, double MPL, and higher PTFE content, there is no significant difference in α at each current density and in fact, some of the data points overlap. At 150 mA/cm^2 α values of MEA-4 and MEA-5 are 0.312 and 0.302, respectively, compared to 0.335 of MEA-3 as shown in Table 7.1. The MEAs with

thicker MPL and higher PTFE content in the MPLs show almost the same α value, and the α value difference between the two cases is only 0.01, within the experimental errors. Enhancement of MPL surface hydrophobicity by increasing PTFE loading would be limited, since 60 wt.% PTFE is probably sufficient to coat surfaces of carbon particles constituting the MPL. Further increase of PTFE content would only thicken the coating layer without changing the surface hydrophobicity appreciably (Lim and Wang, 2004). Furthermore, 2M methanol solution is easier to wet a substrate than pure water at 60°C because of its lower surface energy. Therefore, reducing α by using higher PTFE content in MPL has limited potential. It would be challenging to find more hydrophobic materials than PTFE.

7.5 Summary

Effect of anode MPL on water transport in DMFCs has been studied experimentally and theoretically. Both single cell and anode polarization tests indicate that methanol transport in the anode is negligibly influenced by a hydrophobic MPL, but is inhibited by a hydrophilic MPL, due to reduced porosity by ionomer hydration and swelling. Constant-current discharge reveals that the MEA with hydrophobic MPL displays much smaller voltage fluctuation than the hydrophilic one, probably due to the diminished cathode flooding resulting from its higher water back-transport to the anode. MEA-3 with a hydrophobic MPL is verified to have α values several times smaller than those without MPL or with hydrophilic MPL at various current densities. Theoretical calculations indicated that hydrophobic MPL has a high entry liquid pressure, and thus renders the anode more gaseous with a very small liquid saturation. The present study clearly

suggests that hydrophobic anode MPL is critical to reducing α while achieving high performance. The calculation also shows that improving MPL hydrophobicity is more effective for α-reduction than increasing the MPL thickness, although experiments have not shown effective reduction of α value. Future work is needed to understand and control water transport between the anode and cathode and to develop highly hydrophobic diffusion media.

Table 7.1 Electrochemical performance parameters of MEAs using different anode diffusion media.

Sample	Anode diffusion layer	HFR ($\Omega.cm^2$)	MeOH crossover at open circuit, $I_{c,oc}$ (mA/cm^2)	Average cell voltage@150 mA/cm^2 (V)	α value @150mA/cm^2
MEA-1	carbon paper w/o anode MPL	0.190	257	0.379	1.153
MEA-2	carbon paper w/ hydrophilic MPL	0.183	223	0.328	1.743
MEA-3	carbon paper w/ hydrophobic MPL	0.212	242	0.398	0.335
MEA-4	carbon paper w/ 2-layer MPL	0.218	240	0.387	0.312
MEA-5	carbon paper w/ higher PTFE fraction (60%) in anode MPL	0.191	237	0.379	0.302

Table 7.2 Parameters used in analysis.

Parameters	Value
Liquid surface tension (60°C), σ (N/m)	0.07
Density of 2M liquid methanol solution, ρ_l (kg/m^3)	988.2
Liquid kinematic viscosity, ν_l (m^2/s)	7.10×10^{-6}
Gas kinematic viscosity, ν_g (m^2/s)	3.06×10^{-4}
Density of saturated vapor, ρ_g (kg/m^3)	0.977
Saturated water vapor molar concentration, $C_{sat}^{H_2O}$ (mol/m^3)	7.20
Methanol concentration in GDL, C_l^{MeOH} (mol/m^3)	2000
GDL permeability, K_{GDL} (m^2)	1.0×10^{-13}
GDL thickness, ΔX_{GDL} (μm)	260
Contact angle of GDL, θ_{GDL} (°)	100
Porosity of the GDL, ε_{GDL}	0.45
MPL permeability, K_{GDL} (m^2)	7.0×10^{-15}
MPL thickness, ΔX_{GDL} (μm)	30
Contact angle of hydrophobic MPL, θ_{GDL} (°)	100
Porosity of hydrophobic MPL, ε_{GDL}	0.2
Contact angle of hydrophilic MPL, θ_{GDL} (°)	30
Porosity of hydrophilic MPL, ε_{GDL}	0.2
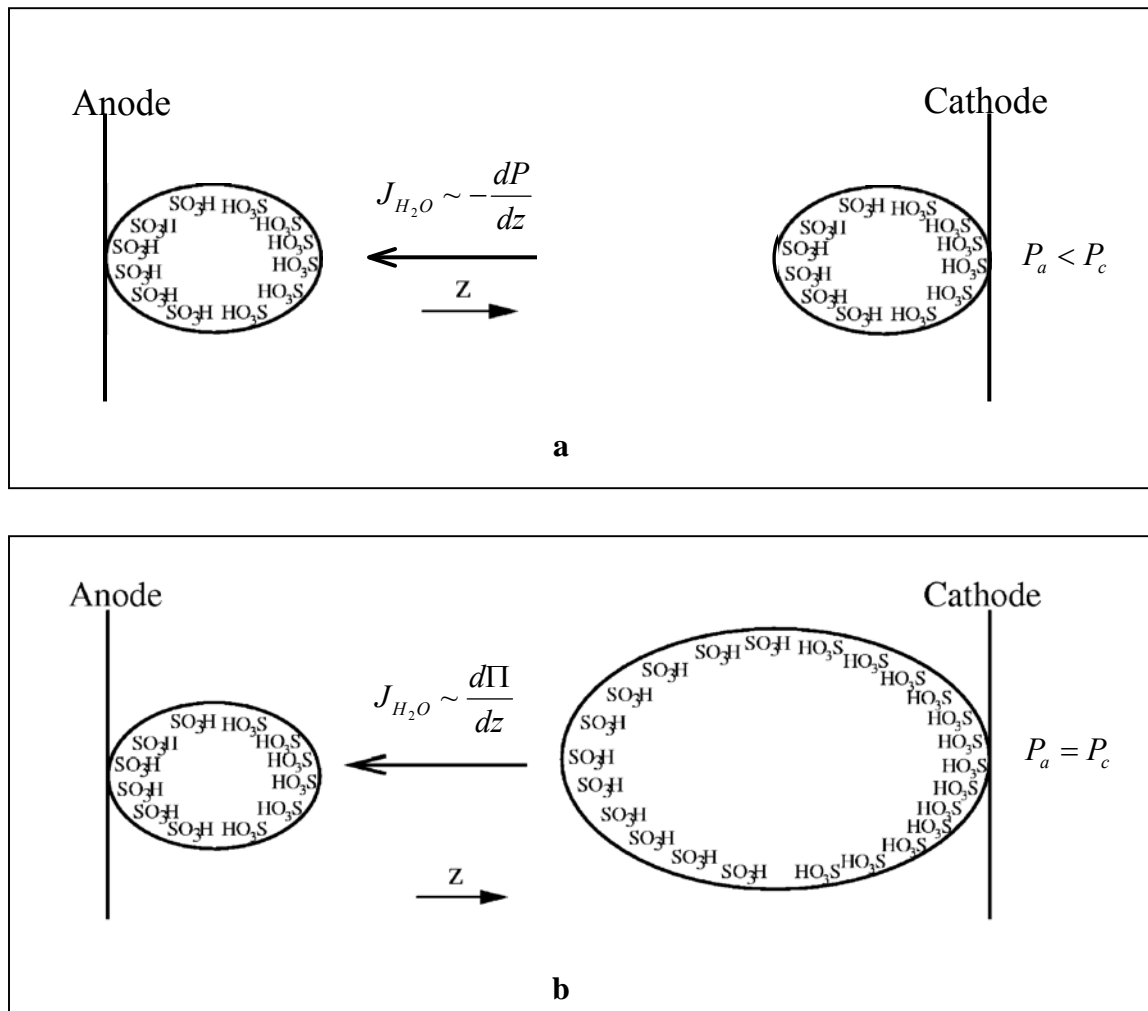
Figure 7.1 Schematic diagram of two different water back-transport modes: (a) hydraulic permeation (assisted by a hydrophobic cathode MPL) and (b) osmotic permeation (Meier and Eigenberger, 2004). Different size of the hydrophilic domains within the membrane microstructure is resulted from a gradient in the water content or saturation between the cathode and anode.
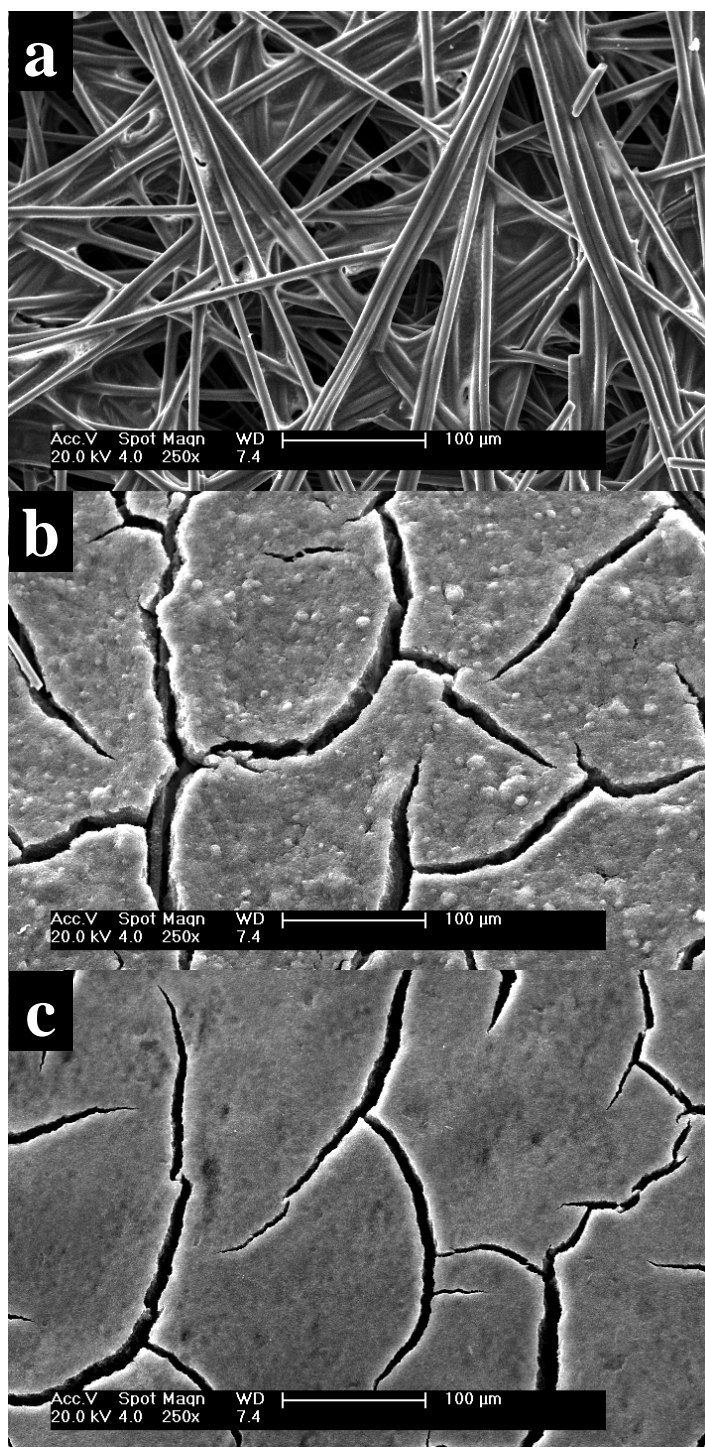
Figure 7.2 Surface morphologies of different anode diffusion media: (a) 10% wet-proofing Toray carbon (TGPH-090), (b) hydrophilic MPL (40% Nafion), and (c) hydrophobic MPL (40% PTFE).
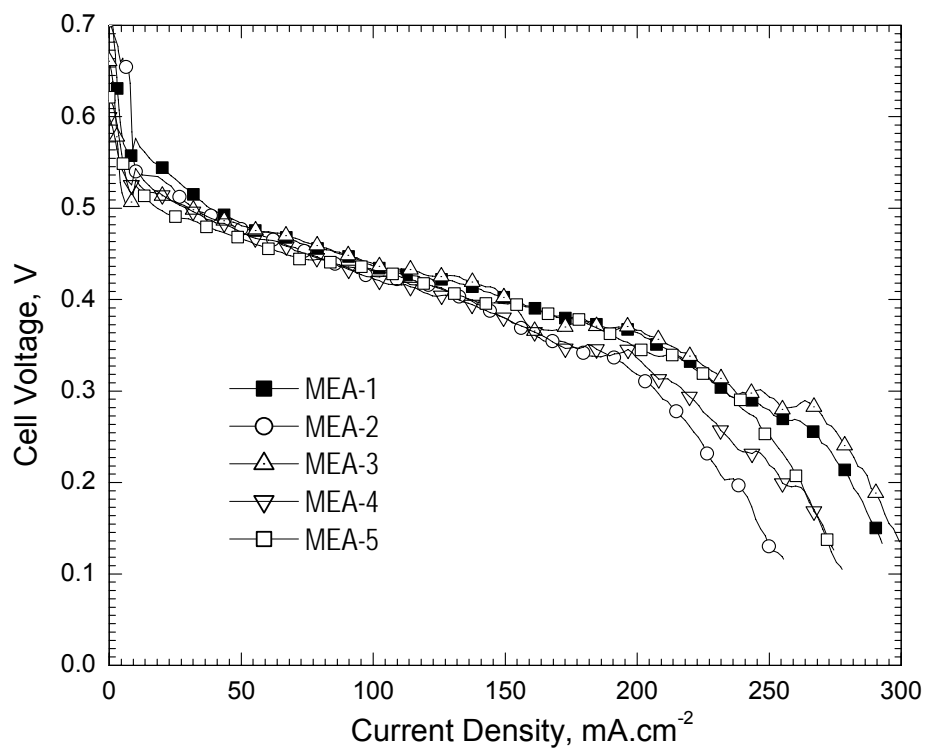
Figure 7.3 Quick-scan DMFC polarization curves of MEAs with different anode diffusion media. Carbon cloth with MPL as the cathode diffusion medium and Nafion 112 were employed. The cell is operated at 60°C, with flow rates of 2M methanol solution and dry air at 0.19 and 97.3 ml/min, corresponding to 2 and 3 @ 150 mA/cm^2, respectively.
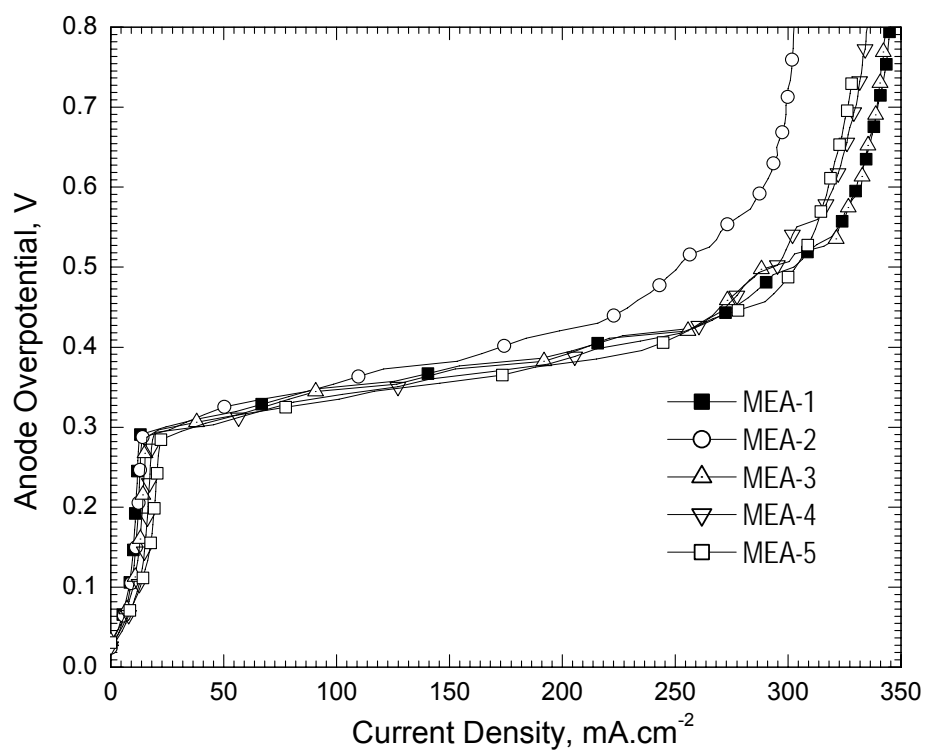
Figure 7.4 Quick-scan anode polarization curves of MEAs with different anode diffusion media.
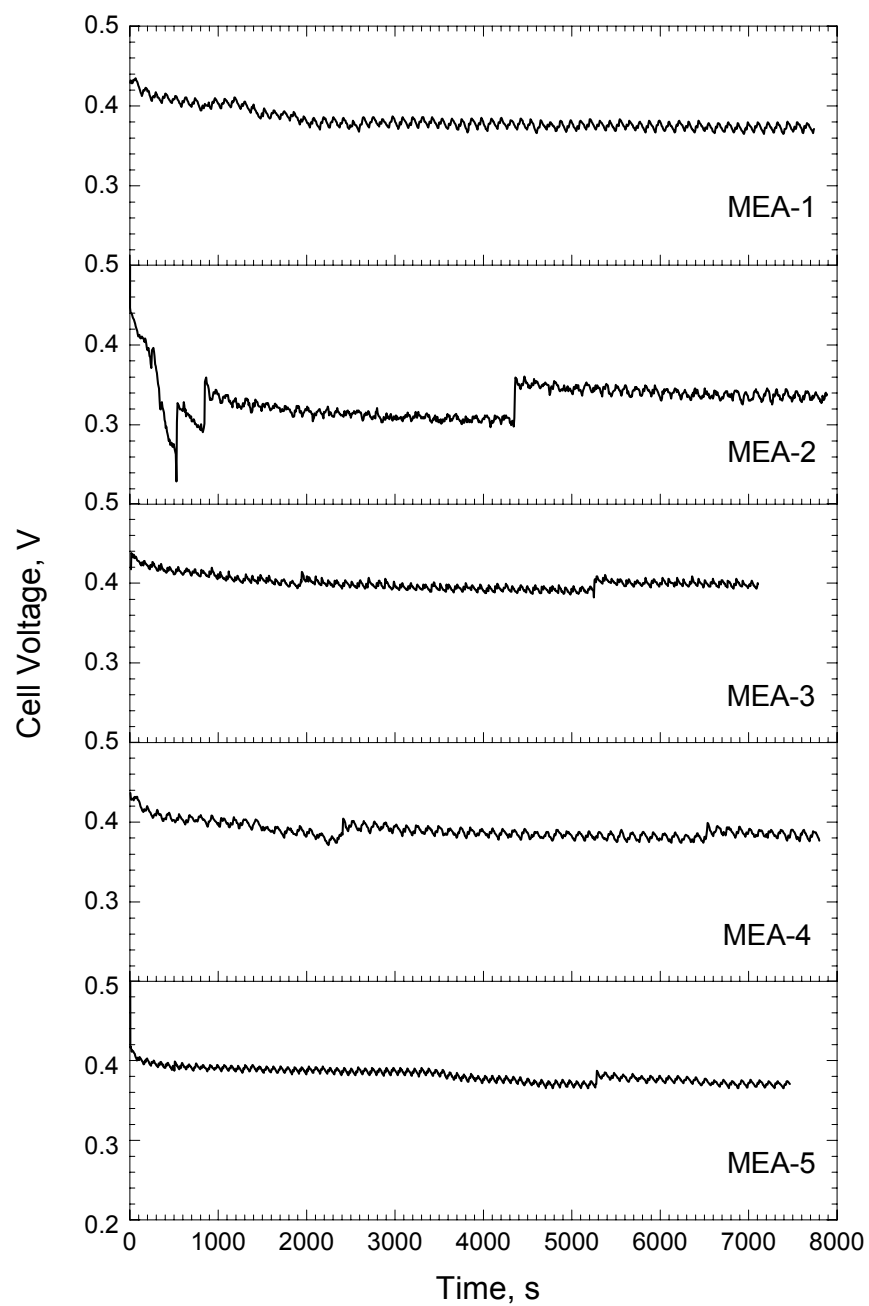
Figure 7.5 DMFC voltage variations with time at constant-current discharge (150 mA/cm^2) for different MEAs with different anode diffusion media.
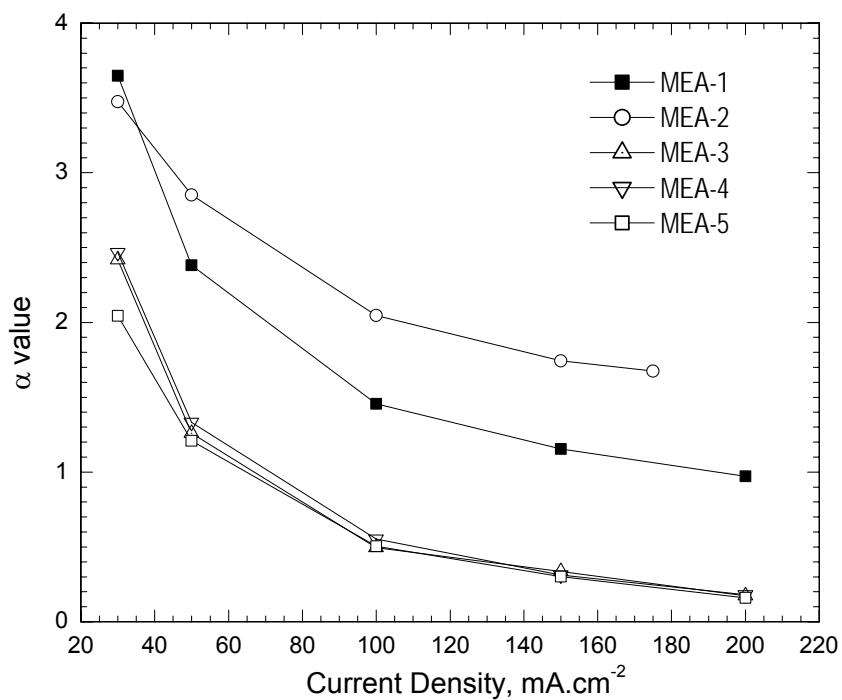
Figure 7.6 Net water transport coefficients (α) across the membrane for different MEAs. α values shown in the figure exclude the water produced by methanol crossover on the cathode.
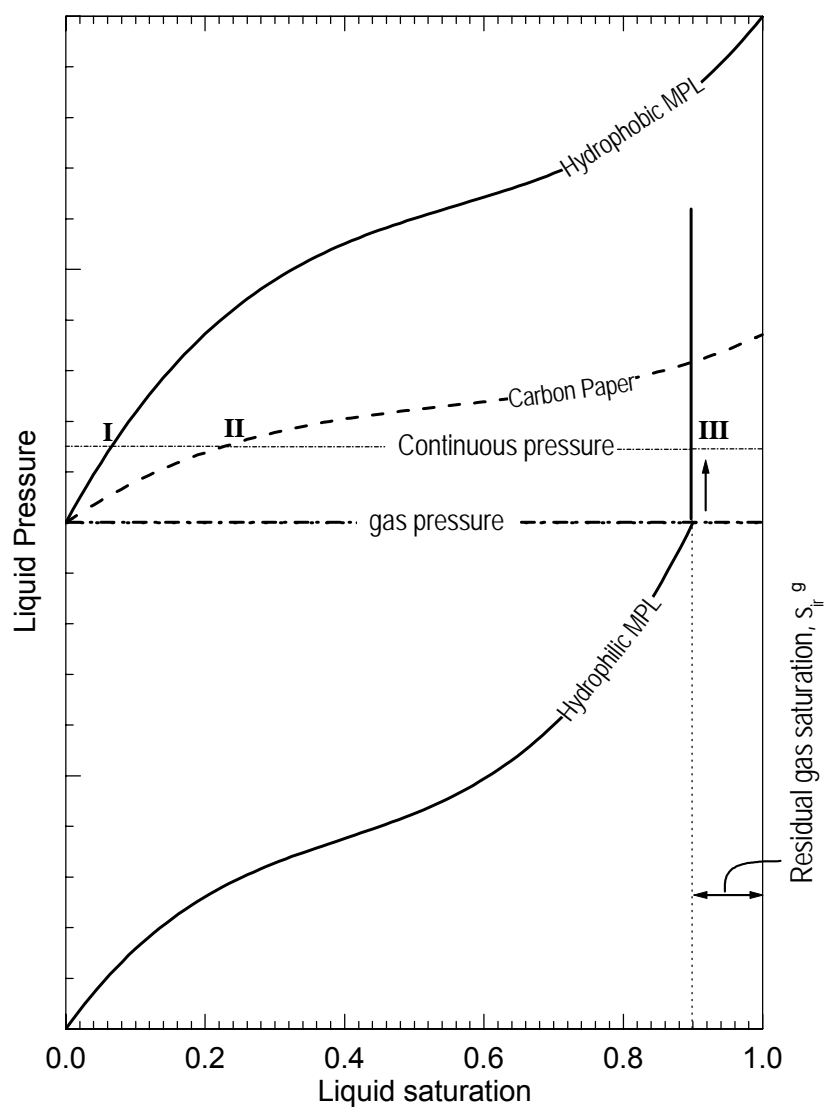
Figure 7.7 Schematic illustration of liquid-phase pressure profiles in different diffusion media. The dotted line is a hypothesized line, indicating a continuous pressure at the interface between different diffusion media. The three points **I**, **II**, and **III** indicate the liquid saturations in carbon paper, hydrophobic MPL, and hydrophilic MPL, respectively.
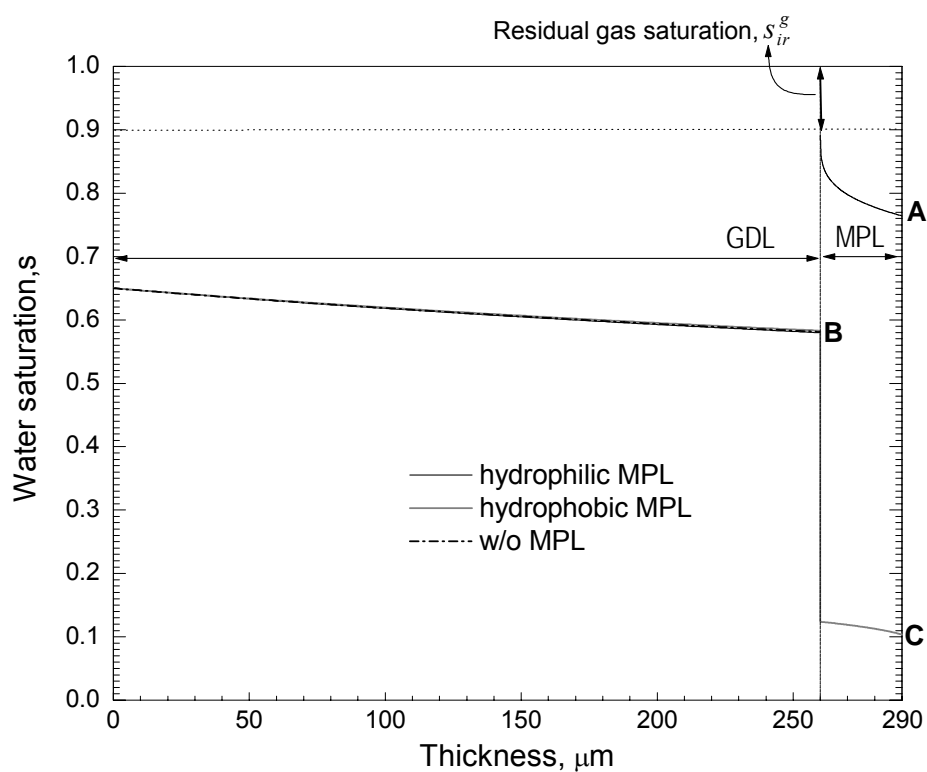
Figure 7.8 Calculated liquid water saturation profiles in three different anode diffusion media. **A**, **B**, and **C** in the figure indicate water saturation levels at the anode catalyst layer interface for hydrophilic MPL, w/o MPL, and hydrophobic MPL, respectively. α-values used in these calculations are obtained from experimental measurements.
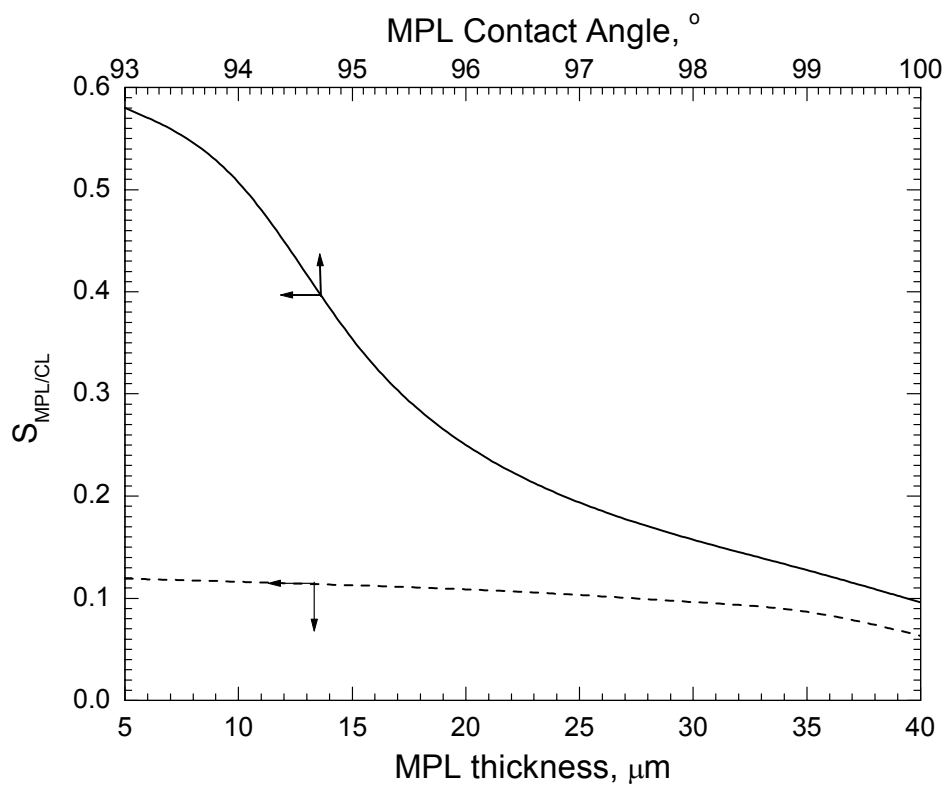
Figure 7.9 Influence of hydrophobic MPL thickness and contact angle on water saturation at the interface of anode catalyst layer/MPL.

Chapter 8 DIRECT FEED OF HIGHLY-CONCENTRATED METHANOL

8.1 Introduction

Feeding high concentration methanol solution directly into the anode is highly desirable for portable applications, as this will dramatically increase the system energy density or run time per charge. Unfortunately, this goal remains a great challenge, and so far no use of high concentration methanol in a common electrochemical cell has been realized. The technical challenges associated with direct-feed of highly-concentrated fuel include methanol and water crossover through the currently available PFSA membranes. An increased methanol concentration results in a high concentration gradient across the membrane and, consequently, methanol crossover is dramatically increased. Kim et al. (2003) used Pd-impregnated Nafion 117 membrane to block methanol crossover; however, only a quick-scan performance of a DMFC was given using 10 M methanol. It is clear that for $\alpha \approx 3$ as in this DMFC based on Nafion 117, high water crossover from the anode would make the methanol solution in the anode more concentrated with time, thus making long-term operation impossible. Although there have been reports on new hydrocarbon membranes that successfully demonstrated three- to ten-fold reduction in methanol permeability and methanol crossover rate, no demonstration of these new membranes featuring low methanol crossover in a DMFC enviroment has shown reasonable cell performance in the presence of 8M and higher methanol. This seemly

surprising situation can be partly explained by the fact that these new membranes have not achieved the sufficiently low water crossover required to operated on high-concentration methanol solution, as discussed in Chapter 6 in relation to Table 6.1. Thus, low-*a* MEAs, such as those developed in previous chapters, are an enabling technology for direct use of concentrated methanol. This chapter describes a novel DMFC to demonstrate direct feed of high concentration fuel (i.e. 10M) without sacrificing cell performance (e.g. fuel efficiency, power density, energy efficiency etc.).

8.2   Face-feed anode flowfiled

Use of high-concentration methanol solution entails a very small flow rate because the methanol concentration is already high. For small flow rates, a serpentine flowfield will experience overly rich methanol solution at the inlet and overly dilute solution at the outlet. Instead, a face-feed flowfield is utilized, in which the methanol solution is injected uniformly into the anode flowfield in the normal direction through a perforated plate. As shown in Figure 8.1, the face-feed is realized by an anode graphite porous plate (pore size of 100 μm) so that every part of the anode is equally accessed by the same methanol concentration. The pore size and permeability of the face-feed plate are carefully designed to control the diffusion of methanol. With direct feed of 10 M methanol, the anode stoichiometry is controlled at ~1.2; thus, methanol crossover must be lower than 20%.

8.3   Results and Discussion

When water is not recovered from the cathode exhaust, the maximum allowable concentration of anode fuel is determined by water and methanol losses from the anode compartment. The molar rate of methanol loss from the anode is represented by

$$N_{CH_3OH} = (1+\beta)\frac{I}{6F} \qquad [8.1]$$

where β is the ratio of crossover methanol to methanol consumed for power generation, and F is Faraday's constant. "1" on the right hand side of the above equation represents one mole of methanol consumed in the anode catalyst layer for power generation, *i.e.* to produce the current density I. Similarly, the molar rate of water loss from the anode is given by

$$N_{H_2O} = (1+6a)\frac{I}{6F} \qquad [8.2]$$

"1" described in the bracket corresponds to one mole of water consumed in the anodic reaction. The molar ratio of methanol to water supplied to the anode is thus equal to

$$N_{H_2O} : N_{CH_3OH} = (1+6a):(1+\beta) \qquad [8.3]$$

In this experiment, methanol stoichiometry is controlled at very small value (around ~1.2 for 10M methanol), indicating that β is less than 0.25 or fuel efficiency higher than 80%. Therefore, the fuel concentration equivalently given by the molar ratio is solely depending upon the water crossover coefficient α, according to Eq. 8.3. In order to enable direct use of 10M methanol fuel, α must be reduced to below ~0.39.

Figure 8.2 compares the quick-scan DMFC polarization using 10 M and 2M methanol. The performance of 10M cell is ~18mV lower than that of 2M cell at

150mA/cm^2, probably due to its slightly higher methanol crossover. Considering the small anode stoichiometry used in this work (1.2~1.3), however, during steady-state operation methanol crossover cannot exceed 20%. This is verified by the cell performance during the long-term constant-current discharge in Figure 8.3, where the 10M cell has almost identical performance as the 2M cell. Using 2 M methanol, the cell performance is fairly stable even with very small cathode stoichiometry (ξ_c=2). The average power densities are 58, 66, and 72mW/cm^2, at 150, 175, and 200mA/cm^2, respectively. α values at different current densities are around ~0.27. Subtracting the water generated from crossover methanol, the net values are only around 0.1, indicating a feasibility of using ~15M methanol concentration. Using 10 M methanol, at 150mA/cm^2, a steady-state power density of ~59mW/cm^2 is reached; and the average power density increases to ~67mW/cm^2 when current density increases to 175mA/cm^2. The relatively large cell voltage fluctuation is supposed to be related to carbon dioxide and methanol transport dynamics in the anode/porous plate interface.

When 15M methanol is used, we encountered a problem, a large periodic cell voltage oscillation, as shown in Figure 8.4. The cell voltage oscillates between ~0.45V and 0.1V. This oscillation is supposed to be related to cathode potential fluctuation due to methanol crossover. After applying a current, the intermediate species of MeOH oxidation are slowly poisoning the cathode Pt surface, forming Pt oxide. CO is widely considered to be the main poisoning residue. Owing to the coverage of poisoning species, the cathode overpotential increases to meet the applied current until the overpotential is sufficiently high for oxidation of methanol and the intermediate species (Krausa and Vielstich, 1995).

The cathode Pt surface is thus cleaned and consequently the overpotential is reduced rapidly. Now the cycle starts again. The whole process is illustrated in Figure 8.5.

The minimum scale of the digital pump in this experiment is 0.01cc/min, which cannot accurately control methanol stoichiometry when highly-concentrated methanol solution is employed. Precise control of anode methanol flowrate by more advanced pump might be the key to solve this problem.

8.4   Summary

Direct feed of highly-concentrated methanol has been successfully demonstrated in this chapter. Using 10 M methanol, a steady-state power density of ~59 mW/cm^2 is reached at 150 mA/cm^2, and increases to 67 mW/cm^2 when current density rises to 175 mA/cm^2. When 15M methanol is used, however, there is a large cell voltage oscillation, which is supposed to be related to cathode potential fluctuation due to methanol crossover.

1. MEA
2. Anode porous plate
3. Cathode graphite endplate
4. Anode graphite endplate
5. High-con MeOH inlet
6. Anode outlet
7. Dry air inlet
8. Cathode outlet
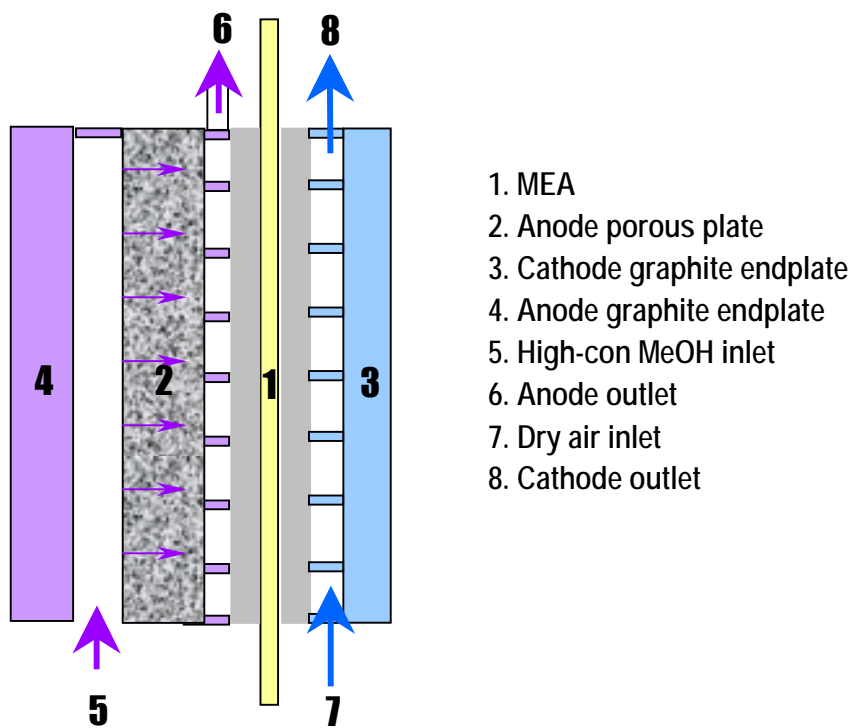
Figure 8.1 Schematic illustration of a DMFC operating directly on high concentration fuel with a face-feed anode flow plate.
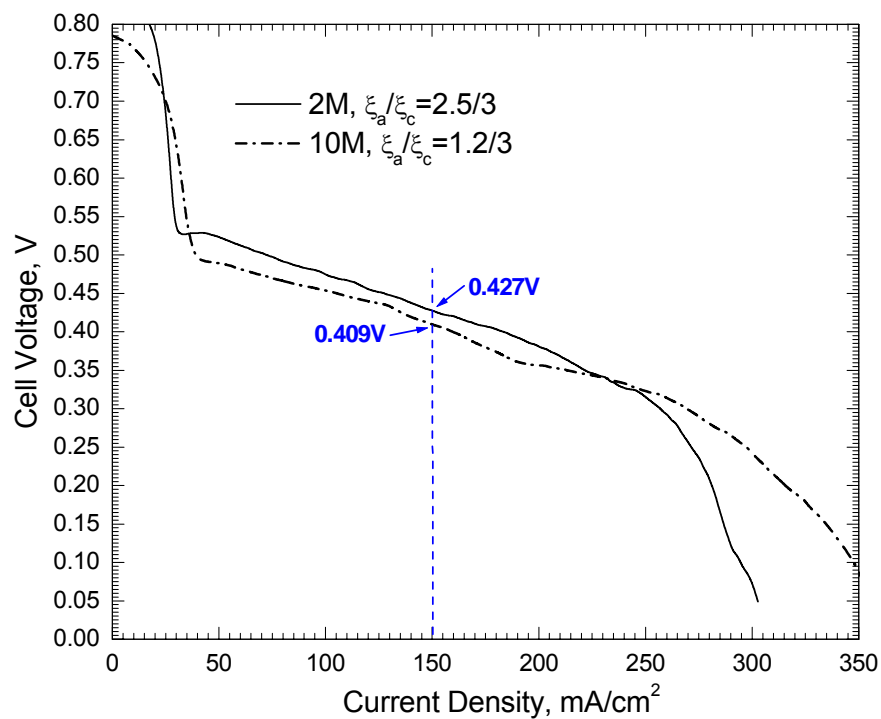
Figure 8.2 Quick-scan polarization curves of 12 cm^2 (Nafion 112) face-feed DMFCs with 2M and 10M methanol feed. Cell temperature 60°C, ambient pressure on both sides. Catalyst loadings: 6.3 mgPtRu/cm^2 at anode, 4.0 mgPt/cm^2 (Pt black) at cathode.
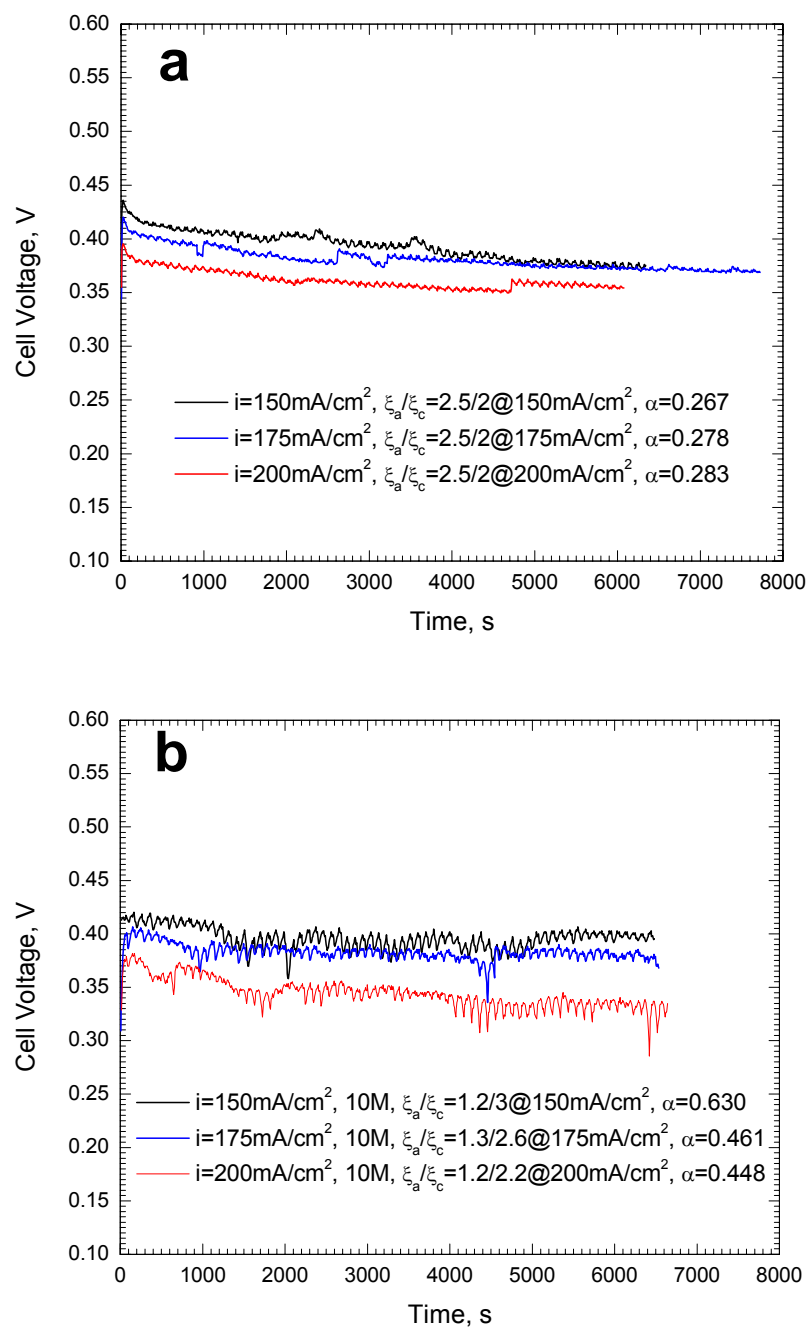
Figure 8.3 Steady-state performance of 12 cm^2 face-feed DMFCs with (a)2M and (b)10M methanol. Cell temperature 60°C, both ambient pressure on both sides.
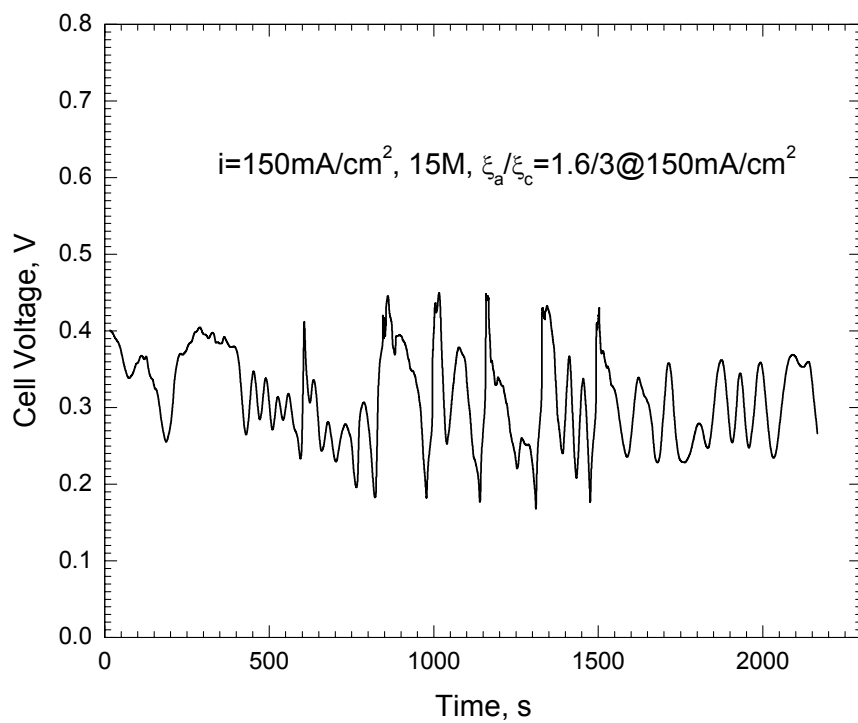
Figure 8.4 Cell voltage oscillation during constant-current discharge using 15M methanol.
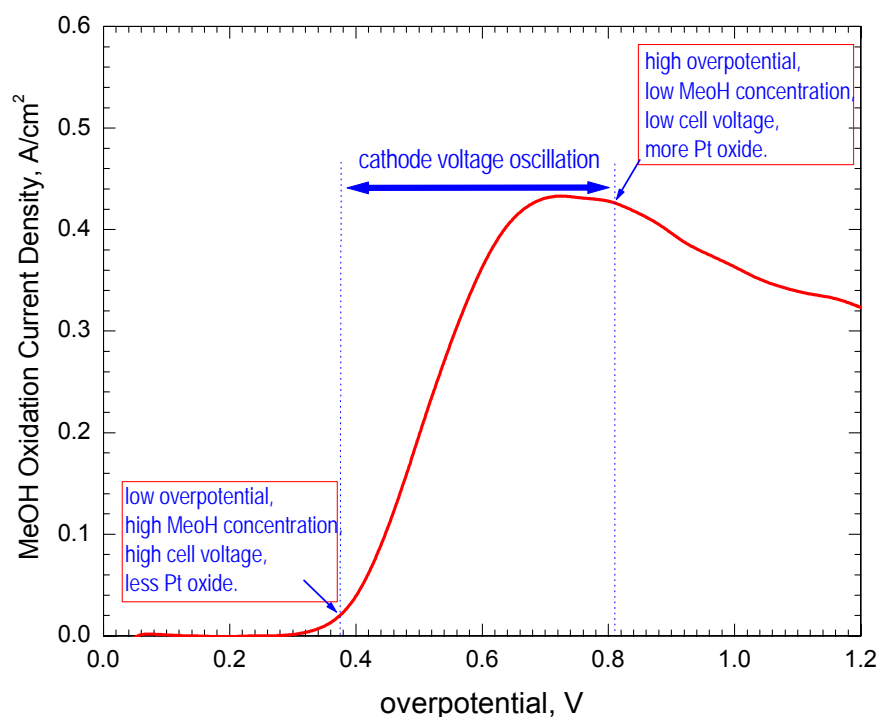
Figure 8.5 Schematic diagram of cathode potential oscillation in the presence of methanol as a plausible mechanism for cell voltage fluction seen in constant-current discharge using 15M methanol. The solid curve in the figure is measured methanol current at the cathode Pt surface. At 60°C, 0.19ml/min 2M methanol and 150ml/min H$_2$ were fed to the cathode and anode, respectively; while voltage was scanned from 0~1.2V.

Chapter 9 CONCLUSIONS

An advanced DMFC MEA has been developed in this thesis, aiming to enhance electrode kinetic and transport properties as well as to reduce methanol and water crossover. MEA fabrication, electrochemical characterization, electron-microscopic surface morphology analysis, and detailed computational modeling are combined to develop a relationship between intrinsic MEA structure/property and cell performance, and to understand fundamental electrochemistry and transport process.

Fabrication procedure and electrode microstructure have a large impact on electrochemical performance of catalyst layers. Heat-treatment influences the characteristics of DMFC anodes. Short-cured anodes have low ionomer crystallinity, and thus swell easily in contact with methanol solution, creating a much denser anode structure and giving rise to higher methanol transport resistance than long-cured anodes. Appropriate porosity, catalyst and ionomer distributions are essential for the cathode catalyst layer to achieve optimized performance at low air stoichiometry. Higher porosity near the GDL is helpful for O_2 transport and byproduct removal. Catalyst layers with a stepwise porosity distribution, with porosity higher near the GDL and lower near the membrane, perform better than those with a linear distribution, exhibiting more uniform O_2 distribution, thus extending the reaction zone inside toward the membrane. Similarly, appropriate ionomer distribution favors oxygen solubility, oxygen transport and proton conduction simultaneously, resulting in better oxygen reduction kinetics and higher limiting current density.

The methanol crossover effect has been studied by a mathematical model. Two-phase, multi-component transport model and multi-step electrochemical kinetics are incorporated for accurate prediction of species transport, polarization curve and DMFC cathode mixed potential. The detrimental effect of methanol crossover is found to be more pronounced when air is used at the cathode. Oxygen concentration diminishes dramatically in the DMFC cathode due to high consumption rate of methanol oxidation and oxygen reduction, resulting in high water saturation. In order to maintain the applied current, the cathode overpotential has to increase to offset the oxygen concentration loss as well as to support the parasitic current. DMFC performance is thus very sensitive to air stoichiometry, and there is a minimum air flowrate required to sustain efficient and stable operation of the cathode. The cathode performance in a DMFC approaches that of the H_2/air cell at high current densities, where methanol crossover and hence its detrimental effects become trivial. Reducing methanol crossover and using methanol-tolerant cathode catalysts are identified as two primary approaches to alleviate the parasitic reaction and increase performance.

Low water crossover and low methanol crossover are essential requirements of a DMFC for portable application. A cathode MPL is coated on backing layers to build up hydraulic pressure, enabling water back-permeation from the cathode to anode. This, in conjunction with a thin polymer membrane, results in 3-4 times lower water crossover coefficient between the anode and cathode than use of Nafion 117. α value has been further reduced by the use of a hydrophobic anode MPL. Methanol transport in the anode is not influenced by a hydrophobic MPL, but is inhibited by a hydrophilic one. α value measurements under various current densities verified that the MEA with a hydrophobic

MPL has α values several times smaller than those with a hydrophilic or without MPL. It was concluded from theoretical calculations that the substantial difference in water transport originates primarily from the surface wettability due to the fact that hydrophobic MPL, with a high entry liquid pressure, pushes liquid water into the hydrophilic media or carbon paper and hence results in a very small liquid saturation in the anode. Subtracting the water generated from crossover methanol, the net values are only around 0.2, indicating the feasibility of using ~10M methanol concentration. The resulting low-α MEA provides a basic element for DMFC systems using high concentration or pure methanol. Direct feed of 10M methanol has been successfully demonstrated. Using 10 M methanol, a steady-state power density of ~59 mW/cm^2 is reached at 150 mA/cm^2, and increases to 67 mW/cm2 at 175 mA/cm^2.

REFERENCES

Antoine O., Butel Y., Ozil P., Burand R., *Electrochem. Acta* 45 (2000) 4493.

Antolini E., Giorgi L., Pozio A., Passalacqua E., J. Power Sources, **77** (1999) 136.

Aricò A. S., Srinivasan S., and Antonucci V., *Fuel Cells,* **1**, 133 (2001).

Aricó A.S., Baglio V., Blasi A.D., Modica E., Antonucci P.L. and Antonucci V., *J. Electroanal. Chem.*, **557**, 167 (2003).

Aricó A.S., Baglio V., Modica E., Blasi A.D. and Antonucci V., *Electrochem. Commun.*, **5**, 164 (2004).

Aricó A.S., Cretì P., Modica E., Monforte G., Baglio V. and Antonucci V., *Electrochim. Acta*, **45**, 4319 (2000).

Baldauf M. and Preidel W., *J. Power Sources*, **84**, 161 (1999).

Bernardi D.M. and M.W. Verbrugge, *J. Electrochem. Soc.,* **139,** 2477 (1992).

Bittins-Cattaneo B., Wasmus S., Lopez-Mishima B and Vielstich W., *J. Appl, Electrochem.*, 23, 625 (1993).

Blum A., Duvdevani T., Philosoph M., Rudoy N. and Peled E., *J. Power Sources*, **117**, 22 (2003).

Carrette L, Friedrich K. A., Stimming U., *Chem. Phys. Chem.,* **1,** 162 (2000).

Carrette L, Friedrich K. A., Stimming U., *Fuel Cells,* **1**, 5 (2001).

Chu D. and Gilman S., *J. Electrochem. Soc.,* 141, 1770 (1994).

Colbow K.M., Bolli G., Pierre J.S. and Wilkinson D.P, in Wieckowski A. and Itaya K. (Eds.), *Electrode processes, The Electrochemical Society Proceedings Series*, Pennington, NJ, PV 96-8, 322 (1996).

Eikerling M. and Kornyshev A.A., *J. Electroanal. Chem*., **453,** 89 (1998).

Eikerling M. and Kornyshev A.A., *J. Electroanal. Chem*., **475,** 107 (1999).

Eikerling M., Kharkats Y.I., Kornyshev A.A., and Volfkovich Y.M., *J. Electrochem. Soc.,* **145,** 2684 (1998).

Fuller T.F. and Newman J., *J. Electrochem. Soc.* 140 (1993) 1218.

Gottesfeld S., and Zawodzinski T.A., in *Advances in Electrochemical Science and Engineering*, Vol. 5 (Eds) Alkire R.C., Gerischer H., Kolb D.M., and Tobias C.W., p.197, Wiley and Sons, New York (1998)

Gurau V., Liu H., and Kakac S., *AIChE J.* 44 (1998) 2140.

Halpert G., Narayanan S.R., Valdez T., Chun W., Frank H., Kindler A., Surampudi S., Kosek J., Cropley C. and LaConti A., in *Proceedings of the 32nd Intersociety Energy Conversion Engineering Conference*, Vol. 2, pp.774, AIChE, New York (1997).

Heinzel A. and Barragan V.M., *J. Power sources*, **84**, 70 (1999).

Hickner M.A., Ghassemi H., Kim Y.S., Einsla B.R., and McGrath J.E., *Chem. Rev*., **104**, 4587 (2004).

Hsu C.H., Wan C.C., *J. Power Sources* **115,** 268 (2003).

Janssen G.J. and Overvelde M.L., *J. Power Source,* **101,** 117 (2001).

Jiang R. and Chu D., *J. Electrochem. Soc*., **151**, A69 (2004).

Johnson E., *Fuel Cell Bulletin*, Nov. **12,** (2004).

Jusys Z. and Behm R.J., *Electrochimica Acta*, 49, 3891 2004.

Kauranen P.S., Skou E., *J. Electroanal. Chem*., **408,** 189 (1996).

Kim Y.M., Park K.W., Choi J.H., Park I.S., and Sung Y.E., *Electrochem. Comm., 5*, 571 (2003).

Kocha S.S., in: Vielstich W., Lamm A., Gasteiger H. (Ed.), *Handbook of Fuel Cells - Fundamentals, Technology and Applications*, Vol. 3, Wiley and Sons Ltd., 2003, Ch. 43.

Krausa M., Vielstich W., *J. Electroanal. Chem*., **399,** 7 (1995).

Kulikovsky A.A., *Electrochem. Commun.,* 6, 1259 (2004).

Kulikovsky A.A., *J. Electrochem. Soc.,* 152, A1121 (2005).

Lee S.J., Mukerjee S., McBreen J., Rho Y.W., Kho Y.T., Lee T.H., *Electrochim. Acta,* 43 (1998) 3693.

Li W.S., Tian L.P., Huang Q.M., Li H., Chen H.Y., Lian X.P., *J. Power Sources,* 104 (2002) 281.

Lim C. and C.Y. Wang, *Electrochimica Acta,* **49,** 4149 (2004).

Lim C. and Wang C. Y., *J. Power Sources*, **113**, 145 (2003).

Liu F. Q., Lu G. Q. and Wang C. Y., *J. Electrochem. Soc.*, **153**, A543 (2006).

Liu F.Q. and Wang C.Y., *Electrochim. Acta*, **50,** 1413 (2005).

Liu L., Pu C., Viswanathan R., Fan Q., Liu R. and Smotkin E. S., *Electrochim. Acta*, **43**, 3657 (1998).

Lu G.Q. and C.Y. Wang, in *Transport Phenomena in Fuel Cells*, B. Sunden and M. Fahgri, Editors, WIT Press, In print (2005).

Lu G.Q., Liu F.Q. and Wang C.Y., *Electrochem. Solid-State Lett.*, **8,** A1 2005.

Marr C. and Li X., *J. Power Sources* **77** (1999) 17.

Meier F. and Eigenberger G., *Electrochim. Acta,* **49,** 1731 (2004).

Mueller J.T., Uran P.M., Hölderich W.F., *J. Power Sources,* **84,** 157 (1999).

Mueller J.T., Uran P.M., *J. Power Sources,* **75,** 139 (1998).

Müller J., Frank G., Colbow K., and Wilkinson D., in *Handbook of Fuel Cells—Fundamentals, Technology and Applications,* W. Lietsich, A. Lamm, and H. A. Gasteiger, Editors, Vol.4, Chap. 62, John Wiley & Sons, Chichester (2003).

Murgia G., Pisani L., Shukla A.K., and Scott K., *J. Electrochem. Soc.,* 150, A1231 (2003)

Narayanan S.R., Frank H., Jeffries-Nakamura B., Smart M., Chun W., Halpert G., Kosek J. and Cropley C., in *Proton Conducting Membrane Fuel Cells I*, Gottesfeld S., Halpert G., Landgrebe A., Editors, PV *95-23,* p. 278, The Electrochemical Society Proceedings Series, Pennington, NJ, (1995)

Nguyen T.V. and White R.E., *J. Electrochem. Soc.,* **140,** 2178 (1993).

Nordlund J., Lindbergh G., *J. Electrochem. Soc.,* 149 A1107 (2002).

Oskada T., Xie G., and Meeg M., *Electrochim. Acta,* **43,** 2441 (1998).

Paik C.H., Jarvi T.D., and O'Grady W.E., *Electrochem. Solid-state Lett.*, **7,** A82 (2004)

Pasaogullari U. and Wang C. Y., *J. Electrochem. Soc.*, **151**, A399 (2004).

Pasaogullari U. and Wang C. Y., *J. Electrochem. Soc.*, **152**, A380 (2005).

Pasaogullari U. and Wang C.Y., *Electrochim. Acta*, **49**, 4359 (2004).

Passalacqua E., Lufrano F., Squadrio G., Patti A., and Giorgi L., *Electrochim. Acta*, **46,** 799 (2001).

Patankar S.V., *Numerical Heat Transfer and Fluid Flow*, Hemisphere, Washington DC, 1980.

Paulus U.A., Schmidt T.J. and Gasteiger H.A., in *Handbook of Fuel Cells— Fundamentals, Technology and Applications,* W. Lietsich, A. Lamm, and H. A. Gasteiger, Editors, Vol.2, Chap. 38, John Wiley & Sons, Chichester (2003).

Peled E., Blum A., Aharon A., Philosoph M. and Lavi Y., *Electrochem. Solid-State Lett.*, **6**, A268 (2003).

Peled E., Livshits V., Rakhman M., Aharon A., Duvdevani T., Philosoph M., and Feiglin T., *Electrochem. Solid-State Lett.,* **7**, A507 (2004).

Piela P., Eickes C., Brosha E., Garzon F., and Zelenay P., *J. Electrochem. Soc.,* **151,** A2053 (2004).

Qi Z., Kaufman A., *J. Power Sources,* **113**, 37 (2003).

Ren X. and Gottesfeld S., *J. Electrochem. Soc.,* **148,** A87 (2001).

Ren X., Wilson M. S. and Gottesfeld S., *J. Electrochem. Soc.,* **143**, L12 (1996).

Ren X., Springer T.E., and Gottesfeld S., *J. Electrochem. Soc*., **147**, 92 (2000).

Ren X., Springer T.E., T.A. Zawodzinski, and S. Gottesfeld, *J. Electrochem. Soc.,* **147**, 466 (2000)

Ren X., Zelenay P., Thomas S., Davey J. and Gottesfeld S., *J. Power Sources*, **86**, 111 (2000).

Sasikumar G., Ihm J.W., Ryu H., *J. Power Sources,* **132,** 11(2004).

Scott K., Taama W.M., Kramer S., Argyropoulos P. and Sundmacher K., *Electrochim. Acta*, **45**, 945 (1999).

Song D., Wang Q., Liu Z., Navessin T., Eikerling M., Holdcroft S., *J. Power Sources,* **126**, 104 (2004).

Song D., Wang Q., Liu Z., Navessin T., S. Holdcroft, *Electrochimica Acta,* **50**, 731 (2004)

Song J.M., Cha S.Y., Lee W.M., *J. Power Sources,* **94**, 78, (2001).

Springer T.E., T.A. Zawodzinski, and S. Gottesfeld, *J. Electrochem. Soc.,* **138,** 2334 (1991).

Staiti P., Poltarzewski Z., Alderucci V., Maggio G., Giordano N., and Fasulo A., *J. Appl. Electrochem.*, 22, 663-667, 1992

Thomas S.C., Ren X., Gottesfeld S., and Zelenay P., *Electrochimica Acta*, **47,** 3741 (2002).

Uchida M., Aoyama Y., Eda E., Ohta A., *J. Electrochem. Soc.* 142 (1995) 4243.

Uchida M., Fukuoka Y., Sugawara Y., Ohara H., Ohta A., *J. Electrochem. Soc.* 145 (1998) 3708.

Um S., Wang C.Y., Chen K.S., *J. Electrochem. Soc.* 147 (2000) 4485.

Vielstich W., Paganin V.A., Lima F.H.B. and Ticanelli E.A., *J. Electrochem. Soc.,* 148, 502 (2001)

Wang C. Y. and Cheng P., *Adv. Heat Transfer*, **30**, 93 (1997).

Wang C. Y. and Cheng P., *Int. J. Heat Mass Transfer*, **39**, 3607 (1996).

Wang C. Y., *Chem. Rev.* (Washington, D.C.), **104**, 4727 (2004).

Wang C.Y., in *Handbook of Fuel Cells—Fundamentals, Technology and Applications,* W. Lietsich, A. Lamm, and H. A. Gasteiger, Editors, Vol.3, Part 3, p. 337, John Wiley & Sons, Chichester (2003).

Wang G.Q., Ph.D thesis, The Pennsylvania State University, 2003.

Wang J.T., Wasmus S. and Savinell R.F., *J. Electrochem. Soc.*, **143,** 1233, (1996)

Wang Q., Eikerling M., Song D., Liu Z., Navessin T., Xie Z., and Holdcroft S., *J. Electrochem. Soc.* **151,** A950 (2004).

Wang Z.H. and Wang,C.Y. *J. Electrochem. Soc.,* 150, 508 (2003).

Xie J., Garzon F., Zawodzinski T. and Smith W., *J. Electrochem. Soc.,* **151,** A1084 (2004).

Yang X.G., Zhang F.Y., Lubawy A., and Wang C.Y.*, Electrochem. Solid-state Lett.*, **7,** A408 (2004).

Zawodzinski T.A., Derouin C., Radzinski S., Sherman R.J., Springer T., Gottesfeld S., *J. Electrochem. Soc.,* **140**, 1041 (1993)

Zawodzinski T.A., Lopez C., Jestel R., Valerio J., and Gottesfeld S., *J. Electrochem. Soc*., **140** 1981 (1993).

Zawodzinski T.A., Springer T.E., Uribe F., and Gottesfeld S., *Solid State Ionics,* **60,** 199 (1993).

Zelenay P., et al., U.S. DOE Energy Efficiency and Renewable Energy, 2004 Merit Review and Peer Evaluation Meeting, Hydrogen, Fuel Cells and Infrastructure Technologies Program, Philadelphia, PA, May 24-27, 2004. http://www.eere. energy.gov/hydrogenandfuelcells/pdfs/review04/fc_47_zelenay.pdf

Zelenay P., U.S. DOE Energy Efficiency and Renewable Energy, 2003 Merit Review and Peer Evaluation Meeting, Hydrogen, Fuel Cells and Infrastructure Technologies Program, Berkeley, CA, May19-22, 2003. http://www.eere.energy.gov/hydrogenand fuelcells/pdfs/merit03/117_lanl_piotr_zelenay.pdf

Vita

Fuqiang Liu

Education
1997   B.S. in Polymer Science and Engineering, Beijing University of Chemical Technology, China

2002   M.S. in Chemical Engineering, Dalian Institute of Chemical Physics, Chinese Academy of Sciences, China

2006   PhD. in Materials Science and Engineering, Pennsylvania State University

Experience
1997.8-1999.7   Chemical Engineer, Dalian Institute of Chemical Physics, Chinese Academy of Sciences, China

2002.7-2002.12   HongKong University of Science and Technology

Publications
F.Q. Liu, G.Q. Lu, C.Y. Wang, *J. Electrochem. Soc.*, 153 (3) A543 (2006).

F.Q. Liu, C.Y. Wang, submitted to *Electrochim. Acta.* (2006).

F.Q. Liu, C.Y. Wang, submitted to *Electrochim. Acta.* (2006).

F.Q. Liu, C.Y. Wang, *Electrochim. Acta.*, 50, 1413 (2005).

G.Q. Lu, **F.Q. Liu** and C.Y. Wang, *Electrochem. Solid-State Lett.*, 8, A1(2005).

D.M. Xing, B.L. Yi, **F.Q. Liu**, Y.Z. Fu, H.M. Zhang, *Fuel Cells*, 5 (3) 406 (2005).

D.M. Xing, B.L. Yi, Y.Z. Fu, **F.Q. Liu**, H.M. Zhang, *Electrochem. Solid-State Lett.*, 7, A315 (2004).

F.Q. Liu, B.L. Yi, D.M. Xing, J.R. Yu et al., *J. Power Sources*, 124, 81 (2003).

F.Q. Liu, B.L. Yi, D.M. Xing, J.R. Yu et al., *J. Membrane Science*, 212, 213 (2003).

J.R Yu, B.L. Yi, D.M. Xing, **F.Q. Liu**, Z.G. Shao et al., *Phys. Chem. Chem. Phys.*, 5, 611 (2003).

Patents
C.Y. Wang, **F.Q. Liu**, Y. Sato, and E. Sakaue, *US Patent application* No. 11/251,763. (2005).

C.Y. Wang, G.Q. Lu, **F.Q. Liu**, T. Akiyama et al, *US Patent application* No.11/020,306. (2004).

C.Y. Wang, G.Q. Lu, W. Liu and **F.Q. Liu**, *US Patent application* No. 11/013,922. (2004).

F.Q. Liu, B.Y. Yi, D.M. Xing, J.R. Yu et al., *Chinese Patent Application*, 01136845.

F.Q. Liu, B.Y. Yi, D.M. Xing, J.R. Yu et al., *Chinese Patent Application*, 02122635.0.

B.L. Yi, J.R. Yu, **F.Q. Liu**, D.M. Xing, and H.M. Zhang, *Chinese Patent Application*, 01136817.9